The Influence of Stent Geometry on Haemodynamics and Endothelialisation

By:

Luke Boldock

A thesis submitted in partial fulfilment of the requirements for the degree of
Doctor of Philosophy

The University of Sheffield
Faculty of Engineering
Department of Mechanical Engineering

August 2017

Acknowledgements

I would like to thank my supervisor, Dr. Cecile Perrault, for her guidance and support throughout this project, from initially mentioning the open position through to making the finished article a reality. I appreciate being given the chance to undertake this research, with funding from the EPSRC, and also the freedom to pursue the many other opportunities afforded me over the last few years.

Thanks also to my co-supervisor Prof. Paul Evans, the members of the Evans lab for a constant supply of cells, and Prof. Julian Gunn and Dr. Ana Paula Narata for kindly providing stents. I'm also grateful to the skelet.AL group for their help with micro-CT scanning; Drs. Christopher Tse, Michele Schirru and Peter Laity for their help with viscometry; and Dr. Andrew Narracott, Amanda Inzoli and Silvia Bonardelli for the collaboration on *in silico* modelling. Thanks to Dr. Sarah Hsiao for the introduction to *in vitro* models and to Dr. Svenja Dannewitz Prosseda for helping to generate data despite uncooperative cells' best efforts, part of co-authored work which is included here with permission.

The members of INSIGNEO have made the group a welcoming, friendly and fun place to spend the last few years, for which I'm very grateful to them all. Special thanks to Ana and Sara for help with ScanIP and Amira, the members of the C+ lab for their support and assistance (in between conversations about risk assessments), and to Claudia, Rob and Liam for always doing Good Science.

Finally, a huge thank you to my family. To my parents, for everything they've done to help me achieve not only this, but everything else in life; and to Emma, for an unending amount of support, help, patience and understanding (and even more cake).

Abstract

Every year, millions of people worldwide undergo stent implantation to widen narrowed arteries or to redirect blood away from aneurysms. The rapid post-operative regrowth of a healthy endothelial layer, a key factor in stented artery repair, would reduce complications and improve quality of life for many patients. While this has long been a clinical or pharmaceutical issue, this project considers the role of local haemodynamics, specifically the effects of stent-modified wall shear stress on the endothelium.

Endothelial cells have a strong mechanobiological response to wall shear stress magnitude, direction and time variance. To understand the impact of stent geometry on this response through altered fluid dynamics, a novel model vessel was developed for the deployment of a wide range of coronary and flow diverter stents *in vitro*. The model allowed the observation of both endothelial cell migration and, via particle tracking, disturbed flow within the stents. High-resolution micro-computed tomography scanning techniques replicated stent geometry *in silico*, enabling computational fluid dynamics simulations for the assessment of wall shear stress distribution.

Coronary stents greatly influenced fluid flow. The orientation and distribution of tracked particle streamlines were transformed proximal to stents struts, which were also areas of reduced wall shear stress. These areas correlated with zones of reduced cell migration. Flow diverter stents had a lesser impact on observable particle flow; yet endothelial cell migration within them was completely arrested. This is likely due to their structure directing flow away from the wall and reducing shear stress to an even greater extent that coronary stents, over a more substantial area.

Dissimilar cell migration between coronary and flow diverter stents is a point of possible significance as the two are treated alike with respect to post-operative care and medication. Continued analysis of various geometries may enable the efficacy of individual stent designs to be quantified or predicted. By applying this knowledge in the future, careful stent design could reduce their impact, or exert an intentional, active influence on endothelial cells, to optimise the healing process.

Table of Contents

List of Figures

List of Tables

Nomenclature

Acronyms:

2/3D	Two-/three-dimensional
ARED	Anti-Restenotic Diffuser
AWA-WSS	Area weighted average wall shear stress
BMS	Bare metal stent
CABG	Coronary artery bypass graft
CAD	Computer aided design
CFD	Computational fluid dynamics
CHD	Coronary heart disease
CT	Computed tomography
DES	Drug eluting stent
DIR	Dynamic image range
EC	Endothelial cells
EDTA	Ethylenediaminetetraacetic acid
EPC	Endothelial progenitor cell
FCS	Foetal calf serum
FE	Finite element
FEP	Fluorinated ethylene propylene
fps	Frames per second
HCAEC	Human coronary artery endothelial cells
HLRFI	Haemodynamic low and reverse flow index
HU	Hounsfield units
HUVEC	Human umbilical vein endothelial cells

ICAM	Intercellular adhesion molecule
ID	Inner diameter
IMS	Industrial methylated spirit
ISR	In-stent restenosis
LSI	Low shear index
MACE	Major adverse cardiac event
MLC	Myosin light chain
MSA	Metal surface area
OSI	Oscillatory shear index
Pn	Cell culture passage number
PBS	Phosphate-buffered saline
PCI	Percutaneous coronary intervention
PDMS	Polydimethylsiloxane
PIV/PTV	Particle image/tracking velocimetry
PMMA	Polymethyl methacrylate
POBA	Plain old balloon angioplasty
PTFE	Polytetrafluoroethylene
ROCK	Rho-associated protein kinase
SSRE	Shear stress response elements
TAWSS	Time averaged wall shear stress
transWSS	Transverse wall shear stress
UDF	User defined function
VEGF	Vascular endothelial growth factor
VSMC	Vascular smooth muscle cells
XG	Xanthan gum
μCT	Micro-computed tomography

Symbols:

D	Diameter
E_L	Entrance length number
L	Entrance length
p	Pressure
Q	Flow rate
r	Radius
R^2	Coefficient of determination
Re	Reynolds number
V	Flow velocity
μ	Dynamic viscosity
ρ	Density
τ_{mean}	Mean wall shear stress

Chapter One

Introduction

The cardiovascular system consists of the heart, blood and blood vessels, and fulfils four main functions: the transport of oxygen, heat, and nutrients, and the rapid removal of metabolic waste products. Circulating blood is carried away from the heart within arteries and delivered throughout the body; including the vital supply to the brain via cerebral arteries, and the heart itself via coronary arteries. However, a variety of conditions can affect these blood vessels, impeding their ability to function and interrupting blood flow. Cardiovascular diseases, which include coronary heart disease and cerebral aneurysms, account for over 17 million deaths annually [1]. This figure is only expected to rise, as many major risk factors are lifestyle influenced: smoking, high fat and high cholesterol diets, obesity and lack of exercise.

Current, routine treatment of cardiovascular diseases involves the use of stents, bio-engineered devices which provide mechanical support or alter local mechanical conditions. This project considers those devices and the impact their mechanical, haemodynamic environment has on cell mechanobiology and, ultimately, on successful patient outcome.

1.1   Engineering solutions for coronary arteries

The coronary arteries are muscular distributing arteries, which supply blood to the heart. They ensure adequate oxygenation of the heart muscle (myocardium), constricting and dilating to match blood flow with oxygen demand. Given their crucial role, the performance of coronary arteries is unique. Blood flow per unit weight of the tissue being supplied is ten times greater than the whole body average. However, despite this high flow rate, the myocardium remains relatively poorly supplied due to its great O_2 demand. To compensate, a high proportion of O_2 is extracted from blood within the coronary vasculature: 65 - 75%, compared to a whole body average of 25% [2].

1.1.1 Coronary heart disease

The vital supply of blood to the myocardium can be affected by a condition known as coronary heart disease (CHD), in which deposits build up within the coronary arteries. This build up is a process known as atherosclerosis, with the deposits referred to as atherosclerotic lesions, or plaques. It can begin in childhood, but typically takes decades to progress to a symptomatic level.

Atherosclerosis is thought to be most likely initiated by endothelial cell (EC) dysfunction. These cells, which line the interior surface of blood vessels, are described in Section 1.3.1.1. Their dysfunction has been shown to be related to mechanical cues, including haemodynamic forces such as shear stress, and plaques commonly develop at areas of disturbed blood flow such as artery bifurcations or curvature. The mechanobiology of EC, the forces they are exposed to and their response, is covered in more detail in Section 1.4.

Once initiated by EC dysfunction, atherosclerosis progresses through a number of stages, listed here and illustrated in Figure 1.1 [3][4]:

1. The growth of a 'fatty streak', made up of lipoproteins (LDL, a form of cholesterol) and white blood cells.
   a. LDL particles penetrate the blood vessel wall, accumulate in small pools and are chemically modified by EC-produced oxidants.
   b. Modified LDL induce an inflammatory response in EC and vascular smooth muscle cells (VSMC), which in turn leads to the expression of molecules which promote white blood cell adhesion and migration.
   c. Macrophages, a form of white blood cell that engulfs target cells, substances or debris, ingest LDL and develop into fat-laden foam cells.
2. The formation and progression of plaque.
   a. The inner layer of the vessel wall continues to thicken with both continuing white blood cell accumulation and VSMC proliferation, triggered by growth factors released by foam cells and EC.
   b. VSMC apoptosis, calcification and fibrosis form a hard plaque cap, surrounding an LDL-rich core.

Fatty streak: gradual accumulation of LDL and macrophages.

Growth driven by lipoprotein accumulation.

Plaque formation: LDL pools form central core.

Plaque formation: growth of core and fibrous cap.

Growth driven by VSMC proliferation and fibrosis.

Plaque instability and rupture.
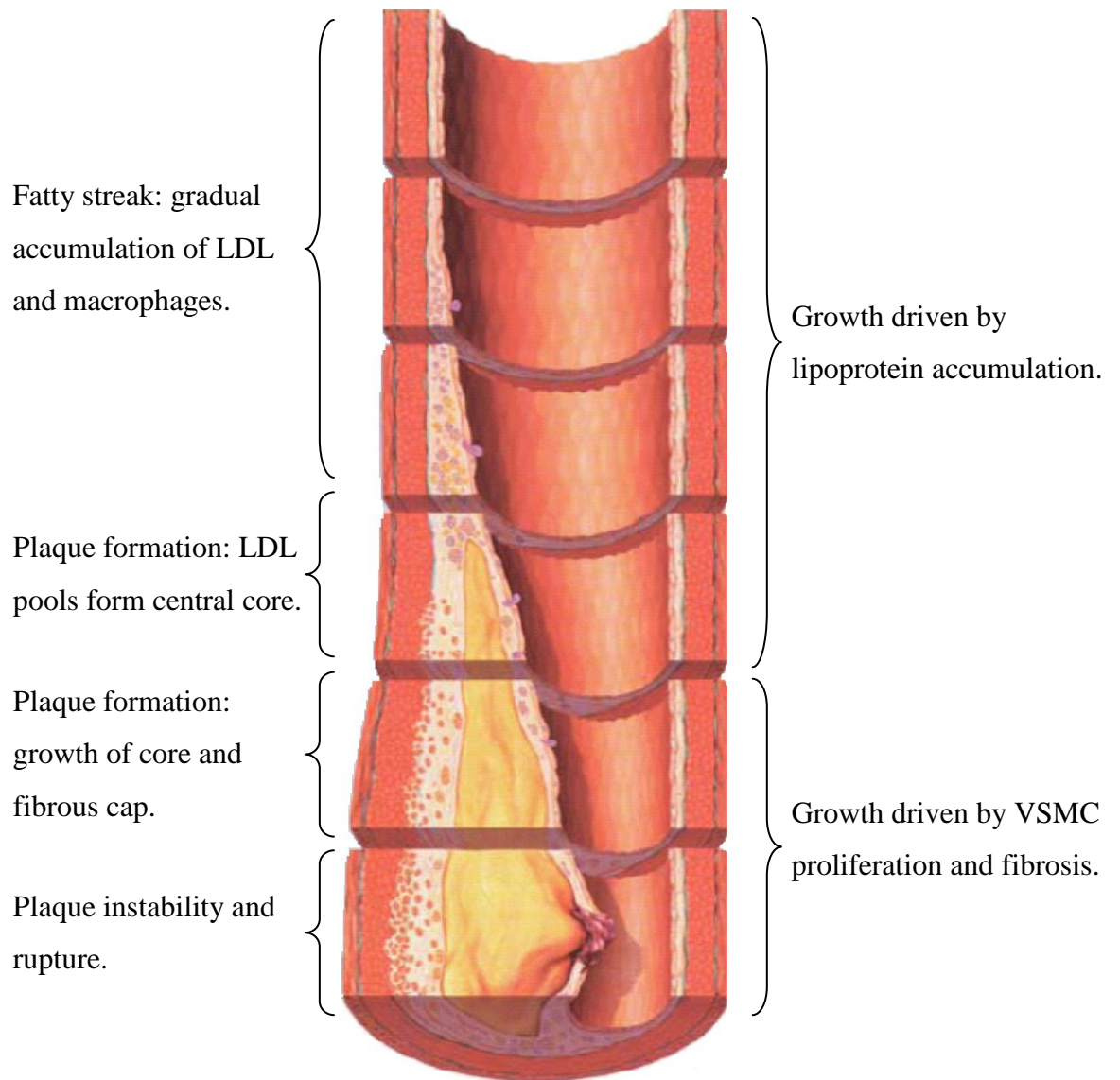
Figure 1.1 The development of atherosclerotic plaque

In coronary heart disease, atherosclerotic plaque gradually builds up within arteries, reducing blood flow. Its development begins with the accumulation of LDL and macrophages in a fatty streak (top), and progresses through the formation of a central LDL-rich core and hard, fibrous cap (centre). This can then lead to stenosis of the artery due to the ongoing growth of a stable, thick-capped plaque, or thrombus due to the rupture of thin-capped plaque (bottom). The process may take place over the course of several decades before becoming symptomatic.

(Reproduced with permission [3]*).*

3. Plaque growth and disruption, which poses two threats:

   a. The first is the risk of the rupture and detachment of plaques, particularly those with relatively thin fibrous caps. Rupture exposes the core and its contents to flowing blood, and the presence of lipoproteins and tissues within the core activates a coagulation response: the accumulation of platelets and deposition of fibrin [5]. A blood clot, or thrombus, is formed and this thrombus (or pieces of detached plaque) can completely block the artery and cause a heart attack (myocardial infarction).

   b. The second risk is a less acute, chronic process in which the lumen in gradually narrowed by the growth of more stable plaques with relatively thick fibrous caps. This reduces the supply of oxygenated blood. When myocardial demand can no longer be met, the deficit leads to tissue hypoxia, which causes chest pain (angina).

Poiseuille's law states that flow rate is proportional to the fourth power of vessel radius; therefore any narrowing will have a significant effect on blood supply. However, alternate collateral coronary circulation means atherosclerosis within a single arterial segment can progress to 75% lumen loss (a 256 fold decrease in flow rate) before symptoms appear and treatment is required [6]. Despite the body's ability to compensate for CHD, the disease claims the lives of 7.4 million people per year; making it not only the most fatal cardiovascular disease, but the single leading cause of death worldwide [1].

1.1.2 Stent treatment of the coronary arteries

There is no cure for CHD, although behavioural adjustment to mitigate lifestyle associated risk factors, such as stopping smoking, taking up exercise or a healthier diet, can help to prevent or slow its development [7]. In some cases, once symptoms develop they can be managed or treated through medication: beta-blockers block the effects of certain hormones (adrenaline, for example) to reduce the workload on the heart and relieve the symptoms of CHD; statins lower cholesterol by reducing its formation and increasing its removal in the liver; antiplatelets thin blood to inhibit

the formation of clots. However, medication may only delay the need for surgical intervention.

CHD has been treated by coronary artery bypass graft (CABG) since 1960. This is open-heart surgery, in which a healthy blood vessel segment from the body is connected to the affected coronary artery to re-route blood around the blockage. A less invasive procedure, percutaneous coronary intervention (PCI) was first performed in 1977 [8]. This involved the inflation of a balloon catheter to open narrowed arteries by squashing lesions and expanding the surrounding vessel ("plain old balloon angioplasty", or POBA). However, the rates of complications requiring re-intervention following POBA were high compared to CABG. Vessel injury and over expansion stimulated the growth of neointima, or arterial scar tissue, and post-treatment lumen diameter could be reduced due to elastic recoil of the wall [9].

In 1986 the minimally invasive percutaneous treatment of CHD was augmented with the use of small devices known as cardiovascular stents [8]. Stents are expandable metal tubes which are transported through the body via catheter and implanted at disease sites. In the coronary arteries, stents are deployed during the PCI procedure and are pre-loaded onto the same balloons which are used to compress plaque and widen narrowed arteries. These coronary stents remain in place when the balloon is withdrawn, to maintain the patency of treated vessels by acting as scaffolds and preventing the recoil of the vessel wall (Figure 1.2). A 'gold standard' stent expansion to artery diameter ratio of 1.1:1 to 1.2:1 is used to balance sufficient widening against the risk of injury [9]. Early bare metal stents (BMS) halved the complication rates seen in POBA [8]. The use of these devices to alleviate symptoms is now routine and has increased success rates in the treatment of CHD. In the UK today, the use of stents is recommended as good clinical practice, and over 90% of PCI procedures involve stent deployment [10]. Globally, over 3 million coronary stents are implanted each year [11].
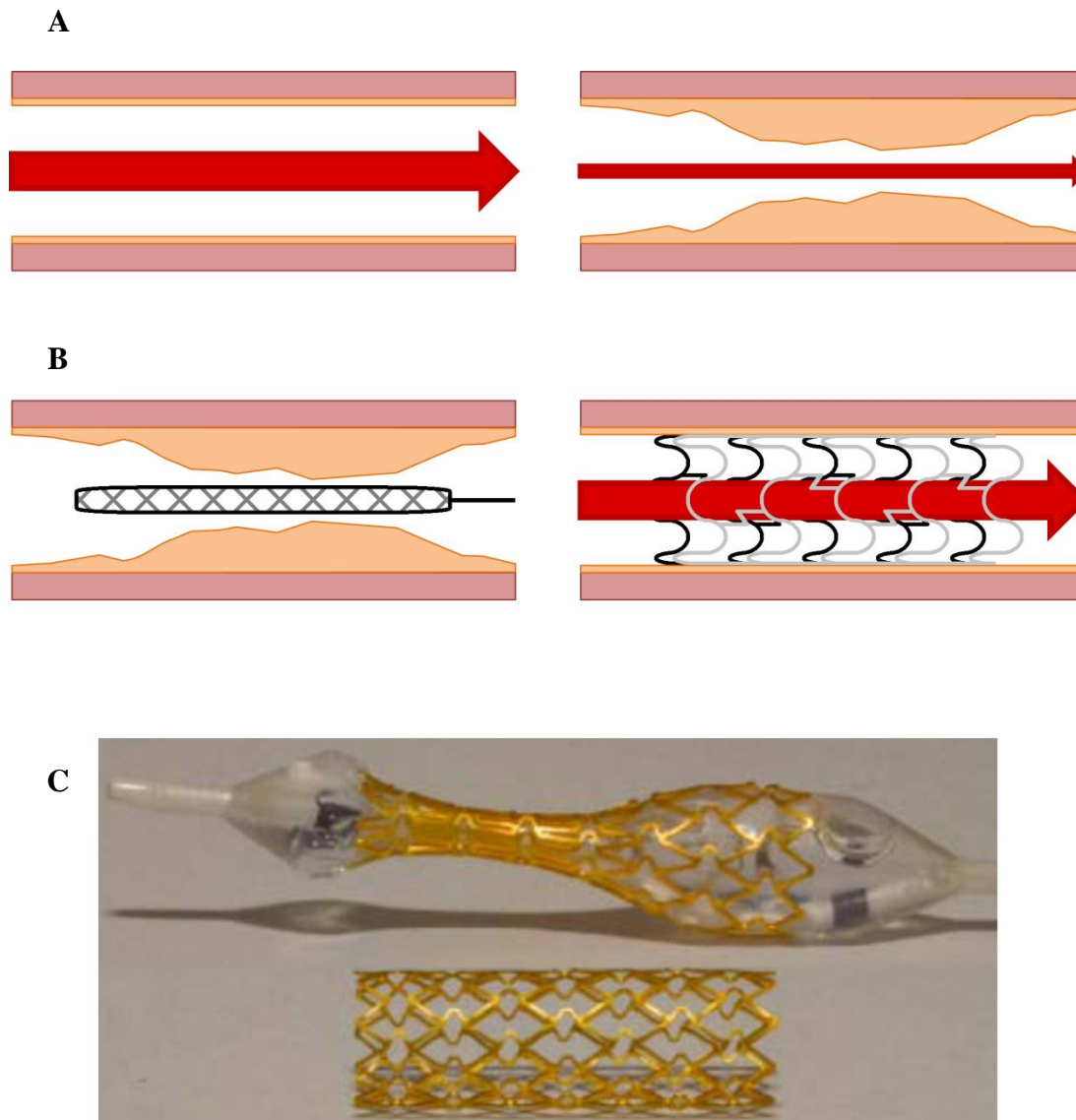
Figure 1.2 CHD and coronary stent deployment

A: The lumen of a normal coronary artery (left) is narrowed following the development of atherosclerotic plaque (right), reducing the supply of oxygenated blood to the heart (arrow).

B: The deployment of coronary stents over lesions (left), via the inflation of a balloon catheter, compresses the plaque, widens and scaffolds the artery, and restores normal blood flow (right).

C: An example of a typical slotted tube coronary stent, deployed via the inflation of a balloon catheter. *(Reproduced with permission* [12]*).*

1.1.3   Coronary stents

1.1.3.1   Requirements and design

A great many coronary stent designs are commercially available and clinicians must select the most appropriate based on a number of characteristics. In an effort to aid this selection, Hindlet *et al* (2005) classify stents according to four criteria [13]:

1. Technical
2. Mechanical
3. Clinical
4. Economic

Clinical criteria include the rates of complications and major adverse cardiac events (MACE) associated with each stent. Economic criteria are important in a public health setting, as the efficacy of stents must be weighed against their cost. Mechanical criteria describe the ability of the stent to perform its intended task. They can include stiffness to prevent elastic recoil and resist wall pressure, flexibility in order to conform to vessel curvature and crossing profile (the size of the packed, pre-deployed stent to be guided through the vasculature).

Technical criteria describe the physical attributes of the stent: its type, design, material and coating, and means of deployment. There are three main types of stent. 'Coil' stents consist of a continuous wound wire and are generally no longer used, as they have poor radial strength. 'Mesh' stents consist of a dense, symmetrical lattice of struts. 'Slotted tube' stents typically take the form of struts arranged in a series of rings, connected by bridge struts. The majority of modern coronary stents are slotted tubes, with the specific design of the rings and bridges varying between model and manufacturer (Figure 1.2C).

The specific design of individual stents can be described by a number of parameters [14][15], which include:

- Number of struts

- Strut thickness and width

- Strut contact angle, or its orientation with respect to the direction of flow

- Cross-sectional strut shape

- Cell size (here referred to as the inter-strut area, to avoid confusion with biological cells)

- Metal to artery ratio, or vessel wall coverage

- Bridge configuration (slotted tube stents only)

- Crown radius (slotted tube stents only)

- Peak to valley alignment (slotted tube stents only)

In improving stent performance, designers must select which of these parameters, illustrated in Figure 1.3, to optimise. For slotted tube coronary stents this process can be particularly complicated. For example, the number of struts and their contact angle affects both scaffolding of the artery wall and radial stiffness. The length of struts also affects stiffness, as well as the overall number of strut rings required along the stent's length. The number of rings can also be controlled with bridge length. Fewer, longer bridges compromise longitudinal stability, but too many bridges make the stent inflexible. The alignment of peaks and valleys further influences the number of rings per unit length, in addition to the chance of strut collision when bending, and the size of the inter-strut area. These areas may be closed (connected at every junction, resulting in smaller areas and reduced flexibility) or open (some junctions remain unconnected, resulting in greater flexibility but the risk of tissue prolapse within larger areas) [15].

The above describes the relationship between geometry and mechanical performance. Optimisation is made more complex by considering the influence on local haemodynamics, which affects the long-term performance of stents and their associated complications (discussed further in Section 1.5).

1.1.3.2 Manufacturing

The majority of slotted tube coronary stents are laser cut from a metal tube (or from a metal sheet which is then rolled and welded), enabling the precise and highly reproducible fabrication of intricate designs [14]. As this method produces struts of square or rectangular cross-section only, electrochemical polishing or tumbling can be used to blunt sharp edges and create rounder, more streamlined struts, in addition to removing slag [16].
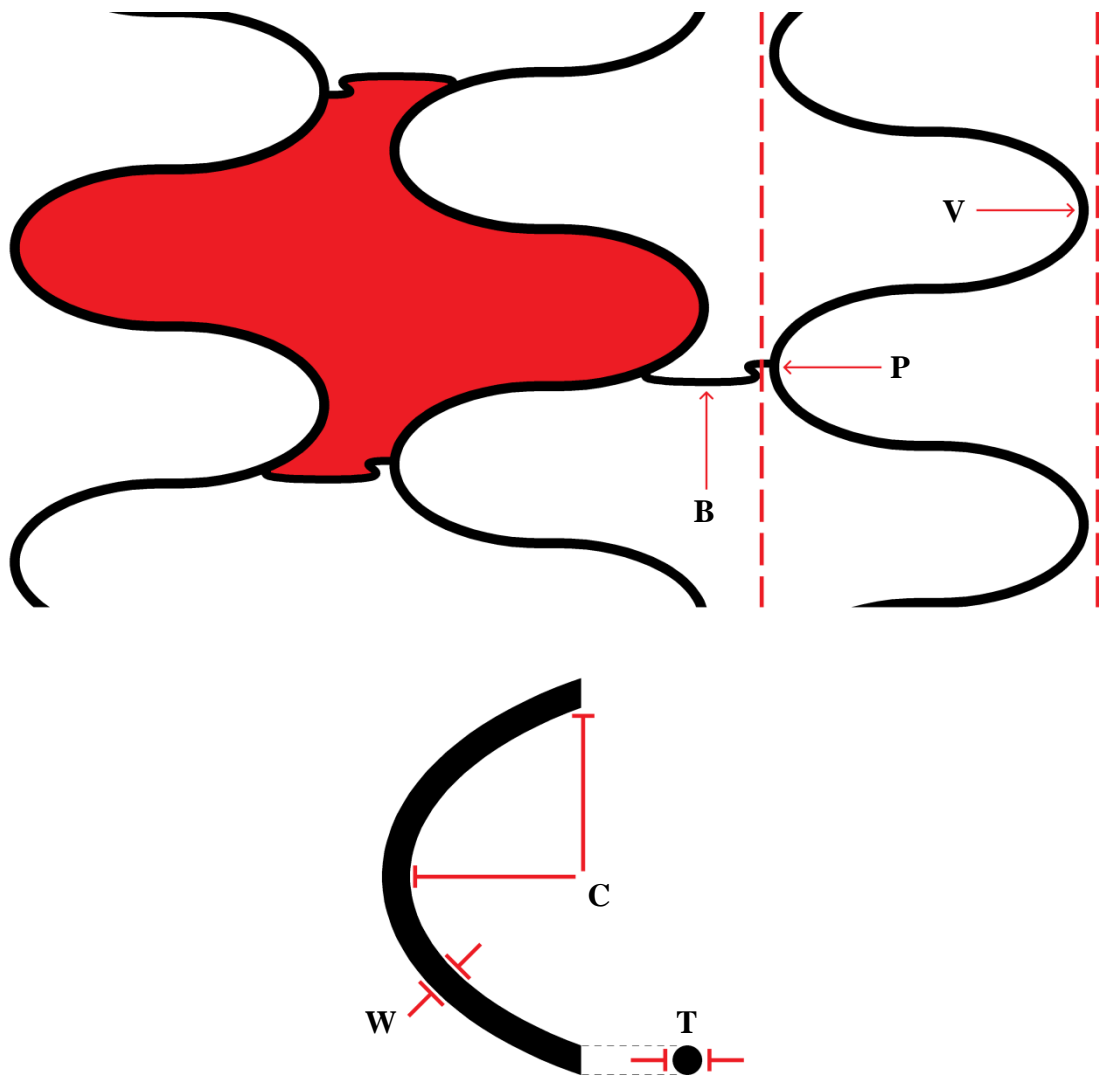
Figure 1.3 Design features of slotted tube coronary stents

Coronary stents consists of a number of variable features and design parameters. Circumferential rings of struts (top, between the dashed lines) repeat along the stent's longitudinal axis, are connected in sequence by bridge struts (B) and form enclosed inter-strut areas known as cells (red shaded region). The typical sinusoidal strut pattern forms peaks and valleys (P and V, assuming flow direction from left to right), of specific crown radius (C). Individual struts, of square, rectangular or rounded cross-section (bottom), have a thickness (T) and a longitudinal width (W).

Stents are manufactured from a range of materials, the majority of which are metal alloys [17]:

- Stainless steel has long been a commonly used material, due to its mechanical properties and resistance to corrosion.
- Tantalum and platinum-iridium alloys have both shown reductions in post-stent complications (Section 1.3.2) due to increased biocompatibility, but lack radial strength.
- Titanium is used in a number of biomedical implants as it is highly biocompatible. However, its low ductility means stents are rarely made of this material alone as they are prone to fracture during expansion.
- Cobalt-chromium alloys have also been previously applied in other biomedical implants. Their use is currently prevalent as, unlike titanium, the mechanical properties of these alloys allow extremely thin struts to be manufactured.

1.1.3.3 Complications in coronary stenting

The majority of PCI procedures with stent deployment are successful. Of the small number of unsuccessful procedures, approximately 90% fail due to an inability to deliver the stent to the lesion site [18]. Failure of correctly implanted stents can occur due to recoil or compression (if struts are too thin, or radial strength too weak), strut fracture (if too stiff) and longitudinal deformation (if too few bridge struts are present) [19].

However, successful PCI can still lead to late-stage stent failure weeks or months post-stent deployment. This is not due to stent selection or the clinical procedure, but rather the biological response of stented arteries, considered in more detail in Section 1.3.

1.2 Engineering solutions for cerebral arteries

The three cerebral arteries (the anterior, middle and posterior) supply oxygen to the brain. They arise from the Circle of Willis, a loop of connected arteries which

enables blood flow to be shunted to different areas of the brain if any of the connecting arteries become blocked. Adequate blood flow to the brain is crucial, and as such it is well controlled: a constant, normal flow of approximately 750 ml/min is maintained even under extreme conditions [20].

1.2.1 Intracranial aneurysms

In comparison to the coronary arteries, the walls of cerebral arteries are relatively thin and lack many structural components (described in more detail in Section 1.3.1) [21]. As such, local weaknesses and defects in the wall can arise, acquired either congenitally or from factors such as smoking or hypertension. Blood pressure can then force the vessel to balloon outwards at these points. This forms intracranial aneurysms, sacs of blood outside of the artery [22] (Figure 1.4A). Aneurysms remain connected to the parent vessel at the neck of the balloon, and continuous blood flow into the sac may allow the aneurysm to gradually grow and potentially rupture. Burst aneurysms lead to subarachnoid haemorrhage, the leaking of blood over the surface of the brain which carries a 60% mortality rate [22], and haemorrhagic stroke. Second only to CHD in mortality, strokes claim the lives of 6.7 million people each year [1].

1.2.2 Stent treatment of the cerebral arteries

As for CHD, lifestyle changes can reduce the risk of initial intracranial aneurysm development, while medication can decrease their rate of growth and risk of rupture by lowering blood pressure and relaxing the blood vessels [22]. Yet, surgical intervention may eventually become necessary. Surgical treatment of intracranial aneurysms includes neurosurgical clipping, which involves the attachment of a small clip at the neck of the aneurysm to isolate it from circulation. This is the most invasive option as it requires a craniotomy, an opening in the skull. A less invasive percutaneous intervention, endovascular coiling, also exists. This involves the release of a coil of thin platinum wire into the aneurysm sac. Packing the aneurysm prevents blood flow from entering at the neck and induces the formation of a clot within the sac [23].
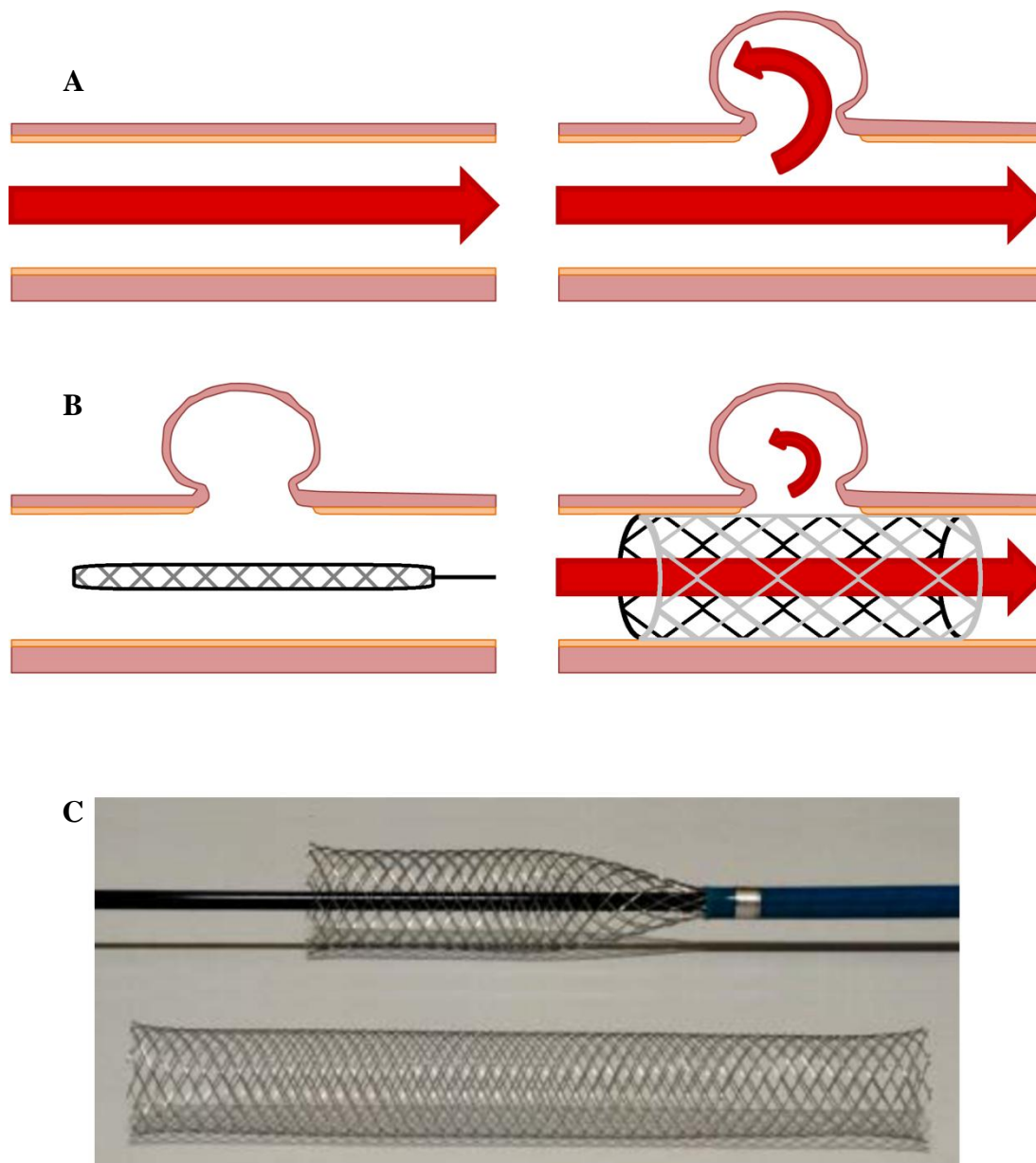
Figure 1.4 Intracranial aneurysms and flow diverter stent deployment

A: Areas of thin or weak cerebral artery wall (left) can be sites of aneurysm formation, which grow over time under the pressure of blood flowing within them (right).

B: The deployment of flow diverter stents in parent arteries over aneurysm necks (left) can redirect blood flow away from the aneurysm sac (right), reducing pressure and therefore growth and the risk of rupture.

C: An example of a typical mesh flow diverter stent, deployed via self-expansion after withdrawal of the introducer sheath. *(Reproduced with permission* [12]*).*

Endovascular coiling was augmented with the use of pre-existing cardiovascular stents, which were deployed to hold coils in place and to prevent their migration into the parent vessel [23]. More recently, a new type of flow diverting cardiovascular stent was developed specifically to treat aneurysms. These devices were based upon the principle of endovascular coiling, preventing blood flow from entering the sac, but reduced the risk of rupture by removing the need to implant within the aneurysm itself. Rather, flow diverter stents are placed within the artery at the neck of the aneurysm, where they divert blood flow through the parent vessel and away from the sac [24]. Flow diverter stents do not need the widening or scaffolding force of coronary stents. As such, they are delivered within an introducer sheath which is removed to allow the gentle self-expansion of the stent, which then sits adjacent to the vessel wall (Figure 1.4B).

1.2.3   Flow diverter stents

1.2.3.1   Requirements and design

The first use of flow diverter stents for the treatment of intracranial aneurysms was clinically approved in 2008 [25]. As a relatively modern development, far fewer designs are commercially available in comparison to the wide range of coronary stents. Flow diverter stents are still classified according to the standards described in Section 1.1.3.1 and many of the same mechanical criteria also apply [13]. Additional requirements specific to the role of flow diverters include elasticity, to allow the compression and subsequent self-expansion of stents.

All flow diverter stents are 'mesh' stents, consisting of a basic lattice of struts (Figure 1.4C). As such, in optimising stent performance there are few design parameters to consider: the size and number of struts affects the metal to artery ratio, the porosity of the mesh and, in turn, the degree of flow diversion and intra-aneurysmal blood flow [26]–[28].

1.2.3.2   Manufacturing

The fine mesh of flow diverter stents is formed by braiding separate, thin wires [29]. In some cases this is performed by hand, despite the small size of the stent. Braiding can, however, lead to the presence of loose struts and untrimmed edges at either end of the stent. The use of extruded wires means that flow diverter struts have circular cross-section.

Nitinol (a 55% nickel, 45% titanium alloy) is the material of choice for self-expanding flow diverter stents due to its shape memory. Nitinol stents can be deformed at room temperature and return to their original geometry at body temperature. However, the material's resistance to corrosion is debated [17]. Alloys of 25% platinum and 75% cobalt-nickel, or 25% platinum-tungsten and 75% cobalt-chromium-nickel are also used in the manufacture of flow diverter stents [23][30].

1.2.3.3   Complications in intracranial stenting

The placement of flow diverter stents can cause collateral effects on local blood flow if, for example, the location of an aneurysm requires the placement of a stent over side branches or smaller blood vessels. The reduction in blood flow as it is diverted away from these adjoining vessels can, in the worst case, lead to a stroke [24]. Incomplete or poor deployment can result in the relocation of stents within the vessel, or vessel occlusion due to unexpanded, tapering ends [31][32]. Manipulation of the catheter and introducer sheath to encourage full deployment can cause local inflammation and vessel perforation [24].

The majority of flow diverter deployment procedures are successful and achieve the primary goal of aneurysm occlusion. However, as for PCI, post-operative complications due to biological responses, detailed in Section 1.3.3, are not uncommon [33][34].

1.3 Biological response to stenting

In addition to immediate or short-term complications due to stent selection or clinical deployment, issues can arise in the weeks or months following stent implantation. These issues are due to the biological response to the presence of stents as foreign bodies and their impact on, and interaction with, local vascular anatomy.

1.3.1 Arterial anatomy

Arteries consist of distinct layers surrounding a lumen, the interior space through which blood flows (Figure 1.5). The endothelium (tunica intima), a flat sheet of endothelial cells, is a mechanically weak but vital component (described in more detail in the following section). The tunica adventitia is a sheath of connective tissue, which holds the vessel in place. The internal and external elastic laminae are the borders of the tunica media, the precise make-up of which varies depending on the role of specific arteries [35]. Elastic arteries, such as the aorta, contain collagen and elastin to allow the vessel to stretch and maintain constant pressure throughout the cardiac cycle. Muscular distributing arteries, such as the coronary vasculature, move blood from elastic arteries and into smaller arterioles which offer resistance to flow. As such, layers of VSMC provide strength and contractive power. Cerebral arteries, while still considered muscular arteries, have fewer VSMC layers and elastic fibres, lack an external elastic lamina and have a thin adventitia [21].

1.3.1.1 The endothelium

The endothelium is a one cell thick sheet of EC which covers the luminal surface of blood vessels. EC are flat, elongated cells, approximately $0.2 - 2$ μm thick and $1 - 20$ μm across [6]. Initially thought to be an inert layer, EC are actually more dynamic than many other cell types, are highly sensitive to extra-cellular stimuli and adapt to their environment [36]. This sensitivity and reactivity is demonstrated by their initial differentiation from endothelial progenitor cells (EPC) into either arterial or venous endothelial cells, depending on the haemodynamic forces they are exposed to as they enter the blood stream [37].
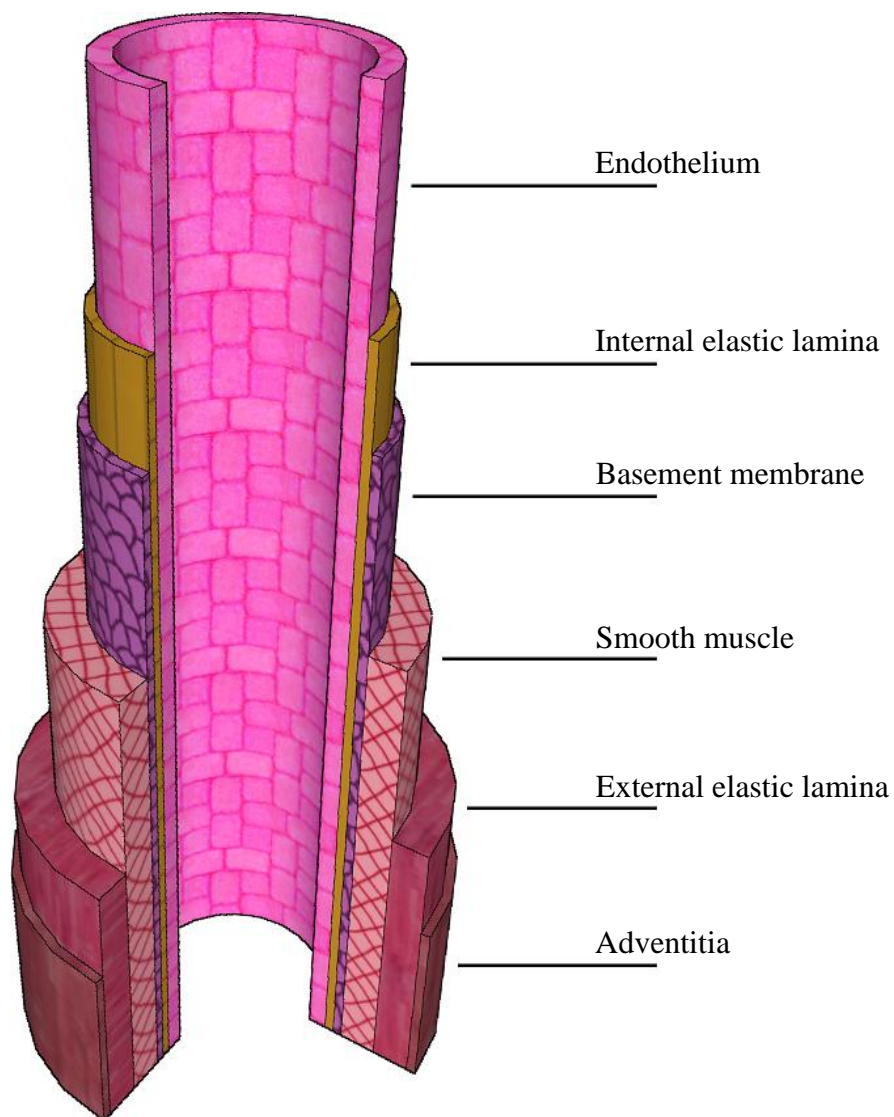
Figure 1.5 Layers of the arterial wall

Shown here in cross-section, arteries consist of a number of distinct layers; from the internal layer of the endothelium, surrounding the lumen, outward to the adventitia. The total thickness of the wall and its precise composition depends upon the role of each specific artery: cerebral arteries have thin walls to enhance the exchange of nutrients and water across them, while coronary arteries contain more smooth muscle cells to work against flow resistance.

EC act as a physical barrier for the exchange of fluids and particles between the lumen and the vessel wall and surrounding tissue. The nature of this barrier varies with location. In capillaries, for example, gaps between EC allow transport into the surrounding tissue. In the cerebral vasculature tightly packed EC form the blood-brain barrier. The cerebral endothelium is highly specialised, and tightly regulates the exchange of water, nutrients and other solutes between blood and brain tissue [38].

In addition to their physical presence, EC have been shown to play a key, active role in many aspects of vascular control and health through their biochemical activity [6]. Many of these functions are directly related to the conditions described in Sections 1.1.1 and 1.2.1:

- EC inhibit platelet aggregation, via the release of nitric oxide and prostacyclin synthesising enzymes.
- EC inhibit white blood cell adhesion and aggregation, via nitric oxide enzymes and surface adhesion molecules.
- EC regulate the function of VSMC through vasodilators and vasoconstrictors, and consequently the resistance to blood flow and blood pressure [36].

In general terms, EC provide an antithrombotic environment and exert a measure of control over vessel dilation and constriction, regulating blood flow and helping to maintain vessel patency [38].

1.3.2 Biological response to coronary stents

The endothelium bears the immediate brunt of PCI injury, as both balloon expansion and stent deployment can cause denudation of EC [39]. Post-stent complications can involve local bleeding, allergic reactions, or infection. However, stent failure is generally caused by two major complaints: stent thrombosis and in-stent restenosis (ISR) [40].

1.3.2.1　Thrombosis

Stent thrombosis occurs via a different mechanism than that described in Section 1.1.1, although the prospective harm remains the same: thrombi can detach, move through and potentially block the vasculature, or they can remain *in situ* and induce rapid lumen loss within the stent.

Stent strut penetration of the vessel wall exposes sub-endothelial, pro-thrombotic and pro-coagulant factors to circulating blood. At critical concentrations, these factors activate 'coagulation cascade' pathways, leading to clot formation [41]. The extent of stent thrombosis is therefore largely dependent on the degree of strut penetration [42], although, acting as a surface for platelet accumulation, the design of the stent also has an impact: stent type, strut thickness, the amount of exposed metal and its composition. In addition, the denudation of the endothelium during stent deployment means that local protective effects attributed to EC, including the production of anti-coagulants and suppression of thrombosis, are lost [43].

Stent thrombosis can develop within the first 24 hours of deployment (acute stent thrombosis), or after a year or more (late stent thrombosis), but current coronary stent thrombosis rates are <1% [40].

1.3.2.2　In-stent restenosis

In-stent restenosis is a less acute, progressive re-narrowing of treated vessels. Although it is a gradual process, clinical diagnosis of the condition is explicit: ISR is diagnosed to have occurred above a threshold of 50% lumen loss [44]. Restenosis is the result of several complex response processes, but is generally considered as the progression of four main stages (Figure 1.6): thrombosis and inflammation constitute the early phase, over days and weeks, followed by proliferation and remodelling [42], [45], [46]. This late phase, and the eventual diagnosis of ISR, can take several months [47].

In the first week post-stent implantation, thrombus formation peaks and thrombotic deposits can build up around struts (the degree to which this occurs can vary, as described in Section 1.3.2.1, and may be insignificant in terms of lumen reduction).
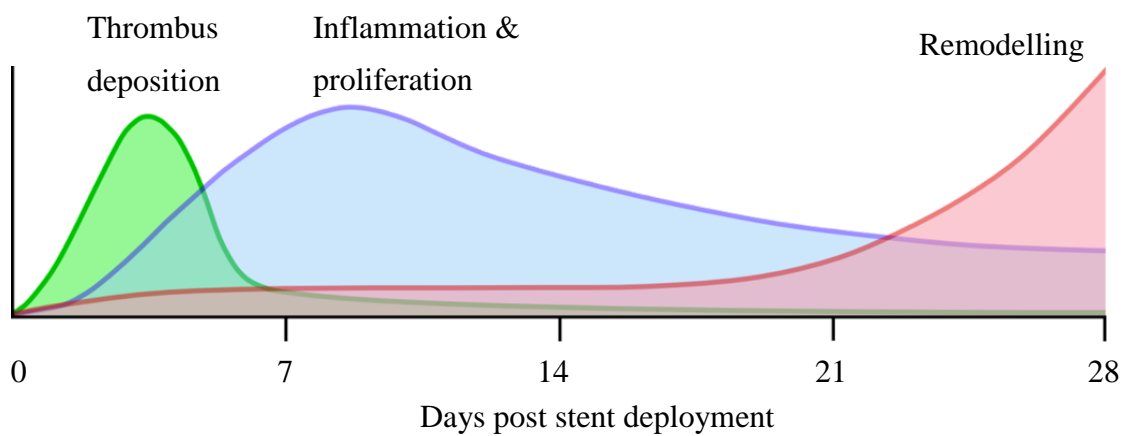
Figure 1.6 The phases of vascular response to stenting

Following stent deployment ISR can gradually re-narrow treated arteries. This process consists of the progression of four main stages:

In the immediate period post-stent deployment thrombus formation peaks (green), a response to vessel injury caused by stent deployment. This is followed by both an inflammatory response and the proliferation of exposed vascular smooth muscle cells (blue). After several weeks, elastic recoil remodels the vessel wall (red) although the lasting presence of stents, acting as scaffolds, minimises its effect.

(Reproduced with permission [42]*).*

Vessel injury and the presence of the stent as a foreign body then lead to a local inflammatory response. This begins a few days post-implantation, and involves the further deposition of fibrin, platelets and white blood cells. Inflammation is, as for thrombus formation, dependent on the degree of vessel injury and the scale of inflammation is in turn linked to the size of neointimal growth [48].

Next, VSMC, which are exposed by stent deployment, migrate into the lumen from lower layers of the vessel wall. Although contact with flowing blood can provoke apoptosis in VSMC [49], vessel injury and inflammation modulates the cells and induces both proliferation and an increase in ECM production. In addition, the cells synthesise and secrete other substances which exacerbate luminal reduction, including vessel contraction and further inflammatory and proliferative activity [50].

The final stage, remodelling, involves elastic recoil or vessel contraction. Although this stage contributes to restenosis post-POBA, it is virtually eliminated when coronary stents are present to act as scaffolds. Despite this advantage, coronary stents are particularly at risk of ISR as it is VSMC, exposed by relatively aggressive balloon and stent expansion, which have the greatest impact on the process (Figure 1.7) [51][52]. ISR develops in approximately 10% of cases, with 5% meeting the threshold for clinical diagnosis [40].

1.3.2.3 Reendothelialisation of stented coronary arteries

The repair of stented arteries involves the covering of the stent and local vessel segment with a renewed endothelial layer. A healthy, functional endothelium can exert a degree of control over the local vasculature; reducing complications by inducing thrombus suppression and the quiescence of VSMC [43].

The precise mechanisms of endothelial renewal are not fully understood. Reendothelialisation had been considered to be due solely to the migration of EC from adjacent, uninjured sites [41]. Local, damaged EC, as well as VSMC and accumulated platelets, release mitogens (chemicals which trigger cell division) [53].
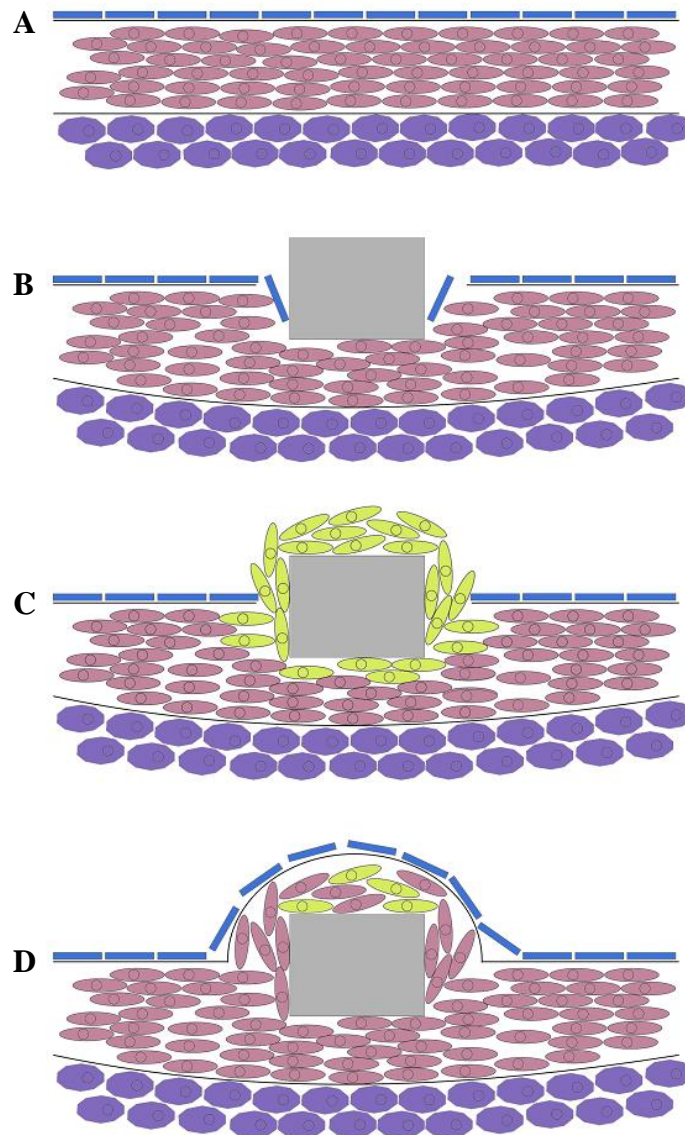
Figure 1.7 In-stent restenosis development

Post-stent deployment, treated vessels can re-narrow due to the development of ISR.

A: Normal vessel wall, with EC (blue), VSMC (pink) and fibroblasts (purple).

B: Stent deployment causes initial wall injury and EC denudation local to struts.

C: Exposed, modulated VSMC (yellow) migrate into the lumen and proliferate.

D: EC reendothelialise the wall and VSMC differentiate back to a quiescent phenotype. The lumen is now occluded local to the stent.

(Reproduced with permission [46]*).*

These mitogens, which include vascular endothelial growth factors (VEGF), cause EC to migrate into damaged and denuded areas and begin proliferating, eventually reendothelialising the injury site (the physical process involved in the movement of an individual EC across a substrate is covered in more depth in Section 1.4.4).

In addition to local EC, the presence of EPC have also been noted [54]. EPC are derived from bone marrow and circulate in the blood. Their mobilisation is induced by VEGF and circulating EPC adhere to proteins and adhesion molecules on the vessel wall. Once captured, progenitor cells can proliferate and differentiate into mature arterial EC [55].

One further potential mechanism involves the accumulation of endothelial cell colony forming unit precursors. These are monocytes and lymphocytes, both types of white blood cell, which exhibit the characteristics of mature EC [56]. Colony forming unit precursors are thought to arrive and cover injury sites relatively early, before secreting more VEGF which further enhances the homing of circulating EPC and the proliferation of accumulated EPC [53]. There is, however, still debate as to the identity and degree of contribution of the cells involved in the process of reendothelialisation.

A 2013 study by Douglas *et al* investigated the origin of cells within a renewed endothelium, by transplanting stented aorta from donor to recipient murine models [57]. Vascular repair was found to involve both local aortic donor EC and circulating recipient EPC, with the degree of EPC contribution varying between animals. Separate studies have contradicted this result, finding that EPC do not contribute to reendothelialisation [58][59]. However, it has been noted that the methods used in these studies could have influenced both the repair mechanism and the ability to properly identify EPC [43].

1.3.3 Biological response to flow diverter stents

An immediate and serious potential response to flow diverter stent deployment is bleeding. Whether caused by vessel perforation or the rupture of treated aneurysms [34], any blood loss will lead to subarachnoid haemorrhage [33]. Further biological responses to flow diverter stents are similar to those in coronary arteries: stent thrombosis and in-stent restenosis (or rather, stenosis, as the vessels are not previously occluded). However, the differences in stent deployment method, and therefore endothelial injury, greatly alter the rates at which these complications arise.

1.3.3.1 Thrombosis

Thrombosis is the most common complication following flow diverter stent deployment, occurring in $6 - 13\%$ of cases [24][33][34]. Thrombus formation develops via the same mechanism described in Section 1.3.2.1, and is thought to be worsened by the higher metal content of flow diverter stents. This is demonstrated by the fact that rates of flow diverter stent thrombosis incidence are higher in patients with larger aneurysms, which require the deployment of longer, or multiple, stents [34].

1.3.3.2 In-stent stenosis

Until recently, little data on in-flow diverter stent stenosis existed. A small number of contemporary studies have found that while incidence of stenosis is seen at a rate comparable to coronary stents, it is generally asymptomatic and does not meet the 50% lumen loss threshold required for clinical diagnosis [32][60][61]. The main cause of in-stent stenosis is the proliferation of VSMC, instigated by vessel injury. As such the gentle self-expansion of flow diverter stents, in cerebral arteries with lower VSMC content than the more muscular coronary arteries [55], carries a lower risk of VSMC exposure and proliferation progressing to the point of clinical stenosis.

1.3.3.3 Reendothelialisation of stented cerebral arteries

In addition to aiding in the reduction of the complications described in the previous sections, reendothelialisation of flow diverter stents is also a key part of the occlusion of the aneurysm being treated. Full endothelialisation of flow diverter stents has been observed over $4 - 8$ weeks in rabbit models *in vivo*, with the rate dependent on the size of aneurysm necks (endothelialisation is delayed over larger necks) and the degree of stent strut apposition (endothelialisation is enhanced where stents are in contact with the artery wall) [62].

As for coronary stents, discussed in Section 1.3.2.3, the contribution of both local EC and circulating EPC in flow diverter endothelialisation has been studied and the results have been contradictory. EPC have been found to be a factor in the healing process for up to 60 days [29] and identified in both fully endothelialised stent struts and aneurysm necks [63]. Conversely, equally complete endothelialisation has been observed with the renewed layer consisting solely of local EC from the parent vessel [62].

1.3.4 Moderating the biological response to stents

Stented vessels can be treated with a secondary percutaneous intervention when the biological responses described in Sections 1.3.2 and 1.3.3 develop to the point where it is required. However, these follow-up procedures themselves show high rates of restenosis [64], and a 30% risk of MACE [52]. As such, prevention is considered better than cure. Current post-operative care following both coronary and intracranial stent deployment includes the use of systemic anti-platelet medication [65][66].

By modifying or augmenting stents themselves localised treatment, rather than systemic, can focus on the vasculature beneath and adjacent to the implanted device. As the more established apparatus, coronary stents have seen the most development. Current technological trends focus on the targeted release of anti-proliferative agents with the use of drug-eluting stents (DES). These stents gradually release a drug into the local bloodstream and arterial wall to inhibit the growth of VSMC [67]. DES

have reduced ISR incidence to the current 5% rate, compared to $20 - 30\%$ associated with BMS [65]. However, one drawback is the relatively short duration of drug delivery in comparison to the period of peak neointimal growth [47]. The development of polymer stent coatings, within which drugs are embedded, extended this duration by reducing the rate of elution [68]. When certain coatings were themselves found to cause inflammation, polymer-free strategies, including the use of microporous films, were developed [39]. DES are the current benchmark in stent efficacy and are used in 75% of procedures [66]. Clinical trials show clear improvement between successive generations of DES and, given their success rate, drug-eluting balloons have also been developed [8]. These can be used in POBA, or in tandem with either BMS or DES.

Various coatings are also used in non-DES. The use of radioactive particle-emitting stents enables a form of internal radiotherapy [69]. Alternatively, coatings such as silicon carbide, phosphorylcholine and heparin can passivate stents and reduce their interaction with local tissue, improving their biocompatibility [70].

A more recent approach is the development of bioabsorbable coronary stents, which aim to reduce complications arising from the presence of the stent as a foreign body. Bioabsorbable stents are deployed in the standard manner, but dissolve after providing initial support to the arterial wall [71]. Several trials have been conducted which show positive results in terms of safety, but also ISR rates higher than those seen with DES [65]. This is often due to vessel shrinkage, as current bioabsorbable materials provide lower radial strength than metallic stents. Thicker, more intrusive struts are required to compensate and ISR may still occur in the time required for full stent dissolution [68]. In addition, bioabsorbable material such as poly(L-lactide) can be too stiff to move with its parent artery [72]. Subsequent fractures which may be caused by this lack of flexibility can further reduce radial strength.

Other than bioabsorbable stents, which seek to minimise the impact of stent deployment, the strategies described here are designed to exert a more active influence on the local artery. The common aim is to reduce inflammation and narrowing by targeting VSMC. However, their impact is broader and EC can also be

sensitive to their effects, which can delay the regrowth of the endothelium [11], impeding vascular repair and increasing the risk of complications.

The ongoing presence of stents can also be detrimental to the endothelium by inducing EC dysfunction. Following the deployment procedure, which can physically damage and remove cells, stents do not directly affect EC themselves. Rather, it is the impact of stents on local blood flow, and therefore the conditions EC are exposed to, which is thought to cause this dysfunction [43]. As mentioned in Section 1.3.1.1, EC are sensitive and reactive to their environment. It is therefore necessary to consider this environment, its alteration via stent structure and the induced EC response.

1.4   Endothelial cell mechanobiology

1.4.1   The mechanical environment

As they form a layer on the luminal surface of blood vessels, EC are subjected to radial stress caused by blood pressure. In the arteries, mean blood pressure is approximately 13 kPa [73]. This pressure also causes the blood vessel to distend: diameter increases at systole (the contraction phase of the cardiac cycle), before decreasing at diastole (the relaxation phase). EC attached to the vessel wall are subjected to a circumferential stress, or hoop stress, as the wall pulses and stretches throughout the cardiac cycle. In medium-sized arteries hoop stress is on the order of 10^5 Pa [73], and strain is typically $5 - 10\%$ [74][75]. In addition to the cyclic stress caused by cardiac rhythm, the coronary arteries are also continuously subjected to stretch and compression as they ride on the surface of the heart itself, which is in constant motion [55].

1.4.2   The haemodynamic environment

EC are exposed to flowing blood which, at its simplest, can be seen as an incompressible fluid flowing through straight, cylindrical, rigid tubes [76]. Flow is steady and laminar in normal arteries. Although repetitive disturbances can form, Reynolds numbers are below transition (~300) and turbulent flow is not present *in*

vivo. The Womersley parameter is also low (~3) [73]. As such, viscous forces dominate. Normal pipe flow can be considered and blood velocity forms a parabolic profile [35]. In reality, blood flow is more complex. The magnitude and direction of flow varies temporally (through the cardiac cycle) and spatially (with different vascular anatomy) [77]. Secondary flow and complex patterns are generated near curves and branches [73].

Further complicating the picture of simple flow is the fact that blood is not a continuous fluid: 55% of blood volume is plasma (water, proteins and ions) and the remaining 45% consists of discrete elements (red blood cells, white blood cells and platelets). As a particulate suspension, blood is non-Newtonian and viscosity is dependent on shear rate [78]. However, when considering the arteries, vessel diameter is large (>0.5 mm) compared to the size of the individual elements and shear rates are high enough (>100 s^{-1}) for viscosity to be independent of them. Arterial blood is therefore generally treated as a Newtonian fluid [73][76], and viscosity considered to be 3.5 - 4.0 mPa.s [79]–[81].

The laminar, viscous flow of blood generates a shearing stress on the EC lining vessel walls [74][81]. For the simple flow assumptions described above, the Hagen-Poiseuille equation ($\tau = 4\mu Q/\pi r^3$) provides a reasonable estimate of wall shear stress [73]. The specific range of wall shear stress magnitudes found *in vivo* is investigated further in Section 1.7.3, but is orders of magnitude lower than the forces described in Section 1.4.1 [73]. However, EC are particularly sensitive to wall shear stress; it is essential for EC function, and abnormal levels can cause dysfunction [82].

1.4.3   Wall shear stress and endothelial cell response

Despite being several orders of magnitude weaker than either radial or hoop stress, above a threshold of 0.08 Pa wall shear stress is the dominant force affecting EC behaviour [83]. Under basal levels of shear stress, EC function normally and contribute to good vascular health [81]. Deviation from these levels can cause dysfunction within the vessel. This arises not from direct injury (wall shear stress of

50 Pa is required to damage EC [84]) but from the effects of EC biochemistry influenced by shear stress.

Initial exposure to flow generated wall shear stress induces differentiation between progenitor cells and functional EC [37]. In addition, dissimilar levels of shear stress between vessels influence differentiation between venous and arterial EC. Ongoing sensitivity and reactivity to shear stress enables the endothelium to help arteries adapt to changes in blood flow, via the expression of vasodilators and vasoconstrictors. If shear stress levels become too high, vasodilators are expressed to widen vessels. Too low, and vasoconstrictors narrow vessels to return shear stress to baseline levels [73][85]. This behaviour aids in the maintenance of normal blood pressure and allows the supply of oxygenated blood to meet demand.

The influence of wall shear stress on vascular health can be illustrated by the fact that, although the entire cardiovascular system is exposed to the systemic risk factors of CHD, atherosclerotic lesion formation is focal. This discrepancy has been attributed to local haemodynamics for over a century [86]. After some debate over what specific aspect of blood flow causes this outcome, it was suggested that low and oscillatory shear stress was responsible [87]–[89]. It is observed that lesions preferentially progress around bifurcations and at the inner wall of curved arteries, which are areas of low or even reverse flow [85][90]. This conclusion is supported by a number of studies which combine patient data with shear stress estimates from computational simulations, and find lesions progress in regions of low shear stress [91][92].

This theory is widely accepted, but not universally. Peiffer *et al* (2013) performed a systematic review of 27 papers, several of which did not find the expected correlation between low shear and atherosclerosis [86]. Those that did interpreted disease progression and haemodynamic factors in different ways. In addition, there was little consistency between the magnitudes of shear stress defined as the low/high thresholds (this point is considered further in Section 1.7.3).

Poor vascular health can be related to the endothelium by examining EC behaviour under low wall shear stress. Chien *et al* (1998) [93], Chatzizsis *et al* (2007) [87] and Van der Heiden *et al* (2013) [43] detail the changes in EC biochemical functions which may occur under low or oscillatory shear stress, examples of which are shown in Table 1.1. It is clear that vasodysfunctional effects are induced, particularly those related to vessel narrowing, and plaque and thrombus formation (and therefore atherosclerosis, and the post-stent complications described in Section 1.3).

In comparison, contrasting behaviour under high shear stress confers a protective effect [43]. High shear stress also enhances EC migration, a fact which is of special relevance to post-treatment vascular repair and the endothelialisation of stents [94][95]. However, while the response of EC to shear stress can be observed, the exact mechanisms and structures through which they sense it are not yet fully understood [77].

1.4.4   Wall shear stress and endothelial cell mechanotransduction

EC modify their local environment via mechanotransduction, the conversion of mechanical stimuli into chemical activity. Mechanotransduction may be local (the activation of a single mechanoreceptor on the cell) or decentralised (forces are transmitted throughout the cell, activating many mechanoreceptors) [81].

The specific sensors which enable EC to detect wall shear stress magnitude or direction are not known, but candidate mechanoreceptors have been identified [43][96]. These include the action of wall shear force upon the following structures:

- The glycocalyx, a protein which covers the luminal surface of EC [97].
- Primary cilia, small organelles which project from the EC into the bloodstream [98].
- The cytoskeleton, the network of protein filaments and microtubules that give cells their shape. The cytoskeleton can resist deformation, but also induces it to enable cell migration [99].
- Integrins, proteins that attach cells to the underlying extracellular matrix.

Function	Effect of low shear stress
Vascular tone: release of vasodilators	↓
Vascular tone: release of vasoconstrictors	↑
VSMC: release of growth promoters	↑
VSMC: release of growth inhibitors	↓
Release of oxidants	↑
Release of antioxidants	↓
Cholesterol accumulation	↑
Reduction of inflammation	↓
Extracellular matrix synthesis and degradation	↓ ↑
Plaque calcification	↑
EC apoptosis	↑

Table 1.1 Specialised functions of EC related to vessel patency and their up or down regulation under low shear stress conditions

Low wall shear stress can induce endothelial dysfunction, which in turn leads to a number of vasodysfunctional effects (particularly related to vessel narrowing) due to the influence EC have on their local vasculature.

- Ion channels, proteins which form pores in the cell membrane and allow ions to pass through.

- A combination of cell adhesion and signalling proteins, known as the VEGFR2/VE-cadherin/Pecam-1 complex [100].

As has been previously mentioned, EC are not only sensitive to wall shear stress, but also reactive. Once the force has been detected, this reaction is due to the presence of DNA sequences known as shear stress response elements (SSRE) which activate the expression of certain genes. For example, Nagel *et al* (1994) studied the expression of three intercellular adhesion molecules (ICAM) at wall shear stress levels between 0.25 and 4.6 Pa [101]. The only molecule to be affected by the change in mechanical conditions was ICAM-1, which was up-regulated with increased shear stress. The ICAM-1 promoter gene was also the only molecule which contained an SSRE.

One explanation for the observed effects of shear stress on EC migration is the influence of flow on cell polarity. Polarity is essential for cell migration via cytoskeleton rearrangement: it defines a leading edge for protrusion and adhesion of the cell body, and a rear for retraction. This combined, repeated action propels cells over their substrate [102]. High, uniform shear stress can enhance polarity, whereas low or oscillatory shear stress can prevent it.

This was demonstrated, and a proposed mechanism suggested, by a series of experiments by Hsiao *et al* (2016) [103]. EC within an empty channel were observed to migrate in the direction of flow, while EC within a ridged channel (replicating stent geometry) accumulated immediately downstream of the first obstacle (Figure 1.8A and B). This area was identified, via particle tracking and computer simulation, as a site of bidirectional flow.
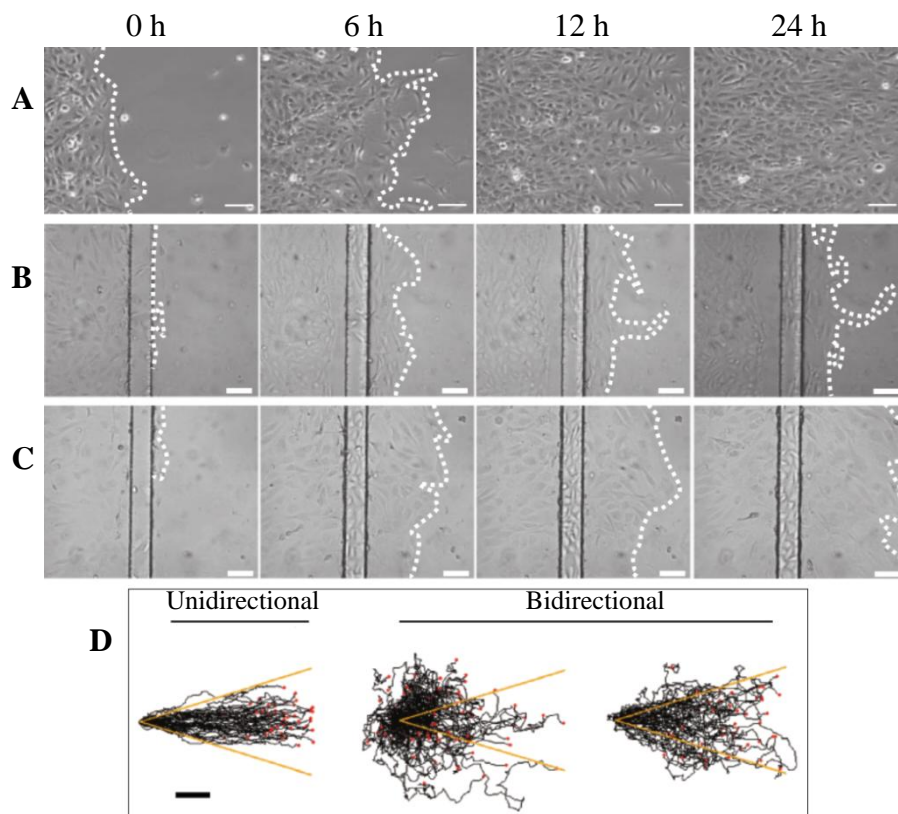
Figure 1.8 Endothelial cell migration under disturbed flow

HUVEC within a parallel plate chamber were exposed to unidirectional flow and the leading edge of the migrating cell monolayer (white line) was monitored over 24 hours.

A: HUVEC in an empty chamber rapidly migrated through the field of view.

B: HUVEC in a ridged chamber, representing stent struts. A low number of cells crossed the ridge, where their migration was inhibited within a region of disturbed, bidirectional flow.

C: HUVEC in a ridged chamber, with a ROCK inhibitor to silence bidirectional mechanical cues. A greater number of cells crossed the ridge, and continued to migrate beyond the region of disturbed flow.

D: Migration paths of individual HUVEC (red dots) over time. Yellow lines represent a 15% deviation from the direction of flow. Bidirectional flow reduced HUVEC persistence (centre), hindering overall downstream migration compared to cells within an empty chamber (left) or in the presence of a ROCK inhibitor (right).

Flow from left to right.

Scale bar: 100 μm (A-C), 500 μm (D).

(Reproduced with permission [103]*).*

It was proposed that bidirectional flow increases MLC activity (myosin light chain, a motor protein involved in cell motility [104]), which in turn induces multiple protrusions around the cell. This reduces polarity and thus inhibits migration. The above experiment was then repeated with the addition of a Rho-associated protein kinase (ROCK) inhibitor. ROCK up-regulates MLC activity, therefore ROCK inhibition was expected to reduce MLC activity, increasing cell polarity and EC migration [105]. Indeed, EC in the presence of ROCK inhibitors were observed to migrate beyond areas of disturbed flow, their sensitivity to bidirectional mechanical cues having been essentially suppressed (Figure 1.8C).

Tracking individual EC at multiple time-points revealed that cell migration distances were not always reduced in bidirectional flow due to arrested movement, but rather by a decrease in the directional persistence of that movement. EC were in continuous motion but, in the presence of disturbed flow induced by replica stent geometry, the direction of this motion was not consistent (Figure 1.8D).

1.5 Stent geometry and endothelial cell behaviour

The effect of stent geometry on EC behaviour has been investigated both directly and indirectly. Clinical studies tend to be indirect: particular stent designs have associated rates of ISR and thrombosis, from which the presence or absence of a healthy, functional endothelium may be inferred [106]. The relationship between stent design and endothelial function can also be assessed via *in vitro* and *in silico* methods [107]. Once again, this is often indirect: the effect of stent structure on haemodynamics is studied in *in silico* models and cell-free *in vitro* models, and conclusions are drawn by relating those results to separate studies of EC under similar conditions [108]. In other cases, EC seeded within *in vitro* models can reveal links between their behaviour and stent-induced flow directly [103]. In considering the impact of stent geometry in this section, all of these approaches are taken into account.

1.5.1 Stent length

Many studies believe stent length to be the most important factor related to stent design, based on the link between length and rates of ISR (only initial lumen diameter is considered to be a greater predictor) [9][109][110]. This would appear to be a logical conclusion. Increased stent length means more struts, a greater amount of exposed metal and, it may be assumed in the case of coronary stents, a wider extent of plaque within the vessel necessitating the stent to begin with. This means greater initial injury to EC, and requires reendothelialisation over a larger vessel area under disrupted blood flow.

However, other than diameter, length is perhaps the only aspect of stent design that cannot be altered. Although it is minimised where possible, surgeons must select stents based on the size of the plaque, narrowed arterial segment, or aneurysm neck in each individual case [109].

1.5.2 Stent structure

As shown in Section 1.1.3.1, 'stent design' is a broad term which includes many different parameters. *In silico* study is therefore particularly useful, providing the ability to consider variation in individual components while keeping all other factors equal [111]. LaDisa *et al* (2004) found that the area of vessel wall exposed to low shear stress increases with the number of struts, their longitudinal width and thickness, and stent to vessel expansion ratio (Figure 1.9A) [112]. Hsiao *et al* (2012) agree that wall shear stress is particularly sensitive to strut thickness (Figure 1.9B), but they did not find the same for longitudinal width. In addition, they suggest that crown radius and the overall design pattern have little effect on wall shear stress distribution [113]. Pant *et al* (2010) altered the shape of bridges connecting strut rings, and found that different designs had an influence on blood flow and wall shear stress even in stents of otherwise similar strut dimensions and spacing (Figure 1.9C) [111].
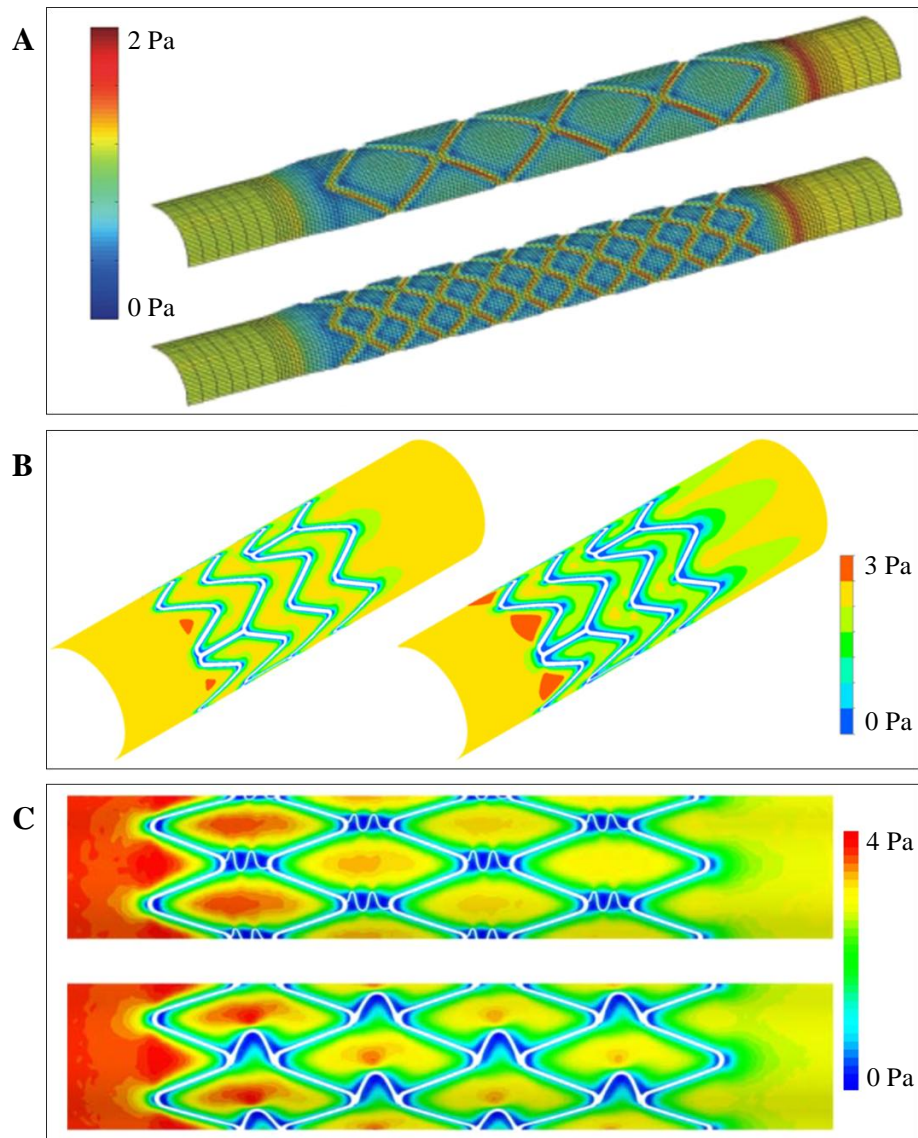
Figure 1.9 Parametric studies of stent design and local wall shear stress

Computational models of stented vessels have been widely used for the parametric study of stent design features, investigating their effect on haemodynamics and shear stress.

A: Increasing the overall number of stent struts reduces wall shear stress [112].

B: Increasing the thickness of stent struts reduces wall shear stress [113].

C: Wall shear stress distribution is altered with different connecting bridge designs [111].

Flow from left to right.

(All images reproduced with permission; image B by permission of the Institution of Engineering & Technology).

In their review, Sangiorgi *et al* (2007) touch upon the substantial differences in wall shear stress and haemodynamics between different stent designs, and particularly between stent types (slotted tube, mesh, etc.). However, they also state that this does not necessarily translate into different vascular response *in vivo*: they propose that, unlike stent type or strut diameter, the geometry of stents (the various designs used in commercial models) does not seem to influence clinical outcome [70]. Despite this conclusion, they concede that 'hydrodynamic compatibility' should be recognised as an important feature of stent design, classification and selection.

Peacock *et al* (1995) demonstrated flow disturbances arising from the shedding of vortices from stent struts *in vitro* [84]. These instabilities decayed relatively rapidly (within 5 cm) but the influence of stents could still extend beyond their own length. Coil stents were found to create larger instabilities than slotted tube stents (although the latter model also had thinner struts). Benard *et al* (2003) also found areas of recirculation downstream of struts which were oriented perpendicular to flow [94]. These locations were areas of lowest shear stress, whereas regions of highest shear stress were located adjacent to struts which were parallel to flow. This study also examined slightly different stent designs, with differences in fluid dynamics only becoming apparent at very low flow rates.

Simon *et al* (2000) studied the migration of seeded EC around objects of various sizes while under flow [114]. Cell coverage and migration was reduced when the thickness of these objects passed 75 μm, and was non-existent around 250 μm thick samples. Cell free areas were smallest where edges were parallel to flow, and largest downstream of perpendicular edges, correlating with areas of high and low shear stress in Benard's model. Hamuro *et al* (2001) investigated stent edge angle, the angle of the strut face exposed to oncoming flow [115]. Cell migration was greatest at 35° (leaning away from oncoming flow) and lowest at 90° (upright). Intermediate migration was seen at both 70° and 135° (leaning into oncoming flow), with little difference between the two.

It should be noted that the preceding concerns dimensions and designs related to coronary stents only. As a more recent development, flow diverter stents have not been as extensively studied. However, recent work by Marosfoi *et al* (2016) offers initial evidence that flow diverter design (strut size and orientation) also influences endothelialisation [29].

1.5.3   Modifying stent impact

The current clinical methods to reduce post-stent complications described in Section 1.3.4 tackle the issue with a pharmacological approach, via drugs or material coatings, or with the eventual break-up of the stent. All of these techniques carry associated risk factors and the use of medicines in particular can worsen vascular health through their effect on the endothelium. The impact of stent structure on local blood flow discussed in the previous section, and its subsequent effect on EC, allows vascular repair to be addressed from a new angle: stent design and the altered haemodynamic environment.

The most common approach is to lessen the impact of the stent on local haemodynamics while using existing designs. The application of stronger materials in stent manufacturing enables the use of 'ultra-thin' struts (>70 μm), reducing flow disturbance [116]. Other techniques encourage reendothelialisation through micropatterning of the stent surface. EC migration has been shown to increase in stents containing evenly spaced parallel microgrooves 14 – 15 μm across and 2 μm deep [117]. A more extreme method is the use of a microporous elastomer film to completely cover the stent (and the entire circumference of the vessel wall), leaving a flat, unbroken luminal surface [39].

While these techniques aim to reduce areas of stent-induced low shear stress, others take a more active approach and aim to increase EC migration by augmenting local shear stress. In recent years, stents have been designed to induce helical or spiral blood flow through the artery. This secondary motion is often seen in natural blood flow, and can prevent the formation of stagnation points and flow separation [53][118]. The use of secondary devices has also been trialled. In 2003 the Anti-Restenotic Diffuser (ARED) flow divider was developed, to be deployed

following coronary stent implantation [119]. This is a solid cylinder of 1 mm diameter and 10 – 15 mm length which sits at the centre of the lumen within the stented arterial segment, anchored to the stent via a series of self-expanding legs. The device essentially reduces the local fluid volume, doubling the wall shear stress magnitude found in unaltered control stents. The ARED was studied *in vivo* in animal models, but has not been implanted in humans [53].

1.6 Experimental techniques

1.6.1 *In vivo* models

Following stent implantation, angiography can monitor subsequent vessel occlusion. This data can identify the presence of ISR or thrombi but, save for histology samples in the unfortunate case of patient death, the detailed progression of disease or reendothelialisation cannot be studied [40]. More specific data is available in the form of animal models, typically larger mammals such as rabbit or porcine models, which are histologically similar to humans [51]. The progression and regrowth of cells can be examined at a specific time point by dissection of the stented vessel, *en face* staining and microscopy.

However, *in vivo* models have several drawbacks. Animals are typically too young, or in good health, to see the formation of initial cardiovascular disease, which must therefore be induced. Atherogenesis can be stimulated by cuffing vessels [120], or by maintaining animals on high-fat diets over a period of several months [121][122]. Aneurysms can be created by treating vessels with elastase, to weaken the wall via the destruction of elastin fibres, or by genetically modifying animals to be predisposed to the condition [55][63][123]. Although plaques or aneurysms are not necessarily required to study the biological response to the presence of stent structure, the deployment of even oversized stents does not sufficiently denude healthy vessels in order for reendothelialisation to be monitored [51]. Finally, where endothelialisation and arterial healing is seen, it typically progresses at a much more rapid rate within animal models than in human patients [41][47]. This is of particular importance when *in vivo* data is used to inform the duration of post-operative medication or DES release.

1.6.2 *In vitro* model design and fabrication

In vitro models provide the ability to monitor biological responses in much greater detail than *in vivo* models, over multiple time points and in repeated experiments. They also allow experimental parameters to be adjusted, to enable the study of cellular response to particular conditions. A thorough review of the *in vitro* techniques used for the mechanical stimulation of EC over the last 40 years is provided by Davis *et al* (2015) [124]. The majority apply shear stress to cells via cone and plate devices, or orbital shakers. Initial *in vitro* models of continuous flow, such as those created by Levesque and Nerem (1985) [125] and Tsuboi *et al* (1995) [126], used parallel plate flow chambers. Early studies of stents within these models used small metal coupons to replicate their structure [127]. Although simple approximations, these methods are often sufficient to test hypotheses [94][95][114], and are still used to evaluate the use of different materials and surface treatments [117]. Yet, parallel plate studies are ultimately limited as representations of blood vessels and channels of circular cross-section and appropriate diameter provide a more realistic model. These have been created by dip coating glass rods in an elastomer [128], continuously applying small amounts of the same material to a rotating mandrel [74], or pouring into a mould between a mandrel and outer shell [129]. Bifurcations, aneurysms, and stenosis have also be modelled through simple additions to these methods [130].

The replication of accurate stent geometry began by creating models around casts of *ex vivo* histological coronary artery samples [84]. Following this, the actual deployment of clinical-grade stents *in vitro* was performed by Cardinal *et al* (2006) [131]. A tissue-engineered blood vessel mimic was created, into which a coronary stent was inserted. A simpler model, again fabricated via dip coating, was created by Punchard *et al* in 2007 [132], and used two years later for the deployment and testing of a commercially available coronary stent [107].

The choice of material for these *in vitro* models is limited as several criteria must be fulfilled, primarily cell biocompatibility and transparency for microscopy if real-time imaging is required. To recreate realistic vessel geometry and stent deployment, the ability to shape the material is also necessary; glass [95], PMMA [94], and

PTFE [133] are therefore unsuitable. Polydimethylsiloxane (PDMS), a silicone elastomer, meets these requirements and is credited for the rapid growth in microfluidics and biological labs-on-a-chip [134]. PDMS consists of a pre-polymer (base) and cross-linker (curing agent), which are mixed and cured [135]. PDMS is ideal for rapid prototyping, compatible with a variety of fabrication techniques and cheap enough to use in relatively large quantities [136].

Although it is heavily used in the literature [124], PDMS has its disadvantages and opinion is split. It is generally considered well suited to cell culture as it is transparent, gas permeable, and biocompatible [137]. However, PDMS can be hydrophobic, and leach potentially toxic cross-linked oligomers. It also has a tendency to absorb small molecules, which can change solution concentrations and effect results [136][137]. In their review of the material, Sackmann *et al* (2014) suggest that these points may make the description of PDMS as 'biocompatible' somewhat misleading [134].

Nonetheless, PDMS has been shown to support cell attachment. Lee *et al* (2004) analysed the effect of various mixing ratios and recommend the standard 10:1 base to curing agent ratio, as cell growth is similar to that seen on standard tissue culture apparatus [138]. Curing temperature and time (which influence the final stiffness of the material) had no effect on attachment or proliferation. Brown *et al* (2005) also recommend a 10:1 ratio, which both they and Khanafer *et al* (2009) [139] consider to have a physiologically relevant elastic modulus (described in Section 1.7.1). Pre-soaking PDMS in culture media to prevent absorption was found by Mata *et al* (2005) to have little effect on surface chemistry, although the deposition of a variety of media ingredients was suggested [140].

A biocompatible model is essential as a complete understanding of the influence of stents on EC is not possible without the inclusion of cells in research. The EC most commonly used within *in vitro* models are human umbilical vein endothelial cells (HUVEC) [132][141], as umbilical cords provide a readily available source. Venous cells, as opposed to arterial, are used due to the comparative size of the umbilical vessels and the ease of isolation. The culture of EC was first described in 1973 by Jaffe *et al* [142], who maintained populations of HUVEC for up to 5 months. Despite

being isolated from umbilical veins, HUVEC are deemed suitable for *in vitro* studies of coronary arteries as the differences between specific *in vivo* environments are small in comparison to the differences between *in vivo* and *in vitro* culture [143]. In addition, local mechanical conditions can induce EC to demonstrate arterial-like characteristics [37][144].

When used in combination with PDMS, HUVEC attachment requires surfaces to be pre-coated in fibronectin [145], with concentrations ranging from 5 to 100 µg/ml [138][146]. HUVEC are seeded at approximately $2x10^6$ cells/ml, resulting in coverage of around 75% [75][141]. In some model vessels cells are attached around the full circumference of the channel, by slow rotation over 12 hours [132], or by simply turning the model upside down after just 10 minutes [141].

1.6.3   Applied conditions

The application of fluid flow is an obvious necessity in the study of model arteries. In simple parallel plate models this has been achieved using gravity driven flow [127]. Specific conditions (flow rate, wall shear stress, etc.) are met by altering the dimensions of the channel. Full size models require higher flow rates to generate physiologically relevant conditions. These are typically supplied by syringe drivers [141], peristaltic pumps [147], or pressure pumps [103], all of which can supply a range of flow rates. A small number of studies have combined the application of realistic pulsatile flow with thin, compliant vessel walls to expose EC to the combined action of the multiple forces described in Section 1.4 [75][128][148][149]. However, the majority simply consider wall shear stress alone, applying whatever flow conditions are necessary to generate the desired magnitude. Figure 1.10 illustrates the levels of wall shear stress applied in *in vitro* and *in silico* models. Interest in the link between regions of low shear stress and EC dysfunction can be seen as most studies applied no more than 1.5 Pa.
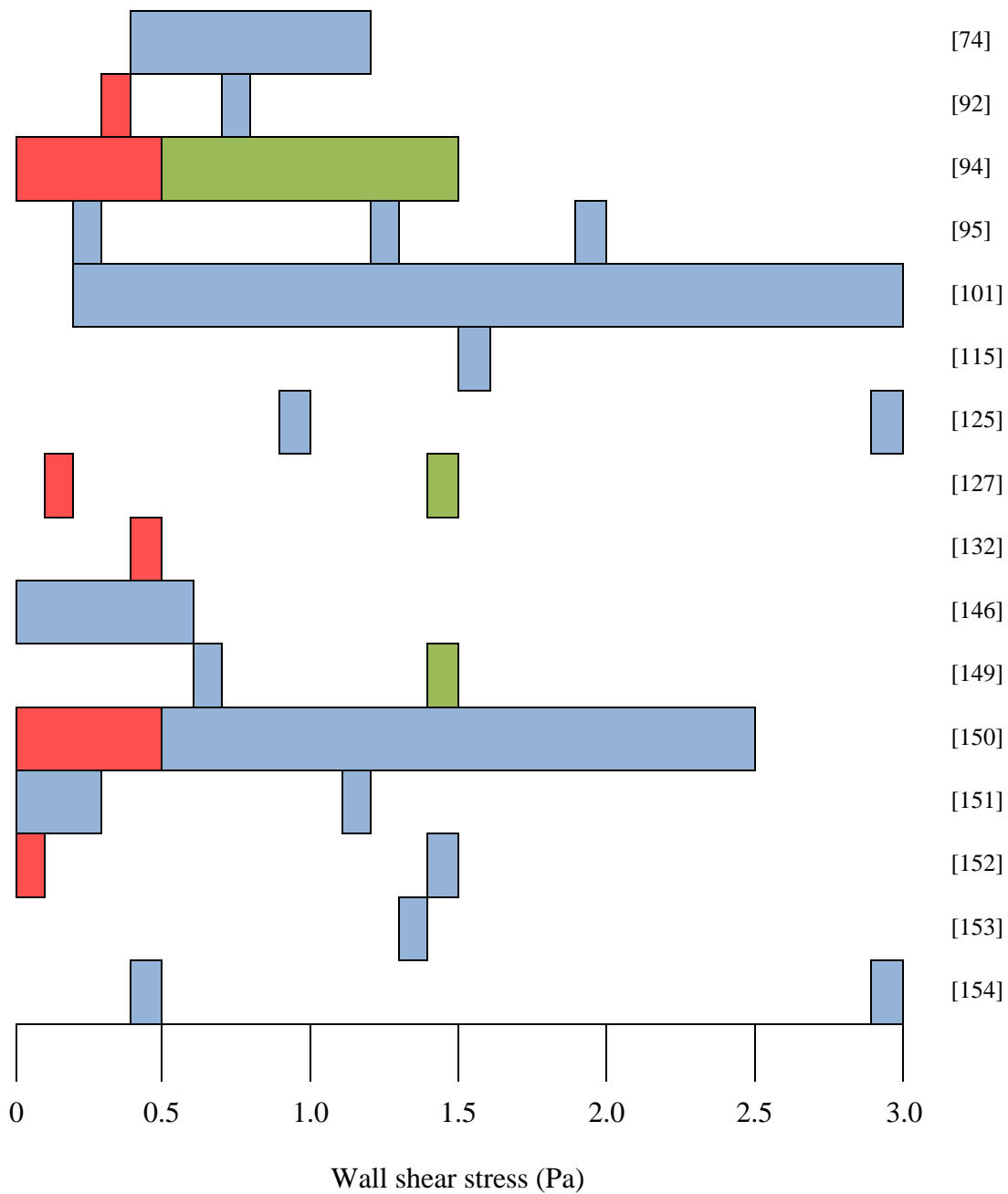
Figure 1.10 Wall shear stress magnitude applied *in vitro* and *in silico*

The magnitude of wall shear stress applied in a number of *in vitro* models and computer simulations is shown, with colours corresponding to the descriptions used by the authors.

Red: Low shear stress.

Blue: Intermediate or average shear stress.

Green: High shear stress.

In a number of models, dextran (a polysaccharide) is used to increase the viscosity of cell culture media so that its rheological behaviour approximates plasma or whole blood [37][74][101][146][147][155]. This reduces demand on the pump when applying specific levels of shear stress, and can bring the flow rate and Reynolds number into physiologically relevant ranges. However, relatively high concentrations are required (>15% w/v, depending on molecular weight) [156]. van den Broek *et al* (2008) suggest that this addition leads to adverse side effects, such as the increase of osmolality (a measure of salt or electrolyte concentration) [157]. They, and others, recommend a different polysaccharide known as xanthan gum (XG) which is required in much smaller amounts (0.7 gl^{-1} is stated as the required concentration to reach blood viscosity), keeping osmolality within a safe range [158].

1.6.4   *In vitro* **model experimentation**

Examples of *in vitro* experiments studying the effects of wall shear stress on EC under flow are detailed in Table 1.2. Experiments must balance the duration of cell viability against the time required to observe noticeable effects. A 24 hour time frame is most often chosen, as EC regrowth has been seen to occur *in vivo* within the first day post-neointimal injury [107]. Most studies use a control: cells kept in static conditions, uninjured cells, or cells not subjected to stent deployment. The majority of analysis is performed at a single time point once the experiment is complete and any mid-experiment analysis, where it exists, is limited to easily observable parameters such as cell size and migration distance.

Studies not listed in Table 1.2 include those by Liu *et al* (2014), in which a stent was placed onto static EC culture [159]. Cell-free models were created by Peacock *et al* (1995) and Bernard *et al* (2003) to study stent-induced flow disturbance, using static probes and laser particle image velocimetry (PIV) [84][94].

Study	Duration	Method of assessment	Model	Time point
Albuquerque, 2000. [95]	24 hours	Cell proliferation, spread, migration rate and distance. Area of wound closure.	Parallel plate	Peri
Antoine, 2016. [160]	4 days*	Rate of wound closure.	FEP tube with hydrogel lining, clinical stent	Peri & post
Cardinal, 2009. [161]	14 days	Area of coverage, morphology.	Tissue engineered vessel, clinical stent	Post
Hsiao, 2016. [103]	96 hours	Cell migration distance, persistence and orientation. Area of coverage.	Parallel plate, mock stent	Peri
Moore, 1994. [74]	24 hours	Cell orientation and elongation.	Silicone tube	Post
Punchard, 2009. [107]	24 hours	Cell proliferation, orientation, morphology, gene expression and metabolic activity.	Silicone tube, clinical stent	Post
Simon, 2000. [114]	24 hours	Cell migration distance. Areas of coverage and exposed wall.	Parallel plate, mock stent	Post
Sprague, 1997. [127]	7 days	Cell proliferation, migration distance, apoptosis rate and Nitric oxide production.	Parallel plate, mock stent	Post
Sprague, 2012. [117]	7 days	Cell proliferation, migration distance, apoptosis rate and Nitric oxide production.	Parallel plate, mock stent	Post
Ziegler, 1998. [146]	24 hours	Cell orientation and elongation, gene expression and protein concentration.	Silicone tube	Post

Table 1.2 *In vitro* experiments assessing HUVEC under laminar flow

To the author's knowledge, commercially available clinical stents have only been deployed in *in vitro* models with seeded EC, and exposed to laminar flow, in three previous studies (Table 1.2): a tissue engineered blood vessel mimic (Cardinal *et al*, 2009 [161]), a dip-coated silicone tube (Punchard *et al*, 2009 [107]), and an FEP tube with a hydrogel lining (Antoine *et al*, 2016 [160]). A complete cell monolayer was present in each model and, as such, the only assessment of EC migration, in the work of Antoine *et al*, was limited to wound closure.

1.6.5 *In silico* modelling

As mentioned in the previous section, studies have employed PIV and particle tracking velocimetry (PTV), optical methods of visualising and analysing flow patterns and extracting velocity data. These techniques are advantageous in their ability to offer rapid or instantaneous data, their non-destructive nature, and their ability to be performed on cell migration models *in situ*. However, disadvantages include the accuracy and resolution of resultant velocity (and therefore shear stress) data.

As such, a substantial amount of the literature employs *in silico* model vessels and computational fluid dynamics (CFD) simulations to study local haemodynamics. CFD is a useful tool, allowing the extraction of detailed information on flow patterns, areas of recirculation, velocity profiles, wall shear stress magnitudes and various shear indices [92][111]. The ability to run multiple simulations *in silico* allows models to be quickly assessed under a range of applied conditions and enables parametric study.

The flow of blood is generally simulated, in some cases even when modelling *in vitro* experiments which use cell culture medium [130]. Based on the assumptions described in Section 1.4.2, the majority of these simulations consider blood as a Newtonian fluid. Blood density is always taken as 1050 - 1060 kg/m^3 and viscosity as 3 - 4 mPa.s [88][111][133][162][163]. Studies which do not rely on this assumption use the Carreau method to describe non-Newtonian flow with generalised Newtonian fluids (viscosity is dependent on shear rate, but not on shear

rate history. This is not true non-Newtonian flow, but is a good approximation) [113][164]–[166].

Stent models can be created with various complexity and accuracy with computer-aided design (CAD) software, ranging from basic geometric shapes to idealised commercial designs [113][167]. Models have been employed for parametric analysis of specific features such as strut thickness, using CAD generated mesh patterns by LaDisa *et al* (2004) [112], and rigid rings by Barakat and Cheng (2000) [168]. This latter example also compared simple 2D geometries with more complex 3D models. The importance of model accuracy and realism is illustrated by the fact that 2D simulations overestimated flow disturbance in comparison to 3D (this is assumed to be due to 3D models allowing secondary flow to develop, which inhibits radial velocity and the size of flow separation zones).

Unlike the above examples, which simulated steady-state flow around stents in straight vessels, Balossino *et al* (2008) applied pulsatile flow and a deformed artery wall [167]. The total area exposed to <0.5 Pa of wall shears stress (the value they assume to be the critical threshold for ISR development) was seen to decrease in stents with thicker struts, contrary to the findings of the above simulations and those described in Section 1.5.2. These results were presumed to be due to the combination of pulsatile flow and modified wall geometry, and could further demonstrate the value of increased model realism.

In addition to measuring wall shear stress across surface area, or at specific points, various wall shear metrics have been proposed for the assessment of stent designs. Time averaged wall shear stress (TAWSS) considers the force on the wall over the entire cardiac cycle [165]. The oscillatory shear index (OSI) quantifies flow reversal [86], while the haemodynamic low and reverse flow index (HLRFI) quantifies the effect of both flow reversal and areas of low flow [111]. Transverse wall shear stress (transWSS) is the time-average of wall shear components perpendicular to flow direction [169]. Each of these metrics returns different results. It is up to the user to decide, depending on the research question, which wall shear qualities they deem to be the most important. In terms of identifying or predicting locations of EC dysfunction, it has been suggested that the low shear index (LSI) is

superior to the above. Rather than simply labelling a specific wall shear magnitude as 'low' and applying this threshold globally, LSI defines low shear in relation to the normal or intermediate conditions in each individual environment [170].

1.6.6 Replicating accurate stent geometry *in silico*

More accurate *in silico* data can be obtained by basing computational models on realistic stent deployment. Clinical scans of patients' vessels have been used, however the available resolution is only high enough to reproduce arterial segments, not the stents themselves [88][163]. Their structure can be replicated by creating finite element (FE) models of crimped stents and simulating their deployment within the vessel [167][171], but there is no guarantee that the final geometry is faithful to that *in vivo*.

In order to properly compare *in vitro* EC behaviour to precise local wall shear stress, the specific geometry of the model vessel must be replicated. CAD is sufficient for simple representations of stents, e.g. ridged channels [103], but to capture entire, complex clinical stents some form of scanning is most often employed.

Optical coherence tomography is widely used *in vivo* and the technique can also be applied within *in vitro* models [172][173]. A catheter is pulled through the vessel and uses reflected near-infrared light to build an image of the surrounding structure. The use of relatively long wavelengths means light can penetrate 1 – 2 mm below the surface, enabling a 3D picture of stent strut penetration to be created. However, the resultant images can be low resolution (~20 μm), and any vessel curvature is lost as readings are taken perpendicular to the catheter.

Micro-computed tomography (μCT) scanning is more commonly used to obtain the geometry of stented models, and can resolve features of just 0.5 μm. However, simultaneous imaging of stents and vessel walls, whether tissue or *in vitro* model, is problematic due to their different radiopacity. One solution to this problem involves capturing the stent only and recreating the wall *in silico* using FE software. The stent is then modelled as a rigid body and the wall collapsed around it as far as applied material properties will allow, essentially shrink-wrapping the stent [162]. As per the

previously described model of stent expansion, this method is half faithful reproduction of geometry, half virtual model.

A second solution to the visualisation issues inherent to μCT is to better define the wall/lumen boundary, and allow simultaneous imaging, by increasing the visibility of the otherwise empty lumen. This has been carried out by corrosion casting, in which the lumen is filled with a radiopaque material and the surrounding vessel is destroyed [174], and with the use of contrast agents. Contrast agents have the advantage of leaving the model intact, and have been shown to produce good results in both *ex vivo* and *in vitro* examples [133]. Figure 1.11 illustrates the level of detail that can be obtained and shows that even in simple, straight vessels stent deployment can result in non-symmetrical expansion and strut misalignment that would not be replicated in idealised models, proving the advantage of capturing realistic geometries.

1.7 Physiological data

Relevant literature was reviewed for information on which to base the structure and size of *in vitro* models, and the conditions applied within both them and accompanying *in silico* models. Conforming, where possible, to anatomical values of the properties described in the following sections ensured that *in vitro* and *in silico* models were physiologically relevant, and increased the translational potential of resultant data. Sources were restricted to studies of arterial segments unaffected by disease, to omit extreme or abnormal results and to provide an idea of a 'normal' artery. In addition, the properties described below are, where possible, those of the coronary arteries only.
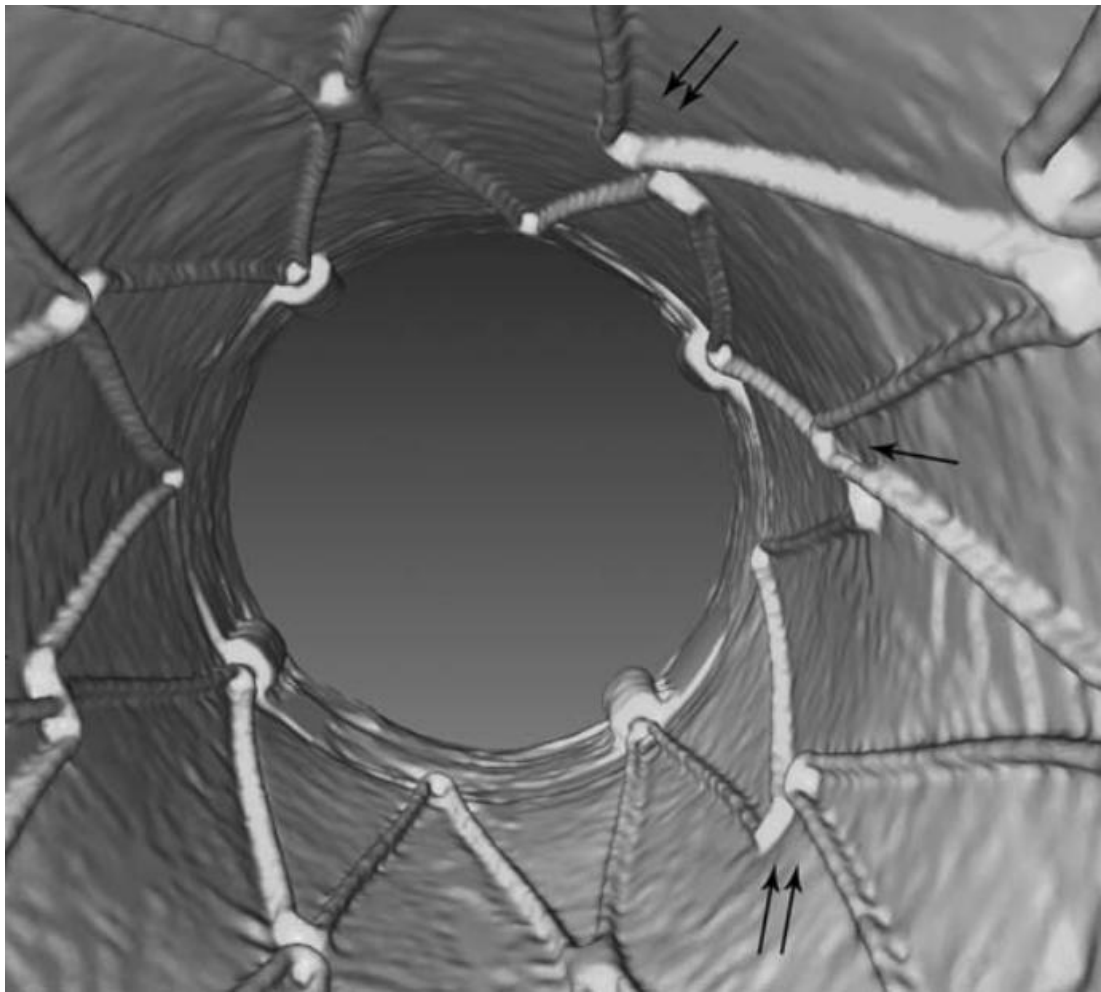
Figure 1.11 3D model of a stented tube reconstructed from μCT data

A flow diverter stent deployed within a PTFE tube was scanned using high-resolution μCT. Both the wall and stent were reconstructed via the use of a contrast agent to better define the wall-lumen boundary. In this 3D reconstruction of the scan data, the level of detail attainable enables strut prolapse (single arrow) and misalignment (double arrows) to be captured.

(Reproduced with permission [133]*).*

1.7.1 Mechanical properties of the arterial wall

A number of studies consider the mechanical properties of diseased coronary arteries only, and often the plaque itself, in order to investigate its structure and stability (similarly, research focuses on the properties of aneurysmal sacs with the aim of predicting rupture and the need for intervention) [121]. Data on the stiffness of healthy arterial segments typically varies over several orders of magnitude. This wide range highlights the great impact of both age and lifestyle on vessel stiffness, but is also due to the variety of material being tested: from macrostructure (whole vessels and tissue) to microstructure (tissue components such as collagen and elastin) [175].

A general idea of arterial wall stiffness is required to ensure that stent deployment can be modelled accurately, in terms of the degree of strut penetration and local wall distention. The elastic modulus of macrostructure bulk tissue has been found to vary between $0.1 - 100$ MPa, whereas individual microstructural components are a stiffer $1 - 1000$ MPa [175]. One example of a specific arterial segment, the stiffness of a carotid artery, was found to be at the lower end of this first range, at 0.9 MPa [176].

1.7.2 Coronary artery diameter

The size of coronary arteries varies greatly and has been found to differ with age, sex, race, and body surface area. Specific values of coronary artery diameter for healthy adult populations were found in 14 studies. 132 averaged measurements were taken from a total of 1001 samples, which represented a range of arterial segments [177]–[190].

From this data, the minimum coronary artery diameter was 1.29 mm, in a branch of the left anterior descending artery. The maximum was 4.89 mm, in a segment of the left main artery. The mean coronary artery diameter was found to be 2.90 mm, ±0.90 mm SD.

1.7.3 Wall shear stress

In investigating the response of EC to wall shear stress, a sound understanding of the magnitude of the force reached in coronary arterial flow is crucial. This not only aids in the application of appropriate conditions in *in vitro* and *in silico* models, but also in defining the bounds of what is considered to be low, high, etc., for conclusions to be drawn. Further to the applied values in Section 1.6.3, Figure 1.12 illustrates quantitative data for physiological wall shear stress, with accompanying qualitative categories. The coronary arteries are generally exposed to wall shear stress ≤3 Pa, although in three cases the maximum stated value was found to be 7 Pa [82][85][87].

Mean, or intermediate, wall shear stress levels range from approximately 1 to 2.5 Pa, and the majority of the sources reviewed here considered 1 Pa to be the threshold below which shear stress may be described as low. Beyond this, there is little consistency. There is no single threshold above which shear stress is described as high. Many studies' low and high ranges are considered by others to lie within the mean, and in some cases the two opposed definitions actually overlap. For example, Stone *et al* define low shear stress as <1.2 Pa [89], a value within the range Chiu *et al* describe as increased/higher [82]. Such examples are of note, given that conclusions are often drawn based upon these definitions.

1.7.4 Velocity and flow rates

Reaching the desired magnitude of wall shear stress within *in vitro* models requires the application of a specific flow velocity or volumetric rate. These values may or may not be physiologically relevant, depending on the size of the model and the viscosity of the fluid being used. An impression of the flow found *in vivo* can be used to assess just how disparate the necessary *in vitro* values are, and can provide further information on local wall shear stress levels.
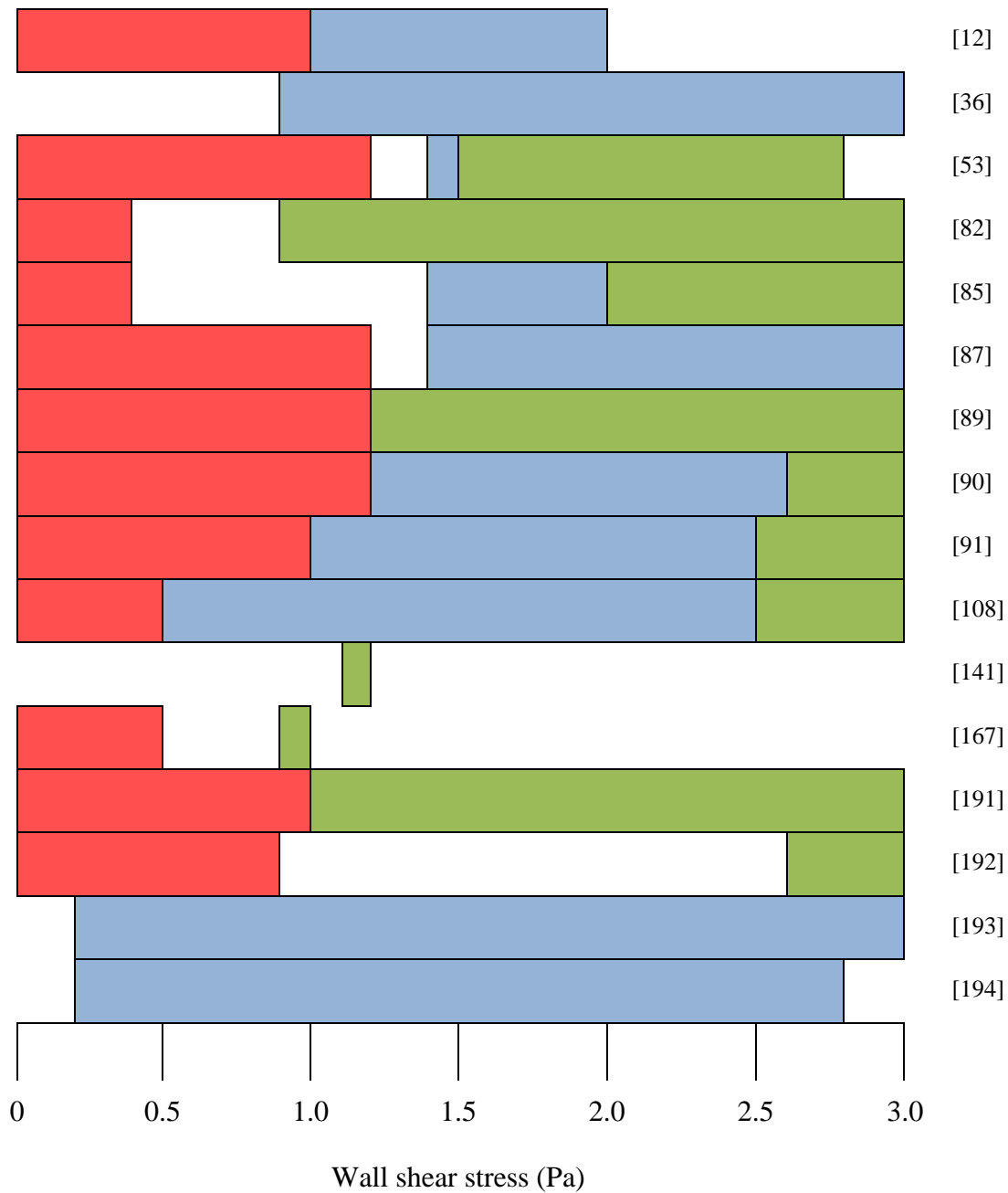
Figure 1.12 Physiological magnitude of coronary artery wall shear stress

The magnitude of coronary artery wall shear stress measurements from a number of sources is shown, with colours corresponding to the descriptions used by the authors.

Red: Low shear stress.

Blue: Intermediate or average shear stress.

Green: High shear stress.

5 studies stated volumetric flow rates for individual arterial segments [180][186][190][194][195]. The minimum rate was 18 ml/min and the maximum 161 ml/min, both measured by Hundley *et al* [190]. The mean was found to be 80 ml/min. Data regarding coronary artery flow velocity was limited to 5 measurements in 2 studies [195][196]. Blood flow was measured and time averaged, to provide mean velocities for the whole cardiac cycle. The minimum velocity was 0.06 m/s, the maximum 0.149 m/s and the mean 0.08 m/s.

To equate this data to that in Section 1.7.3, corresponding levels of wall shear stress can be calculated. Assuming coronary arteries of 2.9 mm diameter (the average found in Section 1.7.2), the minimum, maximum and mean volumetric flow rates induce shear stress of 0.44, 3.92 and 1.95 Pa respectively. Minimum, maximum and mean velocities induce shear stress of 0.62, 1.54 and 0.83 Pa. These values lie within the range seen in the previous section.

1.8 Study rationale

The regrowth of a healthy endothelial layer, whether by local EC migration or circulating EPC capture, is a key component of vascular repair and vital to the reduction of post-procedural complications. It is known that this process is hindered by EC dysfunction, caused by the presence of cardiovascular stents and their effect on local haemodynamics; specifically modified wall shear stress. Considered design could improve vascular health by minimising the impact of stents, or enable them to exert an active, beneficial influence on their environment.

Optimising stented artery repair requires knowledge of precisely how particular stent design features influence wall shear stress and EC behaviour. Previous studies have considered these two factors separately, with simple representative geometry and idealised computational models. Only with the use of a physiologically relevant system, realistic complex stent geometry and accurate computer simulation can a full understanding of stent-induced biomechanics be achieved.

1.9 Aims

This work aimed to create an experimental platform through which the biomechanical conditions of stented vessels could be studied, by developing a unique combination of *in vitro* and *in silico* techniques:

- A novel, physiologically relevant, biocompatible *in vitro* model vessel for the deployment of clinical cardiovascular stents.
- An experimental protocol for the real-time study of endothelial cell migration local to stent geometry within the *in vitro* model.
- An experimental protocol for the study of stent-induced fluid dynamics within the *in vitro* model, enabling the rapid acquisition of flow data *in situ*, via non-destructive means.
- A protocol for the precise reproduction of *in vitro* vessel and stent geometry *in silico*, to permit the study of stent-induced fluid dynamics via computer simulation, enabling the acquisition of flow data of higher accuracy and resolution.

Ensuring the above techniques were effective, accurate, repeatable and time-efficient would allow their application to a wide range of coronary and flow diverter stents. This would enable the assessment of the effect of diverse stent geometry on wall shear stress modification and its subsequent impact on endothelial cell behaviour.

Chapter Two

Materials and Methods

2.1 *In vitro* model

2.1.1 Fluid properties

To aid in model design and ensure that appropriate conditions were applied during experiments, the density and dynamic viscosity of fluids was required. This was obtained from reference data where possible. However, for cell culture medium, values for the specific mixtures used here (listed in Section 2.2.2) were unavailable and were therefore measured.

Density was measured by transferring 1 ml of medium, warmed to 37°C, to a digital scale (ABS-N/ABJ-NM, Kern & Sohn) to obtain the mass to volume ratio. Medium viscosity approached the lower limit of available viscometers, particularly at cell incubation temperature. Therefore, two different techniques were used and the findings compared to the literature:

2.1.1.1 Reflectance viscometry

Reflectance viscometry was performed in collaboration with Michele Schirru (The Leonardo Centre for Tribology, University of Sheffield). 0.5 ml of cell culture medium was placed onto a sensor plate. This was connected to a waveform function generator (TG5011, TTi) and a transmitting transducer, to produce an ultrasonic wave. The reflection of ultrasonic shear waves from the solid-liquid interface was detected by a receiving transducer and recorded on an oscilloscope (LT342, LeCroy). Algorithms developed by Schirru were then applied to correlate the reflection coefficient to viscosity [197].

2.1.1.2 Vibrational viscometry

2 ml of cell culture medium warmed to 37°C was transferred into a vial and placed in a vibrational viscometer (SV-1A Vibro Viscometer, A&D Company). Three sensor plates were lowered into the fluid: one temperature sensor and two vibrating viscosity sensors. The viscometer measured the electric current required to maintain this vibration at 30 Hz and these measurements were then converted to viscosity.

Viscosity was recorded as the fluid cooled over time. Results were calibrated against, and compared to, equivalent data obtained from a 2 ml reference sample of water.

2.1.2 Material properties

In vitro model vessels were fabricated using PDMS (Sylgard 184, Dow Corning Corp.). Samples with various cross-linking densities were created for mechanical testing to compare the material to arterial tissue and to assess suitability for stent deployment. PDMS base and curing agent components were combined at 5:1, 10:1, 15:1, 20:1, 30:1, 40:1, 50:1 and 60:1 ratios by weight and mixed for 10 minutes. 34 g of each mixture was poured into a 90 mm diameter Petri dish, to form a layer 5.5 mm deep. To account for small, unavoidable variations in this process, three separate batches of each mixing ratio were prepared.

As curing temperature is known to affect the mechanical properties of PDMS, test samples were prepared under the same conditions as the final model (Section 2.1.4). Specifically, PDMS was cured at room temperature for 24 hours, followed by 15 minutes in a 100°C oven. To eliminate bubbles, which could act as defects and distort results, samples were kept in a vacuum desiccator (5311-0250, Nalgene) for the duration of the room temperature curing period. Cured PDMS was cut into test pieces of 30 mm length, 10 mm width and 5.5 mm depth and the three most uniform pieces from each batch were selected for testing.

Test pieces were inserted into a dynamic mechanical analysis instrument (EnduraTEC ELF 3200, BOSE) for tensile testing. Grips were attached over 10 mm at either end of the sample, leaving a pre-extension initial length of 10 mm in the centre. Each PDMS sample underwent a maximum 5 mm of extension, at a speed of 0.1 mm/s. The applied load and extension were recorded, stress and strain calculated

and plotted, and the gradient of the linear elastic region identified to then obtain the elastic modulus.

2.1.3 Mould design and preparation

Moulds were designed to create channels of 1.5, 2 and 2.5 mm internal diameter which were exposed to an average wall shear stress of 1 Pa (the use of these specific values, which take into account both physiological relevance and practical limitations, is discussed in Sections 3.1.1 and 3.1.3). The volumetric flow rate required to attain this level of shear stress was calculated using the Hagen-Poiseuille equation:

$$\tau_{mean} = \frac{4\mu Q}{\pi r^3}$$

Q is the volumetric flow rate, τ_{mean} the mean wall shear stress, r the vessel radius and μ the dynamic viscosity of the fluid. Mean velocity, V, was calculated by dividing flow rate by cross-sectional area:

$$V = \frac{Q}{\pi r^2}$$

The Reynolds number (Re) could then be calculated, using vessel diameter D and fluid density ρ:

$$Re = \frac{VD\rho}{\mu}$$

Finally, the Reynolds number was used to calculate the entrance length (L) required for laminar flow with a parabolic velocity profile to fully develop within the vessel:

$$L = E_L D$$

E_L is the entrance length number, which is dependent on the flow regime. Assuming a transition between laminar and turbulent flow at $Re = 2300$:

$$E_L(laminar) = 0.06Re$$

$$E_L(turbulent) = 4.4Re^{\frac{1}{6}}$$

The above was calculated for 1.5, 2 and 2.5 mm diameter channels using viscosity and density data for the full range of fluids used. This allowed the correct flow rate to be applied in each experiment and ensured that models were long enough for flow to fully develop before reaching the leading edge of deployed stents.

Based on this data, 8 ml polystyrene cuvettes (Sarstedt) were used to create moulds (Figure 2.1). To create channels, 1.5, 2 and 2.5 mm diameter aluminium rods were cut to 100 mm length and inserted into the cuvettes. Holes were punched in rubber caps, which were then placed in the bottom and top of each cuvette to centre the rods. Additional holes were punched around the circumference of the top cap to allow air to escape during degassing.

2.1.4 Model fabrication

PDMS for *in vitro* models was prepared by mixing the base and curing agent components at a 10:1 ratio by weight for 10 minutes and degassing in a vacuum desiccator for 20 minutes. A minimum of 9 g of PDMS was prepared per mould, to ensure a usable model length of at least 80 mm.

PDMS was poured into the cuvette with the bottom cap and aluminium rod already inserted and the top cap was then applied. To ensure the model was properly filled, and to remove any remaining bubbles, the PDMS within the cuvette was degassed for a further 20 minutes, then centrifuged for 10 minutes at 626 g (Centrifuge 5702, Eppendorf). The PDMS was then left to cure at room temperature for 24 hours.

Once hardened, the PDMS was released by breaking the cuvette apart. The rod and end caps were removed, and cleaned for re-use. The ends of the PDMS were trimmed, leaving an 80 mm x 10 mm x 10 mm PDMS block, with a 1.5, 2 or 2.5 mm diameter channel in the centre, referred to herein as the model vessel (Figure 2.2A). This was placed into an oven at 100°C for 15 minutes, to fully complete the curing process and eliminate any potentially cytotoxic unlinked monomers.
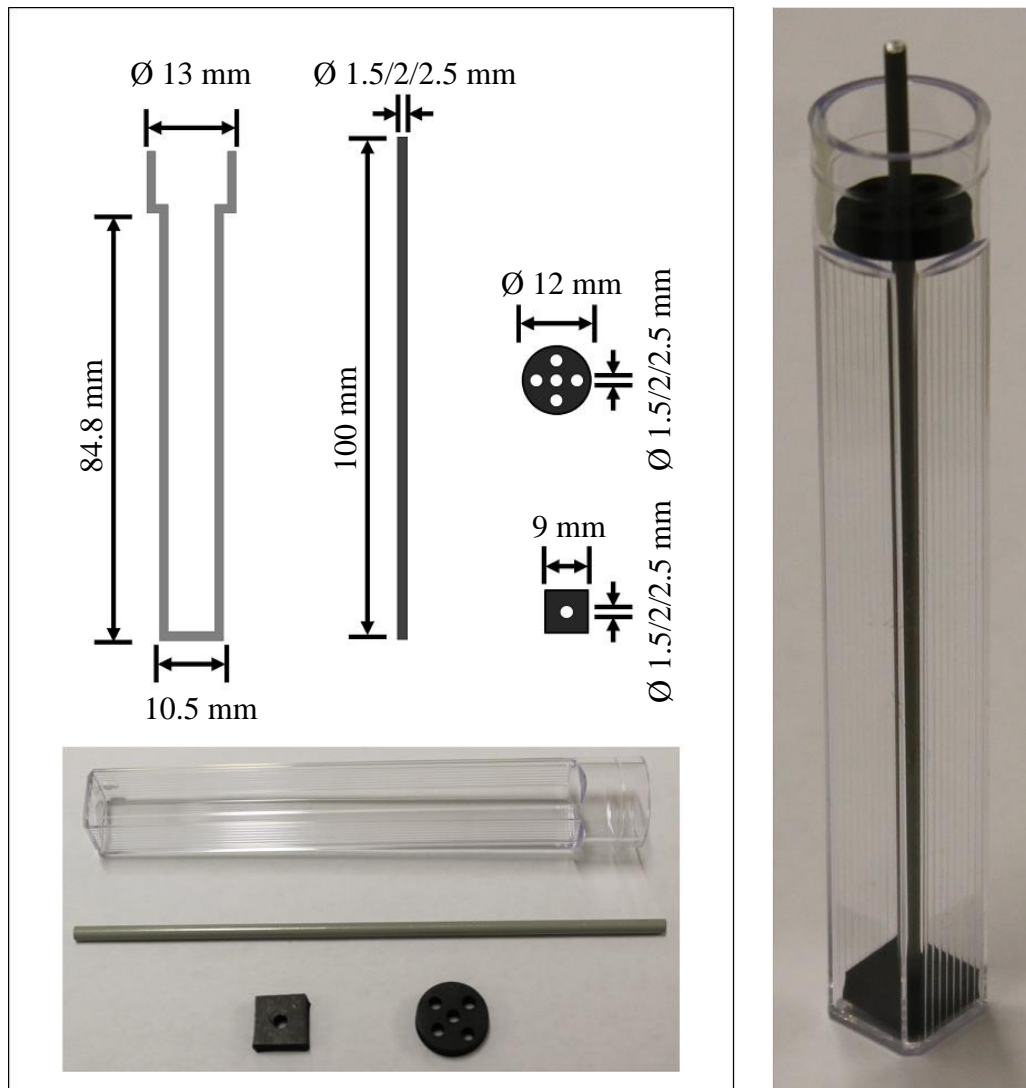
Figure 2.1 *In vitro* model mould

Plastic cuvettes were used a moulds to create model vessels in PDMS, with metal rods of various diameters in place to create circular channels within them.

Left: Individual components used in the mould (cuvette, rod and rubber caps) and their dimensions.

Right: An assembled mould. PDMS would be poured into the mould up to the level of the upper rubber cap.
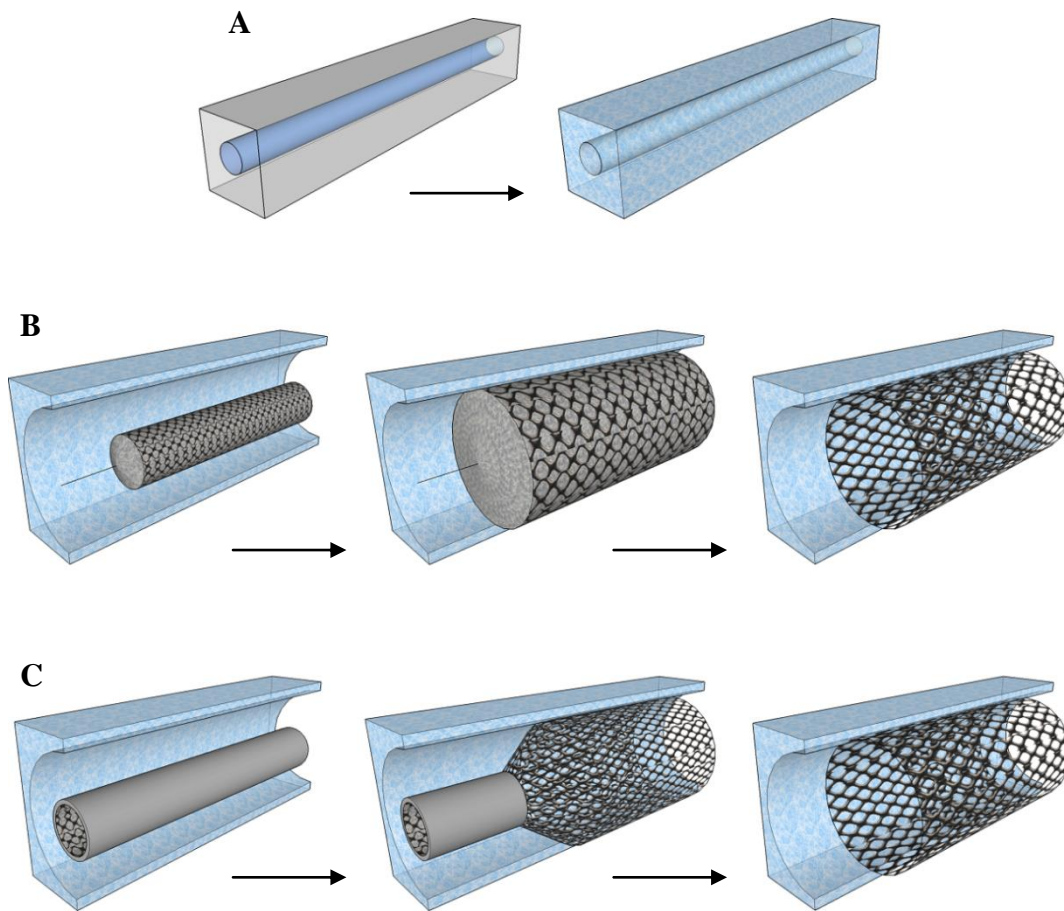
Figure 2.2 *In vitro* model fabrication and stent deployment

A: To create model vessels, PDMS was poured into a mould (left). Once cured, the mould (consisting of a cuvette, rod and rubber caps) was removed, leaving the resultant PDMS model vessel (right).

B: Coronary stents were deployed in the model via the inflation of balloon catheters.

C: Flow diverter stents were deployed in the model via the retraction of introducer sheaths.

For experiments with seeded HUVEC, PDMS vessels were sterilised via autoclave at 121°C for 30 minutes and coated with 10 µg/ml fibronectin, prepared by adding 1 mg/ml fibronectin (fibronectin from bovine plasma, Sigma-Aldrich) to phosphate buffered saline (PBS, Sigma-Aldrich). The solution was injected into the vessel (140, 250 and 390 µl to completely fill each 1.5, 2 and 2.5 mm diameter model respectively) and left for 1 hour at room temperature. The fibronectin solution was then removed and the vessel flushed with 1 ml of PBS.

Model vessels were used for stent deployment and experimentation within 48 hours of PDMS curing and 24 hours of fibronectin coating.

2.1.5   Stent deployment

Coronary and flow diverter stents were deployed following clinical guidelines and manufacturers' instructions where possible. For experiments with HUVEC, stents were deployed after cell seeding and attachment (detailed in Section 2.2.4) in aseptic conditions.

Stent deployment was assessed by visual inspection under a light microscope (AE2000, Motic). Struts were checked for expansion and for some degree of pushing against, or penetrating into, the PDMS wall. If required, a balloon catheter could be reinserted and inflated to complete deployment. Any stents which were not correctly or completely deployed could shift under fluid flow and were not used in experiments.

2.1.5.1   Coronary stent deployment

Balloon catheters with pre-mounted coronary stents were connected to a dilation syringe with pressure gauge. Any protective sheaths or coverings were removed and the catheter was inserted into the model vessel. The catheter was held in place with the mounted stent positioned centrally (Figure 2.2B). The syringe's threaded plunger was rotated to gradually increase the pressure within the balloon to that recommended by the manufacturer. A 1.2:1 balloon to vessel ratio was used, as per clinical guidelines (e.g. coronary stents within 2.5 mm diameter vessels were dilated

to 3 mm), typically requiring a pressure between 6 and 11 atm. The balloon was held at the required pressure for 30 seconds, before the plunger was released and negative pressure applied to contract the balloon, which was then carefully removed.

2.1.5.2   Flow diverter stent deployment

Self-expanding flow diverter stents were inserted into the model on a guide catheter, whilst covered by a protective introducer sheath. Stents were again positioned midway along the vessel length, and held in place as the sheath was gradually pulled back (Figure 2.2C). Flow diverter stents generally started to expand once struts were freed from the sheath; however a slow back-and-forth motion was often required to encourage full expansion along the entire length of the stent.

2.1.6   Assessing stent geometry

The length and nominal diameter of stents was provided by the manufacturer with each sample. However, the size of struts was often only provided in one dimension, given as a range, or simply not stated. Therefore, in an effort to obtain accurate values, struts were measured with a digital calliper (Absolute AOS Digimatic, Mitutoyo) and photographed under magnification, with the image scale calibrated against a haemocytometer grid.

The metal-to-artery ratio of stents was calculated by measuring the lateral surface area of one fully expanded repeating unit of stent geometry (the metal surface area, or MSA), and dividing this by the area of the vessel wall bounded by the repeating unit (Figure 2.3B).

The orientation of struts relative to the direction of flow was measured using the Directionality function in the Fiji ImageJ plug-in (National Institutes of Health), with the software returning a table of structure directionality (angle relative to 0°, the direction of flow) and the length of structure at that orientation (as a percentage of the total). For each stent design the analysis was performed on an image of one repeating unit of geometry (Figure 2.3C), as well as the full stent length at two different orientations, and an average of these results was taken.
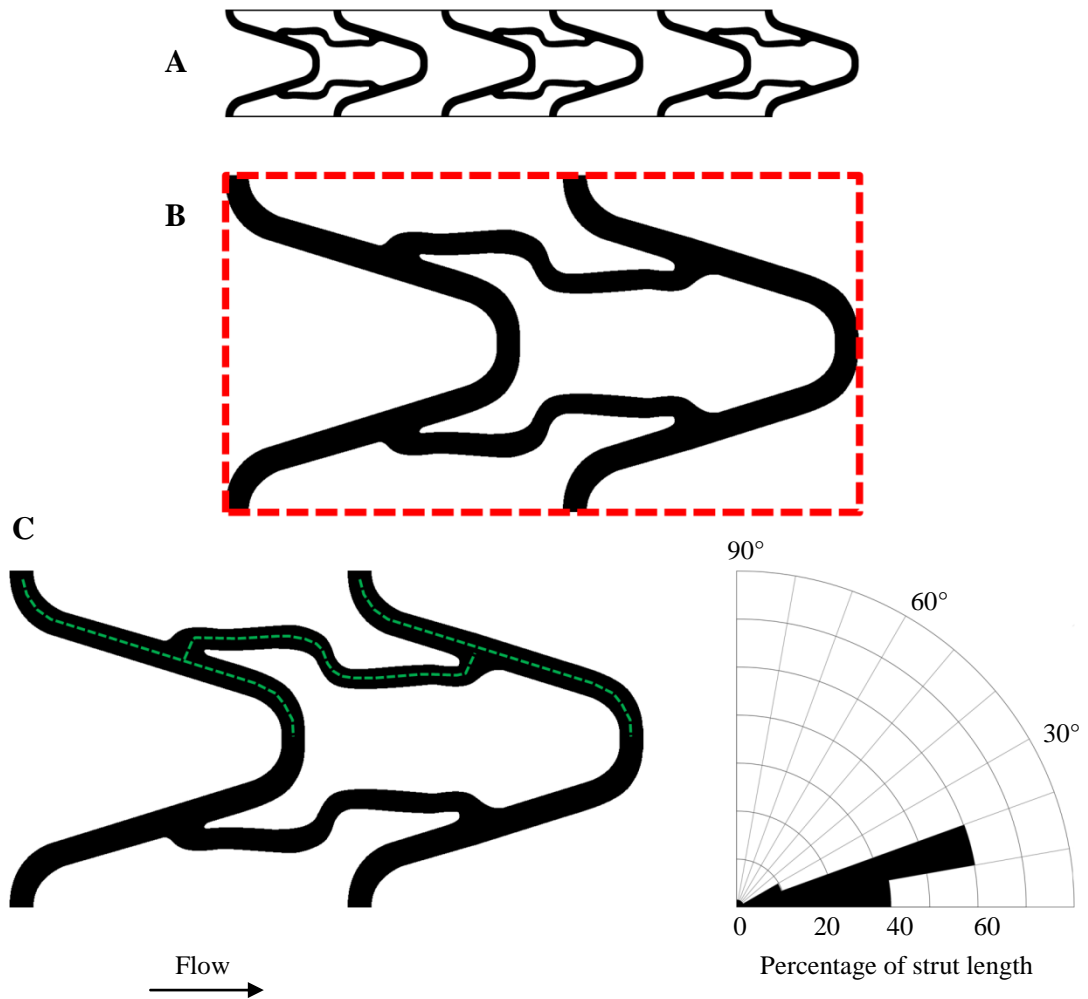
Figure 2.3 Assessing stent geometry

The geometry of deployed stents was assessed by measuring strut dimensions, and calculating the metal-to-artery ratio and strut orientation.

A: Representative image of a deployed coronary stent as they appeared under magnification, along its longitudinal axis.

B: The metal-to-artery ratio of stents was calculated by dividing the lateral surface area of one repeating unit of stent geometry (the MSA, in black) by the area bounded by that unit (within the red box).

C: Strut orientation was calculated by measuring the angle of struts relative to flow (left, green lines) and the length of struts at each orientation as a percentage of the total (right).

2.2   Cell migration studies

HUVEC were seeded within model vessels to assess their migration under flow. The protocol detailed in this section was carried out for a variety of coronary and flow diverter stents, as well as empty non-stented vessels as controls. Unless stated otherwise, work was conducted under aseptic conditions in a laminar flow hood and all cell culture media warmed to 37°C.

2.2.1   Isolation of HUVEC

HUVEC were isolated from umbilical cords collected from the Jessop Wing maternity unit, Sheffield, after informed consent and without patient identifiers. A frequent supply of isolated cells was provided by colleagues from the Department of Infection, Immunity and Cardiovascular Disease, University of Sheffield, using the collagenase digestion method described here in brief [142].

Each umbilical cord was wiped clean, having been stored in serum-free media (M199, Sigma-Aldrich) at 4°C for a maximum of 2 days. The umbilical vein was cannulated and media flushed through to remove blood clots. The vein was then filled with a further 20 ml of serum-free media containing 1 mg/ml of collagenase (collagenase from *Clostridium histolyticum*, Sigma-Aldrich) and left at room temperature for 15 minutes. The cord was gently manipulated to encourage the complete detachment of the endothelium. The collagenase solution and detached HUVEC were then drained into a tube and media flushed through the vein once more to remove as many cells as possible.

The cell suspension was centrifuged at 157 g for 5 minutes and the resultant cell pellet resuspended in EC growth medium (Section 2.2.2.1), seeded into T75 flasks and incubated. If required, the endothelial nature of the cells and the purity of the cell yield could be confirmed by staining for von Willebrand Factor and Pecam-1 [99]. After 24 hours, HUVEC were washed with PBS and fresh media was added. Cells were passaged once they reached 80 – 90% confluence (this method is detailed in Section 2.2.3) and were collected at passage 2 (P2).

2.2.2 Preparation of cell culture medium

2.2.2.1 EC growth medium

A mixture referred to herein as EC growth medium was used for HUVEC culture and experimentation. The concentration of individual components, listed below, is given in relation to a 500 ml mixture:

- Basal media (PromoCell)
- SupplementMix (PromoCell), containing:
    - Foetal calf serum (FCS)   2% v/v
    - Endothelial cell growth supplement   0.4% v/v
    - Epidermal growth factor (recombinant human)   0.1 ng/ml
    - Basic fibroblast growth factor (recombinant human) 1 ng/ml
    - Heparin   90 µg/ml
    - Hydrocortisone   1 µg/ml
- FCS (Labtech International)   20% v/v
- Penicillin (Sigma-Aldrich)   100 units/ml
- Streptomycin (Sigma-Aldrich)   100 µg/ml
- L-glutamine (Sigma-Aldrich)   2 mM

2.2.2.2 Thickened medium

Two thickening agents were used to assess higher viscosity flow. The first, 100,000 M_r dextran powder (dextran from *Leuconostoc*, Sigma-Aldrich), was added to PBS to create a stock solution at 25% w/v. This was sterilised via autoclave at 121°C for 30 minutes and added to EC growth medium in varying amounts to create 50 ml samples of thickened medium at five different concentrations:

1% w/v - 2 ml stock solution, 48 ml medium

2% w/v – 4 ml stock solution, 46 ml medium

3% w/v – 6 ml stock solution, 44 ml medium

4% w/v – 8 ml stock solution, 42 ml medium

5% w/v – 10 ml stock solution, 40 ml medium

The second thickening agent, XG powder (xanthan gum from *Xanthomonas campestris*, Sigma-Aldrich), was sterilised by exposure to ultraviolet light for 2 hours. This was then added directly to EC growth medium, again creating 50 ml samples of thickened medium at 5 different concentrations:

0.2 g/l – 0.01 g XG powder, 50 ml medium

0.4 g/l – 0.02 g XG powder, 50 ml medium

0.6 g/l – 0.03 g XG powder, 50 ml medium

0.8 g/l – 0.04 g XG powder, 50 ml medium

1.0 g/l – 0.05 g XG powder, 50 ml medium

The impact of thickening agents on cell viability was assessed by seeding HUVEC in well plates following the protocol detailed in Section 2.2.3 and, after 24 hours, replacing the standard EC growth medium with the above thickened samples. Cells were detached and counted after a further 72 hours, with the medium refreshed at the midway point. Wells containing standard EC growth medium were maintained as a control and additional control wells contained 80% EC growth medium and 20% PBS to account for the diluting effect of dextran stock solution. The effect of thickening agents on medium viscosity was measured as per Section 2.1.1.

2.2.2.3 ROCK inhibitor

In collaboration with Svenja Dannewitz Prosseda (Department of Infection, Immunity and Cardiovascular Disease, University of Sheffield) additional cell migration studies were performed using HUVEC in standard EC growth medium supplemented with 2 µM Y27632 (Calbiochem). This biochemical tool is a ROCK inhibitor, which enhances cell polarity and migration by silencing bidirectional mechanical cues (Section 1.4.4).

2.2.3 Cell culture

HUVEC were maintained in 0.1% gelatin-coated T75 flasks with 12 ml of EC growth medium, within an incubator at 37°C and 5% CO_2. The medium was changed every 3 – 4 days until cells reached approximately 90% confluency. At this point, the growth medium was discarded and the cells rinsed with 10 ml of PBS. 2.5 ml of trypsin-EDTA solution (Sigma-Aldrich) was added and the flask incubated for 5 minutes as the HUVEC detached, after which 10 ml of growth medium was added to deactivate the trypsin-EDTA. The contents of the flask were then decanted into a 50 ml tube, which was centrifuged for 5 minutes at 157 g to form a cell pellet. The supernatant was removed and the pellet resuspended in 1 ml of EC growth medium. To sustain the HUVEC culture, 100 µl of cell suspension was placed into a new gelatin-coated T75 flask with 12 ml of fresh EC growth medium. This was returned to the incubator to attach and proliferate. HUVEC were maintained up to P5.

2.2.4 Seeding endothelial cells within *in vitro* models

HUVEC were used for migration studies at P3 – 5, at approximately 90% confluence. 24 hours prior to seeding, the flask of cells to be used was removed from the incubator and the medium replaced with 10 ml of fresh EC growth medium and 1 µl of fluorescent dye solution (1 mg of CellTracker Green CMFDA, Fisher Scientific, with 10 µl of dimethyl sulfoxide, Sigma-Aldrich, resulting in a dimethyl sulfoxide concentration of 0.01% within the flask). The cells were re-incubated and the following day detached, formed into a pellet and resuspended as described in Section 2.2.3. 20 µl of the cell suspension was then removed and mixed with 20 µl of 0.4% trypan blue solution (Fisher Scientific). This mixture was injected onto a haemocytometer and the live, unstained cells were counted.

HUVEC were seeded into the *in vitro* models at a density of approximately 1000 cells/mm^2 to attach to the lower half of the vessel only, due to practical requirements which are discussed in more detail in Section 3.6. The 1 ml suspension from a 90% confluent T75 flask would typically contain approximately 3 million cells, which was diluted with additional media to obtain the correct concentration. A final cell suspension of 1.3 million cells/ml was required for vessels of 1.5 mm diameter,

1 million cells/ml for vessels of 2 mm diameter and 800,000 cells/ml for vessels of 2.5 mm diameter.

Cell suspensions were slowly injected into model vessels until the filling front approached the half-way point, leaving the remaining half empty (Figure 2.4A). The vessels were placed in the incubator and left for the HUVEC to settle onto the lower surface and attach over the course of 12 – 18 hours. Successful attachment was indicated by a change in HUVEC morphology and confirmed by flushing the vessel with PBS. The use of PBS rather than media ensured that only well attached HUVEC remained, and vessels were flushed from the cell-free end so that no cells were pushed downstream of the seeding point. Continued attachment was again verified under a light microscope (AE2000, Motic), and the vessel was filled along its entire length with EC growth medium.

For redundancy, multiple model vessels were seeded per stent sample. The best examples, in terms of attached cell confluency and a well-defined border between the cell monolayer and bare wall, were selected for stenting. The leading edge of attached HUVEC was marked and a stent inserted from the cell-free end and deployed as per Section 2.1.5. Coronary stents were deployed with their upstream edge as close to this mark as possible (Figure 2.4B), whereas flow diverter stents were deployed with their upstream edge approximately 2 mm over the cell layer (Figure 2.4C). The reasoning behind this change in protocol, due to variability in flow diverter stent geometry, is discussed in Section 5.5. The vessel was then checked under the microscope once more, to assess the condition of HUVEC post-deployment.

2.2.5   Tracking endothelial cell migration

Following HUVEC attachment and stent deployment, model vessels were linked to one of two flow systems as described below. The system used in each instance was dependent on the maximum flow rate the equipment could supply and the rate required in each model.
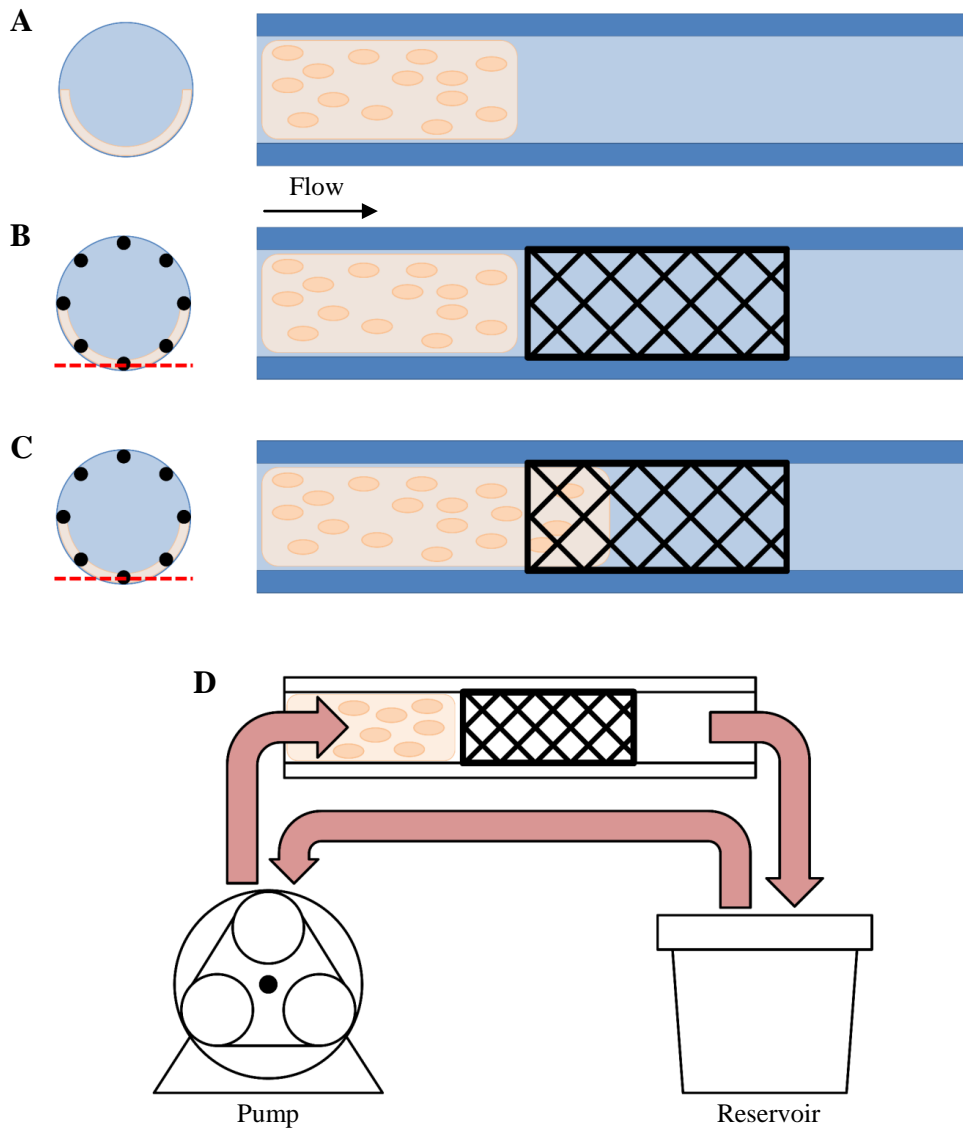
Figure 2.4 Cell seeding and stent deployment

A: Cross-section (left) and longitudinal view (right) of HUVEC seeded partway along the model vessel, on its lower half only.

B: Coronary stents were deployed downstream of attached HUVEC, with their upstream edge as close to the cells as possible. The red line represents the plane of focus used in microscope imaging, the lower edge of the wall and adjacent stent struts.

C: Flow diverter stents were deployed with their upstream edge overlapping attached HUVEC by approximately 2 mm.

D: Stented vessels were connected to a pump and fluid reservoir, via tubing of equal internal diameter. Flow was applied from the cell-covered end of the model.

2.2.5.1   Peristaltic pump

Models of 2 and 2.5 mm diameter were connected to silicone tubing and, as a reservoir, a borosilicate bottle filled with 50 ml of EC growth medium (Figure 2.4D). The tubing was then inserted into a cassette for connection to a peristaltic pump (FH100M Multi-channel Peristaltic Pump, Fisher Scientific) and the vessel and reservoir placed in a 37°C egg incubator (Kingsuro Max. 20, Rcom). The pump was turned on, set to 25% of the flow rate required to generate an average of 1 Pa wall shear stress within the vessel and gradually increased to the required rate over an hour.

2.2.5.2   Air pressure pump

Models of 1.5 mm diameter were connected to an ibidi Pump System (ibidi GmbH), consisting of an air pressure pump, fluidic unit with reservoirs and PumpControl software. The vessel and entire fluidic unit were able to fit within a 37°C CO_2 incubator. The pump was programmed to supply constant unidirectional flow, once again gradually increasing the rate up to that required to generate 1 Pa of wall shear stress. Experiments using the ibidi Pump System were performed in collaboration with Svenja Dannewitz Prosseda (Department of Infection, Immunity and Cardiovascular Disease, University of Sheffield).

Once maximum flow rates were reached experiments were considered to be at time point 0 (t = 0) and an image was captured. The model was then left under flow for as long as possible and, without pausing the pump, periodically removed from the incubator to be imaged over the course of the experiment. 2 and 2.5 mm models were photographed using a digital camera (EOS 1200D, Canon) attached to an inverted microscope (AE2000, Motic), under brightfield illumination or fluorescent light provided by a Stereo Microscope Fluorescence Adapter with a Royal Blue wavelength set (NIGHTSEA). 1.5 mm models connected to the ibidi system were imaged on an Eclipse Ti inverted microscope (Nikon) within a cage incubator (Okolab), linked to MetaMorph microscopy automation and image analysis software (Molecular Devices). This provided the option of leaving the model on the

microscope stage for the duration of the experiment and concurrently programming the software to capture images at specific time points and locations. In each case, the plane of focus was positioned on the lower edge of the wall and adjacent stent struts (illustrated in Figure 2.4).

2.2.6 Data analysis

All images were scaled against a haemocytometer grid. The seeded cell boundary was marked in images from t = 0. In images from later time points the leading edge of the monolayer was located and, if it had moved, marked again. Any discrete cells which may have moved downstream ahead of the monolayer were also located. As individual HUVEC were not identified between time points, their specific migration rates and persistence could not be found. In lieu, maximum distance from the seeded boundary was measured at each time point, from which a general migration rate was calculated. Total cell numbers and location in relation to stent struts were also recorded.

2.3 Particle tracking

Flow patterns and particle accumulation were visualised by tracking the motion of suspended particles through the model. As per the cell migration studies, the protocol detailed in this section was carried out for a variety of coronary and flow diverter stents, as well as empty non-stented vessels as controls. However, 1.5 mm diameter models were not included in this study.

2.3.1 Set up

Vessels were connected to a fluid reservoir and peristaltic pump, as described in Section 2.2.5.1. Any models previously used with HUVEC were first cleaned of debris. Reservoirs were filled with 12 ml of room temperature 70% industrial methylated spirit (IMS). A suspension of 10 µm polystyrene particles (FluoSpheres, Fisher Scientific) with 3.6×10^6 particles/ml was agitated via vortex mixer (Lab

Dancer S42, IKA). 40 μl of the suspension was then transferred to the reservoir at a 250:1 fluid to particle volume ratio. The pump was briefly set to maximum power, to circulate the fluid and distribute the particles around the system. The flow rate was then reduced to 6.5 ml/min for 2 mm diameter vessels, and 12.8 ml/min for 2.5 mm diameter vessels. At these rates, the Reynolds number was 43 and 68 respectively, matching that in blood flow of 1 Pa wall shear stress within the same model.

2.3.2   Image acquisition

Model vessels were placed onto the stage of an inverted microscope (AE2000, Motic), with a connected camera (Moticam 2300, Motic). A 4x objective lens was used to ensure the full diameter of the vessel was in view and a live image was displayed via Images Plus software (Motic). The vessel was oriented so that the leading edge of the stent was within the image, with flow moving horizontally from left to right. The bottommost stent struts were brought into focus (the same plane of focus used in cell migration studies, as illustrated in Figure 2.4), before light intensity, aperture diaphragm opening and camera exposure were adjusted until moving particles could be seen.

The camera software was used to record a 2 minute video. The vessel was then repositioned so that the field of view was moved downstream, with a small amount of overlap with the previous field. Another 2 minute video was recorded and the vessel repositioned again. This process was repeated until the downstream end of the stent was captured in a final field of view (Figure 2.5A).

Once the procedure was complete, particle accumulation was recorded (see Section 2.3.5). Following this, the model was flushed, removed from the system and rinsed with acetone to dissolve and remove any remaining particles. The model was rotated by 90° to expose different stent geometry and reconnected to the pump with a fresh reservoir. The above process was then repeated.

2.3.3 Image processing

Video recordings were split into image sequences using Video to JPG Converter software (DVDVideoSoft). These images were, if required, reoriented to ensure that the direction of flow was exactly horizontal and that adjacent fields of view could be aligned. The software returned images at a frame rate of 20 frames per second (fps), and every second frame was selected. For each field of view two sets of 300 images, each representing roughly 30 seconds of flow, were selected for tracking (Figure 2.5B). One frame from each image sequence was used to isolate the struts by removing the PDMS wall, along with any attached particles or debris, providing a clear image of stent geometry onto which tracks could be overlaid (Figure 2.5C).

2.3.4 Tracking and analysis

Image sequences were opened as stacks in ImageJ. Each particle was individually tracked by marking its centre point in consecutive images in the sequence, and creating a line connecting these points. Multiple particles following the same track were counted. Particles which were out of focus or could not be reliably identified between images were not tracked. This excluded faster moving particles deeper within the vessel and those following wall curvature at the upper and lower edges of the images. Furthermore, any particles that were already within the field of view at the beginning of sequences, or remained within it at the end, were also omitted. This ensured that for later analysis all tracks represented the complete path of particles and that any points at which they appeared to be cut short could be identified as locations of arrested motion.

Once complete, tracks from each sequence were isolated from the background image and exported (Figure 2.5C). To visualise the impact of local stent geometry, tracks were overlaid on the previously isolated strut images (Figure 2.5D). The orientation of tracks was quantified with ImageJ as described in Section 2.1.6. Distribution was quantified by noting the position of tracks, and the number of particles moving along them, in relation to a 100 μm grid of 1.5 mm height x 2.5 mm length in each field of view. This information was used to create heat maps, to visualise distribution and areas of particle dispersal or collection (Figure 2.5E).
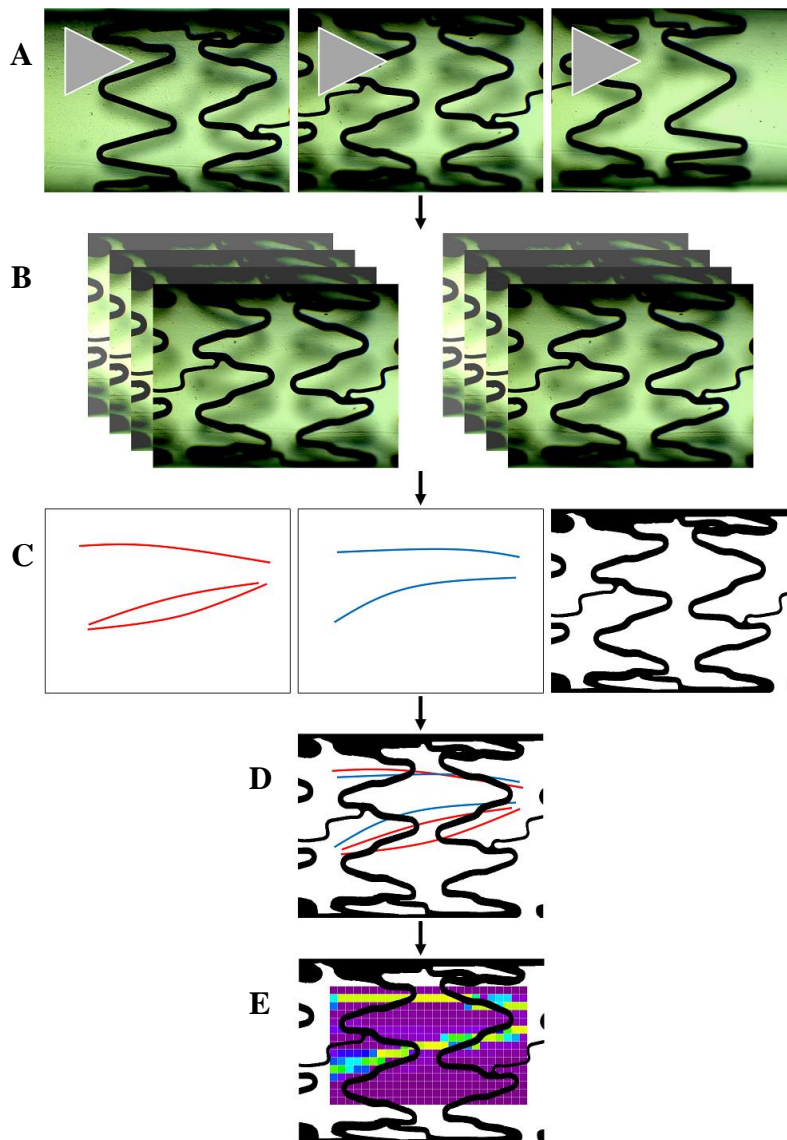
Figure 2.5 Particle tracking protocol

A: Video recordings were taken at overlapping fields of view along the total length of stents.

B: Two image stacks, each representing 30 seconds of flow, were separated from individual recordings at each field of view.

C: Flowing particles were tracked in each stack, and local stent geometry was isolated.

D: Particle tracks and stent geometry were combined, to visualise local flow patterns.

E: Heat maps of particle distribution were created by counting tracks, and the number of particles moving along them, in relation to a 2.5 mm x 1.5 mm grid of 100 μm squares.

2.3.5   Particle accumulation

Following particle tracking, the accumulation of any particles during the experiment was recorded by imaging the entire model under 1x magnification on a stereo microscope (SMZ-171 BLED, Motic). Brightfield images, capturing model and stent geometry, were overlaid by fluorescent light images to highlight particles at this relatively low magnification. All particles within the stents, and 2 mm up and downstream of the leading and trailing edges, were counted.

To compare accumulation between shorter stents, where particle tracking was complete within 3 or 4 fields of view (6 – 8 minutes of flow), and longer stents (8 or 9 fields of view, or 16 – 18 minutes), each 2.5 mm diameter model was left under flow for a total of 20 minutes. With a 50% lower flow rate, 2 mm diameter models were imaged after 20 minutes (to compare accumulation after the same time under flow as 2.5 mm models) and again after 40 minutes (to compare accumulation after the same total flow volume of particle suspension).

2.4   Micro-computed tomography

μCT scanning was performed to reconstruct *in vitro* model geometry *in silico*, for analysis with CFD software. Three techniques were trialled: scanning model vessels alone, scanning model vessels with a contrast agent and scanning casts of model vessels (these methods were also assessed as a means of reproducing *ex vivo* stented artery samples for similar *in silico* modelling and analysis).

2.4.1   Sample preparation

In vitro models which had been used with HUVEC or fluorescent particle tracking were cleaned of debris with acetone and 70% IMS. To minimise sample size, the wall around the stent was thinned and empty sections at either end were cut away, with care taken to ensure stents were not distorted. Scans of model vessels alone were taken (Figure 2.6A). Alternatively, to assess the use of a contrast agent, a 60% w/v barium sulphate suspension was injected into the lumen (Figure 2.6B).
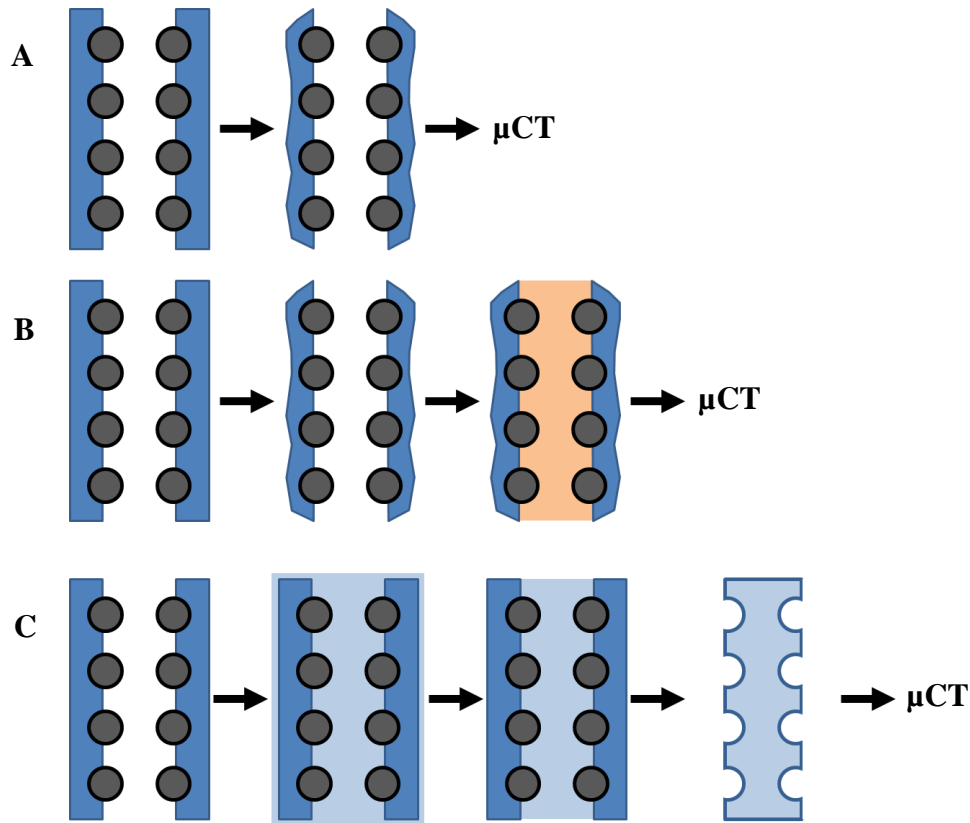
Figure 2.6 µCT sample preparation

µCT scanning of model vessels was used to recreate *in vitro* geometry *in silico*, for CFD analysis. Three techniques of pre-scan sample preparation were trialled, to optimise the faithful reproduction of *in vitro* vessel and stent geometry.

A: Excess PDMS was trimmed from models before stented vessels were scanned.

B: Excess PDMS was trimmed and the lumen filled with a contrast agent before scanning.

C: The model was silanised and covered in additional PDMS. The original wall PDMS and stent were removed from the resultant cast of the lumen, which was then scanned.

To create casts, model vessels were left in a desiccator with 3 – 4 drops of trichloro(1H, 1H, 2H, 2H-perfluorooctyl)silane (Sigma-Aldrich) for 20 minutes, to silanise by evaporation deposition. Each vessel was then placed in the bottom of a cuvette and 5 g of PDMS (prepared as per Section 2.1.4) was immediately poured in to cover the model. Mixing ratios of 5:1, 10:1 and 15:1 were trialled for casting. The cuvette was centrifuged at 626 g for 10 minutes to force the fluid PDMS into the model vessel and to remove air. The PDMS was left to cure at room temperature, for a minimum of 72 hours.

Once cured, the solid block was removed from the cuvette. Without surface treatment, the additional PDMS would have seamlessly and irreversibly bonded with the existing PDMS wall. This was prevented by the presence of the <100 nm thick silane film and, as such, the model vessel was easily removed from the surrounding PDMS. A scalpel was used to create a shallow slit in the wall of the model, which was then gently prised apart. This left only the PDMS which had filled the lumen. Rather than come away with the wall, stents remained attached to this final section and were carefully removed. This process left a cast of the lumen, capturing the geometry of both the wall and stent (Figure 2.6C). Casts were again cleaned with acetone and IMS, and stored in a clean vial prior to scanning.

2.4.2   μCT scanning

μCT scans were performed with a SkyScan 1172 high-resolution desktop μCT scanner (Bruker). Stented vessels (with or without contrast agent) and casts were secured to an 8 mm diameter rotating stage within the machine with double-sided tape, oriented vertically (Figure 2.7A). The x-ray source was turned on and control software was opened to provide a live image via an 11 megapixel x-ray camera, as well as the means to alter scan parameters: voltage, current, resolution, the use of aluminium filters, etc.
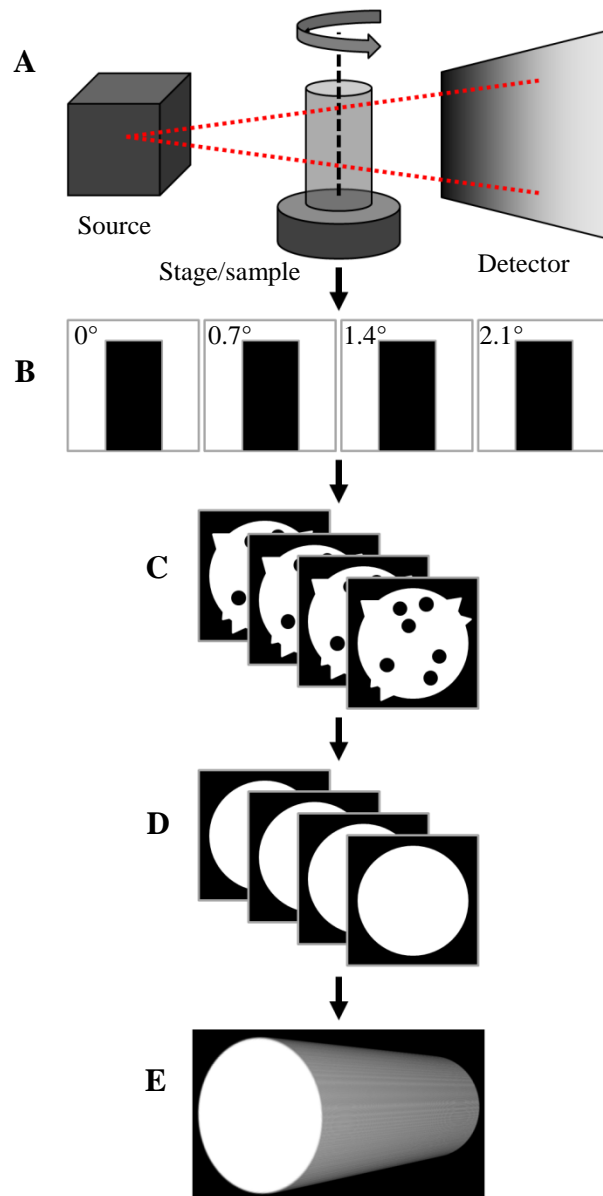
Figure 2.7 µCT scanning and modelling protocol

µCT scanning of model vessels was used to recreate *in vitro* geometry *in silico*.

A: Samples were placed onto the stage within the CT scanner.

B: As the stage rotated, scans produced images of 2D x-ray shadows at each rotation step.

C: Raw projection images were converted into cross-section slices of the sample.

D: Slices were cleaned of noise and interference.

E: Slices were converted into 3D *in silico* models to be used for CFD analysis.

The vertical position of the stage, the camera pixel size (large, 1000 x 500; medium, 2000 x 1000; small, 4000 x 2000) and the proximity of the camera to the sample were set to maximise resolution while ensuring that the region of interest (i.e. the full length of the stent or cast) remained within the field of view. When the sample extended beyond the widest field of view (typically models containing stents longer than 13 mm) multiple oversize scans were performed. The stage, being metallic, was always kept outside of the field of view to reduce interference.

The stage was set to rotate 180°, in 0.7° steps. Additional settings were varied, to optimise parameters for the type of sample being scanned (Table 2.1). Voltage determined the intensity of the x-ray beam, its penetration, and the contrast of the resultant image. Current determined the number of emitted x-ray photons and the brightness of the resultant image. Filters blocked low intensity x-rays when required, improving contrast and reducing noise.

The scan was started and as the stage rotated the camera captured an x-ray tomography projection image of the sample at each rotation step (Figure 2.7B). Scan time was dependent on the settings used and ranged from 10 minutes to several hours.

2.4.3   Reconstruction

μCT image datasets were opened in reconstruction software (NRecon user interface and NReconServer reconstruction engine, Bruker), to convert the projection images of the sample into a series of cross-sectional slices (Figure 2.7C). The upper and lower boundaries of the reconstruction range were selected, as well as a single point located between the two. This point was reconstructed alone, acting as a preview slice to fine tune parameters (beam-hardening correction, ring artefacts correction level and smoothing level) and the dynamic image range (DIR), before the reconstruction process was applied to the entire model. As such, the preview point in heterogeneous samples was selected at locations where the full range of materials was present.

Sample	Source voltage (kV)	Source current (μA)	Aluminium filter
Model vessel	50	180	0.5 mm
Model vessel – low power test	35	180	0.5 mm
Model vessel and contrast agent	50	180	0.5 mm
Ex vivo vessel and contrast agent	50	180	0.5 mm
PDMS cast	50	150	None
PDMS cast – low power test	40	150	None
PDMS cast – high power test	60	150	None

Table 2.1 μCT parameters for *in vitro* and *ex vivo* vessels, and PDMS casts

As samples can consist of a number of different materials, with differing radiopacity, x-ray source voltage and current, and the use of filters, can all be varied to optimise the images captured during μCT scanning.

DIR (the difference between the maximum and minimum pixel brightness) was used to discriminate between materials via differences in x-ray attenuation. This was presented as a histogram, in Hounsfield units (HU), and calibrated by selecting a region of empty space and setting a value of -1000 HU. The applied DIR and reconstruction parameters depended on the requirements of individual scans and are discussed further in Chapter 3.

Following reconstruction, DataViewer software (Bruker) was used to visualise the stacked reconstructed slices as a complete model. This allowed the quality of the reconstruction to be assessed and the dataset to be reoriented. To simplify the process of preparing the *in silico* model for CFD analysis, the dataset was rotated to be as straight as possible and resaved as a series of cross-sectional slices in the transaxial x-y plane (viewing the model down the length of the vessel).

2.5 Computational fluid dynamics

2.5.1 Model preparation

Reconstructed image datasets were opened as stacks in ImageJ and converted from greyscale to binary. The lumen, as the fluid volume to be meshed, was highlighted against a black background in each instance. For reconstructed casts, this was already the case. Contrast agent reconstructions required stent struts and the wall to be subtracted from the image, leaving the agent within the lumen, whereas in reconstructions of unaltered models, struts and wall were simply inverted.

Images could then be edited, to remove interference from bubbles or wall damage, and CT artefacts such as noise and beam hardening (Figure 2.7D). Simple cleaning could be rapidly carried out on the entire stack within ScanIP software (Synopsys Inc.) with the island removal and cavity fill functions removing extraneous voxels. Larger defects, if present, required manual editing on an image by image basis. The amount of editing which was necessary varied greatly depending on scan and reconstruction parameters, and the type of sample scanned, and is discussed further in Chapter 3.

2.5.2 Meshing

Completed models were imported into ScanIP software and the fluid domain selected via thresholding to form a mask (Figure 2.7E). As the images were already in binary format, only white voxels were selected and therefore the exact threshold range was unimportant.

Masks were converted to volume meshes consisting of tetrahedral elements via the ScanIP +FE Module, in FLUENT CFD Output format, using the +FE Free mesh algorithm. Element size and internal volume change rate were altered on a 100-point scale, where element edge length was dependent on voxel size, a product of the original µCT scan resolution (Table 2.2).

Once complete, the Mesh Quality Inspection Tool was checked for errors or warnings, before mesh files were exported.

2.5.3 Simulation

Mesh files were imported into ANSYS FLUENT software (ANSYS, Inc.), a finite volume based solver, to simulate the steady-state laminar flow of incompressible Newtonian fluids via the solution of the governing equations.

The first is the continuity equation, representing conservation of mass, where v is the velocity vector:

$$\nabla . v = 0$$

The second is the Navier-Stokes equation, representing conservation of momentum, where ρ is fluid density, p pressure and μ fluid dynamic viscosity:

$$\rho(v . \nabla v) = -\nabla p + \mu \nabla^2 v$$

Cell culture media was modelled with a dynamic viscosity of 0.0008 Pa.s and density of 1005 kg/m^3. Thickened media/blood was modelled with a dynamic viscosity of 0.0035 Pa.s and density of 1060 kg/m^3.

	Mesh density		
	Coarsest (-50)	Default (0)	Finest (+50)
Min. edge length	4V	V/2	V/3
Max. edge length	10V	V	V/1.5
Target max. error	V/10	V/10	V/20

Table 2.2 Mesh element size as a factor of voxel size

The ScanIP +FE Module was used to create volume meshes from 3D reconstructions of model vessels. Element size could be altered on a 100-point scale, where element edge length was dependent on voxel size (V), equal to µCT scan resolution.

Boundary conditions were set as follows: non-slip conditions were applied at the wall, zero pressure at the outlet and velocity at the inlet. As the *in vitro* models were shortened prior to scanning, an insufficient entrance length for flow development was present. Rather than extend the model, and increase computational expense, a fully developed 3D parabolic flow was applied at the inlet boundary via a user defined function (UDF). Separate UDFs were created for each model, to account for differences in radius and required velocity, and were interpreted by ANSYS Fluent and hooked at the inlet.

As an incompressible flow, calculations were performed using the coupled pressure based solver, in which the continuity and momentum equations are solved simultaneously. The SIMPLE algorithm, suitable for steady-state flow, was selected as the solution method. Default spatial discretization schemes were used: gradients of solution variables were determined via the least-squares cell-based method, pressure was interpolated via the second-order scheme and momentum via the second-order upwind scheme. A convergence criterion of 10^{-6} was used for continuity and x-, y- and z-velocity.

2.5.4 Post-processing

Simulation results were assessed using ANSYS CFD-Post (ANSYS, Inc.). Velocity field volume renders and vector plots were displayed to verify that the UDF was correctly applied and to visualise flow around stent struts. Contour plots of wall shear stress on the vessel wall and stent struts were displayed, and the data extracted to find minimum, maximum and average values for vessels. Reference lines along the wall were selected and used to plot changing wall shear stress magnitude through the length of stents. Where possible, this data was compared to cell behaviour at corresponding locations within *in vitro* models.

2.6   Statistical analysis

Statistical analysis was not carried out where, due to the developmental nature of the work and the limited number of available stent samples, a sufficient number of experiments could not be performed (n=1 - 2).

However, wherever possible, experiments were performed a minimum of three times (n≥3) and in these cases data is presented as the mean ± standard deviation. Statistical significance was determined via two-way ANOVA with Sidak post-hoc test (Prism, GraphPad Software Inc.) where applicable. Statistical significance was defined as a probability value of $p<0.05$.

Chapter Three

Platform Development

This chapter encompasses the development of the fabrication, experimental and modelling methods detailed in Chapter 2. It describes the steps taken to arrive at these protocols, validate their use and assess their efficacy and efficiency. While some stented vessels are presented as examples, full results for coronary and flow diverter stents can be found in Chapters 4 and 5 respectively.

3.1 *In vitro* model

3.1.1 Fluid properties

1 ml of EC growth medium was determined to weigh 1.005 g; the density of the fluid was 1005 kg/m^3. Viscosity data could only be collected from a maximum of 34°C as the temperature of the medium could not be maintained during set-up. Measurements were therefore taken at multiple points as the medium cooled. The viscosity of EC growth medium was compared to that of water over the measured temperature range, and this relationship extrapolated to obtain viscosity at 37°C. Despite some variation between instruments, potentially due to measurements being made at their lower limits, EC growth medium containing 20% FCS was on average 15% more viscous than water (Figure 3.1). EC growth medium viscosity at 37°C was therefore taken to be 0.8 mPa.s, based on a reference value of 0.69 mPa.s for water [198].

For cell migration studies, 1 Pa was selected as the average wall shear stress magnitude to be applied in the model based on the range of applied and physiological parameters from relevant literature (Sections 1.6.3 and 1.7.3), the power of available pump systems and previous work in-group [103]. Wall shear rate was 1250 s^{-1} in each model. Table 3.1 details how the resultant flow properties varied with vessel diameter.
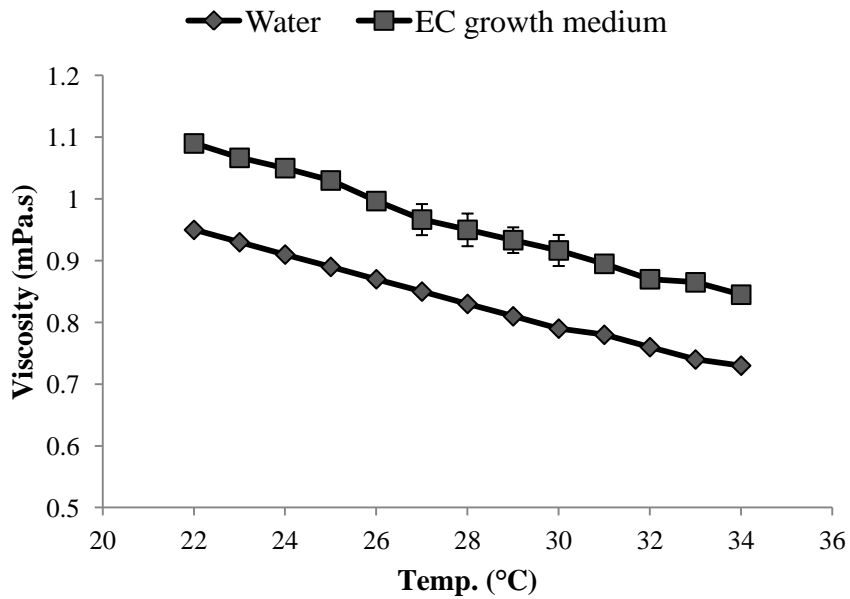
Figure 3.1 Viscosity of EC growth medium

The viscosity of EC growth medium was measured as the fluid cooled and compared to that of water over the same temperature range. The medium, containing 20% FCS, was on average 15% more viscous than water.

Mean with SD (n=4).

Model diameter (mm)	Flow rate (ml/min)	Average velocity (m/s)	Reynolds number
1.5	25	0.23	442
2	59	0.31	785
2.5	115	0.39	1227

Table 3.1 Applied flow properties

In cell migration studies an average wall shear stress of 1 Pa was applied in each model by the flow of EC growth medium. The flow rate was therefore adjusted to maintain this level of wall shear stress across the various model diameters used.

3.1.2 Material properties

Samples of a variety of PDMS base and curing agent ratios were created for mechanical testing. 60:1 samples would not cure and remained fluid, whereas 50:1 and 40:1 samples were gelatinous. 30:1 and 20:1 samples were solid, yet remained tacky due to an abundance of unlinked monomers and were therefore unsuitable for use. 15:1, 10:1 and 5:1 samples were fully cured at room temperature and were tested.

3 batches of each ratio were created and 3 samples from each batch underwent tensile testing. The average elastic modulus was found to be 0.342 MPa (15:1), 0.697 MPa (10:1), and 1.000 MPa (5:1), shown in Figure 3.2.

3.1.3 Model dimensions

Vessel diameter was informed by physiological data from literature (Section 1.7.2). As atherosclerotic lesions were not modelled, and stents were not required to compress material while expanding, data regarding healthy coronary arteries only was sought out. Coronary stents were tested under the assumption that PCI had been successful (i.e. normal lumen diameter and associated blood flow had been restored). Diameters of 1.5, 2 and 2.5 mm, within the physiological range, were selected based on the power of available pump systems and the nominal diameters of available stents. 1.5 mm vessels were the largest within which the ibidi system, with a maximum flow rate of 35 ml/min, could generate 1 Pa of wall shear stress. Flow diverter stents were only available with 2 mm nominal diameter, for deployment in vessels of equal size. The majority of available coronary stents had a 3 mm nominal diameter, for deployment at a 1.1:1 to 1.2:1 stent to vessel ratio. 2.5 mm was the smallest vessel diameter within this deployment range and was used to minimise the required pump power.
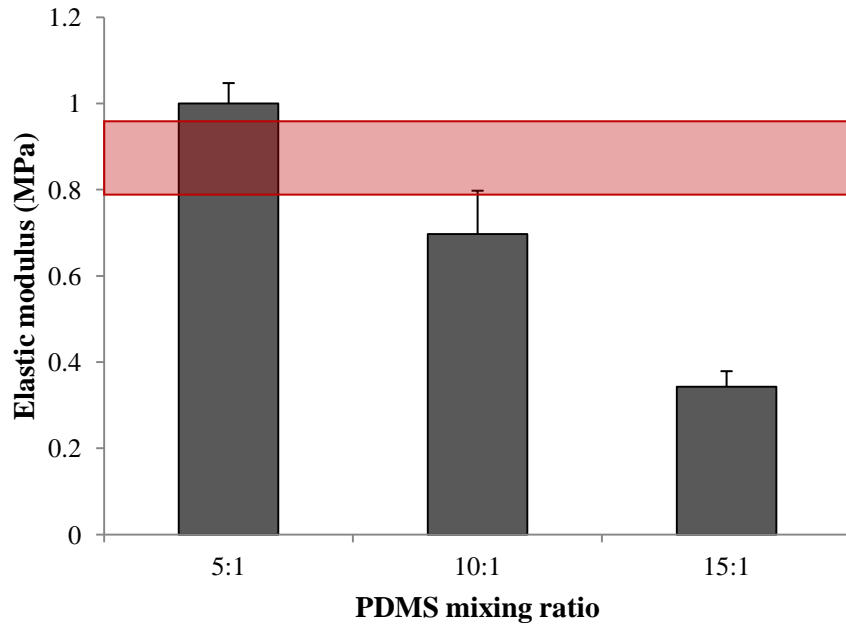
Figure 3.2 Elastic modulus of PDMS

The elastic modulus of PDMS was calculated following tensile testing. Elastic modulus varied greatly between the three curing agent mixing ratios trialled, but was always within the wider physiological range of arterial tissues (0.1 − 100 MPa [175]) and, at lower ratios, comparable to that of a carotid artery segment (red region [176]). All samples were cured at room temperature for 24 hours, followed by 15 minutes in a 100°C oven.

Mean with SD (n=9).

The entrance lengths required for fully developed flow based on the conditions detailed in Table 3.1 were calculated using the equations outlined in Section 2.1.3 and found to be 40 mm (1.5 mm diameter vessels), 95 mm (2 mm diameter), and 185 mm (2.5 mm diameter). The combined length of the model and attached silicone tubing of equal diameter ensured that the distance between the pump head and stented/seeded area was sufficient for flow to fully develop upstream of regions of interest.

The cuvette mould resulted in a wall thickness of 4.5 mm, well within microscope focal length. Flat surfaces provided the stability required for cell seeding and imaging. The mould prevented the need to cut the PDMS to the required size and as such each side remained transparent.

3.1.4   PDMS enabled the rapid fabrication of biocompatible model vessels

PDMS models were cured at room temperature, eliminating shrinkage to ensure that models were of the expected size when applying specific flow conditions. This also prevented the expansion of any small bubbles which may have remained despite centrifuging, which could hamper visibility or distort the vessel wall geometry. After 24 hours the PDMS was solid and cytotoxic unlinked monomers could be eliminated by a brief spell at higher temperature without affecting the dimensions of the model. Despite this, a fibronectin coating was still required to achieve and maintain successful cell attachment under flow (Figure 3.3).

3.2   Stent deployment

3.2.1   Clinical stents could be fully deployed within model vessels

Coronary and flow diverter stents were successfully deployed within model vessels and were stable under flow. Flow diverter stent struts lay adjacent to the vessel wall, where self-expansion was arrested. In contrast, the high-pressure balloon expansion of coronary stents widened the vessel, stretching the wall between struts. Typical deployments are shown in Figure 3.4, and are comparable to equivalent *ex vivo* histology samples.

| **No coating** | **0.1 % gelatin** | **10 µg/ml fibronectin** |
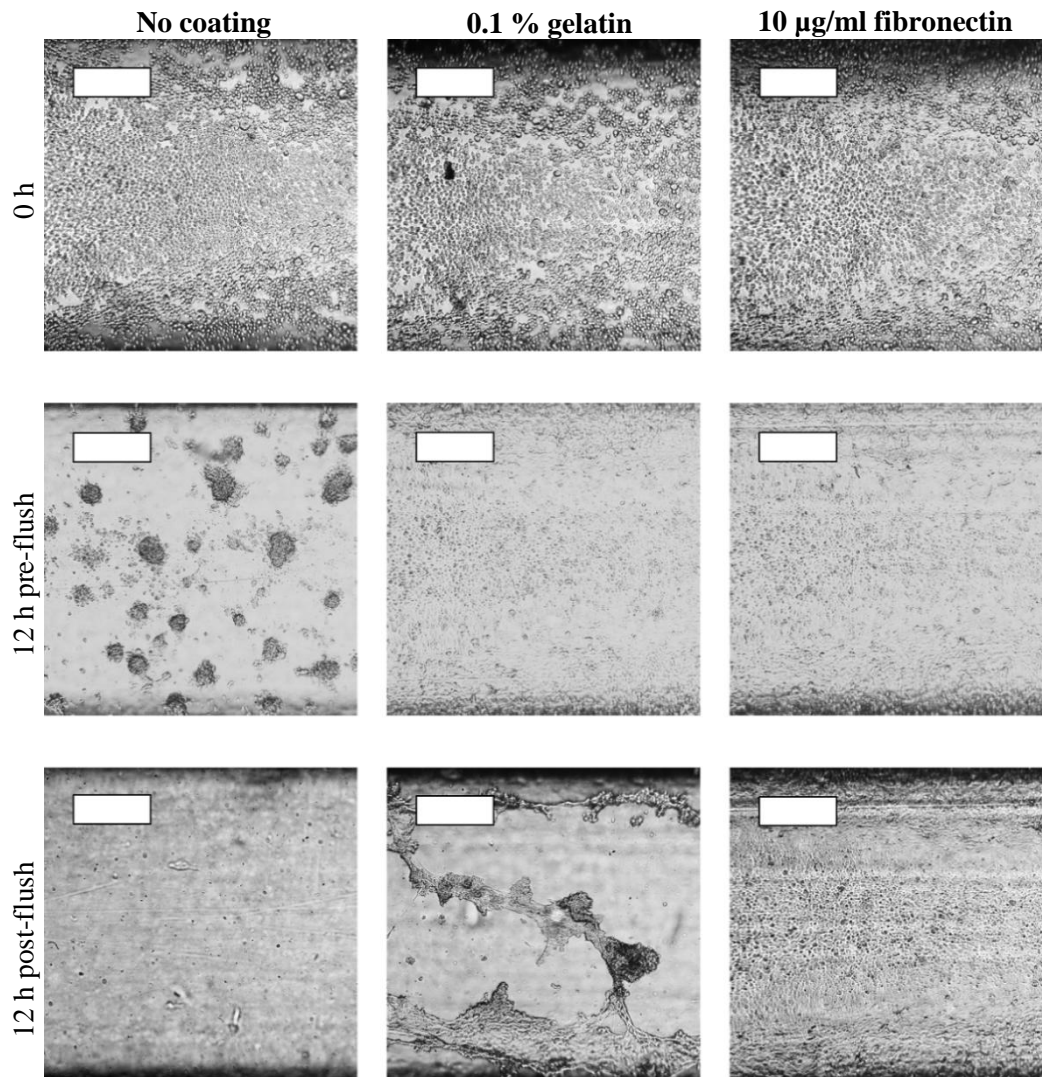
Figure 3.3 Cell attachment within PDMS vessels

HUVEC were seeded within bare PDMS vessels (left), vessels coated with gelatin (centre) and vessels coated with fibronectin (right), and left for 12 hours to attach. HUVEC would not attach onto bare PMDS, and those attached on a gelatin coat were removed under flow. Only 10 µg/ml fibronectin was able to maintain attachment under both static and flow conditions.

Scale bar: 0.5 mm.
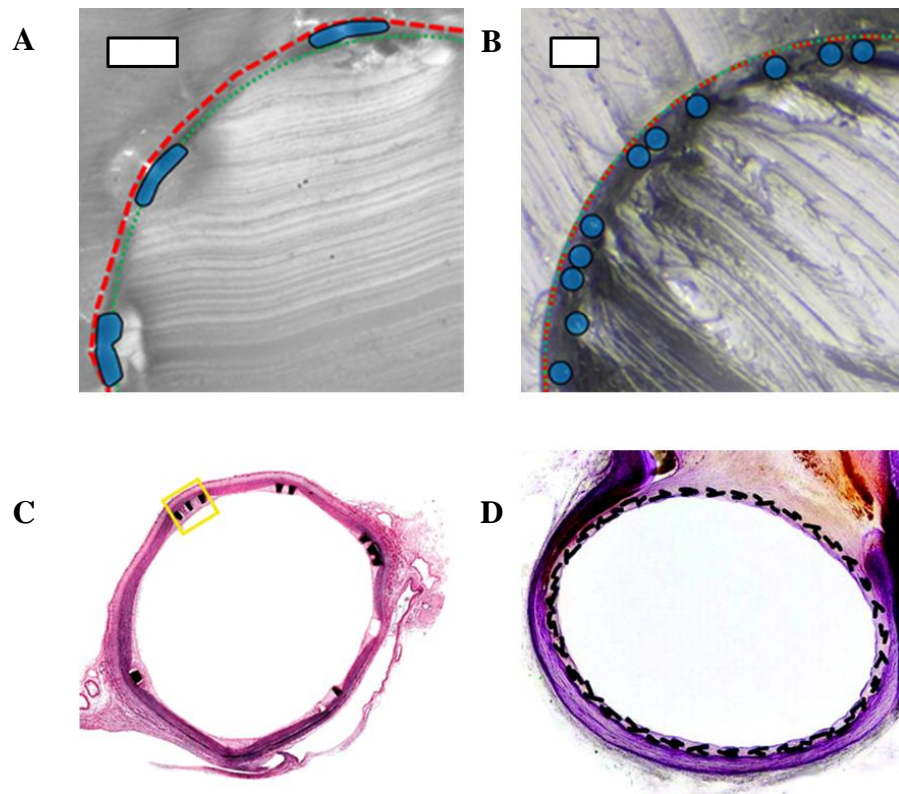
Figure 3.4 Deployed stent strut location *in vitro* and *in vivo*

Following stent deployment in model vessels, images of cross-section slices were taken to compare the final position of struts to those in *ex vivo* histology. In each example, additional PDMS cured within the lumen prevented struts from being moved or distorted when cut.

A: Coronary stent deployment via balloon inflation pushes struts (blue) against the wall (red line), widening the vessel beyond its initial diameter (green line).

B: Self-expanding flow diverter stent deployment maintains the original vessel shape and diameter. Struts lay adjacent to the wall.

C: Photomicrograph of a coronary stent stretching and widening the artery wall, as per *in vitro* deployment [45]. Struts penetrate neointima, but not the wall itself (yellow box).

D: Photomicrograph of a flow diverter stent and unmodified vessel wall, as per *in vitro* deployment [199]. Struts lay adjacent to the wall and aneurysm (at the top of the image).

Scale bar: 0.2 mm.

(All images reproduced with permission).

An accurate, quantitative measure of penetration or stretch was not possible, as stented models could not be cut by microtome to produce thin, high-quality images as per the histological examples. Samples were cut by scalpel, and were therefore relatively thick and outside of focal length. Despite additional cured PDMS present within the lumen to provide support, the examples shown in Figure 3.4 are rare cases of this method not distorting the struts to some degree.

3.2.2 Definitive measurement of deployed stent geometry was unattainable

Strut size, orientation and metal-to-artery ratio was measured for each available stent design. Accurate dimensions could not be attained as attempts to manipulate struts could result in distortion, as mentioned in Section 3.2.1. As such, dimensions were taken to the nearest 5 µm. Measurement using µCT data was also problematic, detailed in Section 3.5.2.

The metal-to-artery ratio of stents could be calculated from images without specific strut dimensions, by comparing the number of pixels filled by the stent (the MSA) to the total number of pixels in the bounded area. For stents with circular cross-section, width varied across the strut and the metal-to-artery ratio depended on the degree of contact with the vessel wall. The MSA was measured at the strut's widest point; therefore the maximum metal-to-artery ratios are stated here. For stents with square or rectangular cross-sections, strut width and MSA was constant and the metal-to-artery ratio did not vary with wall contact.

Strut orientation varied between deployments of the same stent design. Increased expansion rotated struts away from the direction of flow, taken to be 0°, and vice versa. While averages of each of the above properties accounted for variability and reduced errors, definitive measurement of stents *in vitro* was difficult.

3.3 Cell migration study set-up

3.3.1 Cell migration assays began from specific initial HUVEC location

Cell suspensions were injected halfway into model vessels (Figure 2.4). In larger, 2.5 mm diameter vessels, careful handling of the model during attachment was necessary to hold the filling front stationary. In 1.5 mm diameter vessels, care was needed to ensure capillary action did not draw the suspension further through the model. With practice, medium/air boundaries could be maintained at the required points. Following cell attachment, this resulted in monolayers with straight, well-defined leading edges against which stents could be positioned (Figure 3.5).

Attached HUVEC were relatively resilient and able to survive repeated flushing as tubing and reservoirs were connected (cells could also survive stent deployment directly over the monolayer, as shown in Figure 3.6). Minor damage to the monolayer could be caused by guide wires, balloons and sheaths during stent deployment, but wound closure was observed during experiments.

3.3.2 HUVEC migration could be tracked under flow

HUVEC seeded within empty control tubes showed clear migration under flow of 1 Pa average wall shear stress. This consisted of movement of the monolayer leading edge in the direction of flow, often led by the more rapid migration of individual leader cells (Figure 3.7).

Migration distances and rates were obtained for cells within empty control tubes of 1.5 and 2.5 mm diameter, after 24 hours under flow (Figure 3.8). This showed a maximum monolayer migration equivalent to 50 – 60% vessel diameter over that time period with leader cells, where present, covering twice that distance.
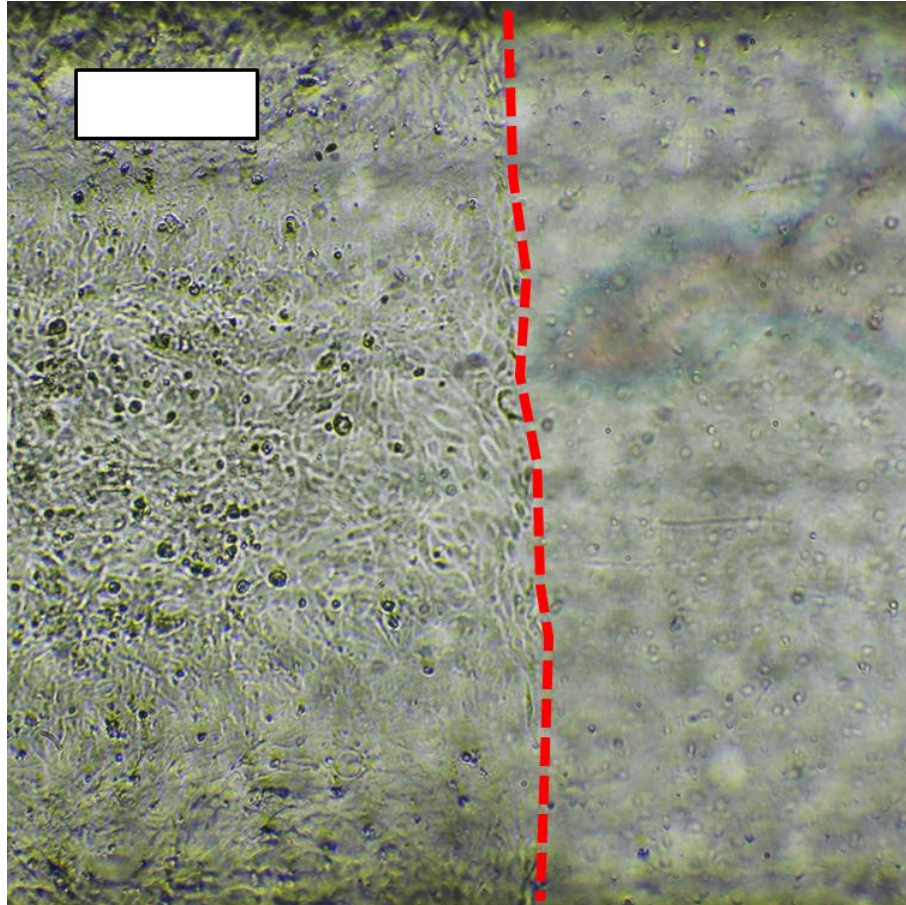
Figure 3.5 Attached HUVEC/empty vessel boundary

HUVEC could be seeded up to specific points within model vessels to attain straight, clearly defined boundaries (red line) between cell covered (left) and cell free areas (right). This technique aided in accurate stent deployment and provided a clear initial position from which cell migration could be measured.

Scale bar: 0.5 mm.
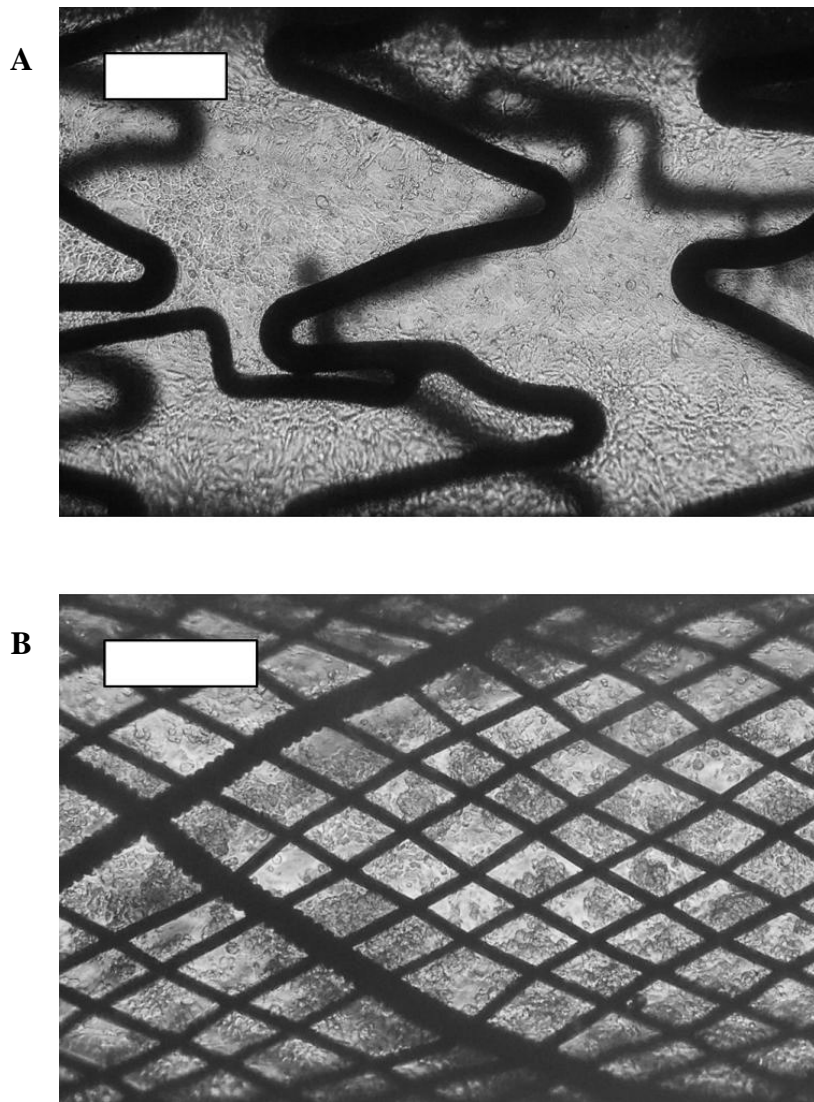
Figure 3.6 Stent deployment over attached HUVEC

HUVEC were seeded along the full length of model vessels and, once attached, stents were deployed over the monolayers. Although some areas of damage were seen, HUVEC remained well attached, even following coronary stent balloon expansion. This prevented the identification of initial positions required to monitor cell migration.

A: Coroflex Blue coronary stent deployed via balloon expansion.

B: Self-expanding Silk flow diverter stent.

Scale bar: 0.5 mm.

Figure 3.7 Cell migration in 2.5 mm diameter empty control vessels

The migration of HUVEC monolayers (green line) and leader cells (green dots) beyond an initial seeding point (red line) was observed in the direction of flow within empty 2.5 mm diameter vessels over 24 hours.

Flow from left to right, 1 Pa average wall shear stress.

Scale bar: 0.5 mm.
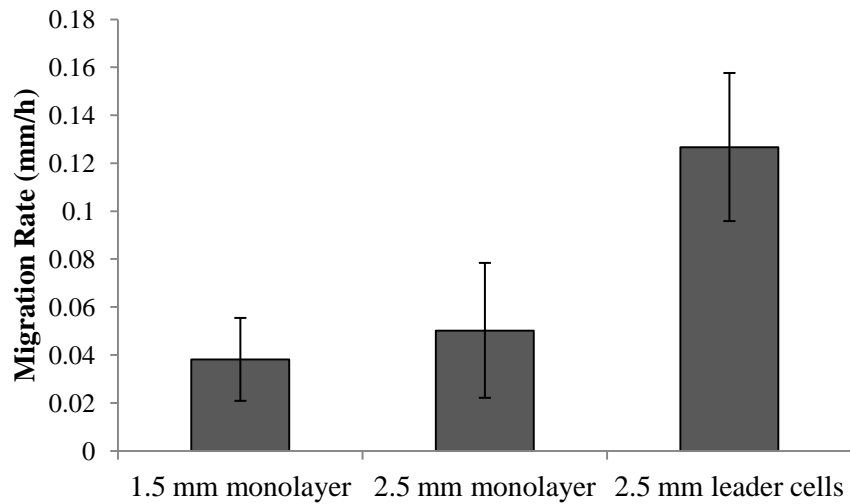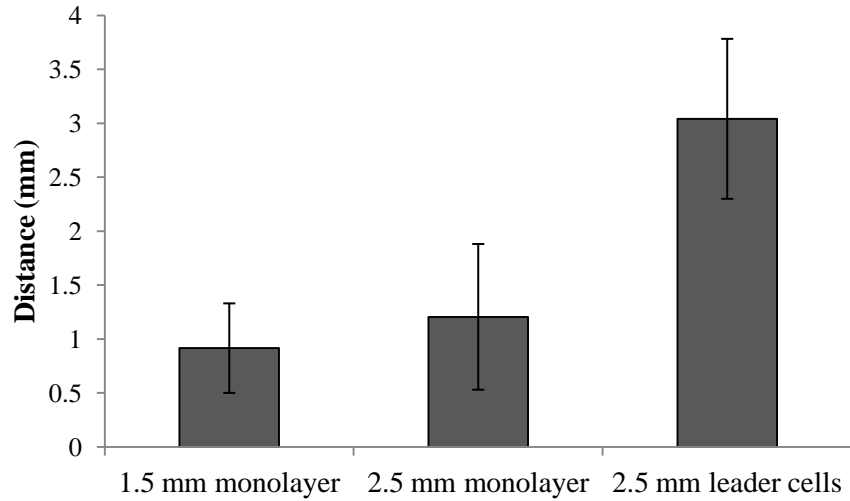
Figure 3.8 Cell migration distance and rate in control vessels

The rate of HUVEC migration over 24 hours within empty vessels was measured. Rate increased with vessel diameter. No leader cells were observed in 1.5 mm diameter models.

Flow of 1 Pa average wall shear stress.

Mean with SD (n=3).

Cells seeded within 1.5 mm tubes and connected to the ibidi system could be monitored over a longer duration (Figure 3.9). Figure 3.10 shows a maximum monolayer migration approximately equal to vessel diameter over 48 hours, but reveals a nearly 50% reduction in migration rate after the first time point at 12 hours, beyond which rates remain steady. Figure 3.10 also shows that, in empty vessels with constant unidirectional flow, HUVEC in medium supplemented with a ROCK inhibitor covered two-thirds the distance of cells in untreated medium.

All model vessels seeded with cells but not selected for use in flow experiments were left as static controls. The majority showed zero migration, or low numbers of cells moving ≤ 50 µm over 24 hours (Figure 3.11A, B, C). However, in one single case, the monolayer within a 2 mm diameter static control was observed to move 800 µm (Figure 3.11D), discussed further in Section 3.6.

3.3.3 Cell migration assays were hampered by practical limitations

Fewer than 1 in 5 of the models with sufficient cell attachment for connection to pump systems saw HUVEC survive long enough under flow for a successful cell migration assay (considered to be t ≥ 24 h). The maximum duration reached by individual experiments was 72 hours (in a model connected to the peristaltic pump) and 90 hours (in a model connected to the ibidi system).

The visibility of cells could hinder accurate measurement of cell migration, particularly around dense stent struts, or as debris began to build up. HUVEC stained with CellTracker dye could be observed under fluorescent light supplied by the NIGHTSEA system. However, individual cells were not bright enough to be imaged and only clusters which were already visible under brightfield could be captured (Figure 3.12).
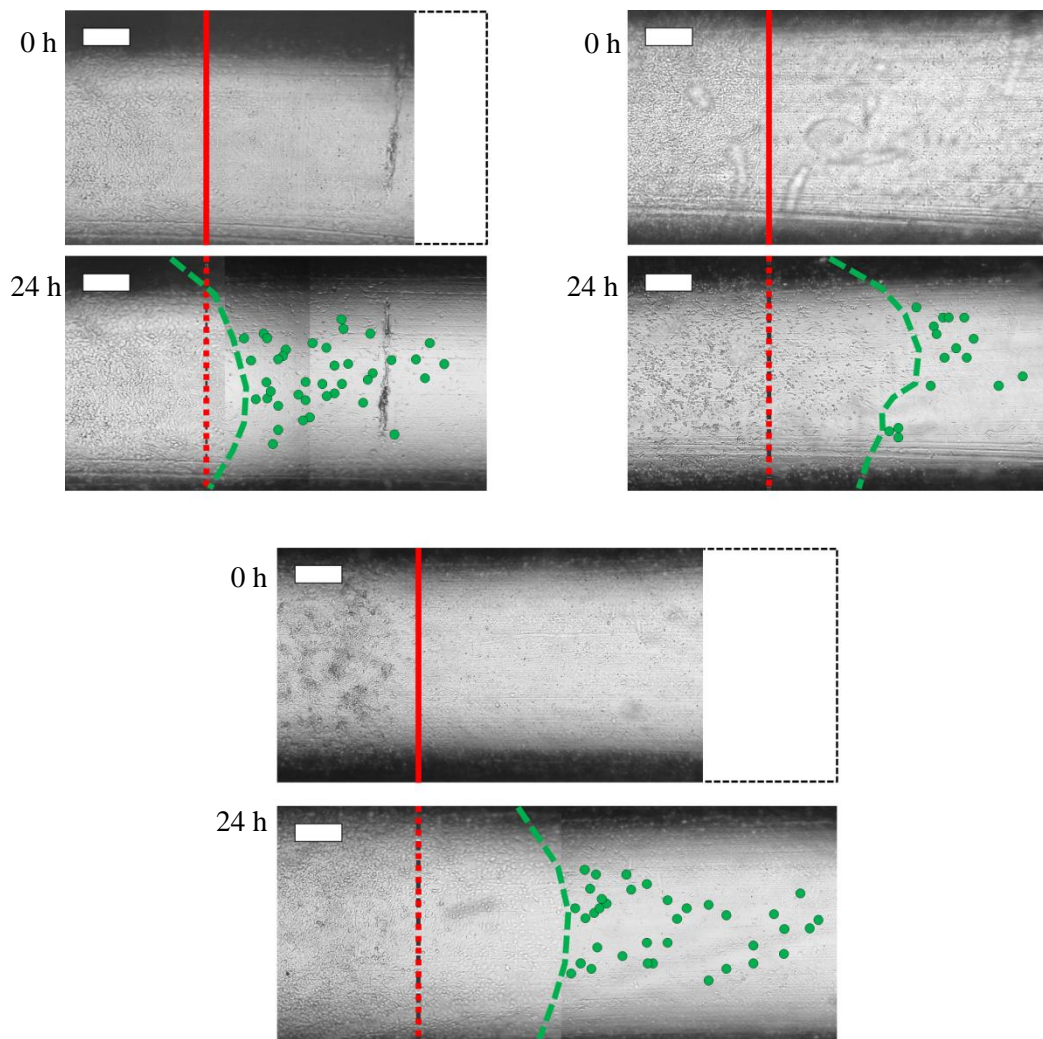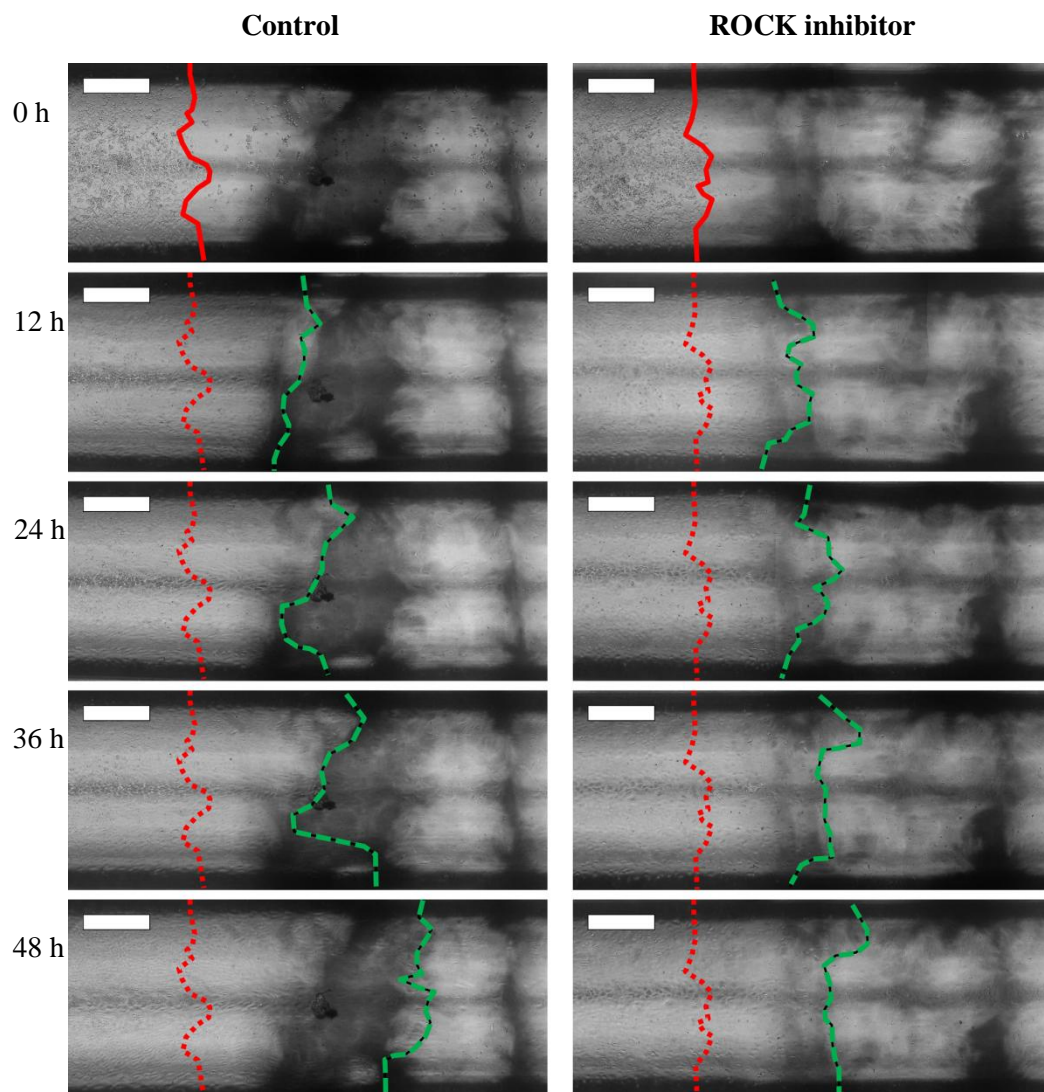
Figure 3.9 Cell migration in 1.5 mm diameter empty control vessels

The migration of HUVEC monolayers (green line) beyond an initial seeding point (red line) was observed in the direction of flow within empty 1.5 mm diameter vessels over 48 hours.

Left: Migration with standard EC medium, as a control.

Right: Migration with EC medium supplemented with + 2µM Y27632 ROCK inhibitor.

Flow from left to right, 1 Pa average wall shear stress.

Scale bar: 0.5 mm.
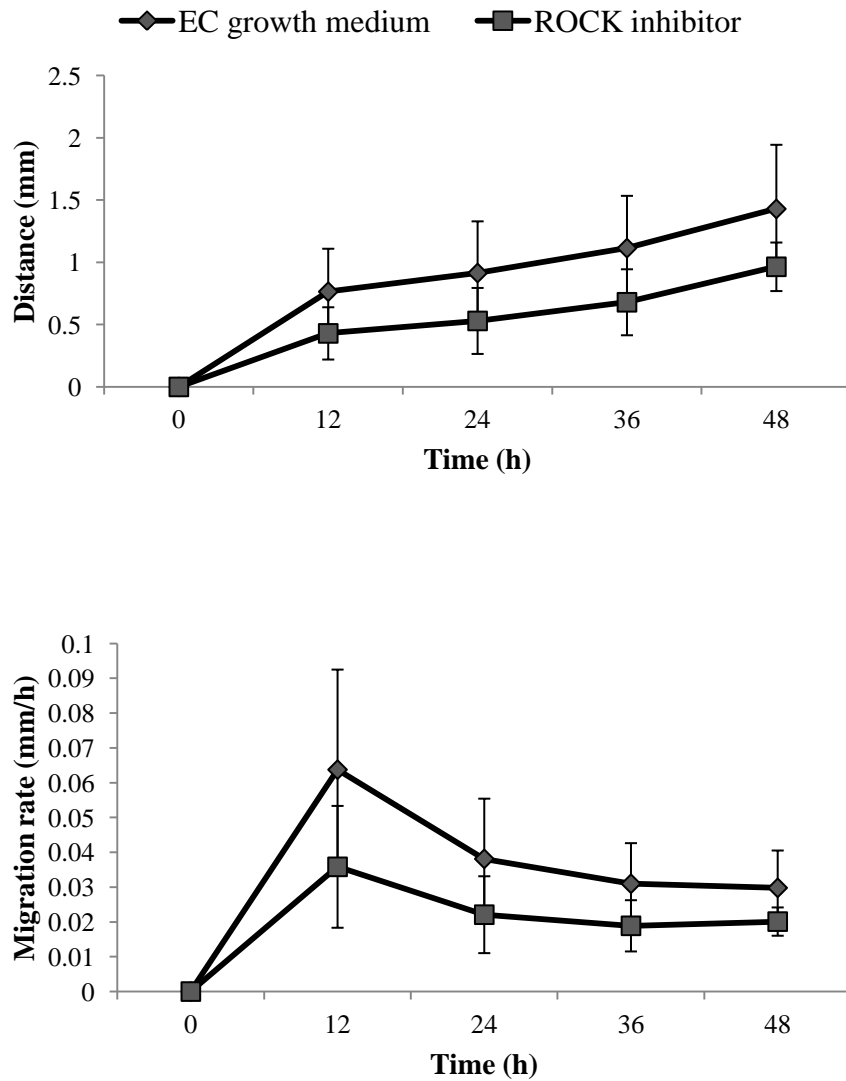
Figure 3.10 Cell migration distance and rate in 1.5 mm diameter control vessels

The distance and rate of HUVEC migration within empty 1.5 mm diameter vessels was measured. Migration rate decreased over 24 hours and, in comparison to standard EC growth medium, was reduced in the presence of a ROCK inhibitor.

Flow of 1 Pa average wall shear stress.

Mean with SD (n=3).
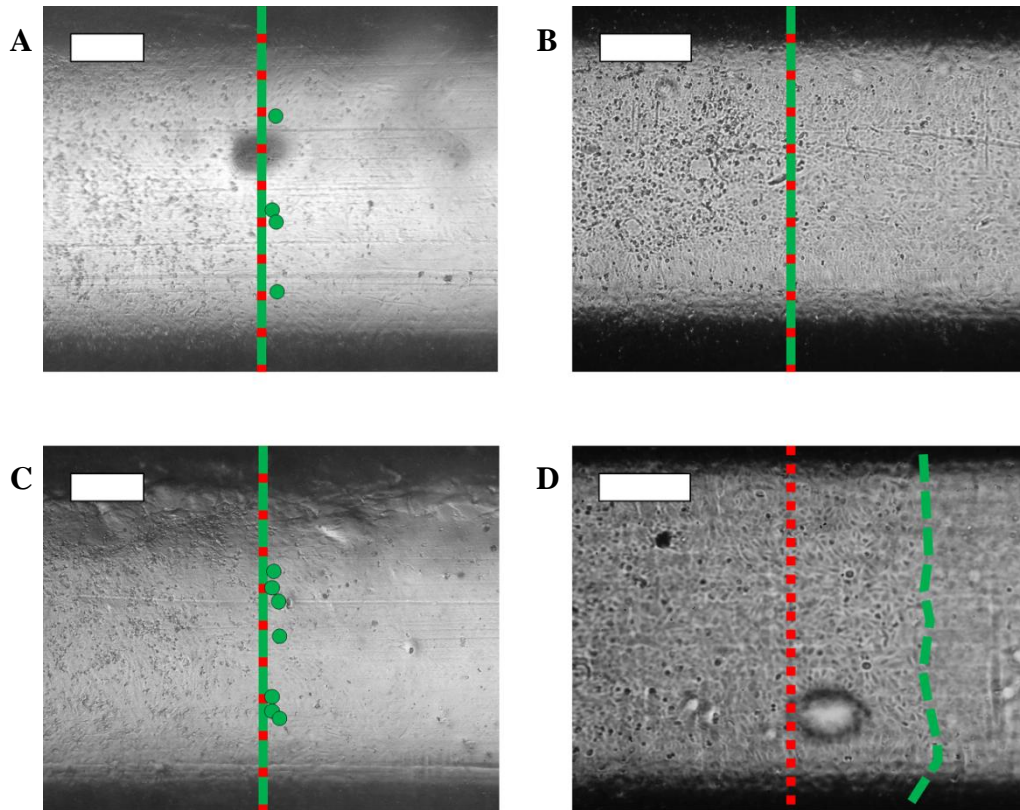
Figure 3.11 Cells in empty control tubes under static conditions

HUVEC were seeded in model vessels and not attached to flow systems, to act as static controls. No migration of HUVEC monolayers (green line) beyond an initial seeding point (red line) was observed after 24 hours under static conditions (representative examples shown in **A**, **B** and **C**), with the exception of one sample (**D**).

Scale bar: 0.5 mm.
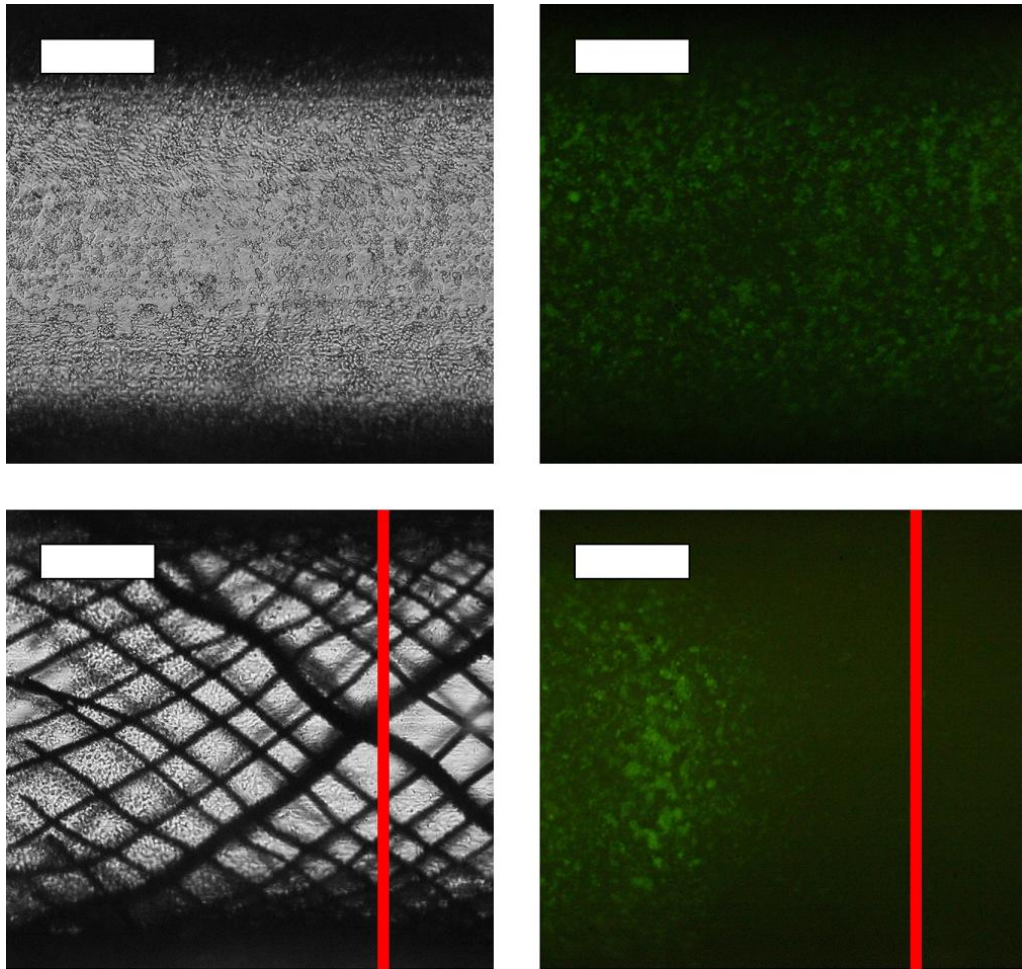
Figure 3.12 Locating HUVEC using the NIGHTSEA fluorescence system

Fluorescent staining was used in an attempt to better image HUVEC within model vessels. However, in both empty and stented vessels only areas of high cell density were visible under fluorescence, rendering the system unsuitable for tracking individual cells.

Top: HUVEC monolayer within an empty vessel, under brightfield (left) and fluorescence (right).

Bottom: HUVEC monolayer seeded up to a point (red line) within a flow diverter stent, under brightfield (left) and fluorescence (right).

Scale bar: 0.5mm.

The addition of both XG and dextran increased the viscosity of EC growth medium, enabling 1 Pa wall shear stress to be generated under more physiologically relevant

flow velocities. Higher concentrations of XG and dextran doubled and trebled viscosity respectively (Figures 3.13 and 3.14). Even so, while a plasma-equivalent viscosity of 1.5 mPa.s could be achieved, the thickest medium would still be less than half of the blood-equivalent 3.5 mPa.s at 37°C. The use of both thickening agents, in any concentration, also saw a decline in the number of live, attached cells after 72 hours of culture (Figure 3.15).

3.4   Particle tracking set-up

3.4.1   Flow patterns were revealed at blood-equivalent Reynolds number

10 μm FluoSphere particles were suspended in room temperature 70% IMS and tracked through model vessels. Fluid density was 790 kg/m^3 and dynamic viscosity 0.00126 Pa.s at room temperature. Thus, the application of 6.5 ml/min (2 mm diameter vessel) and 12.8 ml/min flow (2.5 mm diameter vessel) gave Reynolds numbers of 43 and 68 respectively. This was equivalent to the Reynolds number of blood flow with 1 Pa wall shear stress within the same diameter.

Under these conditions, particles could be clearly identified and tracked local to the vessel wall and stent struts where velocity was reduced. Fluorescence was not required to locate particles and could skew data by highlighting those deeper within the vessel, which would otherwise be out of focus.

Figure 3.16 provides an example of the data obtained from particle tracking studies. As expected for empty control tubes, streamlines are parallel to flow. Tracks are evenly distributed across the vessel, as is the frequency of particles moving along them.
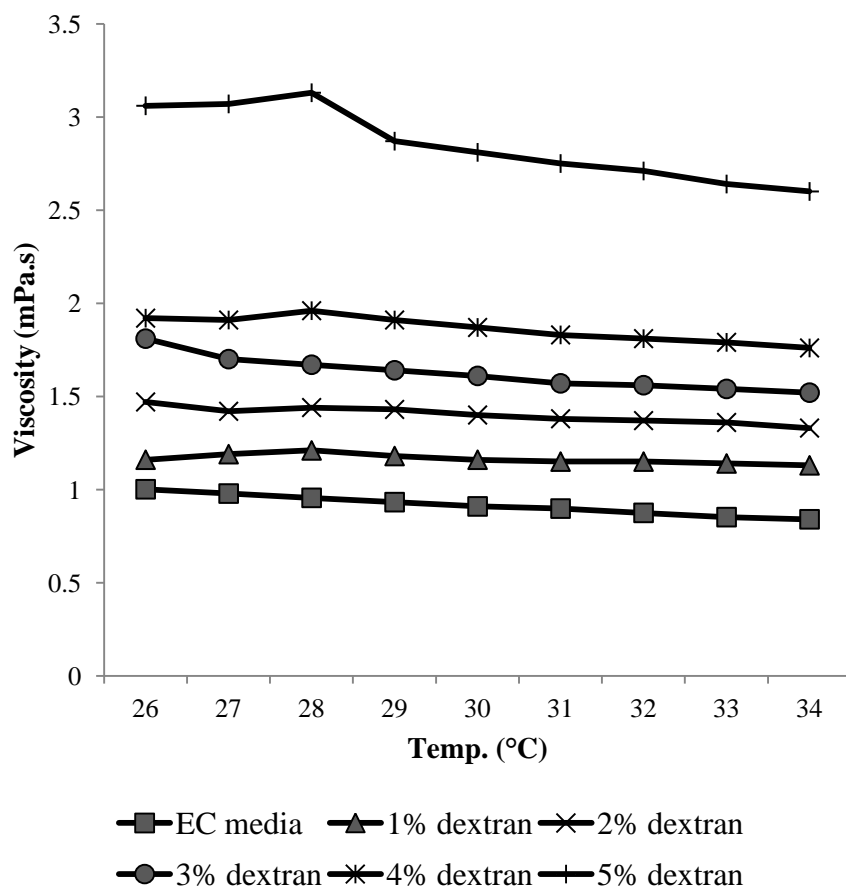
Figure 3.13 Viscosity of EC growth medium with dextran thickening agent

The viscosity of EC growth medium containing dextran at various concentrations (w/v) was measured as the fluid cooled. The presence of dextran increased viscosity beyond that of standard EC growth medium.

(n=1).
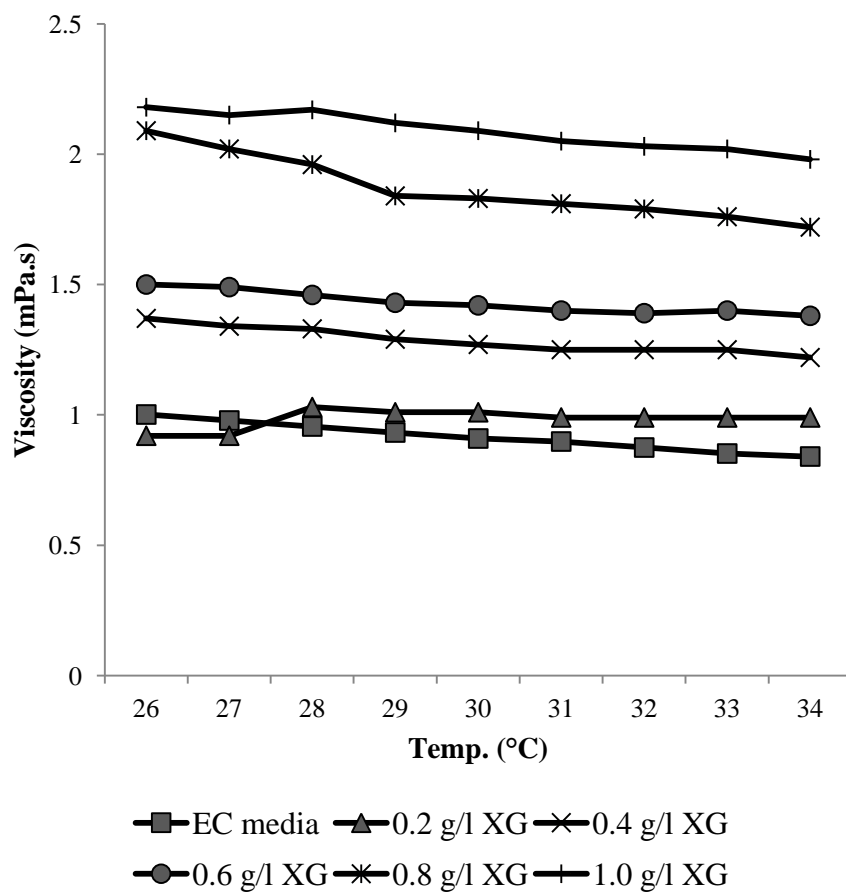
Figure 3.14 Viscosity of EC growth medium with XG thickening agent

The viscosity of EC growth medium containing XG at various concentrations was measured as the fluid cooled. The presence of XG increased viscosity beyond that of standard EC growth medium.

(n=1).
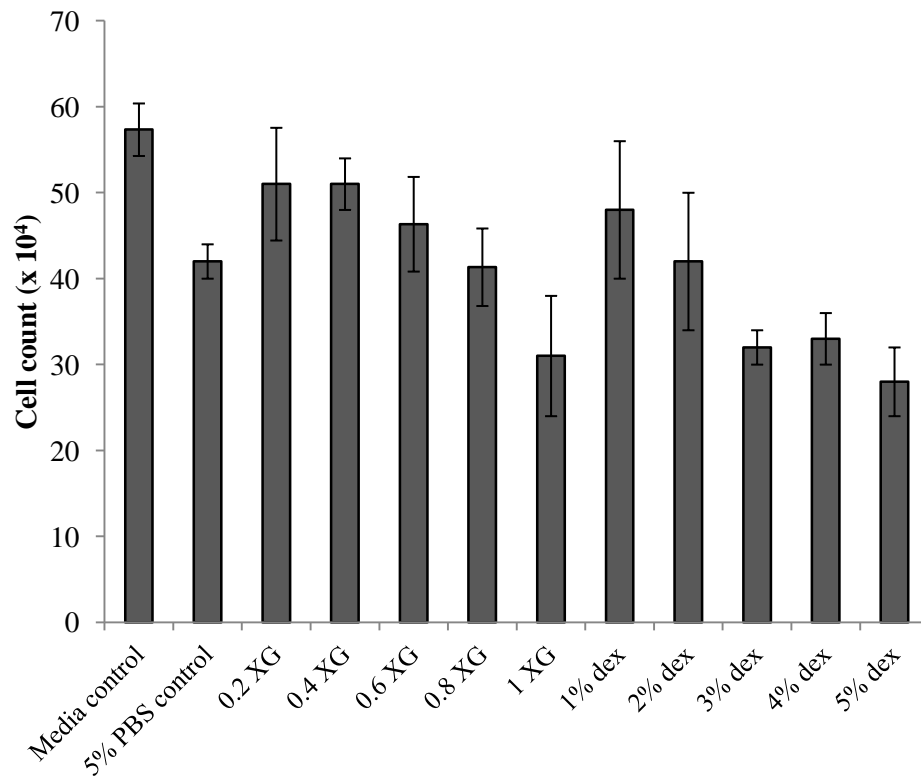
Figure 3.15 Live cell numbers in thickened EC growth medium

HUVEC were cultured for 72 hours in well plates containing growth medium supplemented with various concentrations of dextran and XG. The addition of thickening agents at increasing concentrations reduced the numbers of live, viable cells in comparison to standard EC growth medium.

Mean with SD (n=3).
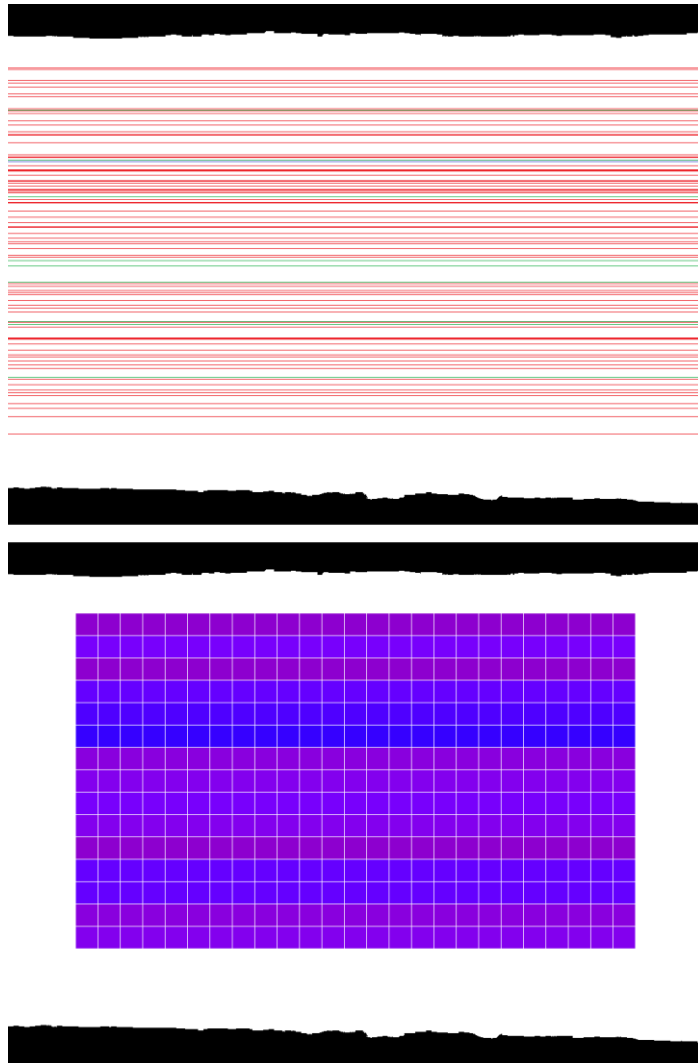
Figure 3.16 Representative particle tracking data

A particle suspension was pumped through an empty 2.5 mm diameter model vessel. A video recording was taken, from which individual particle motion was tracked.

Top: Tracking revealed particles following streamlines (red: 1 particle per streamline, green: 2, blue: 3).

Bottom: Heat map of particle density, illustrating the location of streamlines and the frequency of particles moving along them over a superimposed 100 μm grid.

Flow from left to right, 12.8 ml/min.

3.4.2 Velocity and wall shear stress was not extracted from tracking data

Particle tracking was used to visualise flow patterns only. Beyond the location of tracks, and the number of particles moving along them, no quantitative data was obtained due to a high probability of error.

While image stacks were returned by the software at 20 fps, the frame rate of the original recordings varied and could not be manually controlled. Data was lost when converting from higher rates and frames were duplicated when converting from rates below 20 fps. Selecting every other frame for tracking mitigated this second issue but specific, regular time intervals with which to confidently calculate velocity could not be attained. The possibility of human error in manual tracking was also a factor (Figure 3.17A). This was further complicated by the fact that the manual tracking function in ImageJ would not return position data while simultaneously displaying previous tracks. This made the reliable tracking of hundreds of particles per field of view impossible.

The ability to distinguish between changes in velocity magnitude and direction in 3D space is particularly important when tracking particles moving over and around stent struts. Therefore the use of 2D imaging was an additional problem, illustrated in Figure 3.17B, again preventing accurate velocimetry.

3.4.3 Low particle accumulation was measured in empty models

Following particle tracking, models were left for a total of 20 minutes under flow. The pump was then stopped and the models imaged to assess the accumulation of fluorescent particles to provide an empty vessel control for comparison to stented models. Briefly flushing the vessel with IMS beforehand removed any loose particles and ensured that this was not simply a measure of where particles lay once flow was arrested.

Given the time under flow and the 150,000 particles present in the solution, the number of accumulated particles in empty control models was relatively low (Figure 3.18), suggesting migration to the centre of the vessel and regions of high velocity under Poiseuille flow.
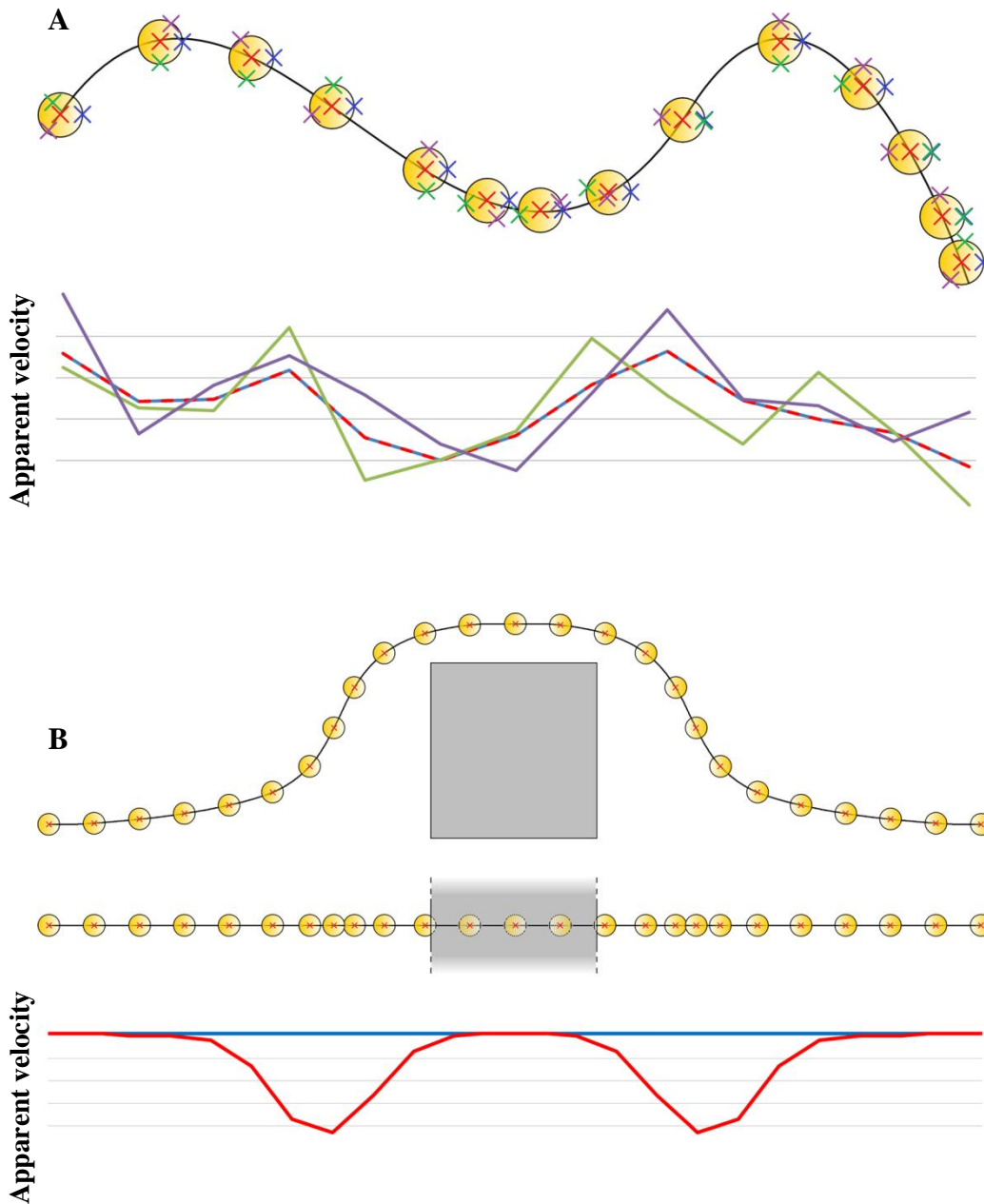
Figure 3.17 Errors inherent in manual particle tracking

A: Apparent particle velocity between points (bottom) varies with inconsistent selection of the particle's location at each point along its path (top).

B: Apparent velocity varies as 2D images do not account for out of plane movement. A particle moving over a stent strut and viewed from the side (upper path) has a constant velocity (blue line). However, when viewing the same particle from below (lower path), as per the particle tracking method used here, the out of plane motion causes apparent velocity to change (red line).
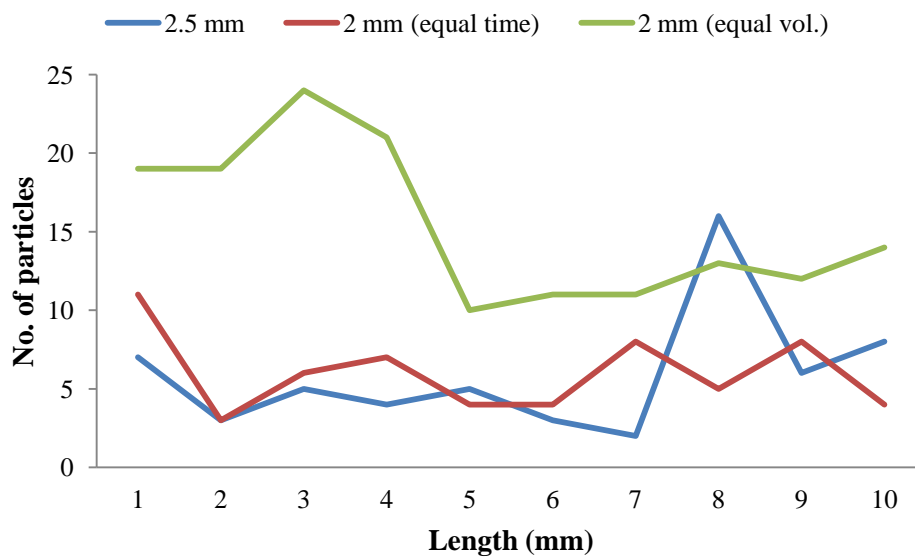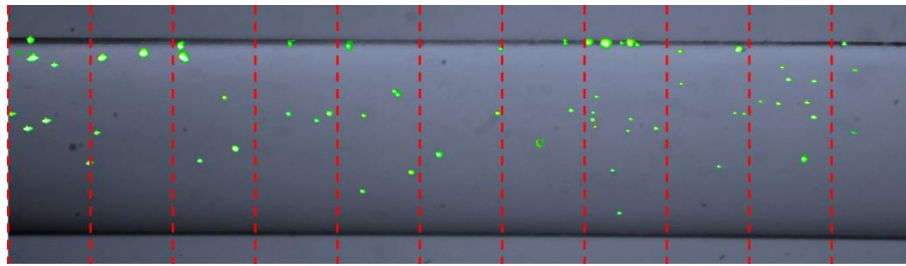
Figure 3.18 Particle accumulation in empty tubes

Top: After 20 minutes, the flow of a particle suspension through a 2.5 mm diameter tube was arrested and the tube imaged under fluorescent light. From this image, the tube was divided into 1 mm sections and the number of accumulated fluorescent particles within each section was counted.

Bottom: Particle count for an empty 2.5 mm tube after 20 minutes under flow (blue), an empty 2 mm tube after an equal amount of time (red), and the same 2 mm tube after an equal total volume of particle suspension (green).

3.5 *In silico* modelling

μCT scanning was used as a means of reproducing *in vitro* vessels *in silico* for modelling and analysis. Three types of sample were assessed – model vessels, model vessels containing a contrast agent and PDMS casts of model vessels. Various scanning and reconstruction parameters were applied in each case in an effort to find and optimise the best method of accurately capturing model geometry. Scan resolution as high as 3 μm/pixel was used to obtain high quality data for final models, and as low as 17 μm/pixel in rapid trials.

3.5.1 μCT scanning of model vessels does not capture both stent and wall

Stents are radiopaque due to the high x-ray attenuation of their metallic struts. Therefore, they could clearly be seen during μCT scanning and were easily isolated during reconstruction. However, optimising reconstruction parameters for stents rendered the wall invisible. PDMS is relatively radiotransparent and lower power was required to visualise the vessel. This increased sensitivity and the widened DIR required to reconstruct both materials resulted in noise and large image artefacts. In effect, the x-ray bright stents were 'overexposed' and obliterated the wall (Figure 3.19).

A high-resolution μCT scan of a coronary stent was performed and a dataset of images was reconstructed, optimised to obtain stent geometry only. This was provided to collaborators, Amanda Inzoli and Silvia Bonardelli (Politecnico di Milano, Italy), for the application of the FE wall method described in Section 1.6.6. A model was successfully created and used to perform CFD analysis and assess wall shear stress along the vessel. However, key information was lost with the omission of the PDMS wall. In this particular example the *in vitro* stent was slightly under expanded. The FE wall was therefore able to constrict further before being arrested by stent structure and the diameter of the resultant *in silico* model was too low. Applying the same flow conditions as those used *in vitro* returned an average wall shear stress approximately 50% higher than that expected (Figure 3.20).
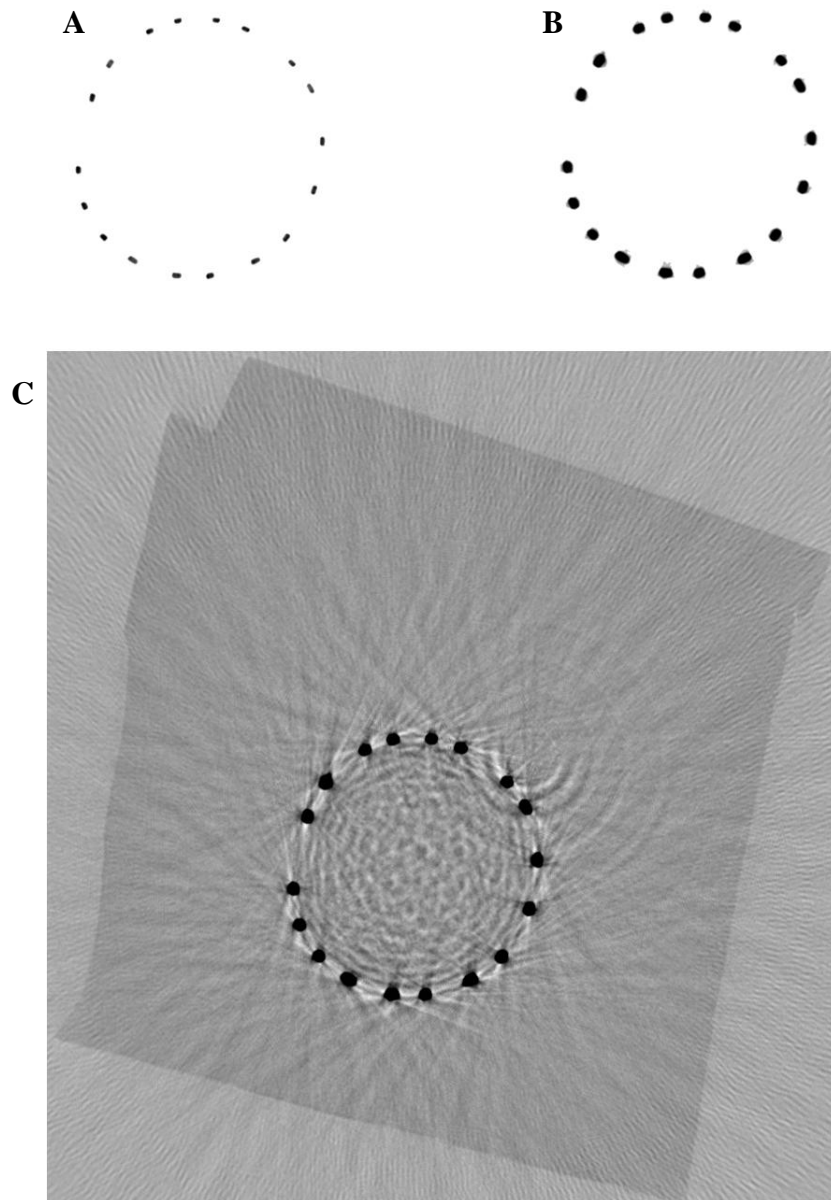
Figure 3.19 Preview cross-sections of µCT reconstruction

Following µCT scans of stents, cross-section previews allowed reconstruction parameters to be changed. Adjusting the DIR both altered the apparent geometry of structures and introduced interference. (Negative images are presented for clarity).

A: Image optimised for stent, producing thin struts (52539.6 – 76750.3 HU).

B: Image optimised for stent, producing thick struts (-138.2 – 32643.9 HU).

C: Altering the DIR so that PDMS becomes visible renders the vessel wall indefinable due to increased interference (-7275.0 – 11239.0 HU).
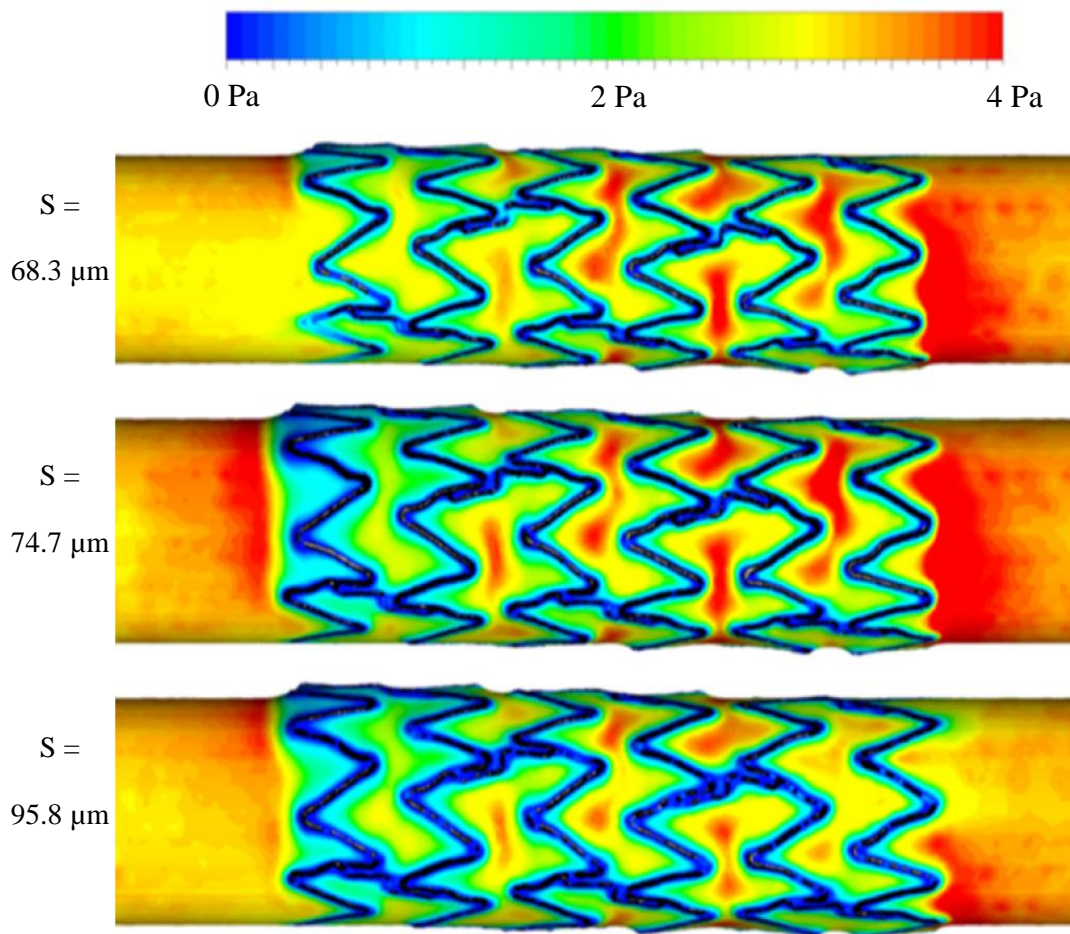
Figure 3.20 Wall shear stress distribution from CFD analysis using an FE wall

μCT data from a Coroflex Blue coronary stent was reconstructed to create a 3D model. The vessel wall was recreated *in silico*, by collapsing a model wall around the stent. The over-contraction of the model wall resulted in a higher average wall shear stress than that applied *in vitro* (1 Pa). Wall shear stress magnitude and distribution was also altered as apparent strut size (S) increased in models created from reconstructions with altered DIR.

Image courtesy of Amanda Inzoli and Sylvia Bonardelli (Politecnico di Milano, Italy).

3.5.2   Stent struts could not be accurately reconstructed from µCT data

An additional complication to that in described in Section 3.5.1 was the variation of strut dimensions with applied µCT and reconstruction parameters. For example, when altering the DIR for reconstruction, the apparent strut size changed (visible in Figure 3.19). Struts would appear thicker as the DIR was widened, with their true diameter at an unknown point in the range (a similar problem was encountered again when thresholding the images for conversion to binary format). In extreme examples, particularly seen in flow diverter stents, thinner struts disappeared entirely. Any attempt to capture them during the µCT reconstruction process resulted in the same interference that obscured the PDMS wall.

The effect of this issue is shown in Figure 3.20. Each case represents the same source µCT data, with various reconstruction ranges applied to produce three different apparent strut sizes. A clear effect on wall shear stress magnitude and distribution can be seen (in this example the effect is pronounced further by thicker struts altering the collapse of the FE wall around the stent).

A small strut section was scanned at high resolution and measured as precisely as possible in an attempt to calibrate the DIR and reduce this error. Difficulties in accurately measuring stent struts have already been described in Section 3.2.2. Figure 3.20 shows that a change of only 6 µm represents a 10% increase in strut size. Furthermore, identical reconstruction parameters affected different stents to varying degrees. Table 3.2 shows the impact of DIR on the total strut volume of four stents. Compared to reconstruction at mid-range DIR, volume increase at high range varied between 0.5% and 13%, whereas volume loss at low range varied between 62% and 90%. These differences may arise from dissimilar materials' x-ray attenuation, or from the different amounts of metal present in each stent design, necessitating calibration on a stent-by-stent basis.

Stent material	Stent length (mm)	Stent volume (mm^3)		
		Narrow range	Mid-range	Wide range
F562 cobalt chromium	10	0.73 (-66%)	2.14	2.42 (+13%)
L605 cobalt chromium	8	0.47 (-62%)	1.24	1.40 (+13%)
MP35N cobalt chromium	9	0.36 (-74%)	1.41	1.51 (+7%)
316L stainless steel	8	0.20 (-90%)	1.94	1.95 (+0.5%)

Table 3.2 Apparent stent volume varying with DIR

During μCT reconstruction apparent strut diameter, and therefore the volume of the final model stent, varied with DIR parameters. Narrowing the DIR decreased apparent volume in comparison to a mid-range, whereas widening the DIR gained volume. Applying the same DIR parameters to coronary stents of different length and material resulted in large differences in apparent volume variation between them. Thus, DIR could not be standardised to ensure the faithful reconstruction of accurate stent geometry in every case.

3.5.3 A contrast agent did not sufficiently define the wall

Model vessels were scanned with a 60% barium sulphate suspension within the lumen. This suspension was used to act as a contrast agent, as it had higher x-ray attenuation than PDMS and was relatively radiopaque. It was hoped that, unlike PDMS, this agent would remain visible while μCT power was increased and DIR was narrowed to optimise for stents. This would provide a clear definition between stent struts (in white, at the upper end of the image range), PDMS (in black, outside of the image range), and the contrast agent (at a greyscale intensity within the range). This would allow struts to be isolated and subtracted from the image, resulting in the contrast agent alone describing the shape of the fluid volume.

However, the 60% barium sulphate suspension was highly viscous and therefore it was difficult to ensure that every part of the lumen was filled, particularly around intricate stent geometry, and gaps were only revealed once the model had been scanned. The contrast agent was more visible under x-ray than PDMS, but was still too radiotransparent relative to metallic stents and the required sensitivity again resulted in noise and artefacts. Although this interference was less pronounced in comparison to scans taken without a contrast agent, and large segments of wall could be defined, image stacks still required extensive manual editing to remove interference and repair sections.

Figure 3.21 illustrates the process required to obtain a final *in silico* model from μCT data using a contrast agent. While some image slices were relatively intact, others required 25% of the wall replacing. In the final model, 6% of the total vessel wall was manually recreated, all local to stent struts where accurate geometry was most essential. In addition, this process was aided by reconstructing and overlaying the stent alone, which raised the same issue regarding true strut dimensions described in Section 3.5.2.
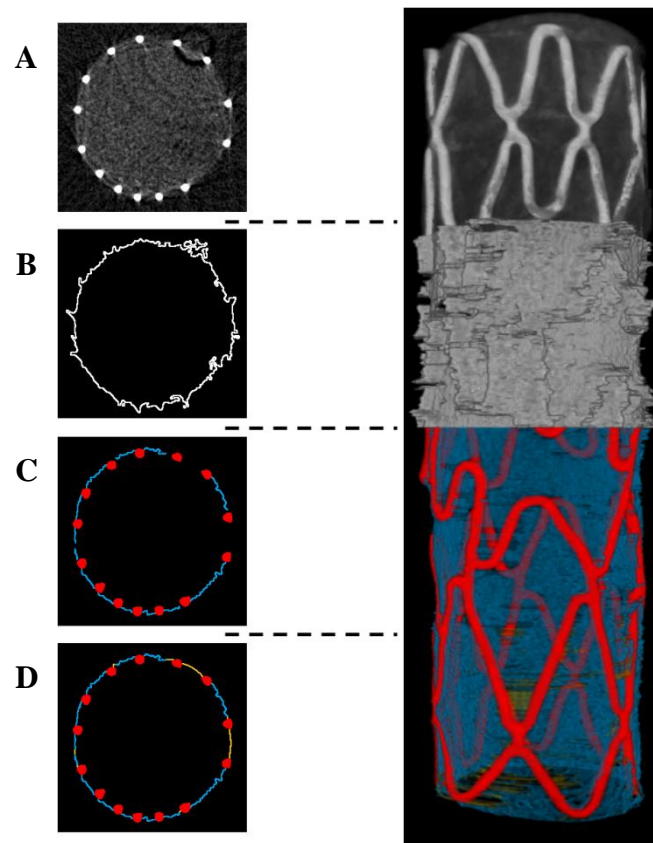
Figure 3.21 Model reconstruction process from µCT data using a contrast agent

A µCT scan of an XTRM-Track coronary stent was performed with a contrast agent within the lumen and image reconstruction performed on cross-section slices (left) to create a 3D *in silico* model (right).

A: Post-reconstruction, the contrast agent provided a visible, but poorly defined wall/lumen boundary.

B: Attempting to visualise this boundary resulted in interference and distorted geometry.

C: Overlaying separately reconstructed stent geometry (red) onto the wall (blue) highlighted areas of interference, which could be removed.

D: Areas of missing wall were replaced (yellow) using information from neighbouring image slices.

3.5.4 PDMS casting reproduced stented vessel geometry *in vitro*

Casts were created by silanising model vessels and filling the lumen with additional PDMS. As the model no longer needed to be biocompatible at this point, the PDMS could be left for as long as required to fully cure at room temperature, preventing any shrinkage. Casts could be cleanly separated from the model. For coronary stents, the tip of a needle was used to pry a single strut away from the cast. Severing this with a scalpel allowed adjoining struts to be carefully pulled away and the entire stent was removed in this manner. 5:1 and 10:1 PDMS mixing ratios were trialled, with 5:1 providing more favourable results (Figure 3.22). It is likely that the lower viscosity of 5:1 PDMS when fluid, and higher stiffness when cured, helped to fill and capture fine geometry.

Any coronary stent struts which were prolapsed into the lumen had to be pulled through the cast. The PDMS around these struts returned to its original position once they were removed, and cast geometry was preserved. However, as all flow diverter stent struts lay adjacent to the wall, the same technique could not be applied (Figure 3.23). For these models the cast and stent were cut at each end and struts pulled out longitudinally through the lumen.

3.5.5 PDMS cast geometry was accurately reproduced *in silico*

The use of homogenous PDMS casts ensured that μCT scan and reconstruction parameters could be optimised for a single material, eliminating the issues found in Sections 3.5.1. The effect on apparent size was also greatly reduced, confirmed by creating and scanning PDMS samples of known size. Settings could therefore be applied to provide a steep, well defined boundary in greyscale intensity for reconstruction and thresholding, with no effect on the dimensions of the model.

Fine structural details were visible, including intact voids representing prolapsed struts. This simple process resulted in accurate reproductions of cast geometry and a vast reduction in effort required to prepare the *in silico* models for meshing (Figure 3.24). Rigid body registration of *in silico* models of stents and their resultant casts was performed in Amira (FEI), resulting in good alignment of the two (Figure 3.25).
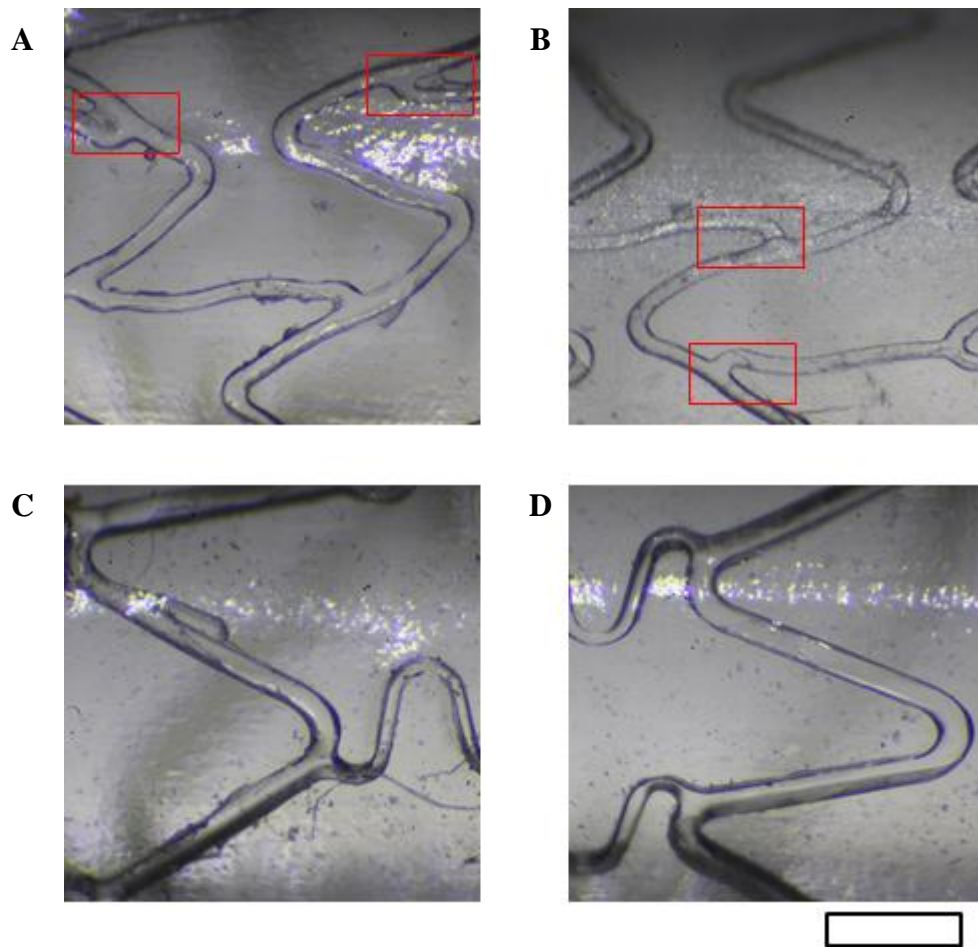
Figure 3.22 PDMS casts of coronary stents

PDMS was cured within the lumen of model vessels containing coronary stents, which were then removed to create casts for µCT scanning. The use of different PDMS mixing ratios was assessed to ensure the accuracy of casts. Casting with a 10:1 ratio resulted in poorly defined struts and damage within complex geometry (red boxes). Stiffer, more damage resistant PDMS with a 5:1 ratio resulted in a much cleaner, well-defined cast.

A: Cast of a Pro Kinetic Energy coronary stent, 10:1 ratio.

B: Cast of a Pro Kinetic Energy coronary stent, 5:1 ratio.

C: Cast of a Velocity coronary stent, 10:1 ratio.

D: Cast of a Velocity coronary stent, 5:1 ratio.

Scale bar: 0.5 mm.
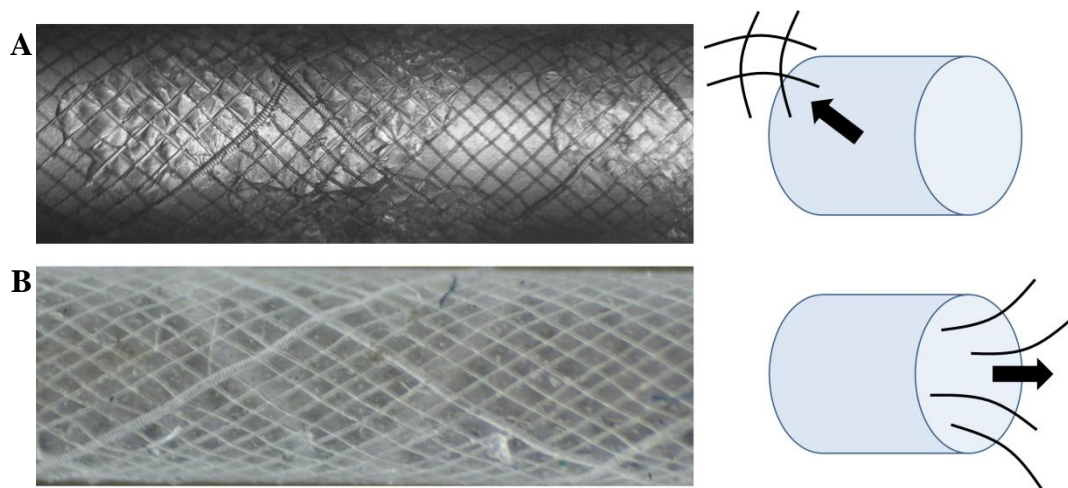
Figure 3.23 PDMS casts of flow diverter stents

PDMS was cured within the lumen of 2 mm diameter model vessels containing Silk flow diverter stents, which were then removed to create casts for µCT scanning. In flow diverter stents PDMS was able to fill gaps between the wall and the struts which lay adjacent to it, hindering the removal of a clean cast.

A: Pulling struts away from the cast through the wall destroyed the surface.

B: Pulling struts out of the lumen from either end of the stent protected the wall from damage and preserved fine details.
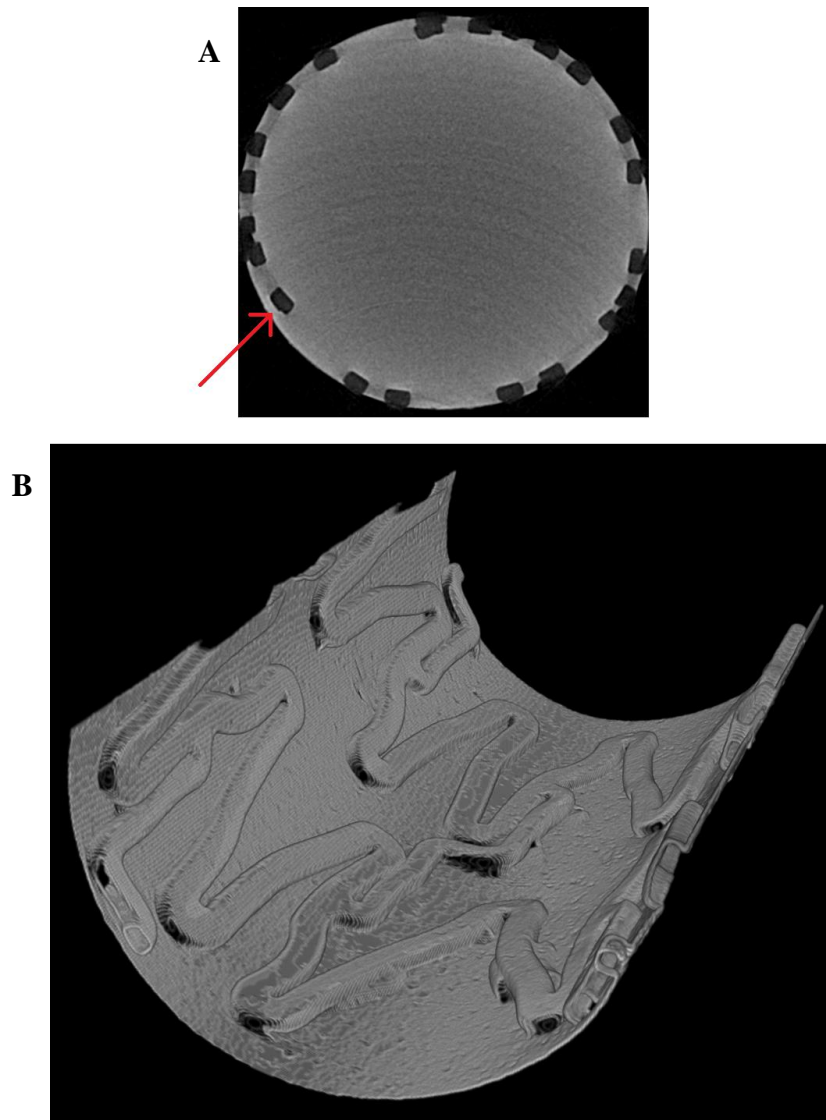
Figure 3.24 Reconstructed µCT data of a stent cast in PDMS

The use of PDMS casts of model vessels provided µCT scan data of accurately sized geometry and captured fine stent strut detail, including prolapsed struts (red arrow).

A: Optimising µCT scan and reconstruction parameters for homogeneous PDMS casts produced an image of the lumen with a clearly defined wall boundary.

B: Cutaway of a section of wall boundary reconstructed from a 9.92 µm resolution scan of a Coroflex Blue coronary stent cast.
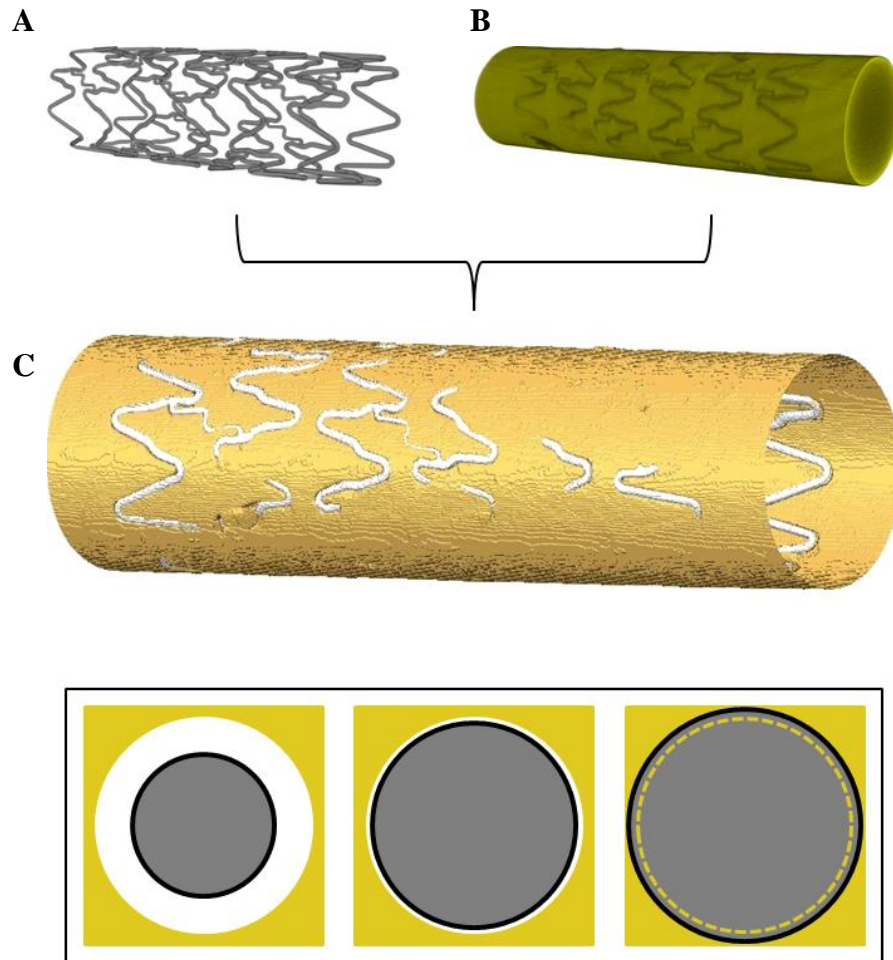
Figure 3.25 Image registration of a stent and associated cast

Rigid body registration was performed on models of a Coroflex Blue coronary stent and its associated cast, reconstructed from data from separate µCT scans. The two were aligned in an effort to measure the ability of casts to recreate the geometry of stents.

A: Reconstructed Coroflex Blue stent model.

B: Reconstructed Coroflex Blue cast model.

C: Rigid body registration between stent and cast models.

Inset: Although good alignment was found between stents and casts, this was a measure of orientation and did not take apparent strut size into account. The struts of varying thickness illustrated here (grey) would all be considered to be equally well aligned with the same cast (yellow).

3.5.6 Computational fluid dynamics models were created from µCT data

All models were successfully meshed in ScanIP and the simplicity of the software offset a relative lack of user control in comparison to ANSYS packages. No smoothing was applied at any stage as this process had too great an impact on smaller struts. The lack of smoothing rendered data from particularly low resolution µCT scans unusable as large voxels formed a stepwise geometry.

Meshing and FLUENT set-up variables were informed by residual analysis and grid independence studies performed by Amanda Inzoli and Silvia Bonardelli (Politecnico di Milano, Italy), on CFD models as mentioned in Section 3.5.1. Computational cost was balanced against the accuracy of results and the ability to confidently compare data from separate models. Stability in their model was achieved with convergence criterion of 10^{-6} and a mesh of ≥ 2 million elements, and these factors were applied here.

3.6 Discussion

Chapter 2 presented a method for the fabrication of an *in vitro* model vessel, and protocols for stent deployment, cell migration studies, particle tracking, and *in silico* geometry reconstruction and analysis. This chapter considered the choice of those techniques and the necessary materials, equipment and means of image and data analysis. In order to directly compare coronary and flow diverter stents the same model and conditions were applied in both. Therefore, the properties discussed in Section 1.7 and replicated in the sections which followed were those of the coronary arteries only. This decision was made based upon the number of available stents of each type, the information available in the literature and the conditions applied in comparable work in-group.

In order to fabricate an *in vitro* model vessel, a reliable value for EC growth medium viscosity was vital. Firstly, this improved the accuracy of the model as using the EC growth medium described in Section 2.2.2.1 while applying pre-existing viscosity data from the literature, for example 0.7 mPa.s or 1.0 mPa.s [141][154], would result in wall shear stress being under and over estimated by 12% and 25% respectively.

126

Secondly, because wall shear stress is inversely proportional to the cube of the vessel radius, flow rates required to generate specific magnitudes of the force increased rapidly with vessel size. Therefore, understanding EC growth medium fluid properties was particularly important as, in larger models, Reynolds number can increase above 2000 and flow begins to transition from laminar to turbulent. Indeed, testing wider coronary stents, or modelling larger artery diameters or higher shear stress levels [125][154], would induce fully turbulent flow. Overestimating viscosity, and therefore underestimating Reynolds number, could result in flow entering an entirely different regime than that assumed, thereby invalidating the model.

The viscosity data therefore put an upper limit on vessel size and applied wall shear stress, and is one of the reasons why the use of medium thickening agents was considered [156]. Thickening agents would also tackle one of the drawbacks of the majority of *in vitro* models: the fact that fluid properties cannot be completely matched to those *in vivo*. Studying wall shear stress with media rather than blood, for example, means that fluid velocity and Reynolds number are much higher than measured physiological levels (Section 1.7). Subsequently, any effort to understand the impact of varying those variables would, in turn, lead to altered wall shear stress. The use of a full-scale model vessel already reduced the disparity between *in vitro* and *in vivo* conditions compared to microfluidic parallel plate experiments [147][153][154], and the addition of thickening agents would allow all physiological flow properties to be met. However, the use of dextran and XG were not further evaluated due to their detrimental effect on HUVEC. This was unexpected as previous studies have successfully used similar concentrations in flow experiments [147]. Other options were available, including the use of higher molecular weight dextran which could be utilised in smaller quantities [200]. However, thickening agents would render any data from cell experiments incomparable to the bulk of work done with standard EC growth medium and would introduce additional variables, due to the potential effects of osmolality and glucose concentration on cell metabolism and behaviour [157].

The comparison between vessels of different size also presented a challenge. Changing diameter not only resulted in different fluid flow variables, but also required the use of different pump systems. Peristaltic pumps, by their nature,

produce a pulse which could potentially induce not only unsteady flow but also the mechanical forces described in Section 1.4.1. This pulse, and its effects, would change with pump power (and is not present at all in the ibidi pressure pump system). To reduce any disparity in pulse frequency, tubing size was carefully selected so that the power required by 2 mm and 2.5 mm models was as similar as possible. 2 mm diameter models were connected to tubing of 3.1 mm inner diameter (ID) and required 53% pump power to generate 1 Pa average wall shear stress. 2.5 mm models were connected to 4.8 mm ID tubing and required 57% pump power. Factoring in maximum power rpm and the number of rollers in the pump head, this resulted in 636 and 684 pulses per minute (or 10.6 and 11.4 Hz respectively). To then minimise the amplitude of these pulses, soft silicone tubing and the air pocket within the reservoir acted as dampeners. This is estimated to reduce pulsation by up to 90% [201]. Indeed, by observing the flow of particles or debris, no pulsation could be seen under any flow conditions.

PDMS was chosen to be used to create *in vitro* vessel walls due to its ease of use, transparency, relative biocompatibility and compliancy, in spite of its many disadvantages (discussed in Section 1.6.2). While alternative materials such as PTFE and PMMA are too stiff, PDMS was well suited to stent deployment [130][133]. The values of elastic modulus seen with different mixing ratios were within the physiological ranges found in the literature (Section 1.7.1). A ratio of 10:1 was selected for use in the model due to its similarity to arterial tissue and the increased biocompatibility of that ratio [138].

When making comparisons to arterial tissue, the elastic modulus of PDMS was measured as it was observed that, rather than penetrating or indenting the vessel, stents pushed against it and caused widening (Figure 3.4), leading to hoop stress and radial compression in the wall. An example of stent deployment was inspected by Dr. Ana Paula Narata (INSERM U930, France) and was considered to be acceptable. This important check confirmed that experiments were not performed on models which were not representative of *in vivo* deployment, for example causing stents to be excessively embedded into the wall, or too far prolapsed into the lumen.

While human coronary artery endothelial cells (HCAEC) are commercially available, and the coronary arteries were being modelled here, HUVEC were selected for use in cell migration studies due to their frequent supply from the Jessop Wing maternity unit, Sheffield. The demonstration of arterial-like characteristics by EC, described in Section 1.6.2, has been found in literature to require 24 hours' exposure to arterial mechanical conditions [144]. As this was the typical duration of experiments in this work, it cannot be assumed that such a change took place in the cells under observation here. Nonetheless, the use of HUVEC was deemed satisfactory given the other arguments made in Section 1.6.2. One disadvantage to PDMS was the requirement of a fibronectin coating for successful HUVEC attachment, as this necessary step prevented repeat experiments being performed on the same models. Applying fibronectin prior to stent deployment ensured that cell migration data was reliable. However, this would not hold true once a second coating was applied prior to a follow-up experiment as stent struts would also be coated and would therefore present a more favourable surface for HUVEC.

Rotating the vessel during attachment, to enable HUVEC to attach around the full circumference of the wall [107], was considered but ultimately not attempted to avoid further complicating the protocol. It was thought that seeding onto the lower surface of the vessel only would allow HUVEC migration to be influenced not only by stent geometry, but also by empty space around the cells that would not normally be available to them. This proved not to be the case: monolayer leading edges remained relatively uniform while the area occupied by individual leader cells tended to narrow as migration distance increased. This result was unexpected and not previously mentioned in literature (the experiments discussed in Section 1.6.4 and Table 1.2 were not designed to study cell migration in vessels of circular cross-section). However, this finding could be due to one or more limitations of the model: the use of relatively low cell numbers, a lack of cell proliferation over the duration of the experiment, or simply the migration of cells outside of the limited surface area within the microscope focal plane.

To accurately measure cell migration an initial position had to be identified. Cells were therefore seeded partway along the model to create a clear boundary between attached HUVEC and empty vessel wall. This was necessary as HUVEC attached too

well to be damaged by stent deployment (Figure 3.6). Even after the high-pressure balloon expansion of coronary stents, or the scraping of flow diverter sheaths, too many cells remained within the stent to consider the vessel de-endothelialised and to enable migration to be monitored. Previous *in vivo* studies have also reported this problem, discussed in Section 1.6.1 and further in Chapter 6 [103][122]. The straightest, most well-defined boundaries of cell attachment were used where possible, as this enabled the most accurate placement of stents. This reduced the time taken for cells to migrate to stents' leading edges (the region of interest) during experiments.

Clear cell migration under flow was seen in empty control models (Figure 3.7). Migration rates were higher than the 0.01 – 0.02 mm/h under similar conditions found in literature [95][127]. However, those studies were examples of microfluidic systems and, accordingly, migration rate reduced with model diameter here (Figure 3.8). Cell migration studies were also performed with the use of a ROCK inhibitor (Section 2.2.2.3) to highlight the impact of disturbed flow on HUVEC. Reduced migration was seen with the use of a ROCK inhibitor in comparison to standard un-supplemented medium. Although ROCK inhibitors have been shown to enhance HUVEC migration and accumulation within stents by allowing cells to migrate within areas of complex bi-directional flow (Section 1.4.4) [103], this advantage is redundant under the steady, unidirectional flow conditions applied here. The complete inhibition of ROCK can prevent cell migration [104][202], but due to the variability between individual experiments it cannot be stated that any reduction in migration seen here is due to the presence of the inhibitor.

A number of unused models provided a large sample of static controls. None showed migration, or no more than that seen in standard static culture as cells spread, except one. This lone example of migration under static conditions, clearly identified against marks on the PDMS (Figure 3.11D), is puzzling. Although some small degree of cell migration under static conditions has been seen in previous studies (50 – 70 μm [95]), the 800 μm found in Figure 3.11D is comparable to that in some experiments under flow (Figure 3.8). While it is possible that the model was disturbed during attachment, the initial image at t = 0 was taken after the vessel was

flushed. Images of the other side of the monolayer were not taken as per the experimental protocol. If extra images had been taken, apparent migration may have been seen in that direction also, in which case this single example could have been due to a particularly fast growing (and spreading) culture.

A maximum experiment duration of 72 hours was possible with the peristaltic pump, however the majority of experiments did not last this long. Experiments were typically stopped between 24 hours (the minimum duration to define an experiment as successful, comparable to those in the literature listed in Table 1.2) and 48 hours due to excessive wear on the tubing caused by the action of the pump rollers. With no moving mechanical parts, the ibidi system could run for longer periods. Although its reservoirs were relatively small, unlike the peristaltic pump system they could easily be replenished with fresh medium.

Although particle tracking in *in vitro* models is typically performed for velocimetry [203][204], it was conducted here as a simple means of visualising flow. This became more pertinent as it became clear that the most viable methods of successfully recreating model geometry *in silico* for more powerful CFD analysis (casting), would be destructive. Therefore, flow data would otherwise only be available at the model's end of life and dependent on successful *in silico* modelling. Particle tracking also allowed the accumulation of bodies with similar size to EPC to be studied.

IMS was used as the particle suspension's fluid phase because, compared to water, it greatly reduced the frequency at which bubbles formed and attached to struts. IMS therefore minimised their impact on particle motion. As particles were only visible at very low flow rates, similitude was applied to enable the use of a less viscous fluid while maintaining a physiologically relevant parameter in the Reynolds number. Equating Reynolds number to that of blood allowed a sufficient reduction in velocity, yet meant that particle tracking and accumulation data could not be directly compared to cell migration or CFD data, as those specific conditions were not simulated. However, tracking data from different stents could still be compared and contrasted, allowing any influence of differing geometry to be investigated.

131

μCT scanning was found to be a good method of converting *in vitro* geometry into *in silico* models, though the processes involved in this conversion had some disadvantages. For example, scanned samples interfered with each other and required scanning individually. Orienting models vertically ensured constant x-ray absorption throughout their rotation but meant that the models were often outside of the field of view and therefore required multiple scans. These factors presented the greatest drawback of μCT scanning: high time and resource cost, especially when scanning at higher, usable resolutions.

If time and expense were not a factor, more comprehensive parametric studies could have been carried out to properly assess the impact of scan parameters on the final model. In particular, investigating resolution would have been of interest. Specifically, if there was a maximum useful resolution beyond which any improvement (and associated costs) conferred no advantage to the accuracy of the final model and CFD simulation.

Post-scan, the FE wall recreation method removed the need to extract low-intensity materials and parameters could be optimised for individual stents. The problems inherent in this method have already been discussed in Section 3.5.1. As the main aim was to faithfully replicate *in vitro* model geometry, the use of a technique in which the entire wall is created virtually was not appropriate [162]. However, an argument can be made that no other method is a truly faithful model, when considering the compounded impact of scanning (power and resolution), reconstruction (DIR), modelling (binary thresholding, smoothing), CFD analysis (meshing) and, in this case, casting.

The use of a contrast agent as a means of better identifying the vessel wall during μCT reconstruction was not continued. The original description of the method in the literature stated that some image editing was required, however the level of effort required to obtain a model of relatively low quality was under-estimated [133].

It was found that μCT scanning and reconstruction most accurately reproduced the geometry of PDMS casts and this method was therefore pursued. The important next step was to ascertain how accurately casts reproduced the geometry of stented vessels. Empty vessels and their resultant casts could be compared with ease. The

presence of a silane film did not have a measurable impact given the <75 nm thickness of the deposition layer [205], nor was it detectable at the μCT resolutions used. Physically measuring intricate stent geometry and the associated sections on casts was problematic, therefore reconstructed *in silico* models were aligned via rigid body registration. Visually, this method returned a good result (Figure 3.25) and the software could provide a measure of alignment, however it was not known where this value lay on a scale from bad to perfect alignment. In addition, alignment was a measure of position and direction and did not necessarily signify a tight fit (Figure 3.25, inset). A more precise, quantifiable measure of fit could be made possible by comparing the stent to a model of the voids the stent struts left in the cast, with the software then able to minimise the difference between the two. This would require accurate strut dimensions to size the model stent and to identify the full volume of voids residing on the exterior of the cast. The problem is therefore circular: casts had to be used as stent geometry could not be accurately reproduced; yet the precision of such casts could not be definitively proven without the use of accurate stent geometry.

The methods and protocols outlined in Chapter 2, and discussed in this chapter, describe the development of a novel model vessel and combined *in vitro* and *in silico* evaluation, suitable for the study of the impact of stent geometry on local wall shear stress and endothelial cell migration. The following chapters consider the application of this experimental platform in the assessment of a range of commercially available, clinical-grade coronary and flow diverter stents.

Chapter Four

In Vitro and *In Silico* Study of Coronary Stent Haemodynamics and Cell Migration

The regrowth of a healthy endothelial layer is hindered by EC dysfunction caused, at least in part, by the presence of cardiovascular stents and their effect on local wall shear stress (Sections 1.4 and 1.5). Chapters 2 and 3 considered the creation of an experimental platform through which the biomechanical conditions of stented vessels could be studied. This chapter concerns the application of that platform to a range of clinical-grade coronary stents, enabling the assessment of the effect of diverse stent geometry on wall shear stress modification, and its subsequent impact on endothelial cell behaviour.

4.1 Coronary stent deployment

4.1.1 Coronary stent geometry showed great variability

Ten different coronary stent designs were made available by Prof. Julian Gunn (Department of Infection, Immunity and Cardiovascular Disease, University of Sheffield). These were deployed within *in vitro* model vessels of 1.5 and 2.5 mm diameter, as discussed in Chapter 3. All were of the 'slotted tube' type, meaning that they were laser cut and therefore had square cross-section and 90° edge angle. Coronary stents were manufactured from a variety of materials and, in general, showed a wide range of distinct strut sizes, MSA and strut orientation (Table 4.1 and Figure 4.1, based on analysis detailed in Figure 2.3). Exceptions were:

- The Orsiro, a drug-eluting version of the Pro Kinetic Energy with identical geometry.
- The Penchant, with identical geometry to the BiodivYsio OC (the difference in trademark being related to the stent delivery system).
- The Coroflex Blue Neo, an updated version of the Coroflex Blue, with reduced strut thickness.
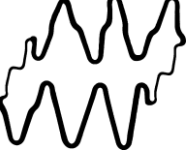
Model	Manufacturer	Strut (μm)	MSA (%)	Unit (not to scale)	Length (mm)	Diameter (mm)	Material	Coating
BiodivYsio OC	Biocompatibles Ltd.	90	17.6		7 – 28	2 – 4	316L stainless steel	Phosphorylcholine
Chroma	Biosensors International	85	16.7		9 – 36	2.25 – 4	MP35N cobalt chromium	None
Coroflex Blue	B Braun Medical Inc.	65	23.1		8 – 25	2.5 – 4	L605 cobalt chromium	None
Coroflex Blue Neo	B Braun Medical Inc.	60	18.8		8 – 33	2.75 – 4	L605 cobalt chromium	None
Matrix	Sahajanand Medical Technologies	80	24.2		9 – 33	2.5 – 4	316L stainless steel	None

Table 4.1 Properties of coronary stents

Only coronary stents of 3 mm nominal diameter were deployed within 2.5 mm model vessels, although the length of those stents varied.
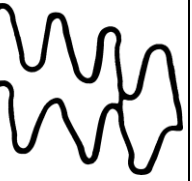
Model	Manufacturer	Strut (µm)	MSA (%)	Unit (not to scale)	Length (mm)	Diameter (mm)	Material	Coating
Orsiro	Biotronik	60/80	18.5		9 – 40	2.25 – 4	L605 cobalt chromium	Silicon carbide, sirolimus in polylactide matrix
Penchant	Biocompatibles	90	17.6		7 – 28	2 – 4	316L stainless steel	Phosphorylcholine
Pro Kinetic Energy	Biotronik	60/80	18.5		9 – 40	2 – 5	L605 cobalt chromium	Silicon carbide
Velocity	Cordis	130	17.9		8 – 33	2.25 – 5	316L stainless steel	None
XTRM-Track	Blue Medical	120	18.7		10 – 32	2 – 4	F562 cobalt chromium	None

Table 4.1 (cont.) Properties of coronary stents

Only coronary stents of 3 mm nominal diameter were deployed within 2.5 mm model vessels, although the length of those stents varied.
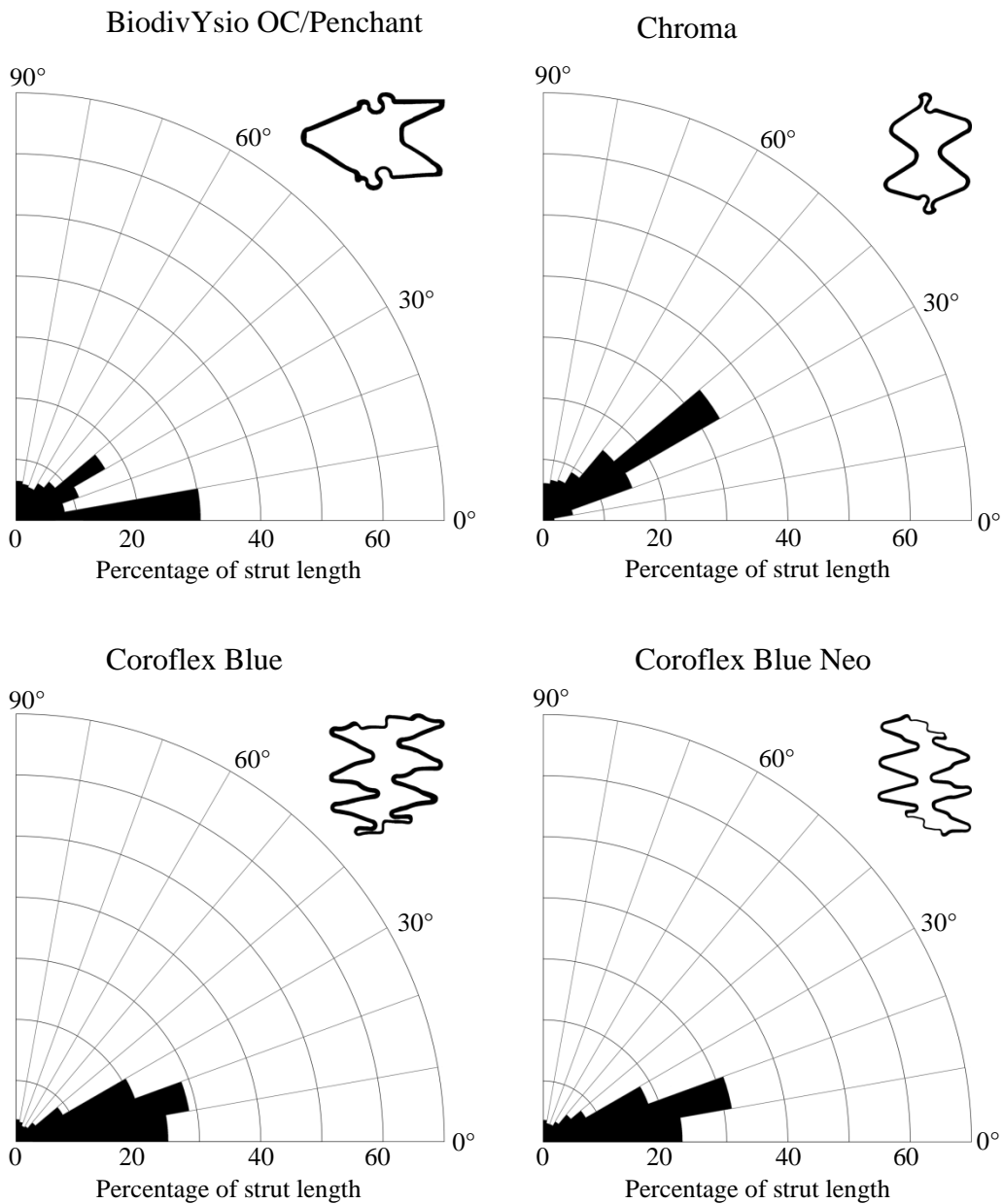
Figure 4.1 Coronary stent strut orientation

The orientation of coronary stent struts was measured in relation to the direction of applied flow (0°), as illustrated in Figure 2.3. The length of struts at each angle (to the nearest 10°) is shown here as a percentage of the total strut length. Each chart represents an average measurement taken from two faces of each stent (rotating the stent 90° between the two) and one repeating unit of stent geometry.
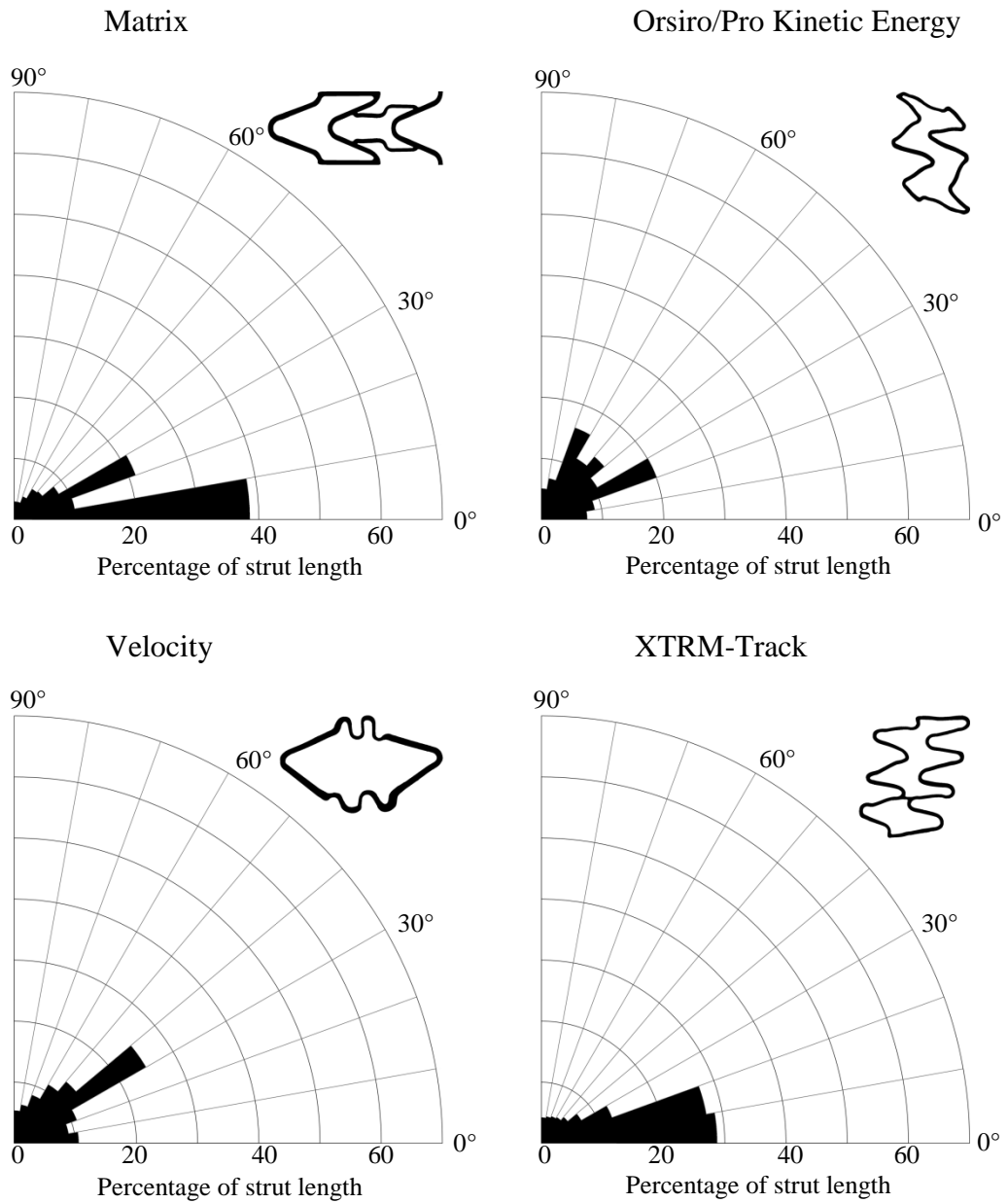
Figure 4.1 (cont.) Coronary stent strut orientation

The orientation of coronary stent struts was measured in relation to the direction of applied flow (0°), as illustrated in Figure 2.3. The length of struts at each angle (to the nearest 10°) is shown here as a percentage of the total strut length. Each chart represents an average measurement taken from two faces of each stent (rotating the stent 90° between the two) and one repeating unit of stent geometry.

4.1.2 Deployment showed slight variation between coronary stents

As mentioned in Section 3.2.2, there was slight variation in the geometry of stent structure even after deployment of examples of the same design. This variability could arise from the orientation of the folded stent during delivery, the application of pressure to the balloon, or perhaps small differences in the PDMS wall. These variations included strut prolapse and under-expansion (Figure 4.2), all of which could influence flow patterns to some degree. The extent of this variability was somewhat limited by following correct deployment procedures and by using stents of appropriate nominal diameter.

4.2 Coronary stent geometry influenced flow patterns

4.2.1 Coronary stent geometry influenced streamline orientation

Particle tracking revealed the impact of the presence of coronary stents on local flow patterns and the disparity in this impact between stent designs. Streamlines through coronary stents are shown in Figures 4.3 – 4.7 (for clarity, representative areas are presented here and streamlines through the full stents are provided in the Appendix). Over the full length of stents there was good agreement between the two sequences taken in each field of view and clear streamline patterns followed from one field of view to the next. Observing more closely, in sections of complex geometry and immediately up and downstream of struts, areas of reversed flow, recirculation and stagnation were identified (Figure 4.8).

Stents were seen to have a large effect on track orientation, as particles would typically follow struts for some distance before crossing them and returning to a longitudinal path. The impact of stent design on flow direction, and therefore on the direction of mechanical cues, was quantified by calculating the percentage of tracks that deviated from a path within $\pm 5°$ of the direction of applied flow (Figure 4.9). This threshold was applied to ensure that stent-induced flow deviation was captured while minor deviations, due to equipment disturbance or manual tracking errors, were omitted.
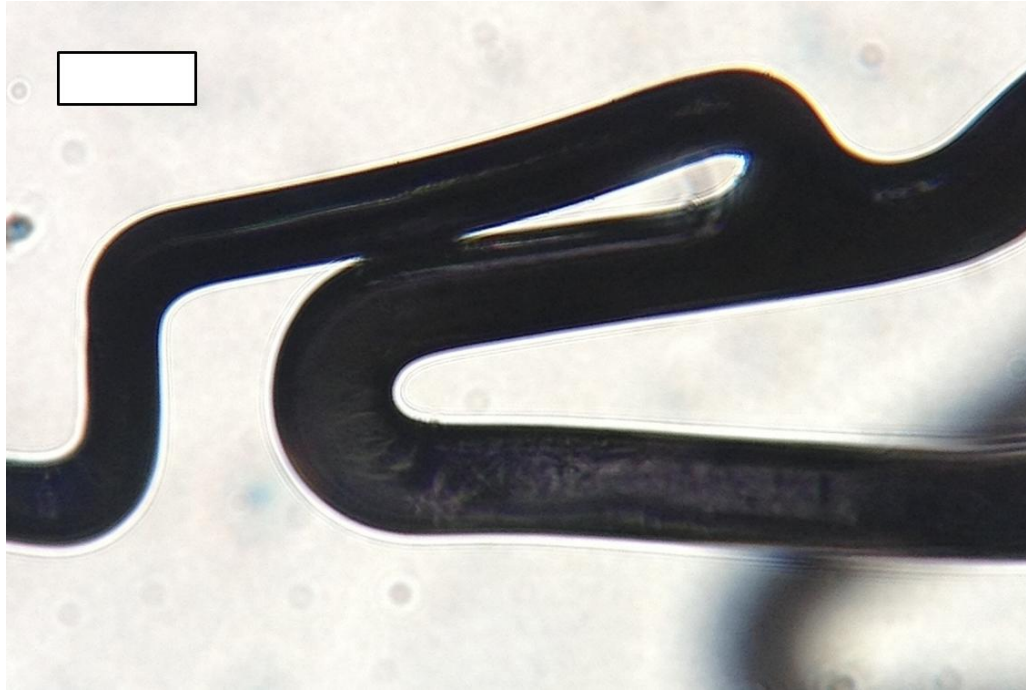
Figure 4.2 Under expanded coronary stent geometry

Each individual stent deployment produced variations in geometry, even between stents of identical design. Segments could under or over expand during balloon inflation, leading to small changes in strut position and orientation. In this example, an under expanded Coroflex Blue bridge strut remained in contact with a main ring strut, creating a small enclosed region.

Scale bar: 100 μm.
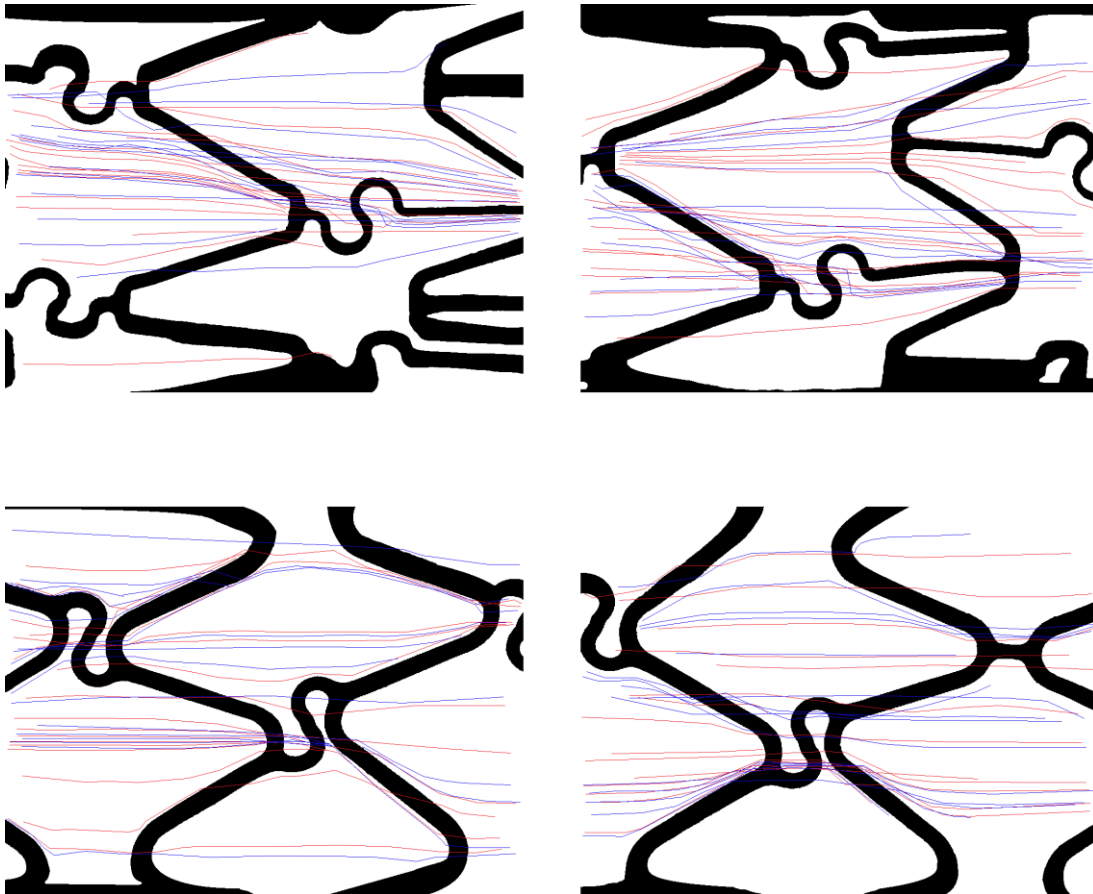
Figure 4.3 Tracked particle streamlines in BiodivYsio OC and Chroma coronary stents

Particles were tracked moving through coronary stents deployed within 2.5 mm diameter vessels. Tracking was performed for two 30-second long sequences (red and blue tracks) on two stent faces, with the stent rotated by 90° between the two faces.

Top: BiodivYsio OC stent.

Bottom: Chroma stent.

Flow from left to right, Re = 68 (equivalent to blood flow with 1 Pa wall shear stress). Representative images are mid-stent length and the plane of focus on the bottom of the vessel.
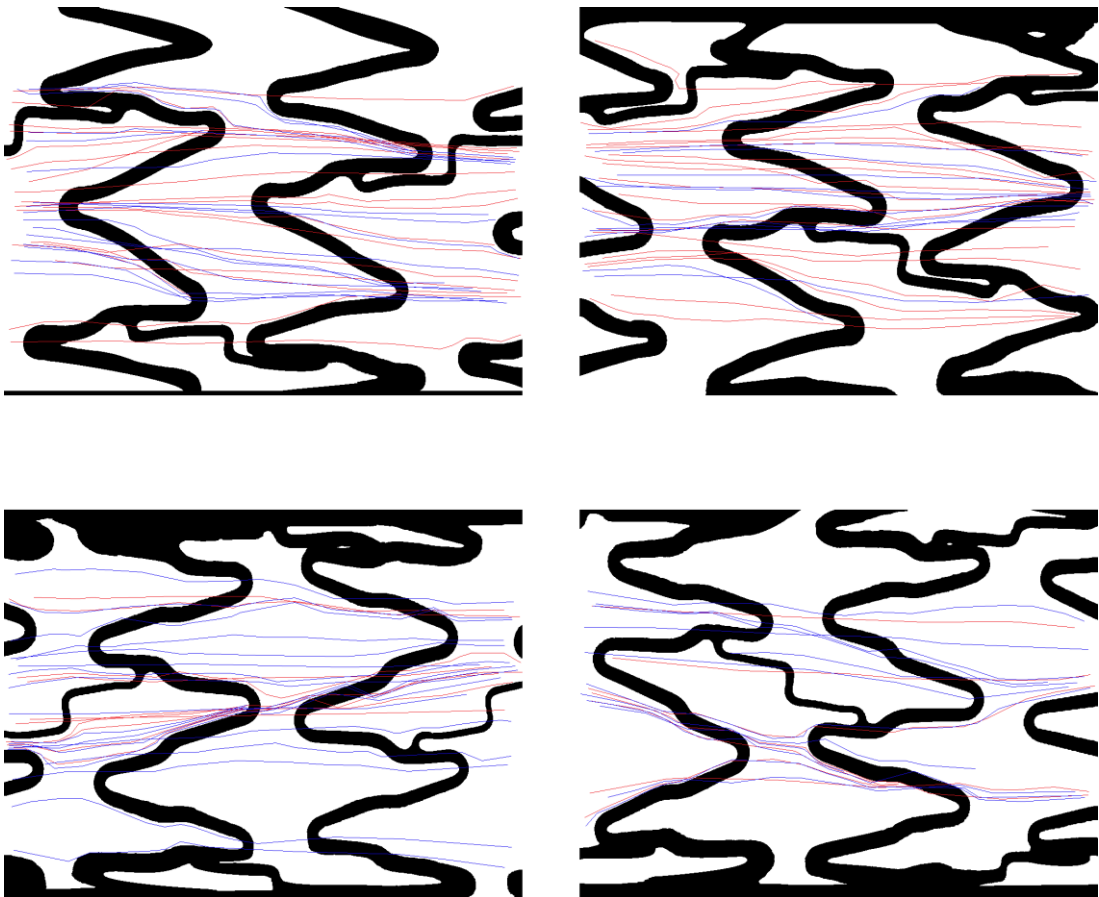
Figure 4.4 Tracked particle streamlines in Coroflex Blue and Coroflex Blue Neo coronary stents

Particles were tracked moving through coronary stents deployed within 2.5 mm diameter vessels. Tracking was performed for two 30-second long sequences (red and blue tracks) on two stent faces, with the stent rotated by 90° between the two faces.

Top: Coroflex Blue stent.

Bottom: Coroflex Blue Neo stent.

Flow from left to right, Re = 68 (equivalent to blood flow with 1 Pa wall shear stress). Representative images are mid-stent length and the plane of focus on the bottom of the vessel.
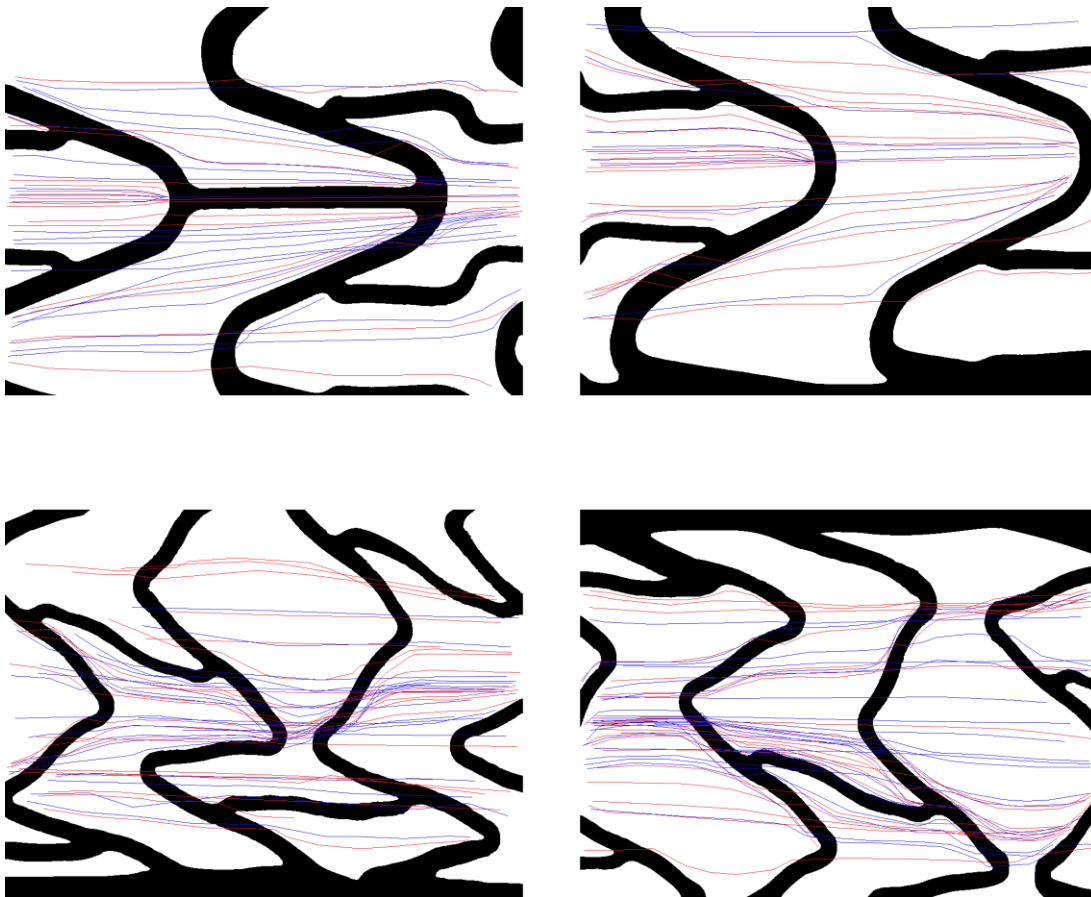
Figure 4.5 Tracked particle streamlines in Matrix and Orsiro coronary stents

Particles were tracked moving through coronary stents deployed within 2.5 mm diameter vessels. Tracking was performed for two 30-second long sequences (red and blue tracks) on two stent faces, with the stent rotated by 90° between the two faces.

Top: Matrix stent.

Bottom: Orsiro stent.

Flow from left to right, Re = 68 (equivalent to blood flow with 1 Pa wall shear stress). Representative images are mid-stent length and the plane of focus on the bottom of the vessel.
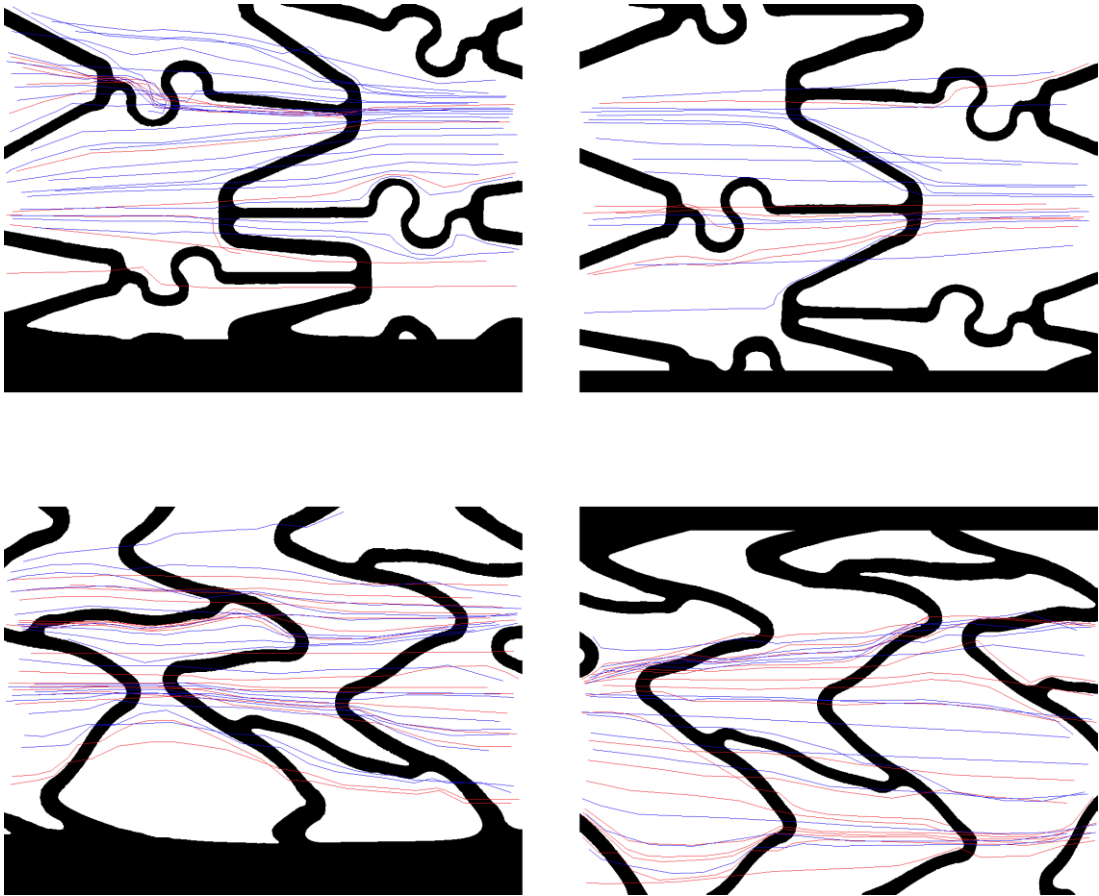
Figure 4.6 Tracked particle streamlines in Penchant and Pro Kinetic Energy coronary stents

Particles were tracked moving through coronary stents deployed within 2.5 mm diameter vessels. Tracking was performed for two 30-second long sequences (red and blue tracks) on two stent faces, with the stent rotated by 90° between the two faces.

Top: Penchant stent.

Bottom: Pro Kinetic Energy stent.

Flow from left to right, Re = 68 (equivalent to blood flow with 1 Pa wall shear stress). Representative images are mid-stent length and the plane of focus on the bottom of the vessel.
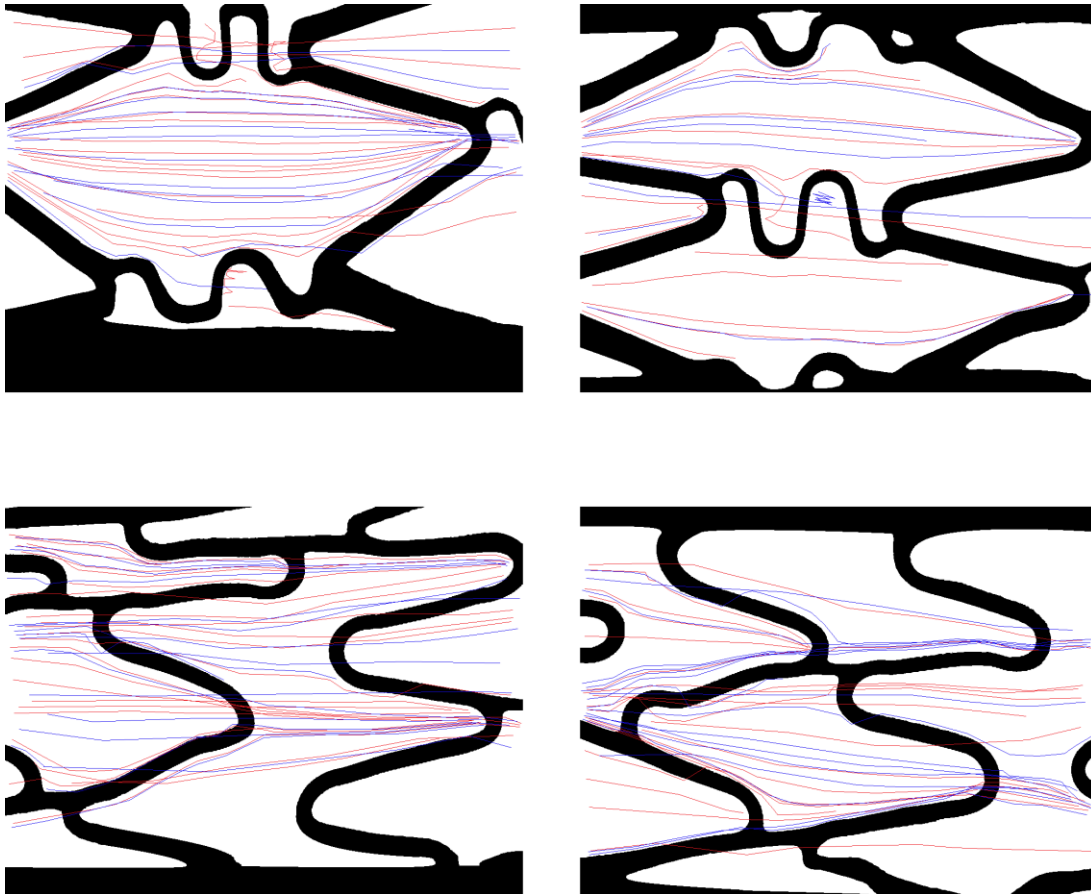
Figure 4.7 Tracked particle streamlines in Velocity and XTRM-Track coronary stents

Particles were tracked moving through coronary stents deployed within 2.5 mm diameter vessels. Tracking was performed for two 30-second long sequences (red and blue tracks) on two stent faces, with the stent rotated by 90° between the two faces.

Top: Velocity stent.

Bottom: XTRM-Track stent.

Flow from left to right, Re = 68 (equivalent to blood flow with 1 Pa wall shear stress). Representative images are mid-stent length and the plane of focus on the bottom of the vessel.
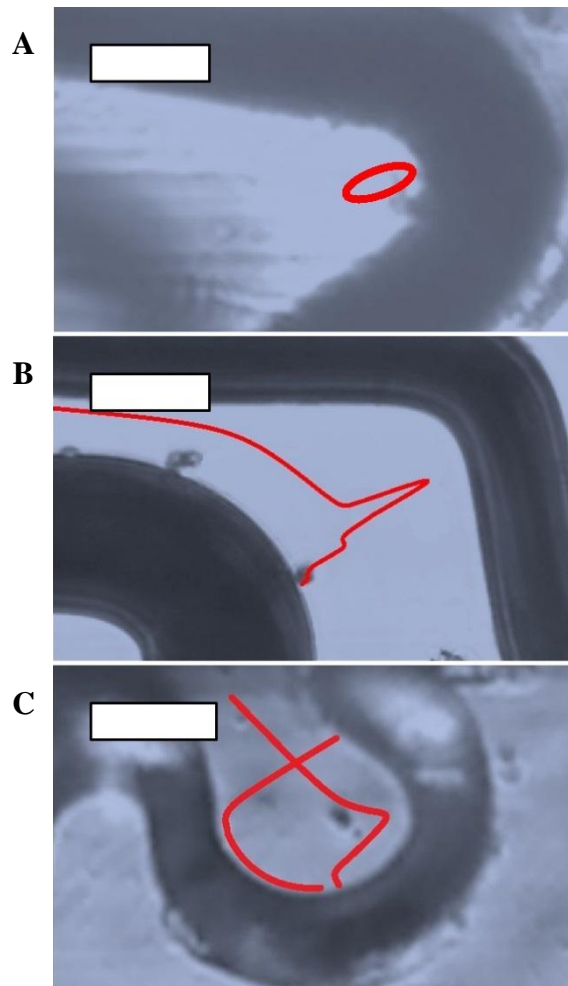
Figure 4.8 Complex flow within coronary stent geometry

Particle tracking revealed areas of complex flow patterns local to struts within coronary stent geometry.

A: Recirculation seen within a valley structure of a Coroflex Blue stent.

B: Flow reversal seen between Coroflex Blue main ring and bridge struts.

C: Flow reversal and recirculation seen within a bridge strut of a BiodivYsio OC stent.

Flow from left to right, Re = 68 (equivalent to blood flow with 1 Pa wall shear stress).

Scale bar: 100 μm.

Figure 4.9 Particle track orientation in coronary stents

The orientation of tracked particle streamlines moving through coronary stents deployed within 2.5 mm diameter vessels was measured to quantify the impact of stent design on the direction of flow and, therefore, the direction of mechanical cues cells would be exposed to. The length of tracks at an angle greater than ±5° of the direction of flow (0°) is shown as a percentage of the total length of tracks within each stent. This threshold was applied to ensure that stent-induced flow deviation was captured while minor deviations, due to equipment disturbance or manual tracking errors, were omitted. As there is variation in stent geometry and strut orientation, so too is there variation in particle track orientation between the various commercially available stents.

Figure 4.10 shows the percentage of tracks deviating from ±5° flow direction varying with the angle of stent struts, and strut thickness. There is no clear relationship between either. For example, the greatest deviation was seen in the Velocity, Coroflex Blue Neo, and XTRM-Track stents, with over 50% of tracked particles deviating from ±5° flow direction in each. However, these three stents represent the full range of mode strut angles (40, 30 and 10° respectively). In addition, the Velocity had the thickest struts (130 μm), whereas the Coroflex Blue Neo had the thinnest (60 μm). After investigating averaged orientation, the percentage of tracks deviating from ±5° of flow for separate faces of each stent was assessed (Figure 4.11), with the stents rotated by 90° between faces. Stent geometry repeats circumferentially, yet each face presents a different alignment of this repeating pattern. As such, while differences in track orientation between faces were present, they were ≤10% for all stents except the Coroflex Blue Neo.

4.2.2   Coronary stent geometry influenced tracked particle density

Controlling for stent length, the total number of particles tracked in Section 4.2.1 varied between 32 per field of view (BiodivYsio OC and Penchant stents) and 95 per field of view (Matrix stent). Figures 4.12 – 4.16 show the distribution of moving particles, displaying track paths and the frequency of particles moving along each one as a percentage of the total. All coronary stents showed wide areas of zero or low frequency as particles tended to follow common streamlines and were funnelled or concentrated by the peak and valley structure. Similar patterns were observed on both faces of each stent and between models of identical geometry, with the exception of slightly higher particle concentration in the Pro Kinetic Energy stent compared to the Orsiro.

The degree to which different stents funnelled particles is shown in Figure 4.17. Areas of zero frequency increased with stent length. Rather than an effect of the stents themselves, this was simply due to the number of tracked particles decreasing over the time taken to record longer stents. As such, the shortest example was identified (the Velocity stent, with 72 columns in the 100 μm grid) and in obtaining the data for Figure 4.17 the remaining stents were only considered up to that same point, equating both length and time under flow.
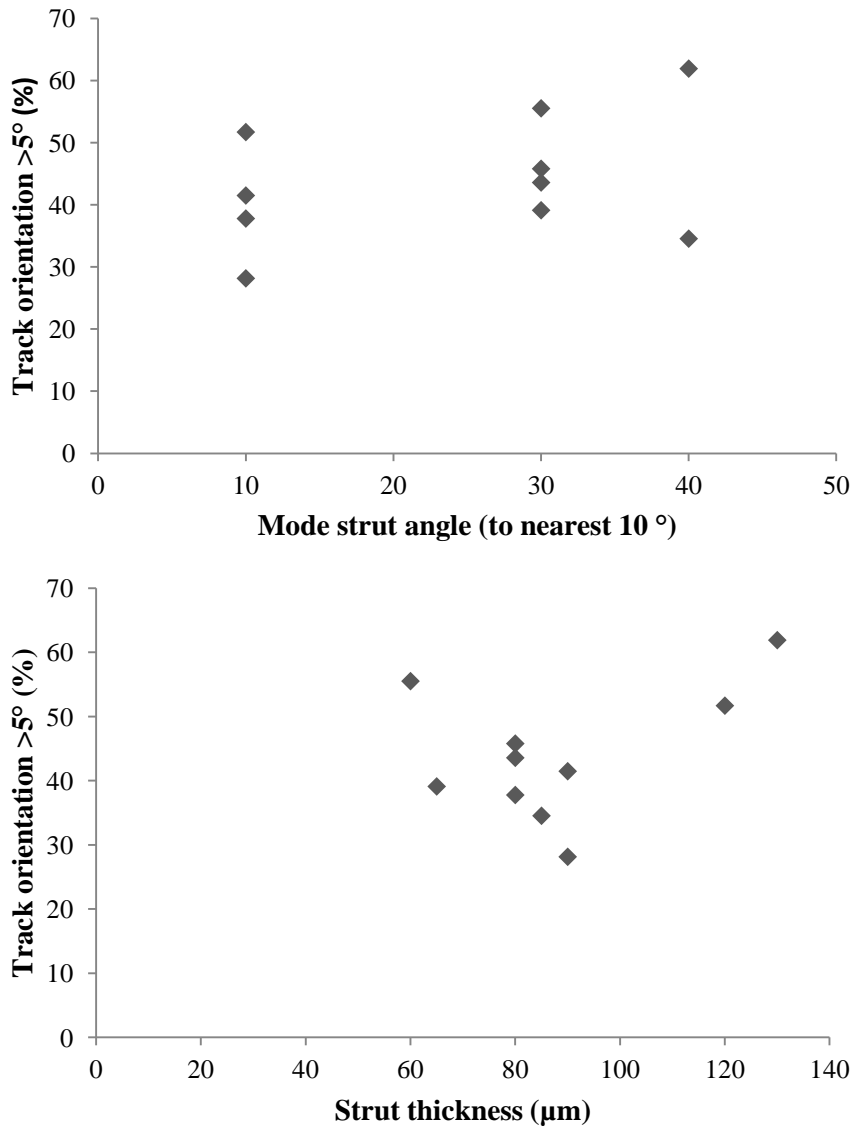
Figure 4.10 Particle track orientation and coronary stent geometry

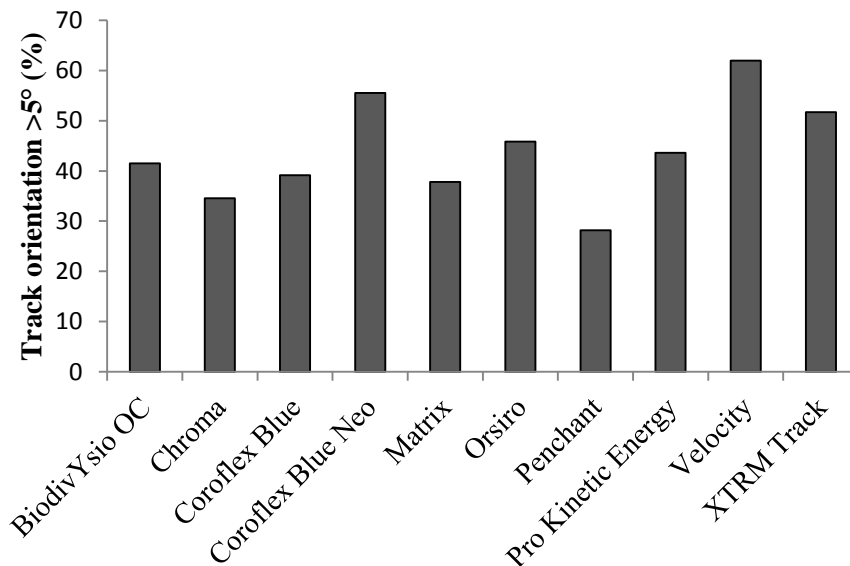The orientation of tracked particle streamlines moving through coronary stents deployed within 2.5 mm diameter vessels was measured to quantify the impact of stent design on the direction of flow and, therefore, the direction of mechanical cues cells would be exposed to. The length of tracks at an angle greater than $\pm 5°$ of the direction of flow ($0°$), as a percentage of the total length of tracks within each stent, is shown against stent geometry. There is no clear relationship between stent strut angle or strut thickness and the deviation of flow.

Top: Track orientation and the mode angle of coronary stent struts relative to flow.

Bottom: Track orientation and coronary stent strut thickness.
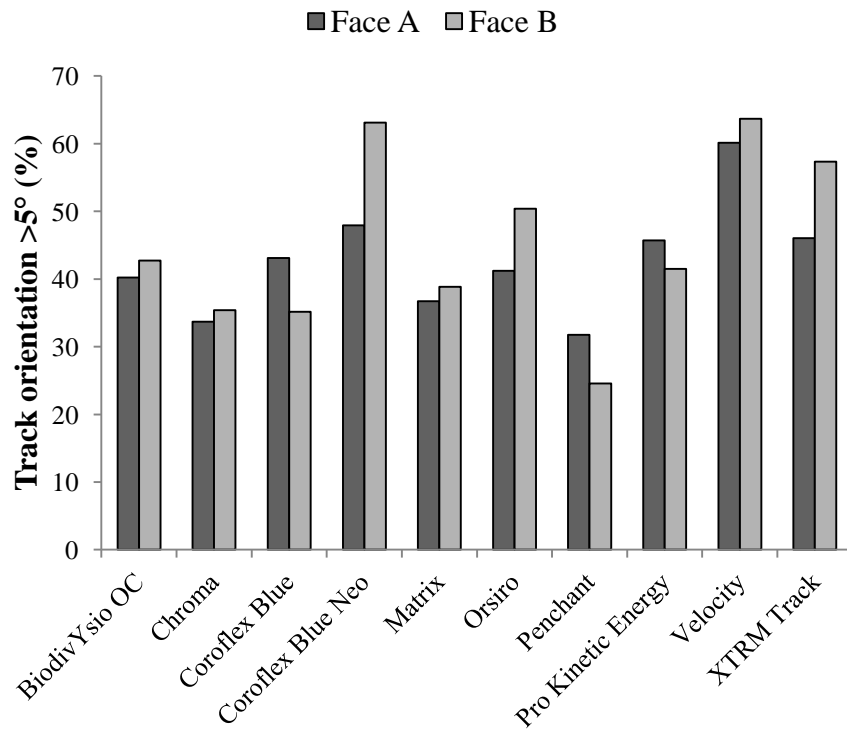
Figure 4.11 Differences in streamline orientation between coronary stent faces

The orientation of tracked particle streamlines moving through coronary stents deployed within 2.5 mm diameter vessels was measured. The length of tracks at an angle greater than $\pm 5°$ of the direction of flow (0°) is shown as a percentage of the total length of tracks within each stent. Tracking was performed on two stent faces, A and B, with the stent rotated by 90° in between the two. The difference in track orientation between faces was $\leq 10\%$ for all stents bar the Coroflex Blue Neo, implying consistency in the effect of specific stent design which repeats circumferentially.

0   **85 %**
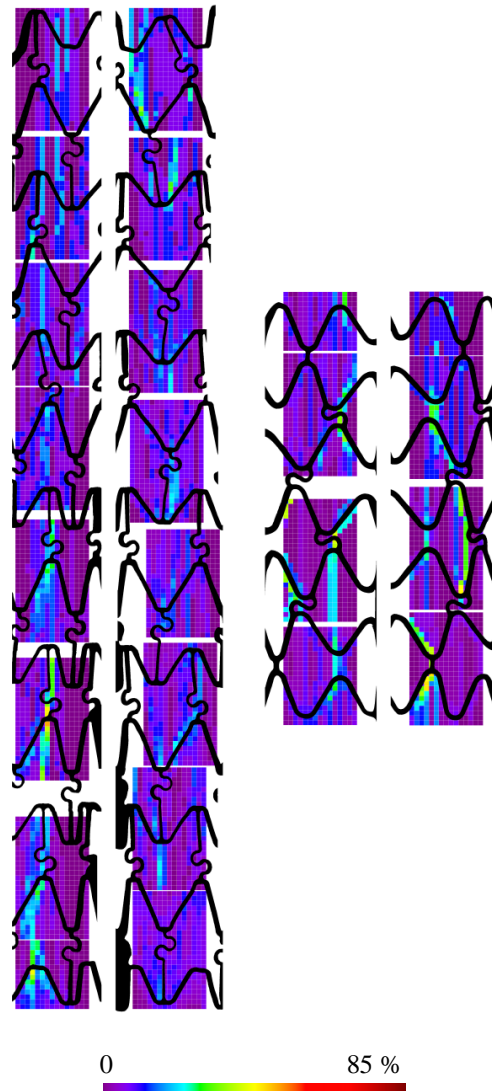
Figure 4.12 Tracked particle density heat maps in BiodivYsio OC and Chroma coronary stents

Particles were tracked moving through coronary stents deployed within 2.5 mm diameter vessels. The position of streamlines and the frequency of particles tracked moving along them was measured in relation to a 100 μm square grid and presented as a percentage of the total number of particles seen in each grid.

Left: BiodivYsio OC stent.

Right: Chroma stent.

Flow from bottom to top, Re = 68 (equivalent to blood flow with 1 Pa wall shear stress). The plane of focus is on the bottom of the vessel.
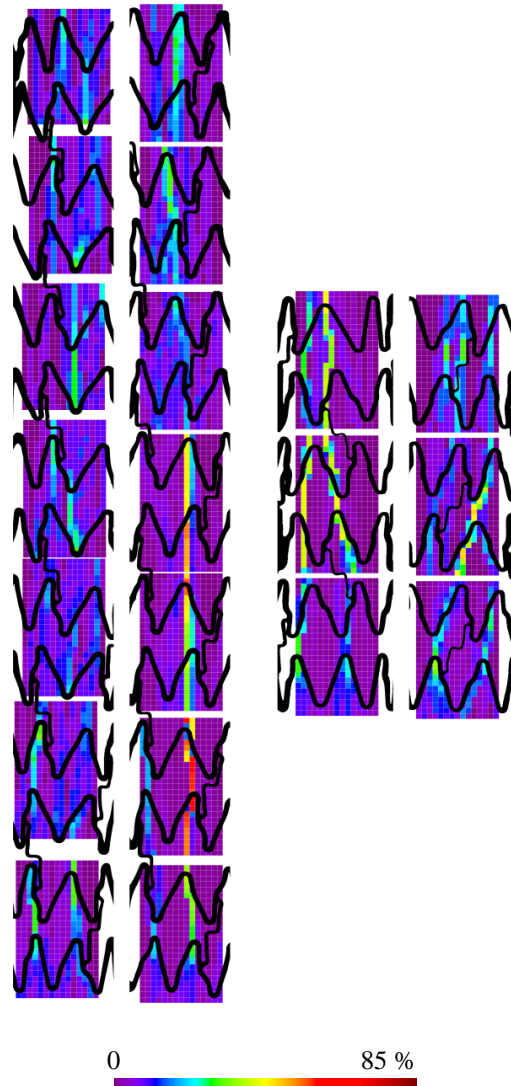
Figure 4.13 Tracked particle density heat maps in Coroflex Blue and Coroflex Blue Neo coronary stents

Particles were tracked moving through coronary stents deployed within 2.5 mm diameter vessels. The position of streamlines and the frequency of particles tracked moving along them was measured in relation to a 100 μm square grid and presented as a percentage of the total number of particles seen in each grid.

Left: Coroflex Blue stent.

Right: Coroflex Blue Neo stent.

Flow from bottom to top, Re = 68 (equivalent to blood flow with 1 Pa wall shear stress). The plane of focus is on the bottom of the vessel.
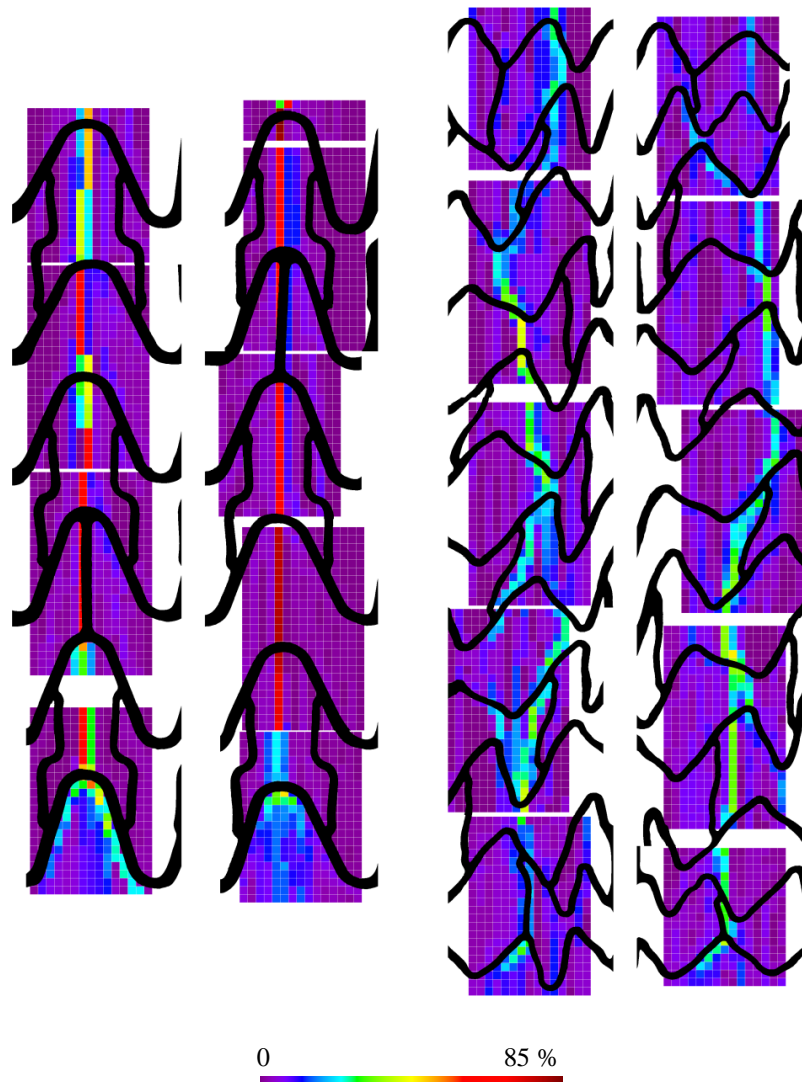
Figure 4.14 Tracked particle density heat maps in Matrix and Orsiro coronary stents

Particles were tracked moving through coronary stents deployed within 2.5 mm diameter vessels. The position of streamlines and the frequency of particles tracked moving along them was measured in relation to a 100 μm square grid and presented as a percentage of the total number of particles seen in each grid.

Left: Matrix stent.

Right: Orsiro stent.

Flow from bottom to top, Re = 68 (equivalent to blood flow with 1 Pa wall shear stress). The plane of focus is on the bottom of the vessel.

0   85 %
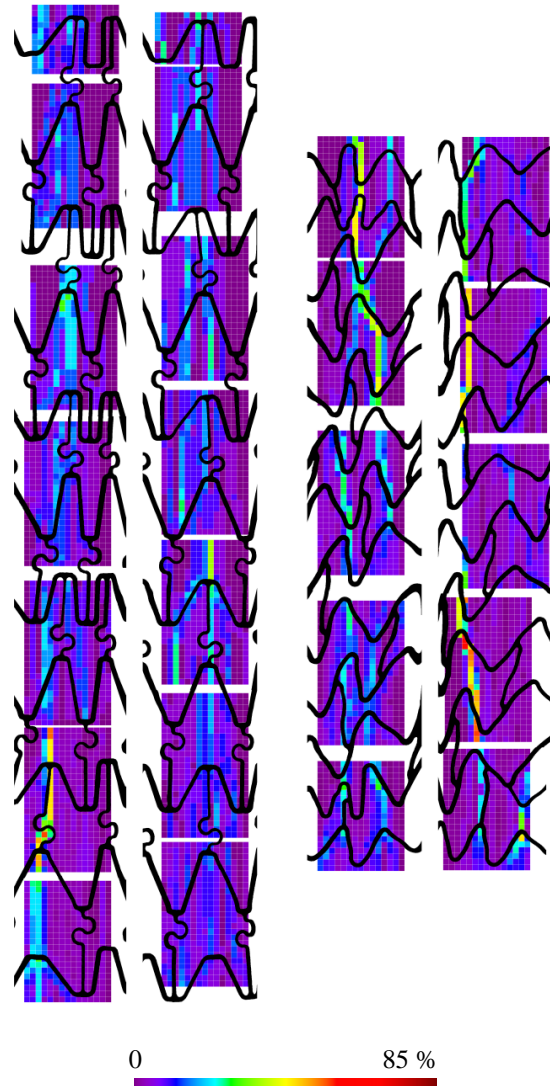
Figure 4.15 Tracked particle density heat maps in Penchant and Pro Kinetic Energy coronary stents

Particles were tracked moving through coronary stents deployed within 2.5 mm diameter vessels. The position of streamlines and the frequency of particles tracked moving along them was measured in relation to a 100 μm square grid and presented as a percentage of the total number of particles seen in each grid.

Left: Penchant stent.

Right: Pro Kinetic Energy stent.

Flow from bottom to top, Re = 68 (equivalent to blood flow with 1 Pa wall shear stress). The plane of focus is on the bottom of the vessel.
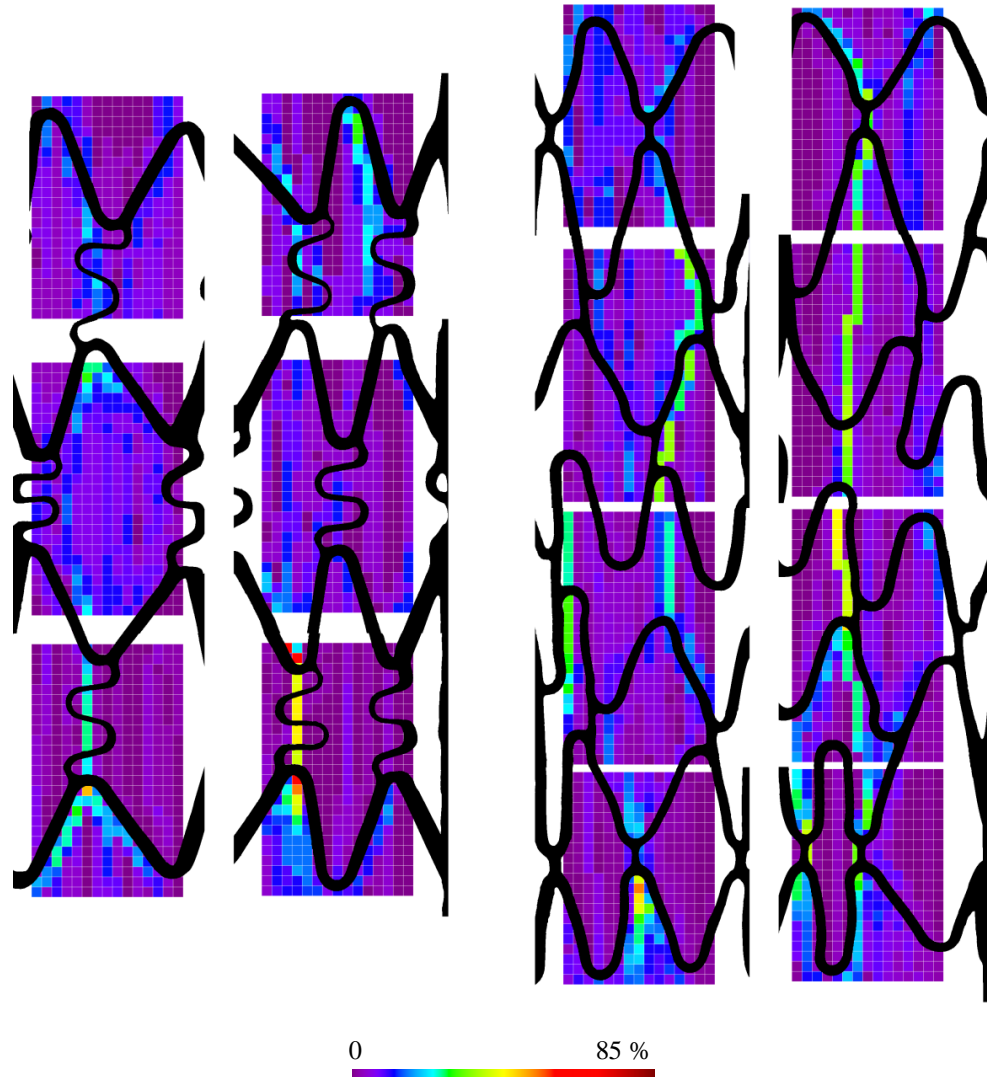
Figure 4.16 Tracked particle density heat maps in Velocity and XTRM-Track coronary stents

Particles were tracked moving through coronary stents deployed within 2.5 mm diameter vessels. The position of streamlines and the frequency of particles tracked moving along them was measured in relation to a 100 μm square grid and presented as a percentage of the total number of particles seen in each grid.

Left: Velocity stent.

Right: XTRM-Track stent.

Flow from bottom to top, Re = 68 (equivalent to blood flow with 1 Pa wall shear stress). The plane of focus is on the bottom of the vessel.
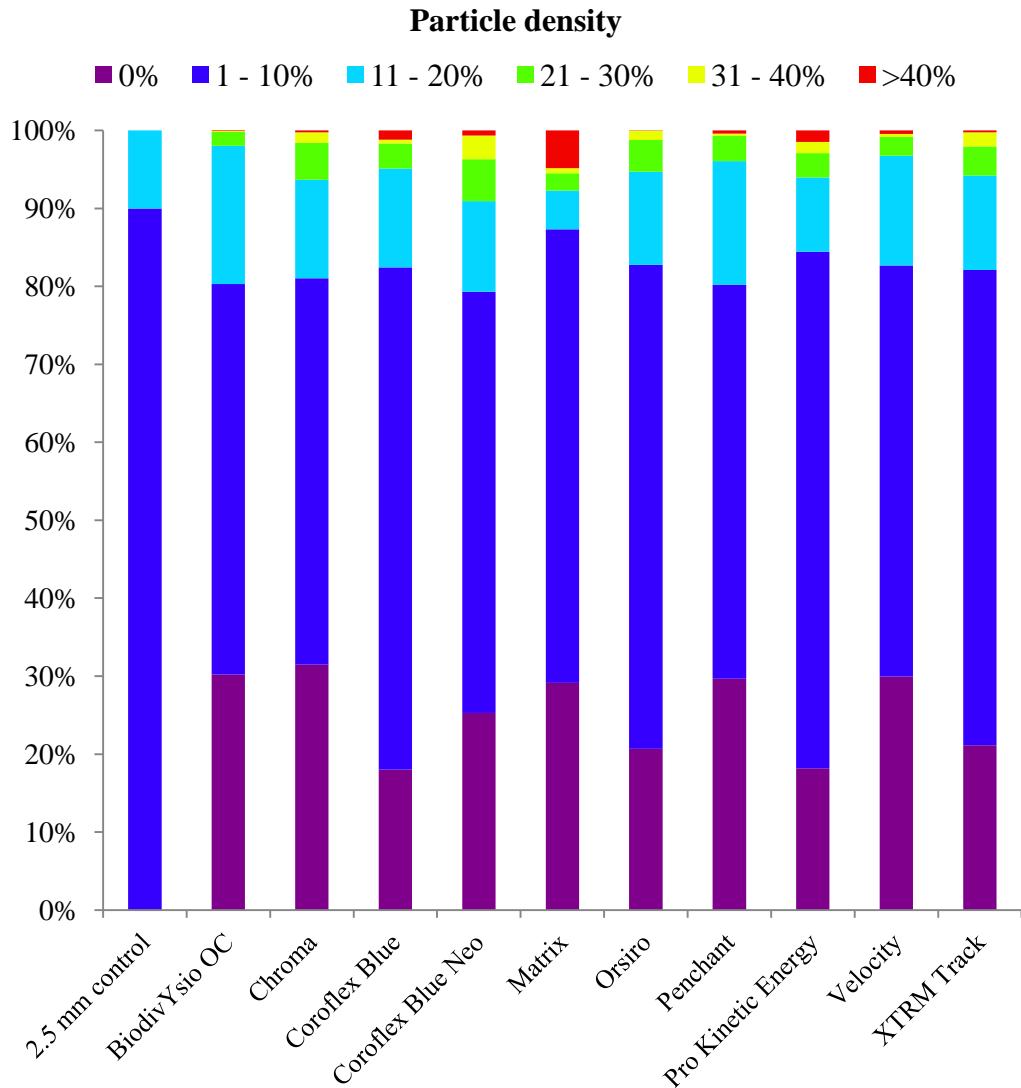
Particle density

Figure 4.17 Streamline and particle density in coronary stents

Particles were tracked moving through coronary stents deployed within 2.5 mm diameter vessels. The position of streamlines and the frequency of particles tracked moving along them was measured in relation to a 100 μm square grid, as a percentage of the total number of particles seen in each grid.

Here, the concentration of particles within each grid square is presented as a percentage of the total number of squares. As there is variation in stent geometry, strut orientation and thickness, so too is there variation in particle distribution and concentration between different commercially available coronary stent designs.

4.2.3 Particle accumulation increased and varied in coronary stents

Once flow was arrested following the acquisition of tracking data in Section 4.2.1 accumulated particles were counted in 1 mm segments along the length of stents, and 2 mm up and downstream of their leading and trailing edges. Controlling for length, the number of attached particles within stented models ranged from 6 per mm (comparable to empty control tubes, seen in Section 3.4.3) to more than six times that amount (Figure 4.18). However, accumulation per segment varied greatly along each stent. There were no clear trends for change in accumulation at stent leading edge, or as length progressed.

The differences in accumulation between stents could not be proved to be an effect of differing geometry, as there was no similarity between stent models of identical design. In fact, there was great variation in the measured accumulation between repeats within the same model vessel, in terms of both absolute particle number and distribution along length. Models were rotated by 90° in between each experiment, but had rotational symmetry. Stent geometry did not appear to have an impact on specific sites of particle accumulation within each segment, as there was no correlation between particle and strut locations, with two exceptions – the Chroma and Matrix stents – in which particles almost exclusively settled immediately up or downstream of struts (Figure 4.19).

4.3 Computational modelling

Casts of vessels containing each coronary stent design were made and struts prised away from the wall. This successfully preserved fine detail, including areas of complex geometry and prolapsed struts (previously illustrated in Figure 3.24).

Due to the wide range of stent lengths, μCT scan resolution varied between casts in order to balance image resolution and quality against time and field of view. Three coronary stents were modelled: the Coroflex Blue, Matrix, and Pro Kinetic Energy. These stents were selected as they were all of similar length. They were therefore scanned at similar resolutions (10 μm ±2 μm) and the same parameters as discussed in Section 3.5.6 could be applied. In addition, successful *in vitro* experiments were performed on each, allowing comparison to EC behaviour.
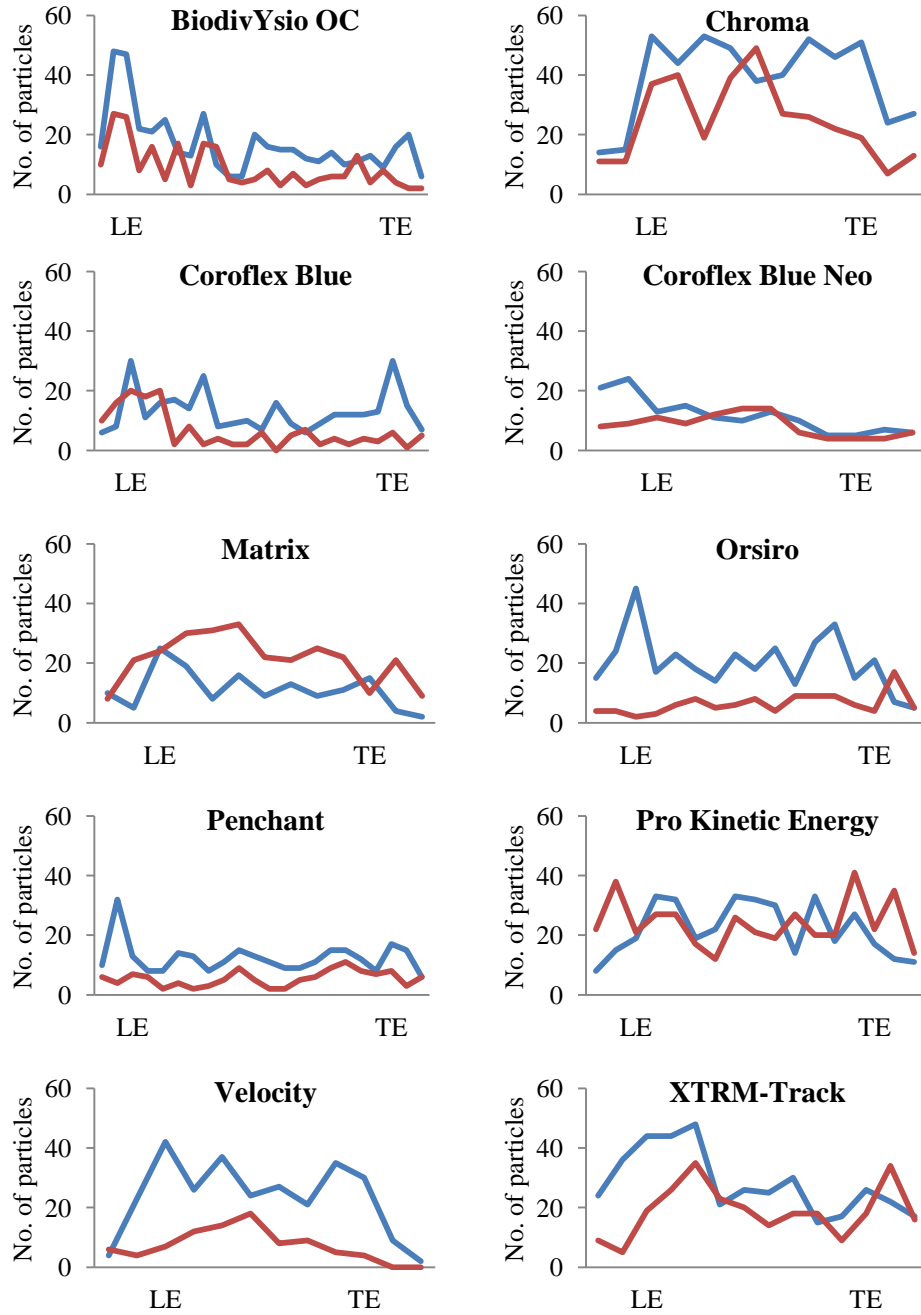
Figure 4.18 Particle accumulation in 2.5 mm diameter stented vessels

After 20 minutes under flow the number of accumulated particles within coronary stents deployed in 2.5 mm diameter vessels was assessed. Particles were counted through each stent, and 2 mm up and downstream of its leading edge (LE) and trailing edge (TE). This was performed twice (red and blue lines) on two stent faces, with the stent rotated by 90° in between the two. There were no trends for change in at stent LE, or as length progressed.
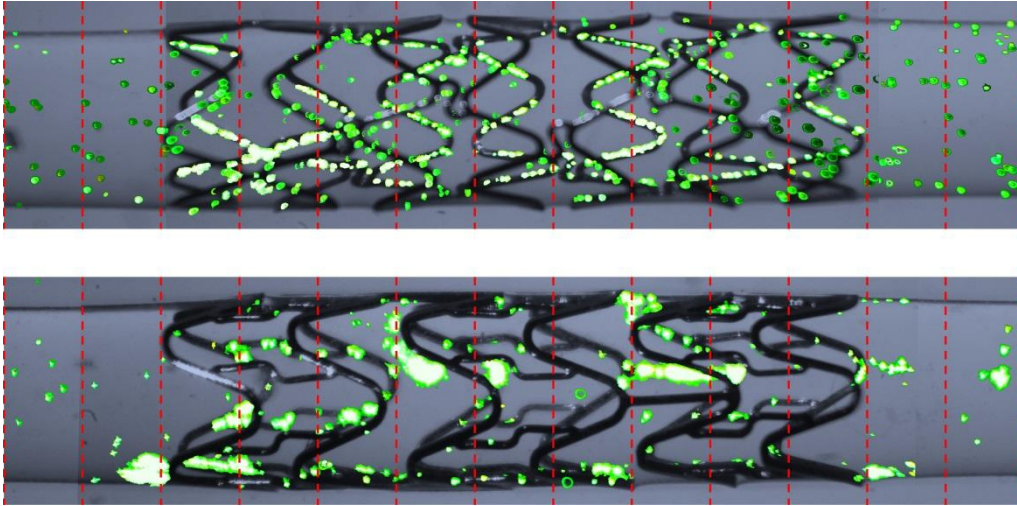
Figure 4.19 Locations of particle accumulation within coronary stents

After 20 minutes under flow, accumulated particles (green) within coronary stents deployed in 2.5 mm diameter vessels were imaged and counted within 1 mm segments (red lines). No pattern in the location or distribution of particles throughout each model was seen, with the exception of the Chroma and Matrix coronary stents shown here, in which accumulation was almost exclusively seen immediately up or downstream of struts.

Top: Chroma stent.

Bottom: Matrix stent.

4.3.1 Wall shear stress is heterogeneous within coronary stents

A UDF simulating fully developed flow was applied in each model, with sufficient velocity to generate 1 Pa average wall shear stress in a 2.5 mm diameter vessel. The presence of coronary stents greatly altered the pattern of wall shear stress distribution and magnitude. Quantitative measures of the area-weighted average wall shear stress (AWA-WSS) were skewed by high shear forces on the luminal surface of prolapsed struts (Figure 4.20A). In this example, struts penetrating the lumen contributed to an AWA-WSS of 1.71 Pa in the Coroflex Blue, compared to the Pro Kinetic Energy (0.43 Pa) and Matrix (0.72 Pa). However, shear stress on the wall below these protruding struts was reduced to as low as 0.1 Pa (Figure 4.20B).

Displaying vectors showed that stents had little influence on velocity magnitude, but altered the direction of flow up and over struts and therefore reduced the longitudinal component of velocity (and thus also reduced wall shear stress) (Figure 4.21). All coronary stents displayed regions of wall shear stress magnitude <0.5 Pa. These regions were focal to bridges and areas where struts from adjacent rings were in close proximity, hindering downstream recovery of longitudinal velocity (Figure 4.21C). Immediately downstream of valleys in circumferential strut rings, shear stress was reduced to as low as 0.1 Pa.

Plotting shear stress along reference lines revealed the impact of stent struts due to this disturbed flow (Figure 4.22). Wall shear stress on their luminal surfaces was elevated even in the well apposed stent shown in this example. However, there were sharp decreases in shear stress immediately up and downstream of struts. In some instances, downstream wall shear stress could reach negative values, indicating flow reversal. Wall shear stress began to increase further downstream from struts as the longitudinal component of velocity began to recover. The degree of this recovery, and inter-strut shear stress magnitude, was gradually reduced by approximately 30% along stent length. Plotting a reference line over more complex geometry (Figure 4.22, blue line) showed that thinner bridge struts had little noticeable effect.
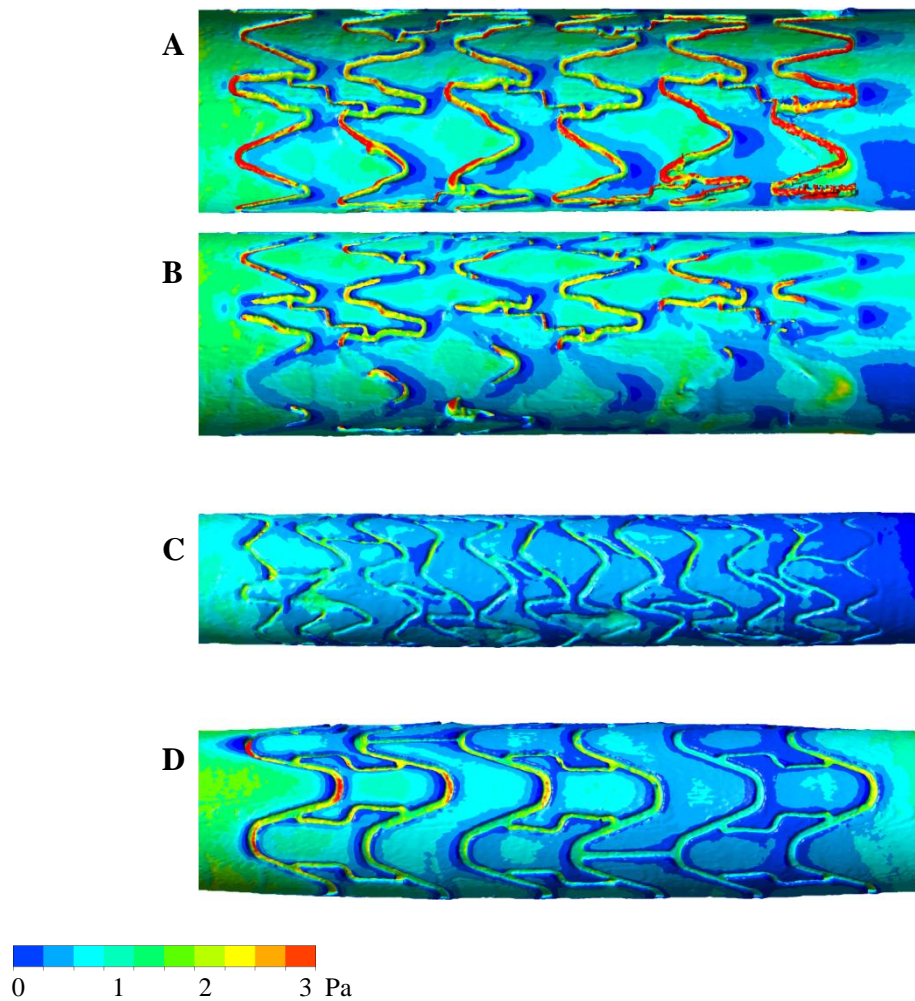
Figure 4.20 Wall shear stress within coronary stents

PDMS casts of coronary stents deployed within 2.5 mm diameter vessels were made and μCT scans taken. *In silico* models were reconstructed from this data and used for CFD analysis to plot wall shear stress along the vessel.

A: Coroflex Blue stent interior, showing elevated shear stress on prolapsed struts.

B: Coroflex Blue stent wall, showing reduced shear stress downstream of struts.

C: Pro Kinetic Energy stent wall, showing reduced shear stress downstream of struts.

D: Matrix stent wall, showing reduced shear stress downstream of struts.

Flow from left to right, 1 Pa average wall shear stress. Note: the maximum value of the scale bar is set to 3 Pa to better illustrate regions of low flow.
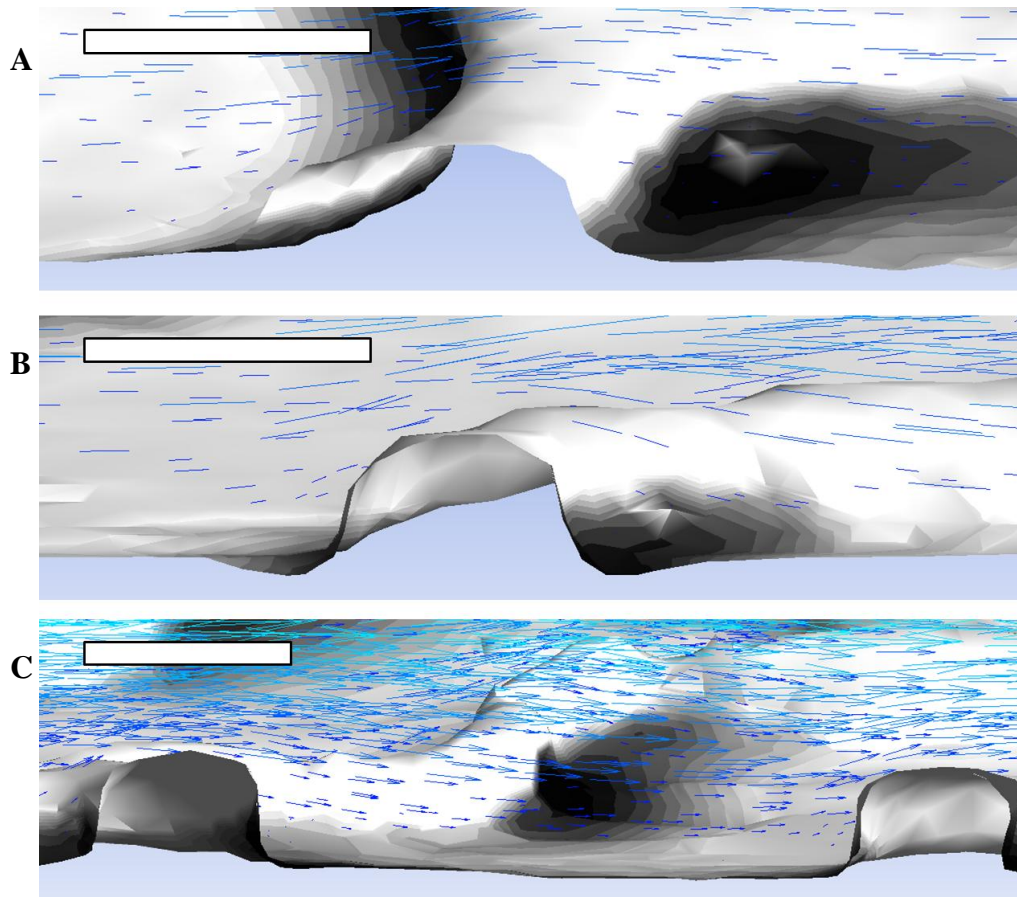
Figure 4.21 Velocity vectors around coronary stent struts

In silico models were reconstructed from coronary stent μCT data and used for CFD analysis. Vectors revealed that while stents had little effect on velocity magnitude they greatly impacted direction as flow moved up and over struts, leading to reduced wall shear stress in those regions.

A: Matrix stent strut.

B: Coroflex Blue stent strut.

C: Coroflex Blue stent, showing reduced flow at the flow in a region of close proximity between adjacent strut rings.

Flow from left to right, 1 Pa average wall shear stress.

Scale bar: 100 μm.

A

B

C
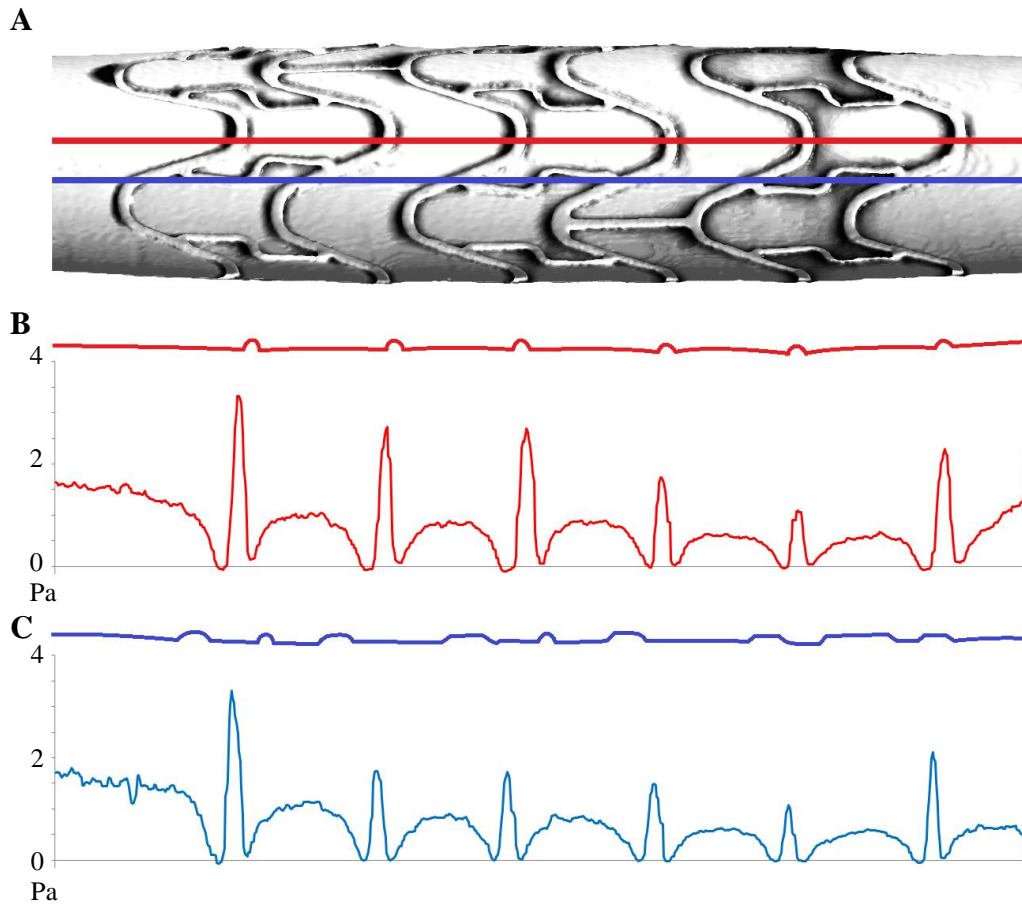
Figure 4.22 Wall shear stress along reference lines within a Matrix coronary stent

In silico models were reconstructed from coronary stent μCT data and used for CFD analysis. Plotting data along reference lines in the direction of flow revealed elevated wall shear stress on stent struts, greatly reduced shear stress immediately up and downstream of struts, and recovery of shear stress in inter-strut regions.

A: Matrix stent, with two reference lines (red and blue).

B: Wall geometry (top) and shear stress along the upper, red reference line.

C: Wall geometry (top) and shear stress along the lower, blue reference line.

Flow from left to right, 1 Pa average wall shear stress.

4.3.2 Wall shear stress variation reduced with increased fluid viscosity

Simulating the flow of a fluid with viscosity and density equal to that of blood resulted in an AWA-WSS decrease of 10% (to 0.79 Pa) within the Matrix stent, due to reduced wall shear stress on the first three struts (Figure 4.23, top).

Wall shear stress magnitude and distribution in between the first four struts were similar to the low viscosity model. However, as longitudinal distance increased this pattern remained constant and inter-strut shear stress was not continuously reduced as per the low viscosity model (Figure 4.23, bottom).

4.3.3 Wall shear stress increased with reduced µCT scan resolution

A second µCT scan of the Coroflex Blue cast was taken at 17.47 µm, almost half the resolution used to create the model in Section 4.4.1 (9.92 µm), and the same conditions were simulated. AWA-WSS decreased by 40% to 1.01 Pa, primarily due to reduced shear stress on the luminal surface of struts. The overall shape of wall shear stress distribution remained broadly similar, and low shear stress regions were again present adjacent to struts, but the width of these regions was reduced. As such, the area of wall exposed to <0.5 Pa was greatly reduced (Figure 4.24).
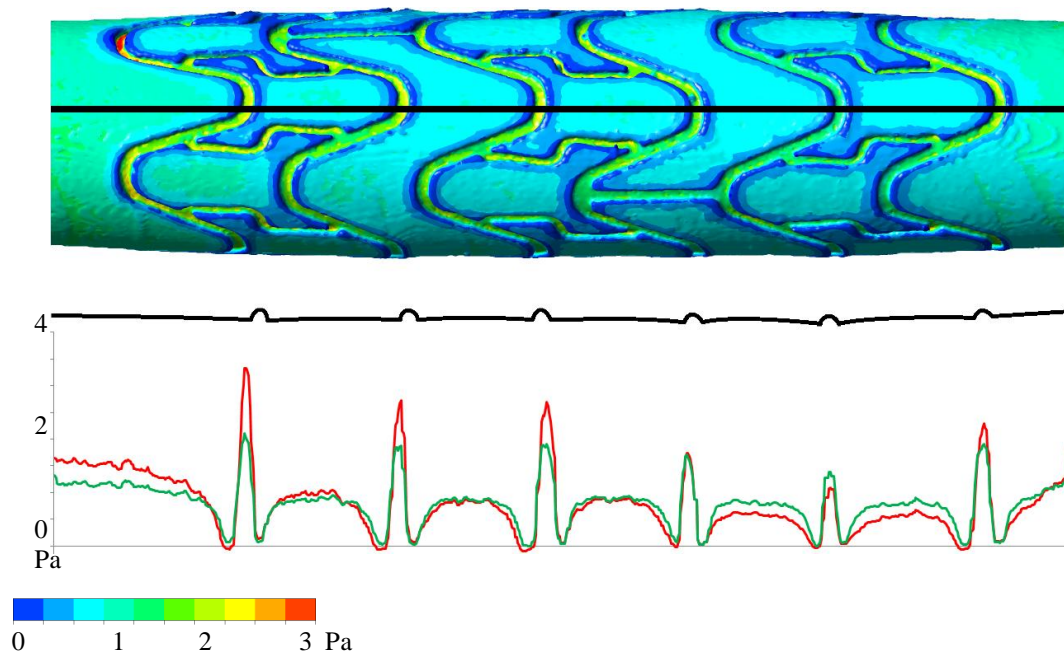
Figure 4.23 Wall shear stress within a Matrix coronary stent modelled with blood-equivalent viscosity

Wall shear stress resulting from the flow of a Newtonian liquid with the equivalent viscosity of blood (3.5 mPa.s) was plotted within an *in silico* model of a Matrix coronary stent.

Top: Wall shear stress magnitude along the length of the stent. Note: the maximum value of the scale bar is set to 3 Pa to better illustrate regions of low flow.

Bottom: Wall shear stress plotted along a reference line (black), as per Figure 4.22, shows that shear stress in the higher viscosity model (green line) is maintained in inter-strut regions in comparison to the standard viscosity model shown in the previous figure (red line).

Flow from left to right, 1 Pa average wall shear stress.
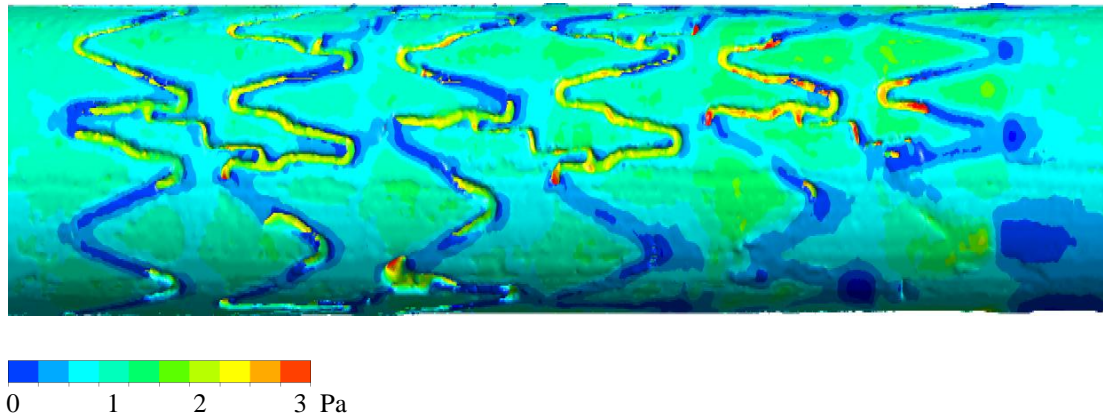
Figure 4.24 Wall shear stress within a Coroflex Blue coronary stent model of reduced resolution

A PDMS cast of a Coroflex Blue coronary stent deployed within a 2.5 mm diameter vessel was scanned via μCT at 50% of the resolution used in Figure 4.20. An *in silico* model was reconstructed from this data and used for CFD analysis to plot wall shear stress along the vessel. The reduced resolution model showed similar distribution, but reduced average shear stress magnitude, in comparison to the full-resolution model.

Flow from left to right, 1 Pa average wall shear stress. Note: the maximum value of the scale bar is set to 3 Pa to better illustrate regions of low flow.

4.4 Cell migration

Cell migration studies were performed on coronary stents, connected to either the peristaltic pump or ibidi system, with flow rates set to induce an average wall shear stress of 1 Pa. Cell migration studies were performed for each of the available stent designs described in Section 4.1, with the exception of the Penchant and the Orsiro (their omission is discussed further in Section 4.5).

4.4.1 HUVEC migration was reduced in coronary stents

The minimum threshold of 24 hours under flow was met for all stent designs other than the Coroflex Blue Neo. However, due to the limited number of available stents and experiment success rates, the threshold was met by just one sample per design, with the exception of the Pro Kinetic Energy (n = 3).

In addition, in four of these stents (BiodivYsio OC, Coroflex Blue, Velocity, XTRM-Track) and one of the Pro Kinetic Energy samples, the cell monolayer did not reach the stent leading edge. The migration distance and rate of monolayers within the empty vessel upstream of each stent was measured and found to be comparable to empty control models, whereas leader cell migration was reduced (Figure 4.25).

In the Chroma, Matrix and remaining Pro Kinetic Energy stents, the monolayer was seen migrating in the direction of flow but was arrested at the stent leading edge (Figure 4.26). In each instance, a small number of cells migrated downstream of this leading strut, with greater cell numbers and maximum migration distance beyond the first strut observed within the Matrix stent. Final migration distance and rate was dependent on the proximity of the cells' initial position to the stent (Figure 4.27).
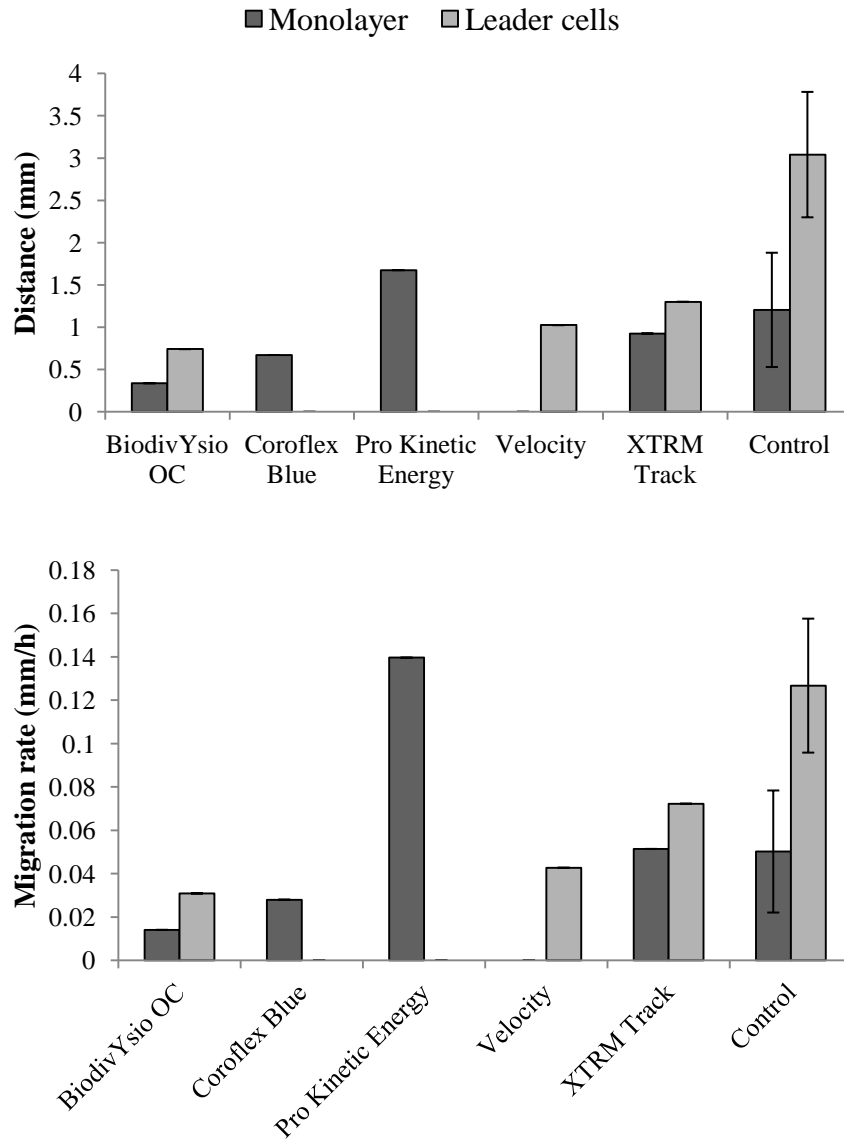
Figure 4.25 Cell migration distances and rates in empty regions of stented 2.5 mm diameter vessels

In several experiments HUVEC, seeded within 2.5 mm diameter model vessels with deployed stents, survived the minimum 24 hours under 1 Pa flow but, due to poor stent placement, were unable to reach the first struts. Migration within the empty section of the vessel was measured and compared to that of an empty 2.5 mm diameter control vessel. Unlike the repeated empty control examples, there was variation in migration distance and rates, and the participation of cell monolayers or individual leader cells.

Control: mean with SD (n=3). All coronary stents: (n=1).
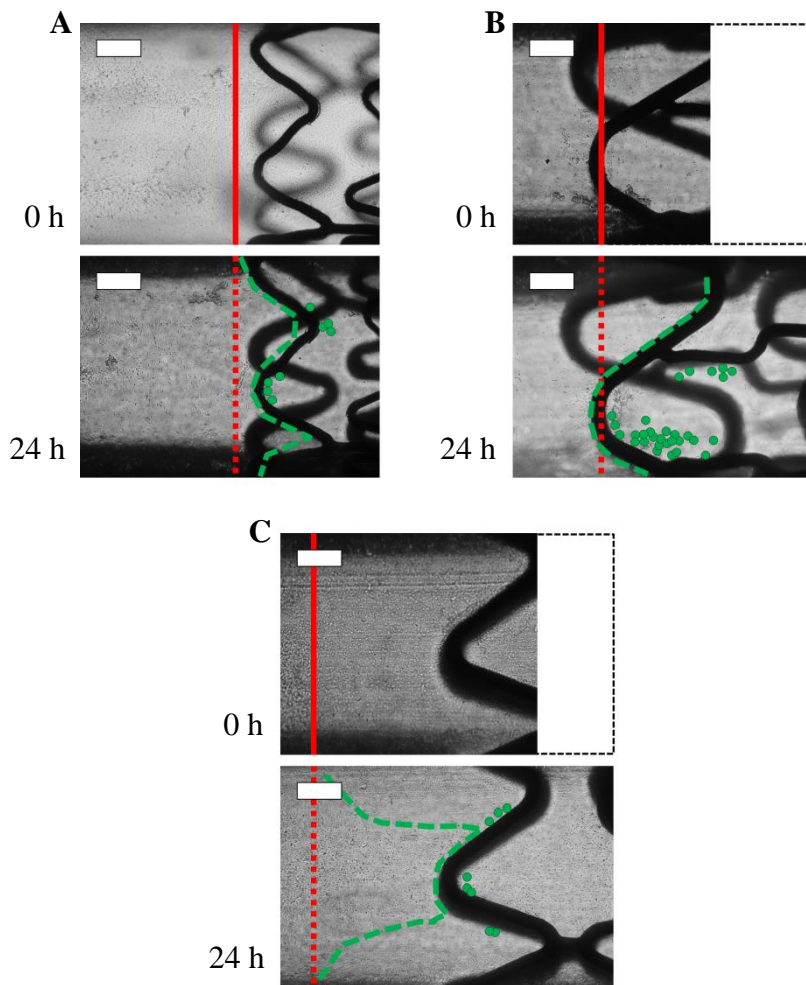
Figure 4.26 Cell migration in 2.5 mm diameter stented vessels

The migration of HUVEC monolayers (green line) and leader cells (green dots) beyond an initial seeding point (red line) was observed in the direction of flow within 24 hours. Monolayer migration was arrested upon meeting the leading edge of the stent. Small numbers of leader cells crossed the first strut, but further migration was reduced.

A: Pro Kinetic Energy stent (n=2, representative image from one experiment shown here)

B: Matrix stent (n=1)

C: Chroma stent (n=1)

Flow from left to right, 1 Pa average wall shear stress.

Scale bar: 0.5 mm.
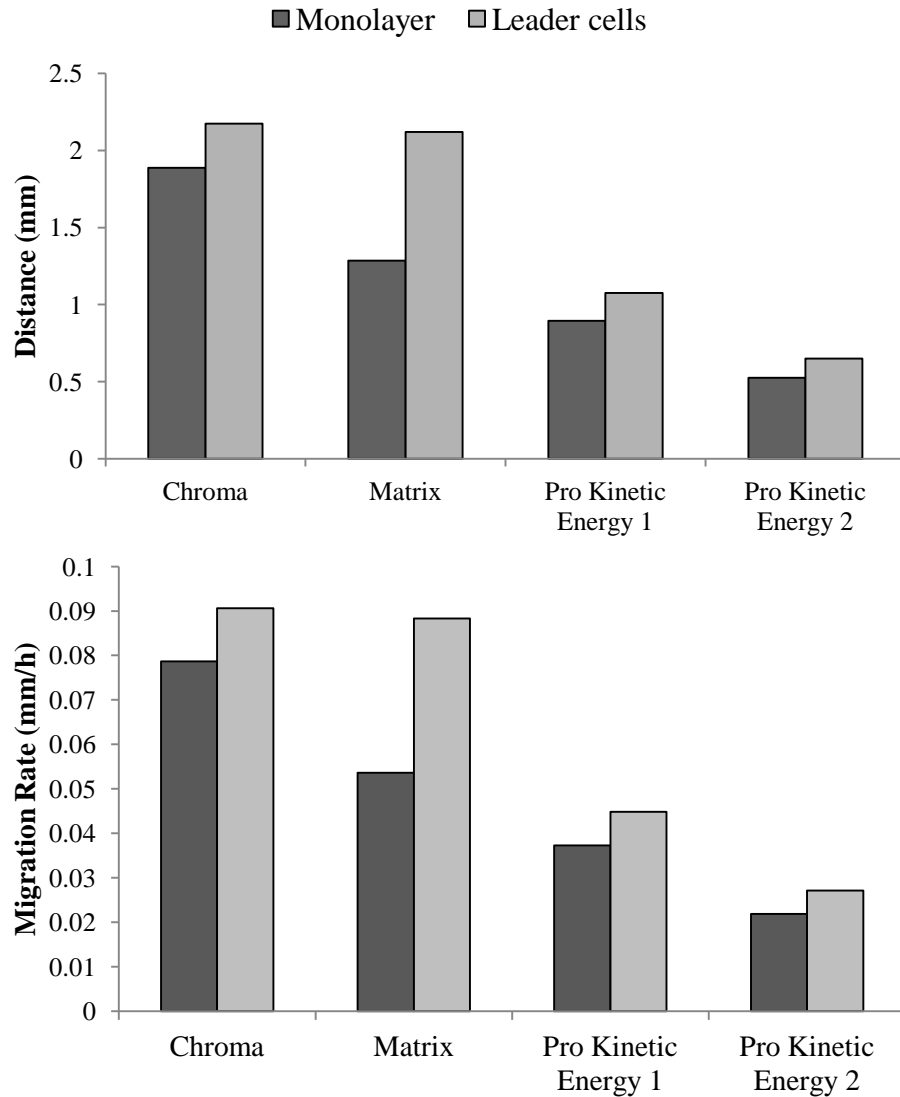
Figure 4.27 Cell migration distance and rate in 2.5 mm diameter stented vessels

The distance and rate of HUVEC migration within stented 2.5 mm diameter vessels under 1 Pa flow was measured. Cells monolayers began upstream of deployed coronary stents and met their leading edges within 24 hours, at which point migration was arrested (monolayer migration distance is therefore a measure of initial distance between the monolayer and stent). The migration of individual leader cells over the first stent struts can be inferred by their increased distance. Within the free space between initial cell positions and stent leading edge, monolayer migration was comparable to that in empty control vessels.

Chroma and Matrix: (n=1). Pro Kinetic Energy: (n=2, plotted here as separate bars).

4.4.2   EC coverage was enhanced in the presence of a ROCK inhibitor

The ibidi pump system was used to study the Coroflex Blue stent alone, as this was the only available design with the correct nominal diameter for deployment within the 1.5 mm models. As per the tests with empty vessels (Section 3.3.2), experiments were performed using standard EC growth medium and medium supplemented with 2 µM Y27632 as a ROCK inhibitor. For both conditions the minimum threshold of 24 hours under flow was met for n = 3, with experiments lasting a total of 48 hours.

Due to difficulties in seeding HUVEC and deploying stents in smaller vessels, well defined cell layer boundaries ahead of stent leading edges could not be attained in 1.5 mm diameter vessels. This meant that migration distance could not be assessed by measuring the changing position of a monolayer or leader cells against the empty wall, as described in Section 2.2.6.   Therefore down-stent cell migration was assessed by counting the number of cells present in stent sections as time progressed, and comparing cell numbers to those found at t = 0 (Figures 4.28 and 4.29). Each inter-strut region was considered separately and an area upstream of the first strut was included as a control.

A small change in cell coverage (0.9%) was seen in all regions after 24 hours of standard EC medium flow. After 48 hours, this rate remained the same upstream of the first strut and downstream of the second strut, but increased to 1.4% downstream of the first strut.

The presence of a ROCK inhibitor significantly increased endothelialisation downstream of the first strut after 24 hours and downstream of both the first and second struts after 48 hours. Furthermore, a very small number of cells was seen downstream of the third strut, again increasing over time (not visible in Figure 4.28). In addition, areas where struts on adjacent rings were in close proximity, seen to remain bare when standard EC growth medium was used, were gradually endothelialised in the presence of a ROCK inhibitor (Figure 4.30).
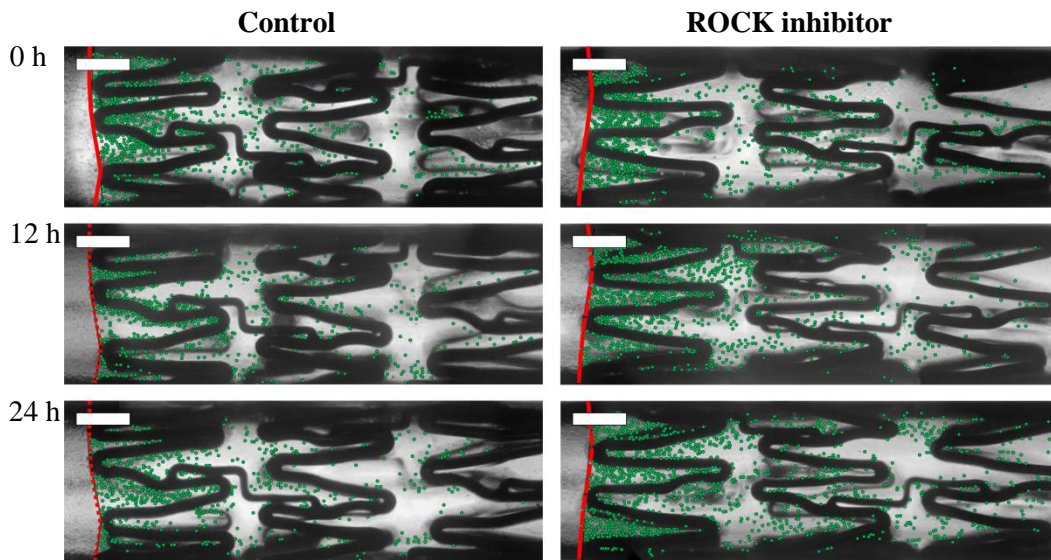
Figure 4.28 Cell migration in 1.5 mm diameter stented vessels

Coronary stents were deployed over HUVEC (green dots) seeded within 1.5 mm diameter model vessels. HUVEC were identified and counted within the stent over time, in three distinct regions: upstream of the stent (between the red line and the first struts), between the first and second struts, and between the second and third struts.

Left: Coroflex Blue stent, with standard EC growth medium.

Right: Coroflex Blue stent, with standard EC medium supplemented with + 2μM Y27632 ROCK inhibitor.

Flow from left to right, 1 Pa average wall shear stress.

Scale bar: 0.5 mm.

(n=3, representative images from one experiment shown here).
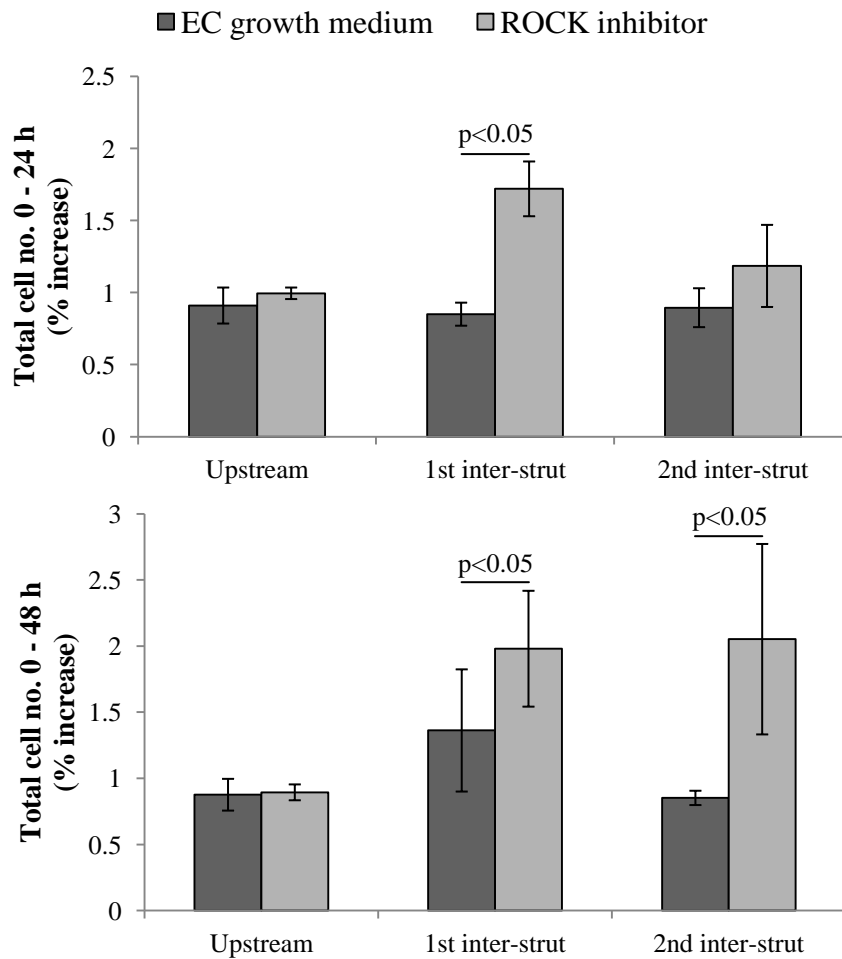
Figure 4.29 Cell numbers in distinct regions of coronary stent geometry

The number of HUVEC present in distinct regions of coronary stent geometry was counted over time under 1 Pa flow. At each time point the increase in the number of cells within each region was calculated, relative to the number present at t=0.

Top: After 24 hours cell numbers in all regions increased by approximately 0.9% when HUVEC were in standard EC growth medium, while the presence of a ROCK inhibitor significantly increased endothelialisation downstream of the first strut.

Bottom: After 48 hours cell numbers downstream of the first strut increased further in standard EC growth medium, while the ROCK inhibitor increased endothelialisation downstream of both the first and second struts.

Mean with SD (n=3), differences between means analysed via two-way ANOVA with Sidak post-hoc test.
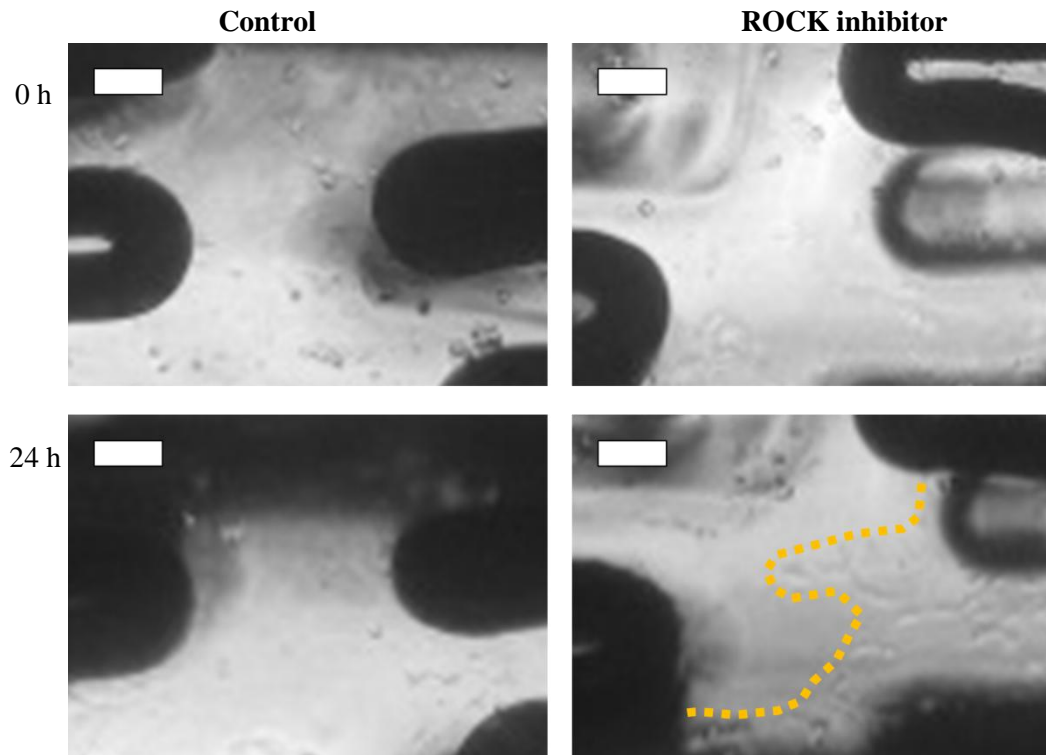
Figure 4.30 Cell migration local to stent struts

Coronary stents were deployed over HUVEC seeded within 1.5 mm diameter model vessels. Post-deployment, denuded areas of vessel wall which were local to stent geometry remained bare when HUVEC were in standard EC growth medium (left). Equivalent areas were gradually endothelialised when HUVEC were in the presence of a ROCK inhibitor (right, yellow line indicates boundary of cell layer).

Flow from left to right, 1 Pa average wall shear stress.

Scale bar: 100 μm.

(n=3, representative images from one experiment shown here).

4.5 Discussion

This chapter investigated the effect of coronary stent geometry on EC migration, local fluid flow and wall shear stress. Coronary stents of ten different designs, detailed in Section 4.1, were deployed in *in vitro* model vessels. All stents tested were of the 'slotted tube' variety, but the range of clinically available geometries was well represented [8][206][207]. Multiple examples of stents from the same manufacturer allowed comparisons between stents of identical geometry and between different iterations of the same general design. The length of available stents could not be controlled, which, for experiments with HUVEC, was not important as the shortest stents (8 mm) were longer than the greatest cell migration distance seen in previous studies (2.5 mm, over 96 hours [127]). However, in particle tracking and computational studies, length was expected to have an effect on flow and was controlled for as much as possible (Sections 4.2 and 4.3).

The extent to which the presence of coronary stents disturbs local fluid dynamics was revealed by tracking the motion of 10 μm particles through their structure. As shown in Figures 4.3 – 4.7, flow was clearly influenced by stent struts and differences in flow direction between stent designs were noted. The degree to which streamlines followed stent struts, were separated or funnelled by peaks and valleys in the stent ring structure (and the degree to which they remained concentrated or re-distributed once beyond each ring), and avoided or became trapped in areas of complex geometry, varied between stents of different design. The extent to which flow was disturbed was quantified as the percentage of streamlines at an angle greater than ±5° to flow. However, no relationship could be found between this and either stent strut size or orientation (Figure 4.10). It was also noted that the BiodivYsio OC and Penchant stents (with identical geometry), and Coroflex Blue and Coroflex Blue Neo stents (with almost identical geometry), produced very different results (Figure 4.9). 41% of streamlines within the BiodivYsio OC stent were outside ±5° to flow, compared to 28% in the Penchant stent. 39% of streamlines within the Coroflex Blue stent were outside ±5° to flow, compared to 56% in the Coroflex Blue Neo. This latter stent had the thinnest struts and therefore might have been expected to have the smallest impact on flow direction.

These results could be due to the fact that, when measuring their orientation, streamlines were not weighted for the frequency of particles travelling along them. For example, a stent may have a definite, noticeable effect on flow with a hundred particles following a single track at 45° to flow direction. If just one additional particle is seen to follow a different path (e.g. travelling with flow at 0°), this second track carries the same weight as the first. In this example, despite >99% of particles travelling at 45°, the percentage of streamlines at an angle greater than ±5° to flow would be just 50%. Therefore, while stents of identical geometry may be expected to produce identical particle tracking data, and there may indeed be a relationship between track orientation and strut size or orientation, this information could be lost in the noise created by every individual particle travelling on an independent path. The sensitivity of this approach could be improved with greater sample sizes. Accepting the limited sample size in this study, the available data could be improved by isolating individual paths, measuring the orientation of each separately and taking particle frequency into account when recombining the results. However, with a total of 5,300 tracks between the ten stent designs, this process would need to be automated, which proves difficult when taking account of streamlines which merge, overlap or cross.

The use of heat maps to display particle density goes some way to rectifying the issue described above (Section 4.2.2). Although orientation data was not preserved, the location of streamlines within the stents were noted and particle frequency taken into account to illustrate the density of particle flow through specific regions of 100 μm square grids. Here, there was good agreement in particle density between different faces of the same deployed stent and between different stents of similar or identical geometry. The impact of stent geometry, and variation between dissimilar designs, is displayed in Figures 4.12 – 4.16. The concentration of particles within each square of the grid, as a percentage of the total grid area, is shown in Figure 4.17. All coronary stents concentrated at least 40% of particles (the top concentration band highlighted in Figure 4.17) within 100 μm square sections at some locations, and the maximum particle concentration was as high as 84% in the Matrix stent. However, although this latter value was consistent throughout the length of the Matrix stent, it

still only represented a small percentage of the total area and this high concentration is thus invisible in the data. Increased streamline and particle density is not clearly shown in Figure 4.17, as concentration naturally occurred within a small area. It was therefore difficult to demonstrate the information illustrated in heat maps quantitatively.

Following particle tracking, any FluoSpheres which may have attached to stents were counted to identify potential areas of accumulation (Section 4.2.3). These data were very variable, with large variation in accumulation between stents of identical geometry and between faces of the same deployed stent (Figure 4.18). Consensus may have emerged with the use of a higher sample size or, alternatively, by increasing the time duration the stents were under flow conditions (although image clarity could quickly be lost with increased accumulation of particles within the model vessel).

Particle accumulation at random points within inter-strut regions, which were expected to be areas of relatively undisturbed flow, was thought to be due to the applied low flow velocity, allowing particles to settle. Alternatively, there was perhaps a propensity for the polystyrene particles to adhere to PDMS. This was compared to currently unpublished *in silico* results from Adrien Lefieux (Emory University, USA, personal communication). In his work the high-end processing power of a supercomputer, which had previously been used to study haemodynamics [208], was employed to simulate a large number of particles flowing through high-resolution models of stented vessels. In agreement with the data here, results from those simulations also showed the accumulation of particles in seemingly random areas of relatively undisturbed flow. This was considered to be an artefact of the conditions applied to the model, with particles approaching the wall, contacting the no-slip boundary and having their velocity reduced to zero. To the author's knowledge, while particle tracking velocimetry has previously been performed on stents [94][204], no measure of the subsequent accumulation of particles of this size has been taken, with which to compare these *in vitro* and *in silico* findings and judge their accuracy.

The effect of stent geometry on both particle flow and accumulation has particular relevance to the regrowth and maintenance of a healthy endothelium, and the prevention of thrombus formation [43]. Blood is a particulate suspension containing formed elements (described in Section 1.4.2). As such, it could be considered that uniform dispersal of these elements would be beneficial. Well distributed EPC over the entirety of a stent, in addition to nutrient and oxygen delivery over the local endothelium via mass transport, could improve vessel reendothelialisation [55]. Good EC distribution could also prevent any single area of the stent becoming a focal point for cell or plaque accumulation, which would in turn prevent thrombus formation. In addition, particle flow and accumulation is of significance to recent technological developments in the use of nano- and micro-particles as drug carriers, for targeted delivery [209].

Cell migration studies were performed on coronary stents, but success rates were low. Although clearly defined cell seeding boundaries could be obtained using the methods described in Section 2.2.4, and stents could be deployed with relative accuracy, the short duration of experiments allowed only models with initial cell positions in very close proximity to stents to provide useful data (Figure 4.26).

If experiment duration was able to be extended, poor stent placement would not be an issue. Assays with distal initial HUVEC location would be of interest, as they would allow a direct comparison between migration rates within both segments of empty vessel and stent structure, in the same experiment. However, this was not possible in the current model due to the constraints outlined in Section 3.6.

Cell migration studies were attempted on all of the available coronary stent designs, with the exception of the Penchant and Orsiro. However, these stents had identical geometry to the BiodivYsio OC and Pro Kinetic Energy respectively, which were tested. Furthermore, the Orsiro was a DES (the only example in this study). Despite exceeding the stated expiration date, it was decided that the sirolimus coating would render any EC migration data incomparable to the other BMS.

While not DES, the BiodivYsio OC and Pro Kinetic Energy stents were coated (see Table 4.1), but were deemed usable to avoid a further reduction in sample size. Unfortunately, poor stent placement prevented data being obtained from the

BiodivYsio OC stent. Two of the five successful cell migration studies using the peristaltic pump were obtained from Pro Kinetic Energy stents, coated with silicon carbide. Silicon carbide is used to passivate stents and improve their haemocompatibility, rather than to exert an active influence on EC like DES (Section 1.3.4) [70]. Migration distance within the Pro Kinetic Energy stents was half that seen within the other two successful models: this could be deemed to be confirmation that the silicon carbide had no positive effect, or alternatively, that the (again, expired) coating was actually detrimental to EC. However, cell migration distance and rate (Figure 4.27) did not take into account the initial location of cells in relation to the stent (Figure 4.26). Cells within Pro Kinetic Energy stented vessels had less distance to travel before they were arrested by the first stent struts, and the same effect would presumably be seen with cells beginning experiments at the same proximity to uncoated BMS.

In each of the examples shown in Figure 4.26, migration of the HUVEC monolayer stopped at the stent and cells that passed the first strut were low in number and remained close to the structure. Stent struts induce areas of recirculation (identified in Figure 4.8) and EC are exposed to bidirectional mechanical cues which hinders effective migration. This behaviour is similar to that shown in the findings of Hsiao *et al* [103], in which bulk HUVEC migration was arrested by a 100 µm ridge and cells that crossed this obstacle remained immediately downstream of it. This similarity to data obtained from a recognized protocol which used established, commercially available equipment (as well as to cell migration data from other existing parallel plate studies), could indicate the validity of the novel model and protocol in use in this work. Here, however, by further developing a model in which data is obtained from clinical-grade stents, in vessels of realistic size and geometry, physiological relevance could be increased, as could the translational potential of results and the confidence with which they could be compared to clinical data and *in vivo* study.

In 1.5 mm diameter vessels HUVEC migration was assessed by counting cells within separate stent sections as time progressed, the assumption being that cells migrating in the direction of flow would increase the total number in that direction (Figure

4.28). Increased cell numbers were indeed seen. In standard EC growth medium the rate of increase remained constant over time, with the exception of an enhanced rate in the first inter-strut region after 48 hours (Figure 4.29). The presence of a ROCK inhibitor did not affect cell numbers upstream of the stent, but greatly increased the rate of change in cell number in the inter-strut regions.

It may be reasoned that, upstream of the stent, cell migration was high and cell confluence was reached quickly, prior to the first time point within the experiment. This could explain why the rate of increase in cell number within this region remained both low and constant over time. Migration was high because cells in this region were exposed to unidirectional mechanical cues from undisturbed flow, as per empty control tubes (Section 3.3). Conversely, migration was hindered within the inter-strut regions due to the presence of bidirectional mechanical cues and reduced wall shear stress [112][113]. Therefore, while a similar level of confluence was eventually reached in the first inter-strut region, the process took longer and the corresponding increase in cell number was not seen until the third time point. The influence of bidirectional flow, via the mechanism outlined in Section 1.4.4 [103], was shown by the large impact of the ROCK inhibitor on cell numbers within the in-stent regions once induced mechanical cues were silenced. This is further supported by the fact that the ROCK inhibitor had an even more pronounced effect in the second inter-strut region where, it may be assumed, flow disturbance was greater still, and had no noticeable effect in undisturbed flow upstream of the stent.

Simulating fluid flow through stents, using *in silico* models created from μCT data provided data on induced flow disturbances and altered wall shear stress (Section 4.3) with which to compare EC migration. In the Matrix stent, a particularly well-apposed example, flow was disturbed immediately up and downstream of struts (Figures 4.20 – 4.22). These areas were subject to low longitudinal velocity and reversed flow, and therefore low and bidirectional wall shear stress. In addition, these areas corresponded to the locations at which HUVEC monolayer migration was arrested (upstream) and at which HUVEC leader cell migration was reduced (downstream) (Figures 4.26 and 4.27). The combined CFD/cell migration data compares well to previous *in vitro* and *in silico* studies of simple stent geometries

[103], as well as in-plane particle tracking [94] and CFD simulations of both idealised models and *in vitro* model- or patient-specific geometries [162][112].

CFD analysis revealed regions of low wall shear stress further downstream of stent struts. In these inter-strut areas, flow began to recover and shear stress increased to some extent, but the presence of additional downstream struts halted this process. Thus, the vessel wall was subjected to wide areas of <0.5 Pa wall shear stress, which enlarged with increased downstream distance. Unfortunately, HUVEC migration studies in 2.5 mm diameter vessels did not proceed long enough to see cells approach these regions. However, cell counts in 1.5 mm diameter vessels illustrated the detrimental effect of these local mechanical conditions (Figures 4.28 and 4.29). In addition, HUVEC were only observed to move and proliferate in areas of particularly low shear stress highlighted by CFD analysis, such as areas where adjacent struts were in close proximity, when in the presence of a ROCK inhibitor (Figure 4.30). This once again implied that the migration of EC in standard growth medium was hindered by bidirectional mechanical cues from disturbed flow. Due to this induced EC dysfunction, these areas could not be considered conducive to rapid endothelialisation [89][163].

Computational simulations were also performed with a Newtonian fluid of the same viscosity of blood. The results showed a reduction in the extent of both flow disturbance and diminishing shear stress along stent length, compared to those obtained using EC growth medium equivalent fluid properties (Figure 4.23). However, it cannot be concluded that HUVEC *in vivo* are in a more favourable mechanical environment to those *in vitro*. Here, blood flow was simulated using the same steady conditions applied *in vitro* whereas, in reality, blood flow is pulsatile and unsteady [55]. In addition, arteries stretch in response to this pulsatile flow and the coronary arteries are distorted when the surface of the heart moves during the cardiac cycle [6]. *In vivo* haemodynamics would therefore be much more complex. Furthermore, as discussed in Section 1.4.2, blood is a non-Newtonian fluid and is more often simulated using the Carreau model as opposed to the constant viscosity model used here. The CFD simulations of higher-viscosity fluid are therefore perhaps best placed to illustrate the flow of the thickened EC growth medium

described in Section 2.2.2.2 and to demonstrate how local fluid dynamics would change if more physiological parameters (e.g. velocity, Reynolds number, etc.) were accounted for in addition to wall shear stress.

As CFD analysis revealed the effect of stent struts on local fluid dynamics and wall shear stress, it also demonstrated the differences in fluid dynamics across dissimilar stent geometry (Figure 4.20). Wall shear stress magnitude, distribution and the extent of its reduction over stent length, were seen to vary with stent structure. The influence of design parameters such as strut thickness and spacing have been shown in parametric studies of idealised models [111][112][113]. Any conclusions drawn from models based on *in vitro* vessels must not only take into account general stent structure, but also the degree to which each strut is apposed or prolapsed into the lumen. This was shown to have a great impact on AWA-WSS (Figure 4.20) and prolapsed struts induced more complex flow than those which were well embedded. Once again, a greater number of samples would aid in investigating the impact of small changes in strut prolapse and apposition between individual deployments.

Simulations using the lower resolution Coroflex Blue model (Figure 4.24) revealed a reduction in areas of low wall shear stress in comparison to the standard resolution model (Figure 4.20). Reducing μCT resolution enabled a crude parametric study, as losing image quality effectively resulted in a model with thinner struts, but otherwise identical strut position and orientation. An increase in shear stress heterogeneity, toward baseline levels of 1 Pa, was seen as strut thickness and therefore the overall impact of stent structure was diminished.

Finally, while it has been shown here, and in the relevant literature, that stents have an impact on local haemodynamics and EC behaviour, a return to physiological flow conditions is not as straightforward as simply reducing the number, or size, of stent struts. For example, Biocompatibles Ltd. produces the BiodivYsio AS stent ('Added Support', as opposed to the OC 'Open Cell' studied here) with increased strut density, as an alternative model. This is a reminder that coronary stents are used to widen and scaffold muscular arteries and that their ability to do this must take precedence, however large their impact on haemodynamics may be.

However, local haemodynamics plays an important role in the reendothelialisation and healing of stented vessels and, where possible (if, for example, specific stent features are designed with copyright or a company's signature theme in mind, rather than function), should be considered a key factor in stent design. The development of the novel model and protocol described in this work, its validation in comparison to data from established, yet less physiologically relevant parallel plate and idealised computational models, and its ability to apply various techniques to study and compare a wide range of coronary stent designs contributes to that objective. Increasing the reliability of experiments, the resolution of resultant data and, through increased physiological relevance, its realism in comparison to *in vivo* data, will aid in the exploration of the impact of modified stent design on reendothelialisation.

Chapter Five

In Vitro and *In Silico* Study of Flow Diverter Stent Haemodynamics and Cell Migration

The regrowth of a healthy endothelial layer is hindered by EC dysfunction, caused by the presence of cardiovascular stents and their effect on local wall shear stress. Chapters 2 and 3 considered the creation of an experimental platform through which the biomechanical conditions of stented vessels could be studied. Chapter 4 considered the application of that platform to a range of clinical-grade coronary stents, highlighting the effect of stent-induced flow disturbance on wall shear stress and EC behaviour. This chapter concerns the application of the platform to clinical-grade flow diverter stents, with greatly dissimilar geometry and function to that of coronary stents.

5.1   Flow diverter stent deployment

5.1.1   Flow diverter stent geometry was relatively uniform

Two different flow diverter stent designs, the Leo and Silk, were supplied by Dr. Ana Paula Narata (INSERM U930, France). These were deployed within *in vitro* model vessels of 2 mm diameter and are detailed in Table 5.1. Both stents were woven from thin wires of circular cross-section. Thick struts, created by coiling one wire around another, supported a mesh of thinner struts. Meshes were formed from regularly aligned struts (Figure 5.1) and the main differences between the two stents pertained to the density of these meshes and the associated MSA. While only two designs were tested, they are representative of the majority of flow diverter stents used in clinical practice [24].
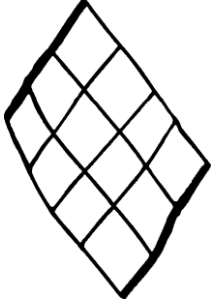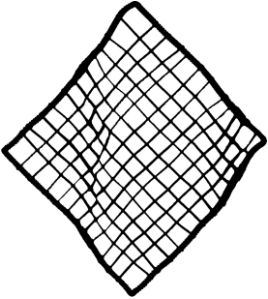
Model	Manufacturer	Strut (µm)	MSA (%)	Unit	Length (mm)	Diameter (mm)	Material	Coating
Leo	Balt	30/70	29.3		10 - 50	2 – 7.5	Nitinol	None
Silk	Balt	40/60	16.2		10 - 40	2 - 5	Nitinol	None

Table 5.1 Properties of flow diverter stents

Only flow diverter stents of 2 mm nominal diameter and 10 mm length were deployed within 2 mm model vessels.
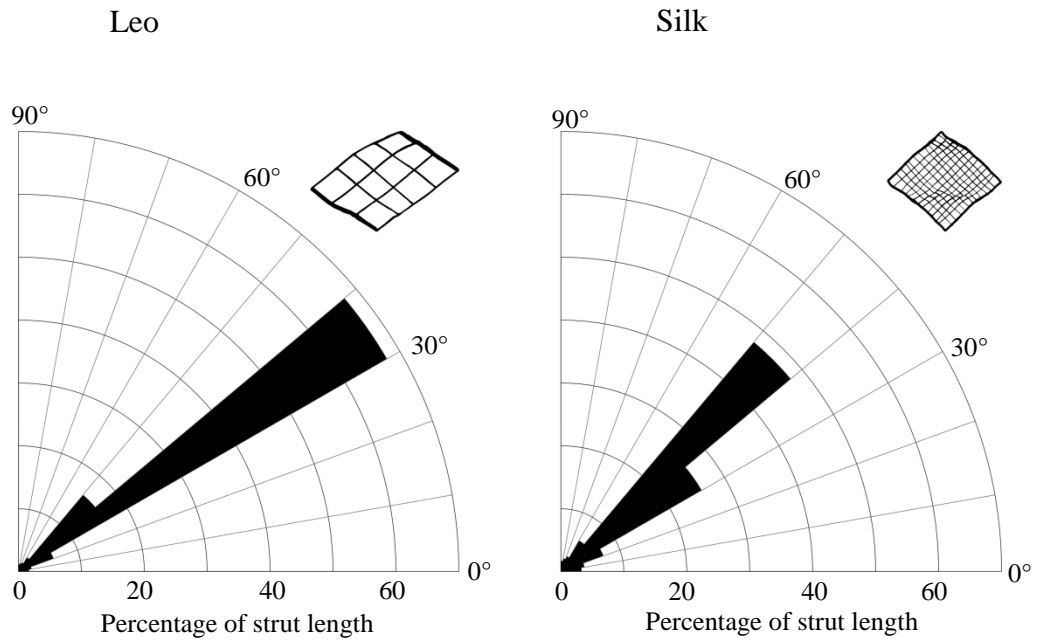
Figure 5.1 Flow diverter stent strut orientation

The orientation of flow diverter stent struts was measured in relation to the direction of applied flow (0°), as illustrated in Figure 2.3. The length of struts at each angle (to the nearest 10°) is shown here as a percentage of the total strut length. Each chart represents an average measurement taken from two faces of each stent (rotating the stent 90° between the two) and one repeating unit of stent geometry. Flow diverter stents show little variation, with regular meshes of struts at 30 - 50°.

5.1.2 Deployment showed variation in flow diverter stent geometry

Variability in stent geometry between deployments of the Leo stent was reduced in comparison to coronary stents (described in Section 4.1.2). In contrast, variability in stent geometry between deployments of the Silk stent was larger in comparison to Leo and coronary stents. The ideal, regular mesh of the Silk stent was affected by three factors, illustrated in Figure 5.2:

1. Silk stent struts, the thinnest seen in any of the flow diverter or coronary stent struts, were more susceptible to slight distortion.

2. At either end of the stent, the interwoven struts were freed and remained unlinked. This resulted in irregular, non-uniform distribution and reduced radial expansion force which meant that this region was particularly prone to prolapse and under-expansion.

3. The self-expansion of Silk stents would often halt as soon as the first, thicker struts came into contact with the wall. This could then result in a gap (~100 μm) between the wall and regions of thinner interwoven struts.

5.2 Flow diverter stent geometry had a reduced impact on visible flow

5.2.1 Influence of flow diverter geometry on streamline orientation

Figure 5.3 shows tracked particle streamlines within representative areas of the flow diverter stents (streamlines through the full stents are provided in the Appendix). Once again, there was good agreement between the two sequences in each field of view and clear streamline patterns followed from one field of view to the next.

30% of the total number of tracks deviated from a path within ±5° of flow direction in the Silk stent (the joint lowest value of all stent types, equal to the Penchant coronary stent) and 40% in the Leo stent (exactly mid-range). The higher value obtained from the Leo could be seen to be due to a number of particles following its relatively thick strut.
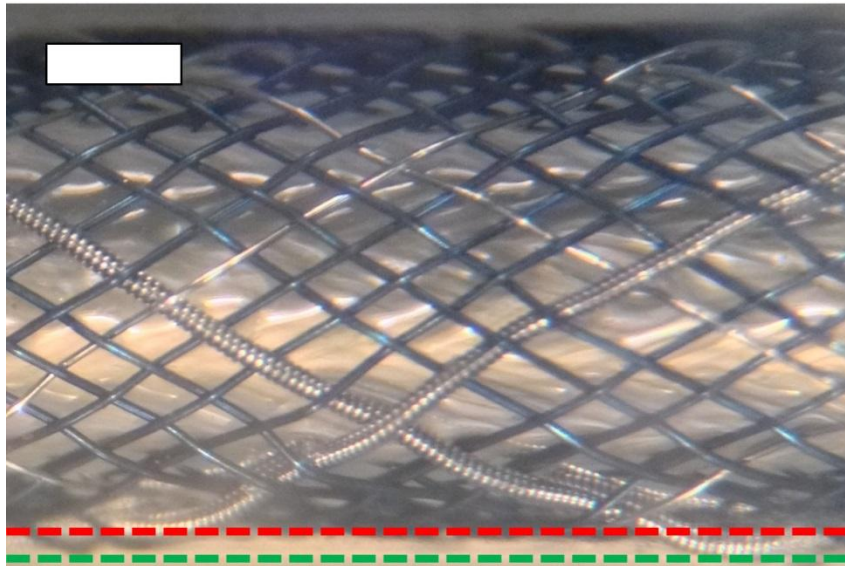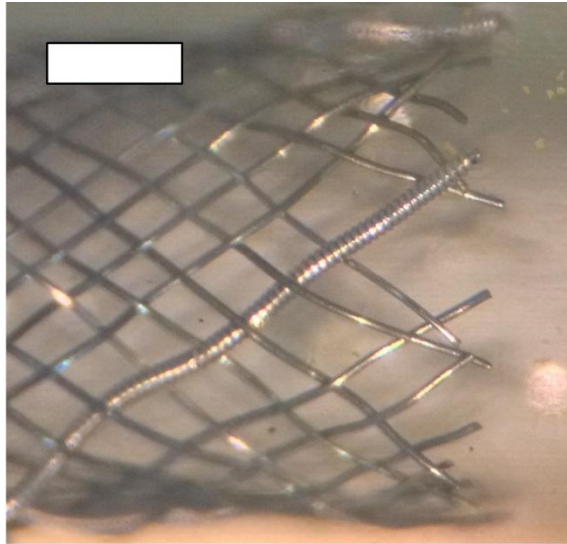
Figure 5.2 Structure of deployed Silk flow diverter stent

A Silk flow diverter stent deployed within a 2 mm diameter vessel was photographed under a brightfield stereo microscope. The stent consisted of thin (30 μm) braided wires and four thicker (70 μm) struts.

Top: Loose struts at either end of the stent were disordered and prone to prolapse into the lumen

Bottom: The braided design and relatively weak self-expansion left gaps between the vessel wall (green line) and struts (red line).

Scale bar: 0.5 mm.
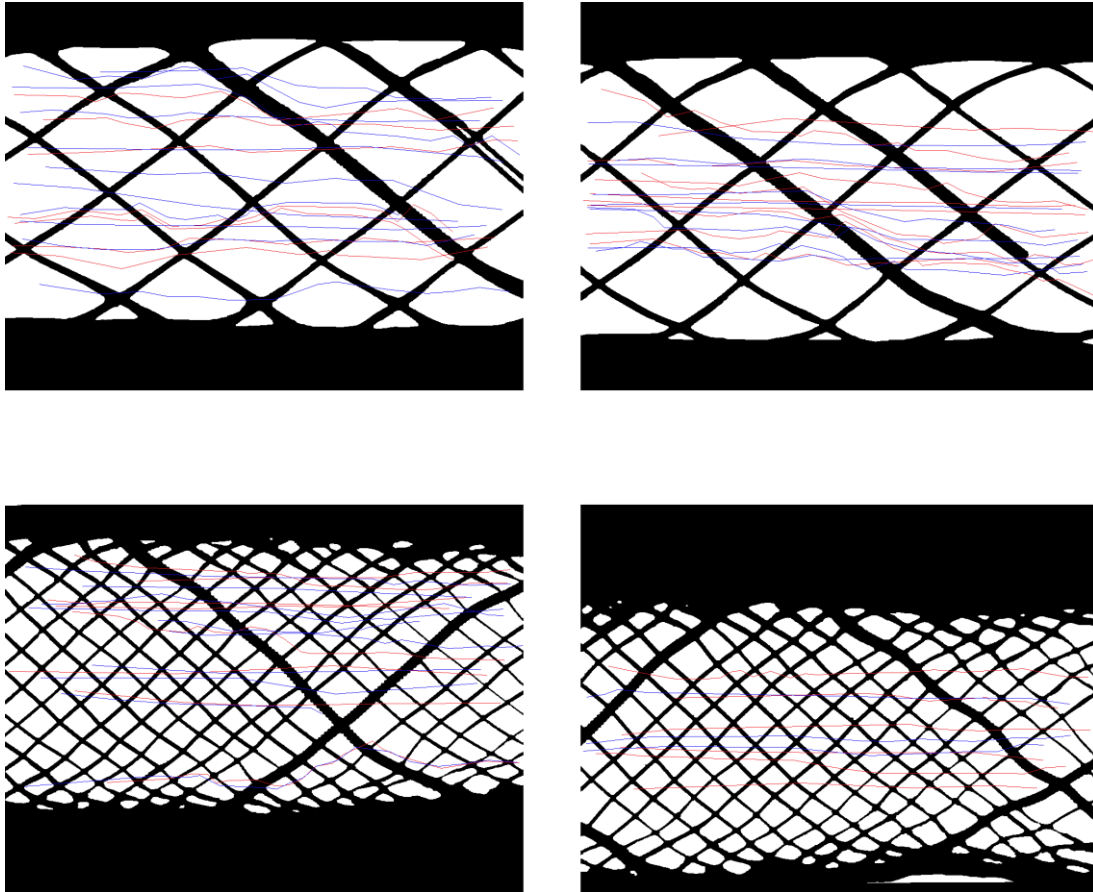
Figure 5.3 Tracked particle streamlines in Leo and Silk flow diverter stents

Particles were tracked moving through each flow diverter stent deployed within 2 mm diameter vessels. Tracking was performed for two 30-second long sequences (red and blue tracks) on two stent faces, with the stent rotated by 90° between the two faces.

Top: Leo stent.

Bottom: Silk stent.

Flow from left to right, Re = 43 (equivalent to blood flow with 1 Pa wall shear stress). Representative images are mid-stent length and the plane of focus on the bottom of the vessel.

The stents had clear strut orientations of ±50° (Silk) and ±40° (Leo). Plotting this additional information on Figure 4.10 further reduced the appearance of any trend. As per Section 4.2.1, the difference in track orientation between different faces of each stent was ≤10% (Figure 5.4).

5.2.2   Influence of flow diverter geometry on tracked particle density

A total of 212 and 195 particles were tracked moving through the Silk and Leo stents, respectively. These values were $40 - 80\%$ lower than the range of tracked particle numbers seen within coronary stents, when controlling for length. Figure 5.5 shows the distribution of moving particles, displaying track path and the frequency of particles moving along each one, as a percentage of the total number of particles. As for the coronary stents, both flow diverter stents contained large areas of low particle flow. However, this was due to low overall particle numbers as there was little funnelling effect seen. Variation in the degree to which stents funnelled particles is shown in Figure 5.6, based on the first 72 columns of each grid as per Section 4.2.2.
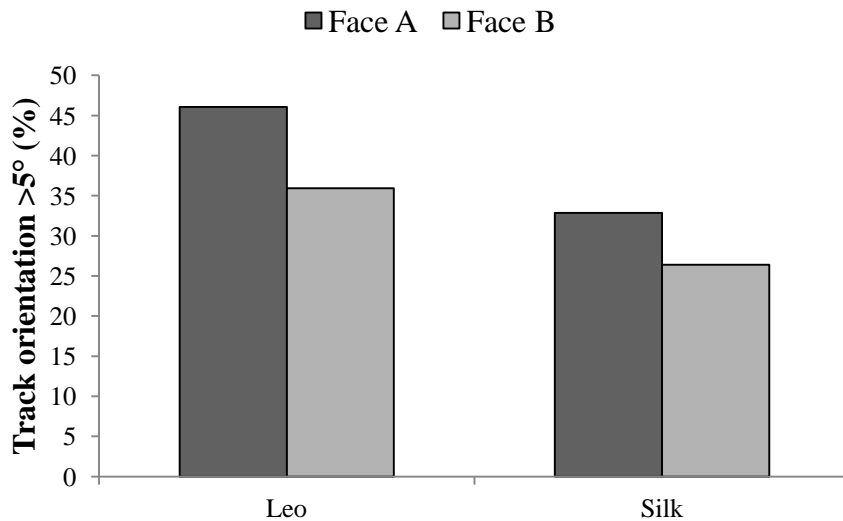
Figure 5.4 Differences in streamline orientation between flow diverter stent faces

The orientation of tracked particle streamlines moving through flow diverter stents deployed within 2 mm diameter vessels was measured. The length of tracks at an angle greater than $\pm5°$ of the direction of flow ($0°$) is shown as a percentage of the total length of tracks within each stent. Tracking was performed on two stent faces, A and B, with the stent rotated by $90°$ in between the two. The difference in track orientation between these faces is shown here. The difference in track orientation between faces was $\leq10\%$ in each stent, implying consistency in the effect of the repeating mesh stent strut design.
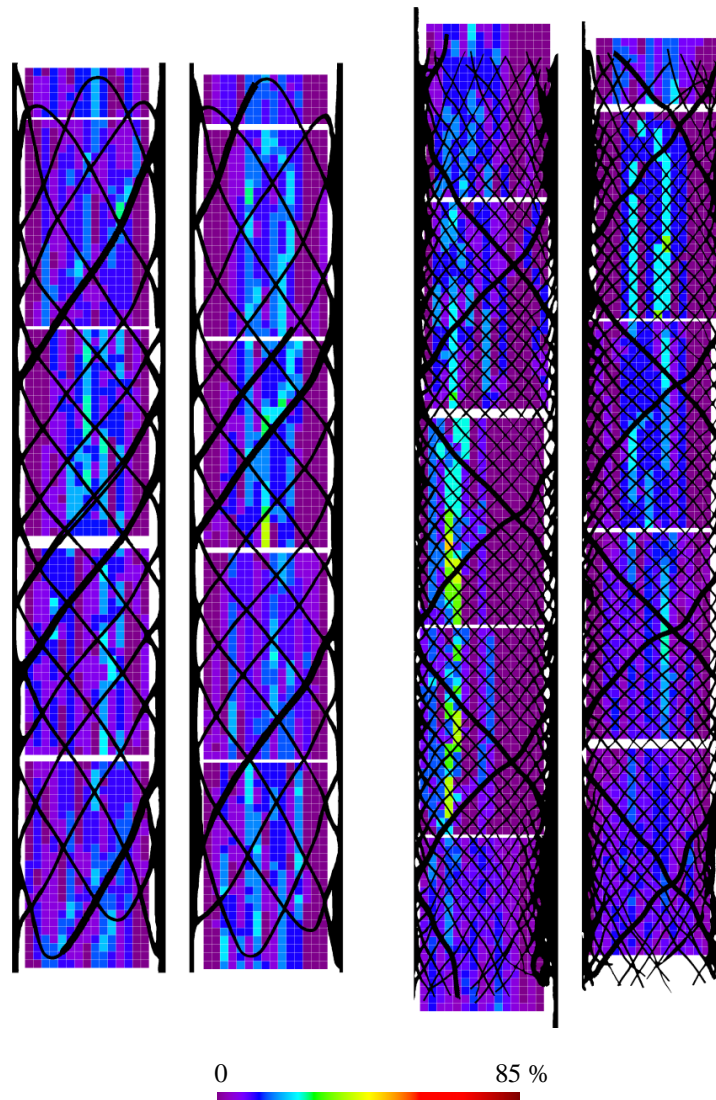
Figure 5.5 Tracked particle density heat maps in Leo and Silk flow diverter stents

Particles were tracked moving through each flow diverter stent deployed within 2 mm diameter vessels. The position of streamlines and the frequency of particles tracked moving along them was measured in relation to a 100 µm square grid and presented as a percentage of the total number of particles seen in each grid.

Left: Leo stent.

Right: Silk stent.

Flow from bottom to top, Re = 43 (equivalent to blood flow with 1 Pa wall shear stress). The plane of focus is on the bottom of the vessel.
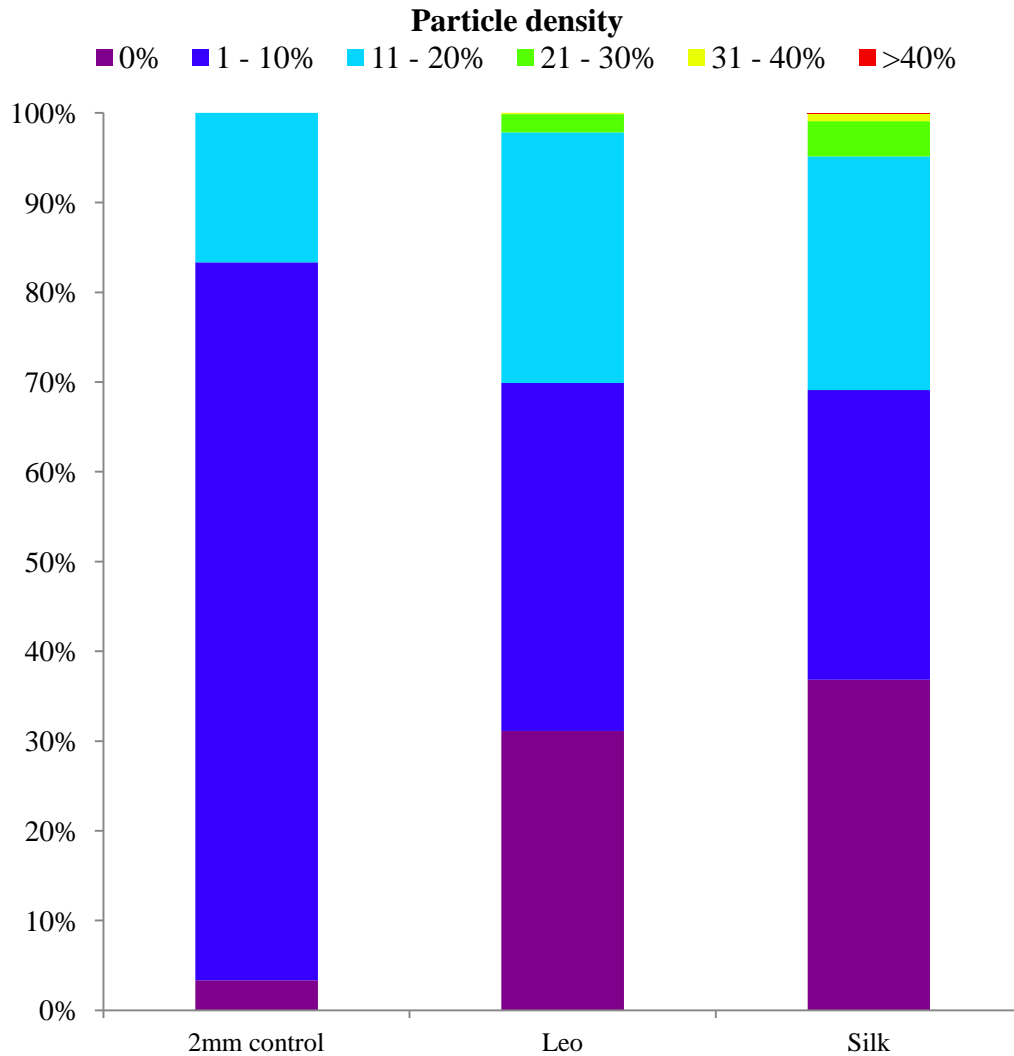
Particle density

Figure 5.6 Streamline and particle density in flow diverter stents

Particles were tracked moving through flow diverter stents deployed within 2 mm diameter vessels. The position of streamlines and the frequency of particles tracked moving along them was measured in relation to a 100 μm square grid, as a percentage of the total number of particles seen in each grid.

Here, the concentration of particles within each grid square is presented as a percentage of the total number of squares. Particles were relatively well distributed throughout flow diverter stents with the large area of 0% density due to low overall particle numbers.

5.2.3 Particle accumulation increased and varied in flow diverter stents

As per Section 4.2.3, accumulated particles were counted in relation to their position along the length of stents and 2 mm up and downstream of their leading and trailing edges (Figure 5.7). As flow diverter stents were only deployed in 2 mm diameter models accumulation was counted twice: once after 20 minutes to compare against coronary stents after the same time under flow, and again after the same total volume of particle suspension.

As expected, particle numbers increased with time. However, at the second time point, after equal flow volume, the number of particles in the Leo stent remained 50% lower than an empty 2 mm vessel, controlling for length. Numbers within the Silk stent were double that of an empty control and comparable to coronary stents. Particle attachment within the Leo stent showed no bias toward stent geometry and the Silk stent's dense mesh rendered any assessment of attachment relative to strut location impractical.

For both stents, linear regression analysis suggested a gradual reduction in particle accumulation along stent length ($R^2 = 0.5 - 0.8$, in comparison to <0.1 in the majority of coronary stents). The highest number of particles at a given location in any flow diverter or coronary stent was seen in the 2 mm of empty vessel up and downstream of the Silk stent (Figure 5.8). Comparing these sections to their immediate in-stent neighbours also produced some of the sharpest reductions in particle number between adjacent regions.

5.3 Computational modelling

Casts of vessels containing Silk stents were made before struts were pulled out through the lumen. This preserved fine details, including areas of interwoven and coiled struts. The cast could be scanned at high resolution (3.48 μm) due to its small size. This high resolution resulted in a complex, computationally expensive model. As such, only half of the *in silico* Silk stent model was meshed (Figure 5.9) and a plane of symmetry applied at the new boundary.
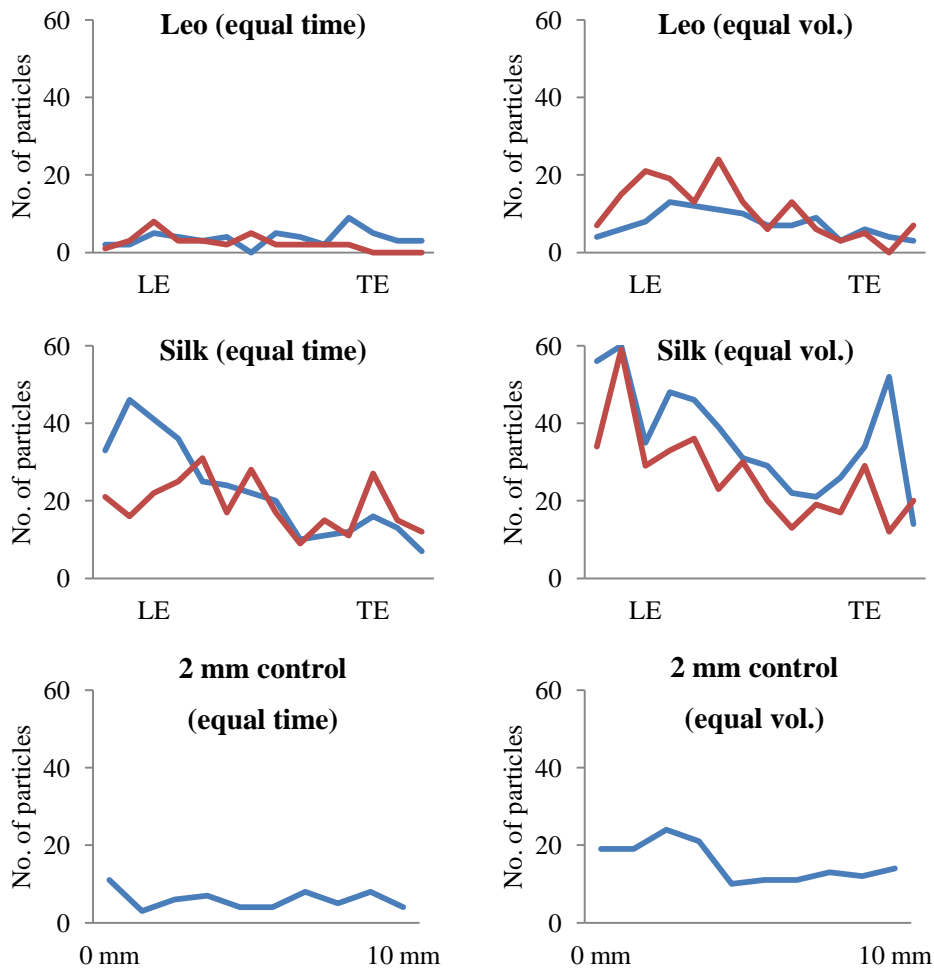
Figure 5.7 Particle accumulation in 2 mm diameter stented vessels

The number of accumulated particles within flow diverter stents deployed in 2 mm diameter vessels was assessed after 20 minutes under flow (the same amount of time as used in coronary stent models), and after 40 minutes under flow (the same total particle suspension volume as coronary stent models). Particles were counted in 1 mm segments through each stent, and 2 mm up and downstream of the stent leading edge (LE) and trailing edge (TE). This was performed twice (red and blue tracks) on two stent faces, with the stent rotated by 90° in between the two. Linear regression analysis suggests a gradual reduction in particle accumulation along stent length ($R^2 = 0.5 - 0.8$, compared to <0.1 in coronary stents).
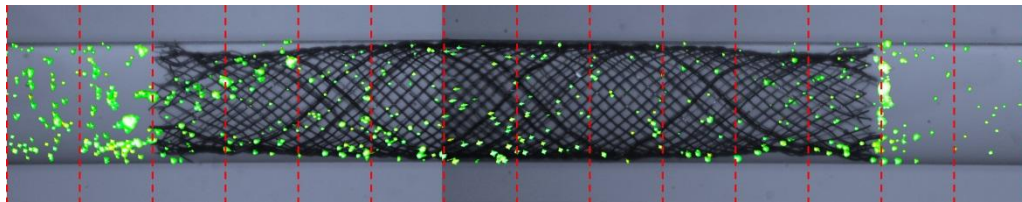
Figure 5.8 Location of particle accumulation within the Silk flow diverter stent

After 40 minutes under flow, accumulated particles (green) within flow diverter stents deployed in 2 mm diameter vessels were imaged and counted within 1 mm segments (red lines). Particle accumulation in the Silk stent was enhanced immediately up and downstream of the structure.
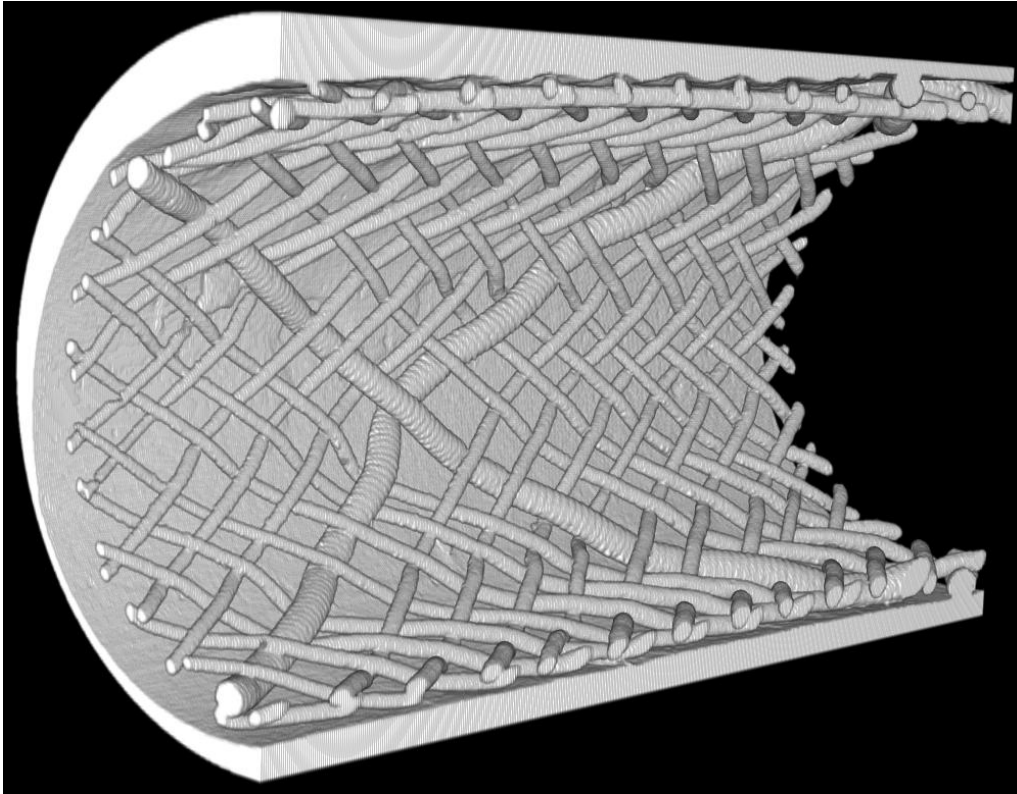
Figure 5.9 *In silico* model of a Silk flow diverter stent

In silico model of vessel wall and stent struts reconstructed from a 3.48 μm resolution μCT scan of a Silk flow diverter stent cast. Due to the destructive nature of strut removal prior to the scanning of the cast, only a short segment of the stented vessel's length contained viable geometry. In addition, due to the high resolution of the scan image, flow through only one half of the stented vessel was simulated in CFD analysis to reduce computational expense, and a plane of symmetry applied.

5.3.1 Wall shear stress was reduced within flow diverter stents

A UDF simulating fully developed flow was applied, with sufficient velocity to generate 1 Pa average wall shear stress in a 2 mm diameter vessel. Maximum shear stress was 28.14 PA (at a single unrepresentative point). The AWA-WSS within the Silk stent was 1.34 Pa, higher than the majority of coronary stents. However, as for coronary stents, prolapsed struts were exposed to higher wall shear stress which moved this average upwards. With a far greater number of struts, all of which lay within the lumen adjacent to the wall, this increase was pronounced in the Silk stent (Figure 5.10A).

Disregarding the stent struts and considering the wall only, wall shear stress decreased towards the centre of model, as flow moved into the mesh. This region was exposed to no more than 0.5 Pa (Figure 5.10B), with areas of <0.1 Pa local to stent struts. Velocity vectors revealed extremely low flow at the wall (Figure 5.11). Wall shear stress recovery between struts was lower than that seen in coronary stents due to the high density of the mesh reducing the inter-strut distance.

Simulating the flow of a fluid with viscosity and density equal to that of blood resulted in an AWA-WSS of 0.85 Pa within the model. Shear stress at the wall was reduced (>1 Pa), as was the longitudinal distance over which shear stress dropped to this level (Figure 5.12).
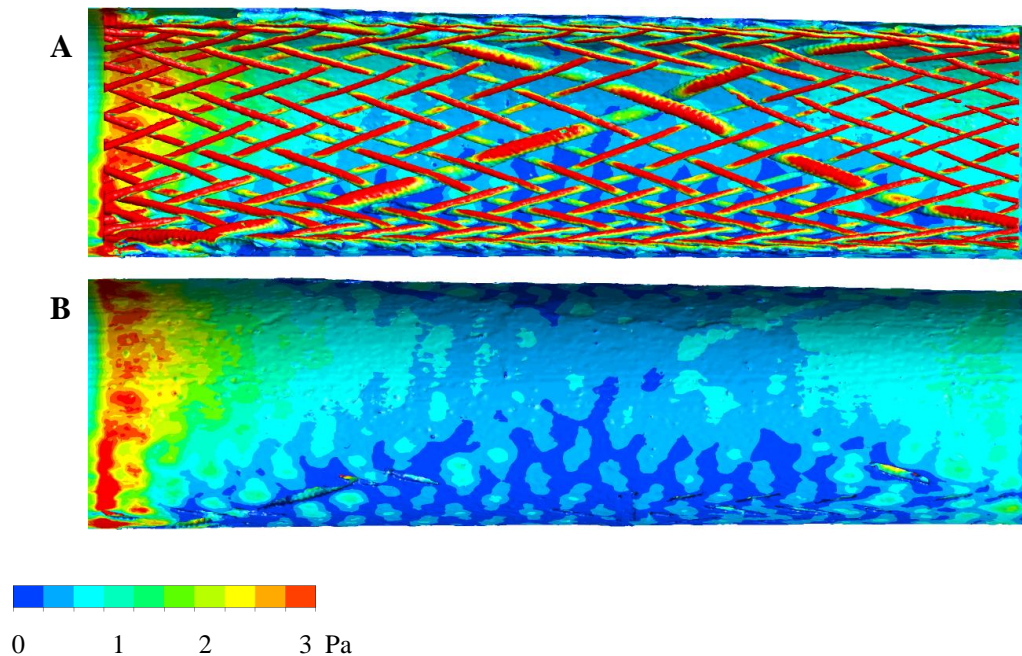
Figure 5.10 Wall shear stress within a Silk flow diverter stent

PDMS casts of flow diverter stents deployed within 2 mm diameter vessels were made and µCT scans taken. *In silico* models were reconstructed from this data and used for CFD analysis to plot wall shear stress along the vessel.

A: Silk stent interior, showing elevated wall shear stress on prolapsed struts.

B: Silk stent wall, showing reduced wall shear stress downstream of thick struts and underneath the thin strut mesh.

Flow from left to right, 1 Pa average wall shear stress. Note: the maximum value of the scale bar is set to 3 Pa to better illustrate regions of low flow.
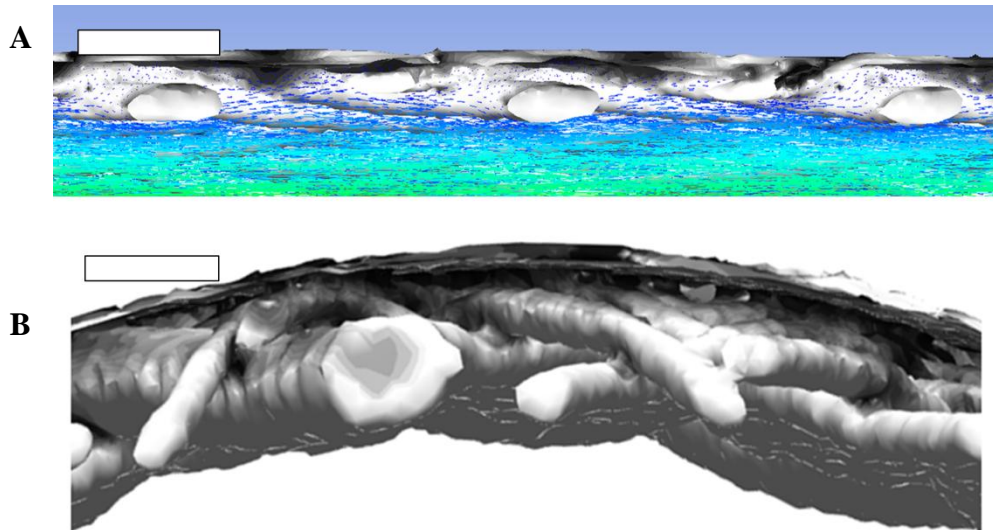
Figure 5.11 Velocity vectors around Silk flow diverter stent struts

In silico models were reconstructed from flow diverter stent μCT data and used for CFD analysis.

A: Longitudinal view. Vectors revealed greatly reduced velocity magnitude at the vessel wall local to Silk stent struts, and little recovery between struts due to the high density of the mesh.

Flow from left to right, 1 Pa average wall shear stress.

B: Cross-section. Gaps were present between Silk stent struts and the vessel wall even when fully deployed, due to the interweaving braided struts, which further reduced velocity and flow recovery at the wall.

Scale bar: 100 μm.

0   1   2   3 Pa
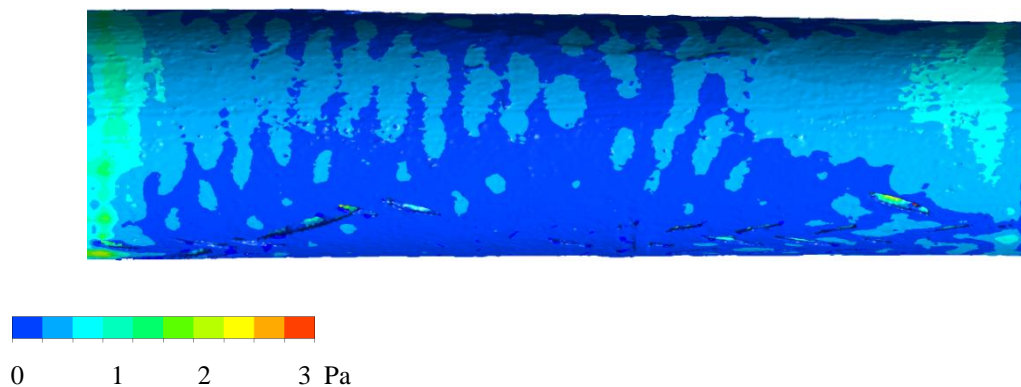
Figure 5.12 Wall shear stress within a Silk flow diverter stent modelled with blood-equivalent viscosity

Wall shear stress resulting from the flow of a Newtonian liquid with the equivalent viscosity of blood (3.5 mPa.s) was plotted within an *in silico* model of a Silk flow diverter stent. Shear stress in the higher viscosity model was reduced in comparison to the standard viscosity model as per Figure 5.14.

Flow from left to right, 1 Pa average wall shear stress. Note: the maximum value of the scale bar is set to 3 Pa to better illustrate regions of low flow.

5.4 Cell migration was arrested in flow diverter stents

Cell migration studies were performed on flow diverter stents, connected to the peristaltic pump system with flow rates set to induce an average wall shear stress of 1 Pa. The threshold of 24 hours under flow was achieved for both Leo (n = 2) and Silk stents (n = 3), with one Silk stent experiment progressing to the maximum 72 hours.

In flow diverter stents, the initial position of HUVEC from which migration was to be measured was within the boundary of the deployed stent (this change in the protocol is discussed in Section 5.5). No HUVEC migration beyond this point was seen in any experiment, for either stent design (Figures 5.13 and 5.14). This applied to both monolayer migration and the migration of individual leader cells. HUVEC were only ever seen upstream of the initial seeding point and all inter-strut regions downstream of this point contained debris only (Figure 5.15).

Flow diverter stent deployment created wounds in the HUVEC monolayer upstream of the stent. These wounds were observed to close within the first 24 hours of experiments, with their boundaries moving in the direction of flow (Figure 5.16).
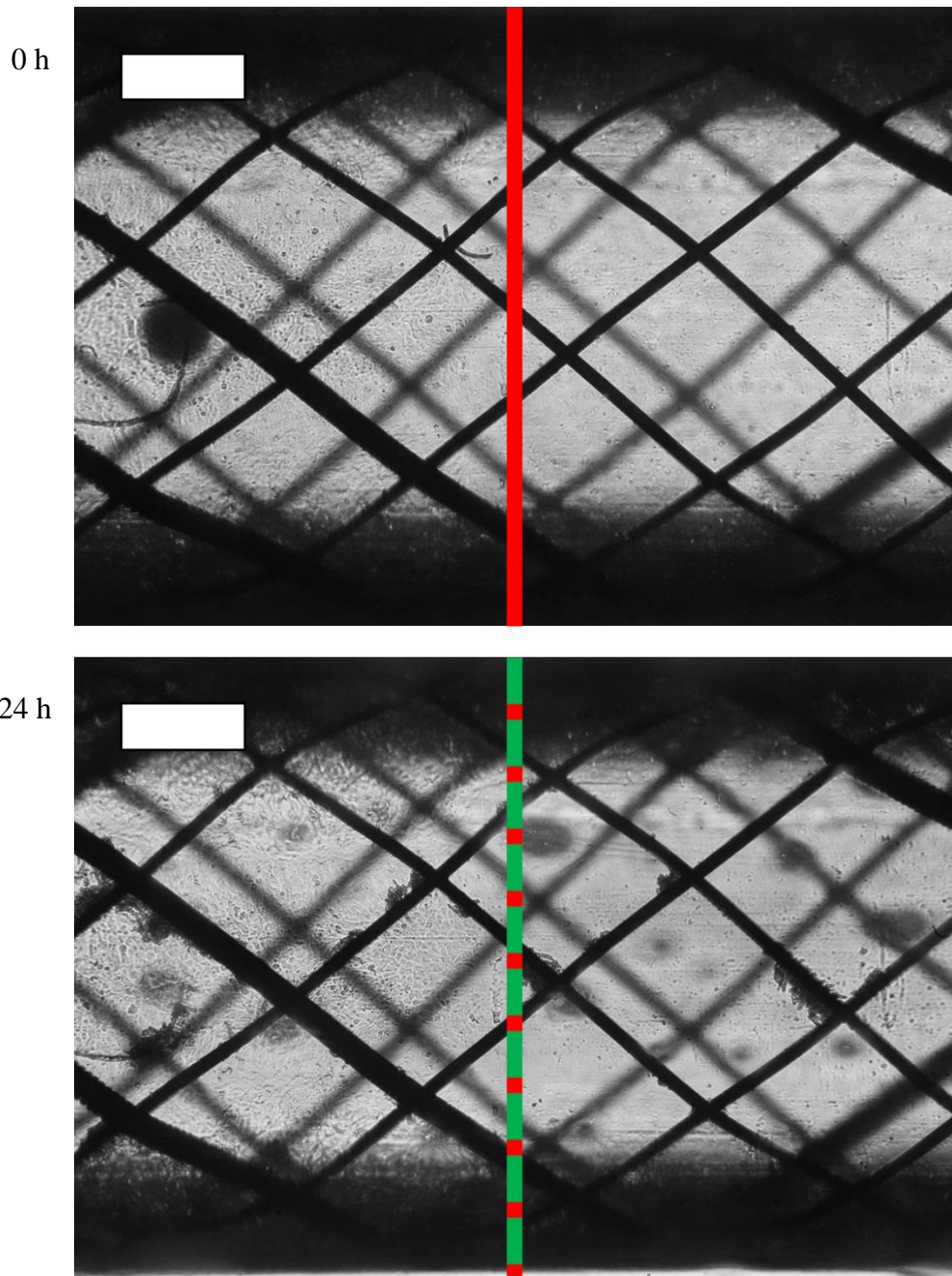
Figure 5.13 Cell migration study in the Leo flow diverter stent

In Leo flow diverter stents, no migration of HUVEC monolayers (green line) was seen beyond an initial seeding point (red line) after 24 hours under flow.

Flow from left to right, 1 Pa average wall shear stress.

Scale bar: 0.5 mm.

(n=2, representative images from one experiment shown here).
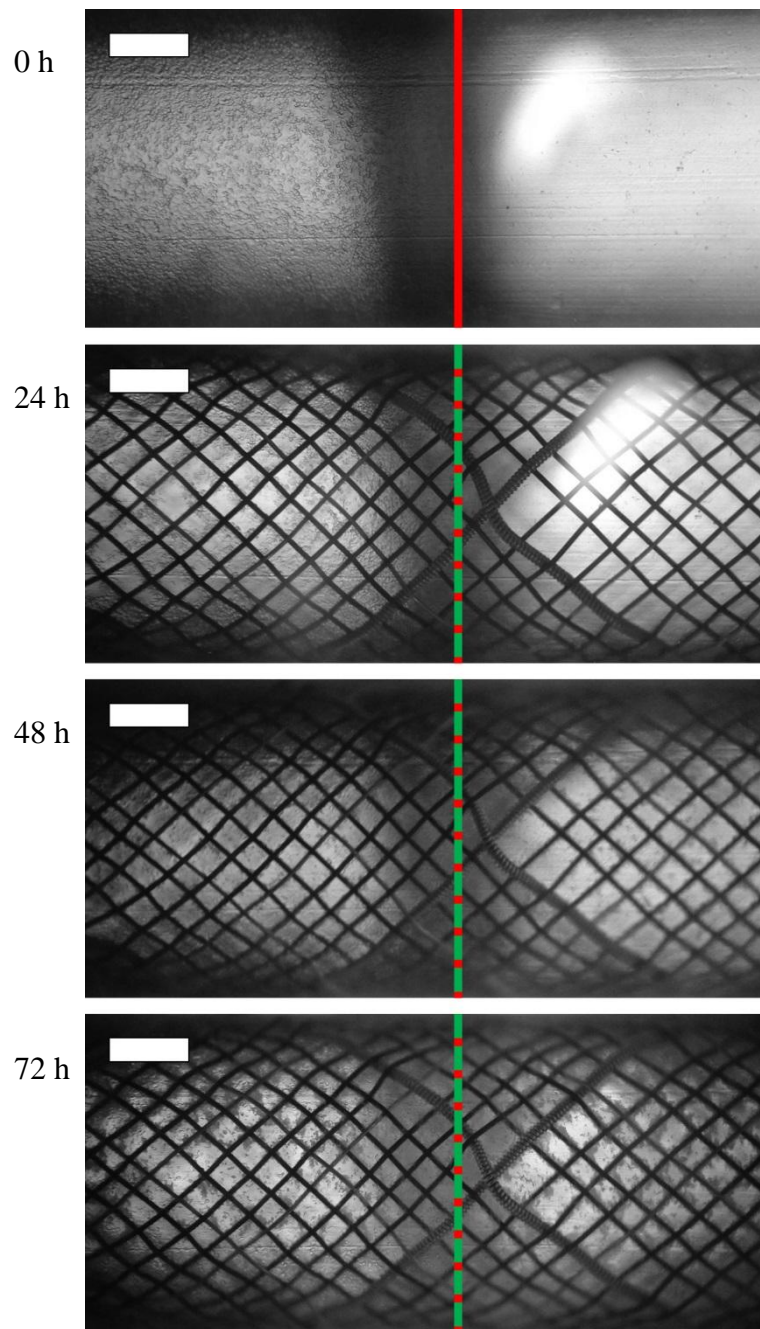
Figure 5.14 Cell migration study in the Silk flow diverter stent

In Silk flow diverter stents, no migration of HUVEC monolayers (green line) was seen beyond an initial seeding point (red line) after 72 hours under flow.

Flow from left to right, 1 Pa average wall shear stress.

Scale bar: 0.5 mm.

(n=3, representative images from one experiment shown here).
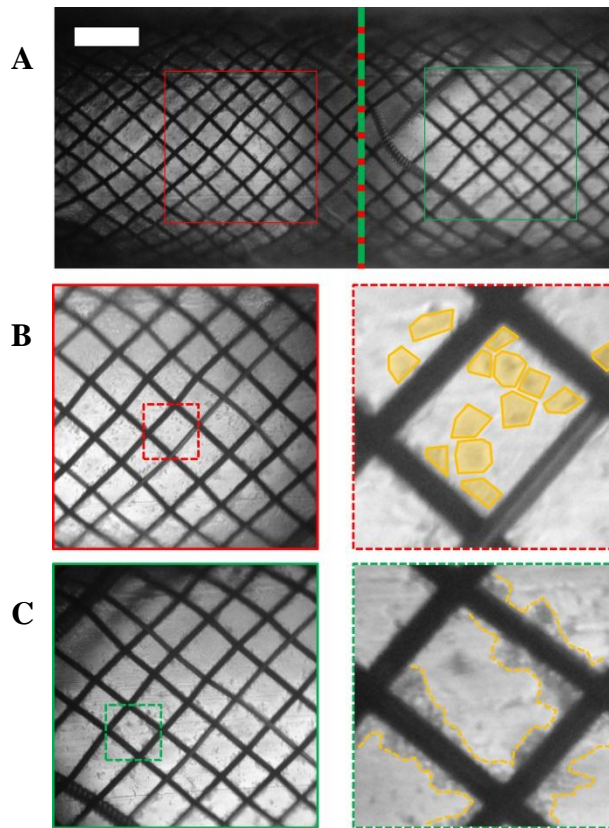
Figure 5.15 Cells within Silk flow diverter stent structure

No cell migration was observed beyond initial seeding points within flow diverter stent structure.

A: Silk stent after 48 hours under flow. Attached HUVEC could be seen in the inter-strut regions upstream of the seeding point (red box), but only debris was present downstream (green box).

B: Magnified inter-strut region upstream of the initial seeding point (left), containing attached HUVEC (yellow, right).

C: Magnified inter-strut region downstream of the initial seeding point (left), containing no HUVEC. Only cell debris (yellow lines, right) could be seen accumulating around struts.

Flow from left to right, 1 Pa average wall shear stress.

Scale bar: 0.5 mm.

Identical results seen in all flow diverter stents: (n=5, representative images from one experiment shown here).
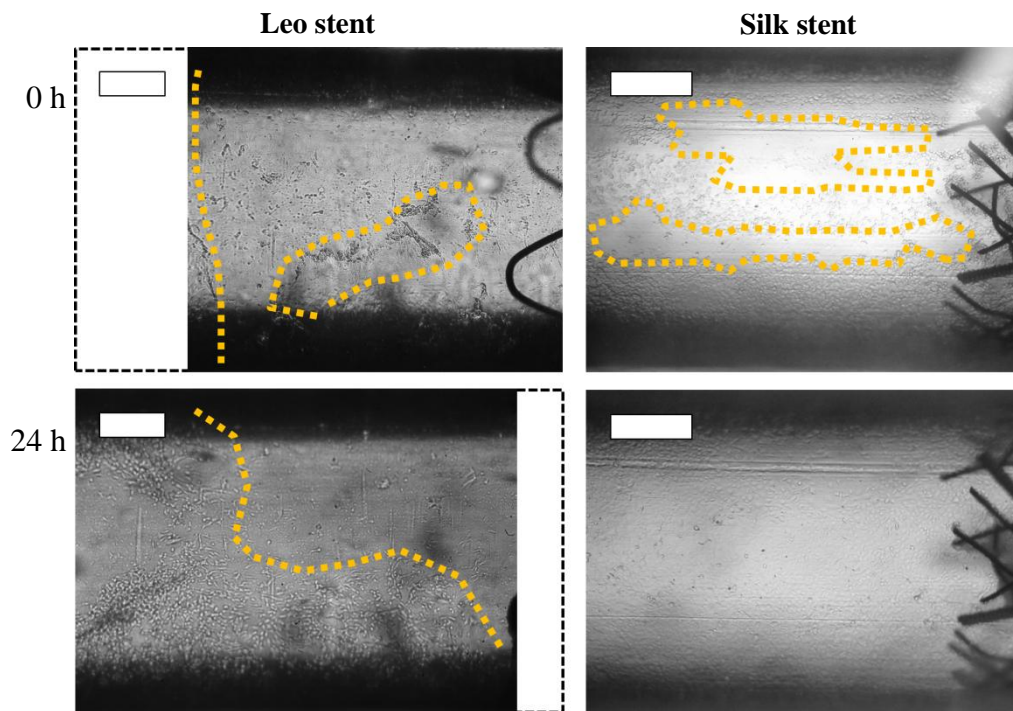
Figure 5.16 Cell monolayer wound closure upstream of flow diverter stents

No cell migration was observed beyond initial seeding points within flow diverter stent structure. However, upstream of the stents, HUVEC were seen to close wounds created where stent introducer sheaths scraped the monolayer, with the wound boundaries (yellow lines) moving in the direction of flow.

Flow from left to right, 1 Pa average wall shear stress.

Scale bar: 0.5 mm.

Leo: (n=2), Silk: (n=3, representative images from one experiment shown here).

5.5 Discussion

This chapter investigated the effect of flow diverter stent geometry on EC migration, local fluid flow and wall shear stress. Flow diverter stents of two different designs, detailed in Section 5.1, were deployed in *in vitro* model vessels. As described in Section 3.6, the result represented stent deployment *in vivo*, although particular care was required to minimise the gap between stent struts and the vessel wall (discussed further within this section). Although only two designs were available, they represented the range of clinically available flow diverter stent geometries [24]. Flow diverter stents typically consist of braided strut meshes of varying density and the stents tested here were at the fine (Silk) and coarser (Leo) ends of the scale. Flow diverter stent lengths were identical and so results which may otherwise have been affected by this parameter could be directly compared. When required, length was controlled for when making comparisons to coronary stents.

The extent to which the presence of flow diverter stents disturbs local fluid dynamics was revealed by tracking the motion of 10 µm particles through the stents' structure. In coronary stents, these studies showed obvious disruption created by struts, including zones of recirculation which corresponded to regions where EC migration was arrested or slowed. These results were in agreement with parallel plate and other particle tracking studies [94][103] which, taken together, implies a link between disturbed flow and cell dysfunction. However, despite the complete lack of HUVEC migration in flow diverter stents, a much smaller effect on particle tracking was observed (Figure 5.3).

An average of 20 particles were tracked per field of view in each flow diverter stent. This is less than 50% of the number within coronary stents (an average of 52 per field of view) and this disparity worsens when controlling for length. In flow diverter stents, values of tracked streamline orientation were similar to those seen within the majority of coronary stents. 30% of streamlines within the Silk stent and 41% of those within the Leo stent were at an angle $>\pm5°$ to flow (Figure 5.4). Mapping the density of streamlines, taking into account both the location and the frequency of particles moving along them, revealed a more uniform distribution of flowing

particles, although small areas of concentration could be seen (Figure 5.5). The overall effect was similar to that seen in many of the coronary stents.

Section 4.5 discussed the ability of individual particles to skew tracking data. In flow diverter stents, this effect was even more pronounced due to the much lower number of particles seen overall: the orientation of one streamline, or the addition of a single extra particle to a 100 μm grid square, could alter results by 10%. In coronary stents, high density represented the concentration of tens of particles, whereas, in flow diverter stents, it could result from just two or three particles moving along separate streamlines that briefly crossed. Comparing quantitative data from flow diverter stents with that from coronary stents (Figures 4.17 and 5.6) is problematic as it is difficult to distinguish between large areas of low density which were a by-product of high concentration, and those which were simply due to low particle numbers. At face value, particle tracking data from flow diverter stents looks comparable to that from many coronary stents. However, when the above is taken into account the former appear more like empty control tubes (albeit with far fewer tracked particles). These results may be due to the stents diverting flow away from the wall, as they are designed to do *in vivo* and are observed to do in separate *in vitro* and *in silico* models [27][28][210]. As detailed in Section 2.3, the bottommost stent struts are brought into focus prior to image acquisition and only particles within focal range are tracked. Thus, if flow diverter stents are diverting and concentrating the bulk of the particles toward the centre of the vessel, only a small number of particles will remain in the suspension's fluid phase local to the wall where data is gathered.

In comparison to empty control models, the accumulation of particles over time was greatly reduced in the Leo stent, again possibly due to the diversion of flow away from the wall. In contrast, accumulation was increased in the Silk stent (Figure 5.7) and equivalent to that within the majority of coronary stents after equal time, despite half the number of particles flowing through the smaller 2 mm diameter model. This could be due to the loose, disordered end struts, where peaks in accumulation were seen. It has been suggested that the used of braided stents with untrimmed edges should be minimised in clinical practice, as any tendency for these areas to be focal

points of cell or plaque accumulation could increase (or potentially be responsible for) the heightened risk of thrombus formation within flow diverter stents [113].

Cell migration studies were performed on flow diverter stents deployed within 2 mm diameter models and connected to the peristaltic pump system. As per coronary stent models, success rates were low. However, samples sizes of n=3 (Silk) and n=2 (Leo) met the minimum experiment threshold of 24 hours. In addition, a Silk stent sample met the maximum experiment duration of 72 hours. As mentioned in Section 3.6, in order to model a sufficiently denuded endothelium, flow diverter stents were deployed within model vessels in which there was a clear boundary between an attached HUVEC monolayer and bare vessel wall. While coronary stents were deployed with their leading edge as close to this boundary as possible, flow diverter stents were deployed with the boundary midway along their length. This alteration to the protocol as described in Section 2.2.4 was altered after initial experiments revealed the disordered geometry of loose, prolapsed struts at the ends of interwoven meshes (particularly within the Silk stent, illustrated in Figure 5.2). The random nature of this structure impaired the ability to compare between repeat experiments of the same design, as the difference in geometry between deployments was even more pronounced than that seen between coronary stents. Additionally, these regions were prone to debris collection which hindered the identification and imaging of HUVEC. The decision was made to begin cell migration assays from a point within the stent, of more ordered, regular strut geometry, to aid comparison between models. This was considered a valid approach as, unlike coronary stents which are deployed in sections of diseased artery, flow diverter stents are deployed within arteries that (other than the aneurysm neck) are relatively endothelialised [29]. Combined with the gentle expansion of flow diverter stents, it can therefore be reasonably assumed that EC will be present within the stent following deployment. However, as EC migration is still required to properly endothelialise stent struts and reduce the risk of thrombus formation [34][62], studying flow diverter stents in the manner described here remains relevant. Applying the protocol described in Section 2.2 to flow diverter stents also provided an interesting contrast to the results obtained in experiments using dissimilar coronary stent geometry.

In each of the cell migration experiments performed, no movement of the HUVEC monolayer or individual leader cells was seen, at any time point up to and including 72 hours (Figures 5.13 and 5.14). In comparison, in each successful experiment with empty control vessels (Section 3.3.2) and deployed coronary stents (Section 4.4.1) migration of a monolayer and/or individual leader cells of some extent was observed. This included individual leader cells within coronary stent structure (Figure 4.26).

Identifying HUVEC was more difficult between the denser struts of flow diverters in comparison to the open inter-strut regions of coronary stents. The use of a fluorescent dye and portable light system was trialled (Section 3.3.3) but individual cells were dim and locating anything other than the bulk monolayer was not possible (Figure 3.12). With practice, brightfield microscopy under higher magnification was used to confirm the lack of migration, by locating individual cells upstream of the initial seeding point and discerning them from gradually accumulating debris downstream (Figure 5.15).

The lack of cell migration could be due to flow diverter stent structure, as opposed to issues with overall cell viability or the PDMS model, as normal cell behaviour was observed upstream of both the Silk and Leo stents. It was noted that the stent introducer sheath used during the deployment of flow diverter stents was wider than the catheter guide wires used to insert coronary stents. Thus, the tip of the sheath tended to scrape the model vessel wall on insertion. This created wounds in the HUVEC monolayer upstream of the stent (the monolayer local to the initial seed point, underneath the body of the sheath, remained intact as was confirmed prior to each experiment). Reassuringly, these wounds were observed to close within the first 24 hours of experiments (Figure 5.16). Confluent monolayers were maintained for the remaining duration of the experiments, so it is unlikely that the lack of HUVEC migration was due to detrimental cell health or viability.

Simulating fluid flow through an *in silico* model of a Silk stent created from μCT data allowed wall shear stress to be analysed and compared to the results of cell migration studies from Section 5.4. This aspect of local mechanical conditions could not be revealed by *in vitro* particle tracking data. The Silk stent showed a high AWA-WSS of 1.34 Pa. As in coronary stent models, this was skewed by high shear

stress on the luminal surface of stent struts (Figure 5.10A). This may have had an even greater effect in the Silk model, as the dense mesh of more prolapsed struts had a larger contribution to the model's total area. Therefore, the AWA-WSS was not a useful indication of the conditions found on the wall of the vessel only.

Considering the wall alone, a pattern similar to that seen within coronary stents was identified (Figure 5.10B). Areas of greatly reduced wall shear stress (<0.1 Pa) were found immediately up and downstream of struts. However, the dense mesh in flow diverter stents increased the number of such areas along the vessel length, in comparison to thicker, but more spaced coronary stent struts. Wall shear stress magnitude began to recover in between struts but could reach no more than 0.5 Pa, 50% of the applied 1 Pa. This was again due to the dense mesh reducing the distance between struts within which flow recovery could take place. The overall effect was a wider area of reduced wall shear stress and a more homogeneous distribution compared to that found within coronary stents.

Wall shear stress in coronary stents was reduced when fluid moved up and over struts and the horizontal component of flow velocity decreased (Section 4.3.1). This phenomenon was more pronounced in the Silk stent due to the presence of a gap between the struts and wall (Figure 5.11). Large gaps were often seen after *in vitro* flow diverter deployment (Section 5.1.2) and this may be a trait of the *in vitro* model. More compliant cerebral artery tissue [21], or the remodelling of stented vessels, might eliminate any substantial gap between strut and wall *in vivo*. Yet, weak expansion of the Silk stent in clinical application has been reported [31][32]. To avoid this issue in this project, only well-expanded stents were used for *in vitro* experiments, subsequent scanning and *in silico* modelling. However, even in optimal examples small gaps between struts and vessel wall were unavoidable due to the woven structure of the stents. Each strut in contact with the wall had another strut moving over it, which was kept apart from the wall by a distance equal to the diameter of the lower strut. This pattern was repeated throughout the entire stent and the problem was amplified where numerous thin struts met and crossed over the four thicker struts. Thus, the recovery of undisturbed flow (and therefore wall shear stress) in the already small inter-strut regions was further hindered by the increased distance to the wall (Figure 5.11).

The ever present gap between flow diverter stent struts and vessel wall also meant that plotting along reference lines, to obtain specific values of wall shear stress magnitude and to visualise how shear stress altered with stent geometry along vessel length (as per Figure 4.22), was not possible for the Silk stent model. This method returned shear stress data from every boundary along the reference line. At any given location along the line within well-apposed coronary stents, this resulted in one data point (from the wall/fluid or stent/fluid boundary). In flow diverter stents, the interweaving of struts and the gap between them and vessel wall increased the number of potential boundaries at any given location (e.g. wall/fluid, bottom of lower strut/fluid, top of lower strut/fluid, bottom of upper strut/fluid, etc.). Wall shear stress data from the wall/fluid boundary only could not be isolated.

In coronary stents, migration studies revealed reduced cell movement and computational analysis revealed a low wall shear stress environment and disturbed flow. This agrees well with the bulk of literature which finds EC behaviour, including migration, is dysfunctional in regions of low shear stress [89][163]. Although wall shear stress was reduced further in the Silk flow diverter stent in terms of the amount of wall area exposed to <0.5 Pa, the absolute lowest magnitudes of shear stress found local to struts, and the amount of wall exposed to those minimum levels, was not dissimilar to coronary stents. However, rather than reduced cell movement, *in vitro* studies of flow diverter stents showed a complete lack of cell migration (Figures 5.13 and 5.14). It would be difficult to conclude, therefore, that the differences seen between these simulations could have such a profound effect on EC.

Previous studies have seen cell migration at both 0.2 and 0.3 Pa wall shear stress [95][127]. It could be reasoned that, as per these studies, HUVEC within flow diverter stents were in motion, but net downstream migration was zero due to low persistence caused by bidirectional mechanical cues (as described in Section 1.4.4). The use of a ROCK inhibitor with flow diverter stents would have been of interest, to observe whether cell movement of any magnitude occurred once these cues were silenced [103]. However, ROCK inhibition experiments were carried out using the ibidi pump system, requiring 1.5 mm diameter models. The 2 mm diameter flow

diverter stents required deployment within vessels of identical size to avoid acute under expansion. Therefore, the introducer sheaths of the available flow diverter stents were unfortunately too tight a fit for 1.5 mm diameter models.

It may also be possible that the lack of cell migration in flow diverter stents is due to a factor, or factors, other than wall shear stress (mass transport volume at the vessel wall, perhaps, or particle residence time) which does not have the same influence or effect in coronary stents. By focusing primarily on variation in wall shear stress magnitude or direction, the bulk of literature rarely considers such factors and, by using mock coronary stent geometry (or simple, empty parallel plate models), cannot recreate them. This, therefore, illustrates the advantage of the novel model and protocol described in this work, in enabling not only the assessment and direct comparison of clinical-grade stent geometry, but of stents of greatly differing design, type and purpose. Furthermore, in applying a more physiologically relevant flow and allowing haemodynamic variation to be generated by stent geometry (rather than the use of separate, distinct flow rates), additional geometry-induced haemodynamic factors and effects may reveal themselves.

However, a more straightforward answer to the discrepancy between the results of cell migration studies and computational analysis may lie in the way the Silk stent was cast and modelled *in silico* in this study. As mentioned in Section 3.5.4 an accurate, undamaged cast could only be created by pulling stent struts out of the lumen. This required the removal of both ends of the stent and resulted in a cast representing only the middle third of the Silk stent structure. Furthermore, the complexity of the *in silico* model created from high resolution μCT data imposed the aforementioned requirement of only simulating flow through half of the model (Section 5.3 and Figure 5.9). Therefore, simulation results were firstly not representative of the entire stent, and secondly may have been unique to the geometry of the specific half of the stent being modelled.

Simulation results were not representative of the entire Silk stent as the cast and *in silico* model did not capture the struts at the leading edge. This was not the region of interest, as HUVEC were seeded midway along the stent. Yet the prolapsed, disordered struts at the front of the stent must surely impact downstream flow, an

effect that could not be considered in the *in silico* model. Nor did the model consider the detrimental effect of the presence of sequential, more regular struts upstream (as shown in coronary stent data, Figure 4.22), as the struts captured in the *in silico* model were essentially considered as the stent's leading edge.

Simulation results may have been unique to the geometry of the specific half of the stent being modelled as, due to the Silk stent's criss-cross pattern, each half contained a different alignment of thicker struts. These struts were in contact with the vessel wall and the degree to which differing alignment diverted or funnelled flow would have an effect on the shear stress of the vessel wall behind them. This effect is illustrated in Figure 5.17, and can be seen in the distribution of wall shear stress in Figure 5.10B. Although the flow between struts and wall was greatly reduced, it may still have been overestimated where the gap was open to the oncoming fluid. The result of this overestimated flow, within the reduced volume of the strut-wall gap, would be elevated wall shear stress.

Taking these factors into account, it could be proposed that the mechanical environment within the Silk stent is actually much worse, in terms of induced EC dysfunction, than the CFD simulations suggest. Local wall shear stress may have been greatly overestimated and, as such, the true environment within the stent *in vitro* could be severe enough to completely arrest HUVEC migration.

As per the conclusions drawn in Section 4.5, the ability of the stent to perform its primary function is paramount, but vessel healing could be improved by taking haemodynamics into account during the design phase where possible. When considering flow diverter stents however, their specific task is to exert a direct effect on blood flow and local haemodynamics is already a crucial design consideration. The stents considered in this chapter must prevent, or reduce, blood flow within cerebral aneurysms and, in doing so, cannot discriminate between diverting flow away from the neck and away from the otherwise unaffected vessel wall. Therefore, all of the above, including the lack of HUVEC migration, the low numbers of tracked particles, the reduced effect on the motion of those particles, and reduced wall shear stress, may be regarded simply as a consequence of flow diverter stents doing the job they were designed for, and diverting flow.
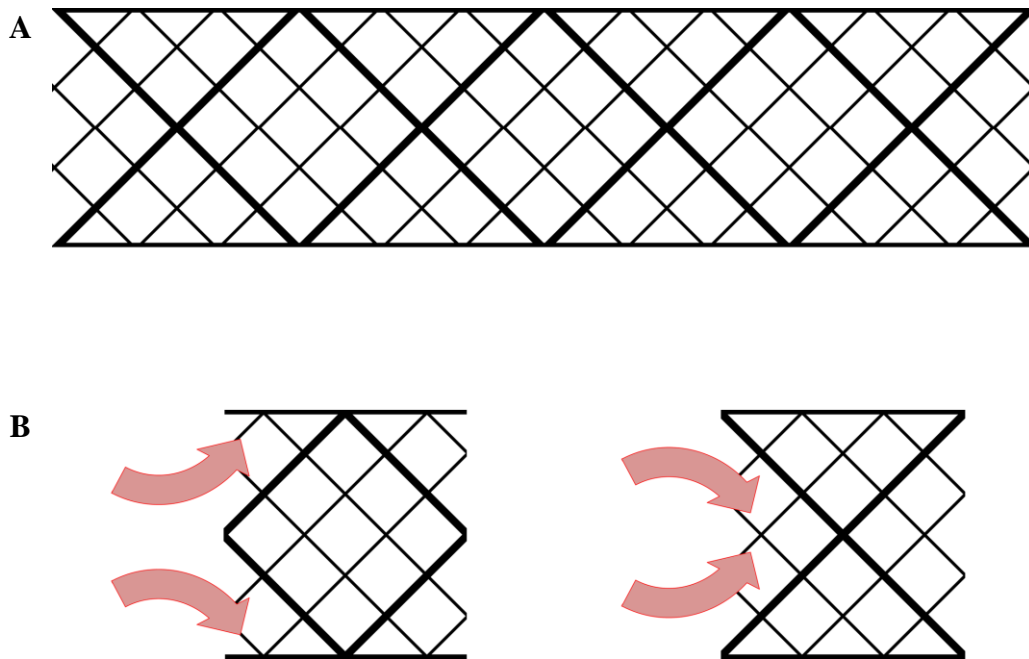
Figure 5.17 The impact of stent structure selection on CFD simulations

The entire length of Silk flow diverter stents could not be captured in PDMS casting. In addition, due to the size and complexity of the model, computational simulations of Silk flow diverter stents were performed on half of the model only (with a plane of symmetry applied). The geometry of the specific section selected for modelling could impact the final results, depending on the position of thicker struts which were in contact with the wall.

A: Representative geometry of a full flow diverter stent.

B: Wall shear stress data from CFD simulations could be affected by the position of thick struts in the smaller regions selected for modelling. Oncoming flow (arrows) could be diverted away from the wall (left), or the wall could be open to this flow (right).

Nonetheless, even if flow diverter stent haemodynamics cannot be modified, it (and its effect on cell migration) must at least be properly understood. The development of the novel model and protocol described in this work, and its ability to apply various techniques to study and compare stents not only of varying design but different type and function, can again contribute to that objective.

Chapter Six

Discussion

This project aimed to create an experimental platform, consisting of a novel model vessel and a unique combination of *in vitro* and *in silico* techniques, to study the impact of stent geometry on local wall shear stress and endothelial cell migration. Vessels of circular cross-section and typical artery diameter were fabricated, allowing the application of more physiologically relevant flow conditions than microfluidic parallel plate studies. The physical properties of PDMS enabled the deployment of coronary and flow diverter stents, in addition to the attachment and real-time monitoring of EC. An advantage of *in vitro* modelling was highlighted by the ability to provide an initial cell-free area in which to monitor migration. As discussed in Section 1.6.1, *in vivo* studies require some effort to induce vascular disease [121][122]. Porcine and small mammal arteries are therefore in good health and even intentionally forceful stent deployment cannot create cell-free zones in which to assess reendothelialisation [103].

The simple, rapid manufacture of model vessels and flow system set-up allowed a number of different cardiovascular stent designs to be studied. EC migration in coronary stents was reduced, particularly at areas of low or oscillatory wall shear stress, which compared favourably to the results of previous studies [103][114]. No EC migration was observed in flow diverter stents. CFD analysis showed decreased wall shear stress in these models and it has already been discussed that the true *in vitro* environment may be even more hostile to EC function (Section 5.5). However, endothelialisation of flow diverter stents is seen clinically, suggesting fundamental differences between *in vivo* conditions and the *in vitro* model. One of the most notable differences is the duration of interest. Endothelialisation *in vivo*, whether by healthy, local EC migration or EPC accumulation, can take months [29][211]. It may therefore not be unusual to see no visible movement of cells in an experiment of only 3 days. An additional difference is that flow diverters were deployed in a model which was primarily designed to represent coronary arteries which included, as

mentioned above, denuded areas. As illustrated in Section 3.3.1, stent deployment over an EC layer *in vitro* did not injure the cells and, *in vivo*, islands of EC remain following flow diverter stent implantation [62]. Local cells at stent deployment sites could potentially endothelialise struts with little net migration required.

If, however, the results of these *in vitro* migration studies were taken as accurate and relevant, they could be considered important in the context of clinical treatment. As the devices are a more recent development, the post-operative protocols for flow diverter stents essentially borrow from those developed for coronary stents (indeed, the first flow diversion procedures were performed using coronary stents [23]), which include the use of medication to inhibit VSMC [24]. In coronary stents the collateral inhibition of EC is deemed to be acceptable given the high risk of ISR. In contrast, flow diverter stent deployment does not cause injury to the vessel wall, VSMC are not exposed and, as such, ISR is of less concern. The high metal content of flow diverter stents means that thrombosis poses the greater risk [24], and stent strut endothelialisation is vital. The potential issue, therefore, is that an effort to reduce a negligible ISR risk (such as the use of anti-proliferative treatment, in a similar manner to coronary stent treatment strategies) could actually increase the heightened risk of thrombosis by further hindering the migration of EC, which are already inhibited by local haemodynamic forces (or a lack thereof).

Particle tracking revealed stark differences regarding the various tested stents' effect on flow. However, there was no significant link between these differences and the aspects of stent design studied here, and there were noticeable disparities between stents of identical geometry. Furthermore, the limited cell migration data did not allow a comparison between EC migration and specific stent design. This method did show that stent geometry affects local flow patterns and that EC are affected by disturbed flow and modified shear stress. However, beyond gross structural differences (i.e. those between coronary and flow diverter stents) the model may not be sensitive enough to identify the contribution or action of small scale design features (i.e. those between different models of the same stent type).

This situation may be optimised by the continued development and improvement of the *in vitro* model. Any increase in experiment success rate would be valuable and

could reduce any noise seen in results which may be obscuring trends or relationships. One particular drawback of this study is the low sample size, as the limited pool of available stents was further reduced by the small number of EC migration experiments that reached the 24 hour time point. The solution may be as simple as altering the system: a greater success rate was achieved with the ibidi system, which was self-contained and compact enough to sit within laminar flow hoods and CO_2 incubators. A peristaltic pump was required for larger diameter vessels, but set-up was more complex and tubing was prone to wear. In addition, the peristaltic pump could not be placed in an incubator and the thick tubing prevented CO_2 incubator doors from closing. 2 and 2.5 mm diameter models were therefore only able to fit within modified egg incubators. These smaller egg incubators did not supply CO_2, and as such the optimum pH of EC growth medium could not be maintained. This was not thought to be an issue given the short duration of experiments and the fact that those which were successful, although less frequent, performed as well as models attached to the ibidi system. A buffer could have been added to peristaltic pump reservoirs to preserve pH, but this was not carried out as these compounds can have their own effects on cell growth and metabolism [157]. The need for a fibronectin coating for EC attachment meant that each *in vitro* model was single-use, as discussed in Section 3.6. If this could have been avoided then repeat experiments would have increased sample sizes, however in all other respects PDMS was the most suitable material available for *in vitro* modelling.

In studying the effects of stent geometry on haemodynamics and EC migration, an *in vitro* model of increased sensitivity may have its own disadvantages. Many of the small scale design features considered in the tested stents (strut thickness for example) differed by a few tens of microns. Any model sensitive enough to resolve the differential effects of these changes would also detect features specific to realistic stent deployment (malapposed struts, varying penetration or prolapse, etc.), which cannot be controlled. In addition, stents contain complex geometry. It may prove difficult to identify which design parameters cause certain effects, to take into account effects which are compounded as flow moves downstream through stents,

and to appreciate the knock-on consequences of altering parameters on other aspects of the structure.

This highlights an advantage of parametric study with simpler models. One option to better understand the effects of specific stent design features could be to combine the mock stent geometry used in parallel plate studies with the *in vitro* system used here. The shape, thickness, orientation and density of ridges, representing stent struts, could be controlled at the fabrication stage, while EC within the model would still be exposed to more physiologically relevant flow in a full-sized vessel of circular cross-section. Alternatively, there is also plenty of scope for added realism as *in vitro* models are far from perfect representations of *in vivo* conditions. Noted drawbacks include the obvious lack of circulating blood, as well as circulating cells, platelets and leukocytes. Furthermore, current models do not replicate additional components such as VSMC, extracellular matrix, and vessel media and adventitia [107][131].

A combination of different PDMS mixing ratios or additional material could be used to model the various layers of the vessel wall, or areas of plaque and stenosis. The geometry of model vessels could also be made more realistic by removing material to create aneurysm sacs, or by modelling branch points or curvature [204]. Patient specific geometry, obtained from clinical scans, has been modelled *in silico* [172]. These computational models could be used to create physical moulds, via 3D printing, for the fabrication of patient specific *in vitro* vessels.

The realism of experimental conditions could be improved with the application of physiological flow rates (requiring the use of thickening agents, as discussed in Chapter 3) and pulsatile flow. Again, *in vivo* cardiac rhythm has already been measured and applied to *in silico* models [103] and the same could be done *in vitro* with programmable pump and control systems. The cellular environment could be better represented by seeding HCAEC and the isolation of VSMC could allow co-culture within model vessels [99]. An EC suspension could be circulated through the model to simulate endothelialisation by EPC accumulation, although given the success rates of standard cell attachment this may not prove viable.

CFD analysis proved to be a useful complementary tool and μCT scanning of PDMS casts was an efficient means of replicating the geometry of stented vessels *in silico*. The technique may yet be optimised. The impact of scan power and, more

importantly, resolution on the accuracy of the final *in silico* model should be more carefully studied, as should the effect of reconstruction and meshing parameters. The creation of stepwise geometry should be reduced as stagnation points are created where flow meets blunt faces [208], and the threshold beyond which increased resolution does not improve the model should be discovered.

As per the *in vitro* system, improvements can be made to the CFD protocol. The added benefit of *in silico* modelling is that the original information is not lost and many of these improvements can be made retroactively. The application of a UDF at the centre of the model inlet to create fully-developed flow allowed the use of smaller, less computationally expensive meshes. However, as stent deployment often distorted vessels their inlets were rarely of perfect circular cross-section. Velocity (and therefore wall shear stress) could be unrealistically high where the parabolic profile applied by the UDF crossed the wall, or zero where it fell short. These issues were limited to the initial upstream segments of *in silico* models and viscous effects would rapidly normalise the flow, but it was still necessary to extend the models somewhat (increasing their complexity and computational expense) to ensure the disturbances were kept away from stent geometry.

Steady Newtonian flow was used in this project but realistic pulsatile flow of non-Newtonian fluid could be simulated, allowing time-dependent metrics such as TAWSS and OSI to be obtained. Simulations by Balossino *et al* (2008), which were discussed in Section 1.6.5, showed wall shear stress increasing with stent strut thickness [167]. These results are in stark contrast to the rest of the literature, and are presumed to be due to the combined use of both realistic pulsatile flow and realistic deformed vessel geometry. It is clear that flowing blood creates a different haemodynamic environment than that which EC are exposed to in cell culture medium, as illustrated in Section 4.3.2. However, Balossino's results suggest that it may also create a completely different relationship between stent structure and wall shear stress than that which is found *in vitro*. Perhaps then, a dual approach is best. Complex, realistic *in silico* geometry and flow could reveal the impact of stent design on wall shear stress magnitude, direction and time variation, while simple, idealised *in vitro* and *in silico* models could explore how EC are likely to respond under those conditions.

A full understanding of the link between stent structure, wall shear stress, and EC behaviour, obtained with reliable, fully developed *in vitro* and *in silico* models, could be used to optimise existing stent designs, or predict the effect of novel designs on endothelialisation. The same techniques could be used to trial novel devices such as the 'Instent' sensor which can inform post-operative treatment by analysing stent coverage *in vivo* [212], and may also be applied to the study of other related subjects: monitoring the breakdown of bioabsorbable stents [72][213], assessing DES drug release and its influence on EC [67][214], modelling nanoparticle accumulation [209] and biofouling [215], and assessing pro-EC stent coatings [8][54].

By allowing the assessment of clinical-grade stents of varying design, type and purpose, and enabling the application of mechanical conditions of increased physiological relevance, the novel platform developed here could be seen as a test bed for techniques which, like many others, could play a role in characterising the complex biomechanics and biochemistry of stented arteries. Furthermore, as the relevant fabrication, experimental, or simulation protocols could modified without compromising separate procedures or overall workflow, any or all of the developments and improvements detailed previously could be applied to the *in vitro* and *in silico* models, in any combination. Indeed, of late, the work of Antoine *et al* has demonstrated the use of both co-culture (EC and VSMC) and a 3D engineered tissue (an SMC-embedded hydrogel) within a stented *in vitro* vessel [160], techniques which could be readily applied here.

In the future, as our knowledge and the capability of our clinical, computational and manufacturing tools increases, there may be a point at which patient recovery is hastened by the use of personalised tailor-made stents. The same scan data used to diagnose cardiovascular disease could be used as the basis of a virtual model, in which a variety of stent designs are trialled and refined to create the most pro-EC haemodynamic environment. Surgeons could be offered the most suitable off-the-shelf stent, or individual devices could be rapidly manufactured for each patient as they await surgery. Until such a time, as millions of people receive stents each year, any small improvement in their impact on vascular repair could reduce mortality and improve quality of life.

References

[1] "Cardiovascular disease fact sheet," *World Health Organisation*, 2017. [Online]. Available: http://www.who.int/mediacentre/factsheets/fs317/en/.

[2] O. L. Wade and J. M. Bishop, *Cardiac output and regional blood flow*. F. A. Davis Company, Philadelphia, 1962.

[3] C. J. Pepine, "The effects of angiotensin-converting enzyme inhibition on endothelial dysfunction: potential role in myocardial ischemia," *Am. J. Cardiol.*, vol. 82, no. 9, p. 23S–27S, 1998.

[4] F. Otsuka, S. Yasuda, T. Noguchi, and H. Ishibashi-Ueda, "Pathology of coronary atherosclerosis and thrombosis," *Cardiovasc. Diagn. Ther.*, vol. 6, no. 4, pp. 396–408, 2016.

[5] L. Badimon and G. Vilahur, "Thrombosis formation on atherosclerotic lesions and plaque rupture," *J. Intern. Med.*, vol. 276, no. 6, pp. 618–632, 2014.

[6] R. E. Klabunde, *Cardiovascular Physiology Concepts*. Lippincott Williams & Wilkins, 2003.

[7] M. D. Huffman, D. M. Lloyd-Jones, H. Ning, D. R. Labarthe, M. G. Castillo, M. O'Flaherty, E. S. Ford, and S. Capewell, "Quantifying options for reducing coronary heart disease mortality by 2020," *Circulation*, vol. 127, no. 25, pp. 2477–2484, 2013.

[8] J. Iqbal, J. Gunn, and P. W. Serruys, "Coronary stents: historical development, current status and future directions," *Br. Med. Bull.*, vol. 106, pp. 193–211, Jan. 2013.

[9] J. Gunn, N. Arnold, K. H. Chan, L. Shepherd, D. C. Cumberland, and D. C. Crossman, "Coronary artery stretch versus deep injury in the development of in-stent neointima," *Heart*, vol. 88, no. 4, pp. 401–5, Oct. 2002.

[10] P. F. Ludman, *National audit of percutaneous coronary interventional procedures*. National Institute for Cardiovascular Outcomes Research, London, 2011.

[11] H. M. M. van Beusekom and P. W. Serruys, "Drug-eluting stent endothelium: presence or dysfunction.," *JACC Cardiovasc. Interv.*, vol. 3, no. 1, pp. 76–7, Jan. 2010.

[12] N. Duraiswamy, R. T. Schoephoerster, M. R. Moreno, and J. E. Moore, "Stented artery flow patterns and their effects on the artery wall," *Annu. Rev. Fluid Mech.*, vol. 39, no. 1, pp. 357–82, Jan. 2007.

[13] P. Hindlet, C. Fargeot, J.-M. Juliard, and R. Farinotti, "Coronary stents: choice criteria and elaboration of a technical standard sheet," *J. Pharm. Clin.*, vol. 24, no. 1, pp. 40–6, 2005.

[14] A. C. Morton, D. Crossman, and J. Gunn, "The influence of physical stent parameters upon restenosis," *Pathol. Biol.*, vol. 52, no. 4, pp. 196–205, May 2004.

[15] M. H. Wholey and E. A. Finol, "Designing the ideal stent," *Endovascular Today*, no. March, pp. 25–34, 2007.

[16]   H. Zhao, J. Van Humbeeck, J. Sohier, and I. De Scheerder, "Electrochemical polishing of 316L stainless steel slotted tube coronary stents," *J. Mater. Sci. Mater. Med.*, vol. 13, no. 10, pp. 911–916, 2002.

[17]   G. Mani, M. D. Feldman, D. Patel, and C. M. Agrawal, "Coronary stents: a materials perspective," *Biomaterials*, vol. 28, no. 9, pp. 1689–710, Mar. 2007.

[18]   E. Nikolsky, L. Gruberg, S. Pechersky, M. Kapeliovich, E. Grenadier, S. Amikam, M. Boulos, M. Suleiman, W. Markiewicz, and R. Beyar, "Stent deployment failure: reasons, implications, and short- and long-term outcomes," *Catheter. Cardiovasc. Interv.*, vol. 59, no. 3, pp. 324–328, 2003.

[19]   D. M. Wiktor, S. W. Waldo, and E. J. Armstrong, "Coronary stent failure," *Interv. Cardiol. Clin.*, vol. 5, no. 3, pp. 405–414, 2016.

[20]   K. B. Chandran, S. E. Rittgers, and A. P. Yoganathan, *Biofluid Mechanics: The Human Circulation*. CRC Press, 2012.

[21]   M. J. Cipolla, *The Cerebral Circulation*. Morgan & Claypool Life Sciences, 2009.

[22]   A. L. Georgiadis, M. D. Ford, D. A. Steinman, N. Tariq, and A. I. Qureshi, "Intracranial aneurysms," in *Textbook of Interventional Neurology*, Cambridge University Press, 2011.

[23]   C. Krishna, A. Sonig, S. K. Natarajan, and A. H. Siddiqui, "The expanding realm of endovascular neurosurgery: flow diversion for cerebral aneurysm management," *Methodist Debakey Cardiovasc. J.*, vol. 10, no. 4, pp. 214–9, 2014.

[24]   Y. J. Alderazi, D. Shastri, T. Kass-Hout, C. J. Prestigiacomo, C. D. Gandhi, Y. J. Alderazi, D. Shastri, T. Kass-Hout, C. J. Prestigiacomo, and C. D. Gandhi, "Flow diverters for intracranial aneurysms," *Stroke Res. Treat.*, vol. 2014, p. e415653, 2014.

[25]   A. M. Brouillard, X. Sun, A. H. Siddiqui, and N. Lin, "The use of flow diversion for the treatment of intracranial aneurysms: expansion of indications," *Curēus*, vol. 8, no. 1, p. e472, 2016.

[26]   B. B. Lieber, V. Livescu, L. N. Hopkins, and A. K. Wakhloo, "Particle image velocimetry assessment of stent design influence on intra-aneurysmal flow," *Ann. Biomed. Eng.*, vol. 30, no. 6, pp. 768–77, 2002.

[27]   L. Augsburger, M. Farhat, P. Reymond, E. Fonck, Z. Kulcsar, N. Stergiopulos, and D. A. Rüfenacht, "Effect of flow diverter porosity on intraaneurysmal blood flow," *Clin. Neuroradiol.*, vol. 19, no. 3, pp. 204–14, 2009.

[28]   M. H. Babiker, L. F. Gonzalez, J. Ryan, F. Albuquerque, D. Collins, A. Elvikis, and D. H. Frakes, "Influence of stent configuration on cerebral aneurysm fluid dynamics," *J. Biomech.*, vol. 45, no. 3, pp. 440–7, 2012.

[29]   M. Marosfoi, E. T. Langan, L. Strittmatter, K. van der Marel, S. Vedantham, J. Arends, I. R. Lylyk, S. Loganathan, G. M. Hendricks, I. Szikora, A. S. Puri, A. K. Wakhloo, and M. J. Gounis, "*In situ* tissue engineering: endothelial growth patterns as a function of flow diverter design," *J. Neurointerv. Surg.*, 2016.

[30]   I. Szikora, Z. Berentei, Z. Kulcsar, M. Marosfoi, Z. S. Vajda, W. Lee, A.

Berez, and P. K. Nelson, "Treatment of intracranial aneurysms by functional reconstruction of the parent artery: the Budapest experience with the pipeline embolization device," *Am. J. Neuroradiol.*, vol. 31, no. 6, pp. 1139–47, 2010.

[31] J. Berge, A. Biondi, P. Machi, H. Brunel, L. Pierot, J. Gabrillargues, K. Kadziolka, X. Barreau, V. Dousset, and A. Bonafé, "Flow-diverter silk stent for the treatment of intracranial aneurysms: 1-year follow-up in a multicenter study," *Am. J. Neuroradiol.*, vol. 33, no. 6, pp. 1150–5, 2012.

[32] J. E. Cohen, J. M. Gomori, S. Moscovici, R. R. Leker, and E. Itshayek, "Delayed complications after flow-diverter stenting: reactive in-stent stenosis and creeping stents," *J. Clin. Neurosci.*, vol. 21, no. 7, pp. 1116–1122, 2014.

[33] M. Zenteno, A. Lee, J. L. H. Bejarano, G. D. Satyarthee, H. R. Alvis-Miranda, and L. R. Moscote-Salazar, "When flow diverters fail: short review and a case illustration of a device failure," *Rom. Neurosurg.*, vol. 30, no. 4, pp. 467–474, 2016.

[34] W. Brinjikji, M. H. Murad, G. Lanzino, H. J. Cloft, and D. F. Kallmes, "Endovascular treatment of intracranial aneurysms with flow diverters: a meta-analysis," *Stroke*, vol. 44, no. 2, pp. 442–447, 2013.

[35] J. R. Levick, *An Introduction to Cardiovascular Physiology*. Butterworth & Co Ltd., 1991.

[36] N. G. dela Paz and P. A. D'Amore, "Arterial versus venous endothelial cells," *Cell Tissue Res.*, vol. 335, no. 1, pp. 5–16, Jan. 2009.

[37] S. Obi, K. Yamamoto, N. Shimizu, S. Kumagaya, T. Masumura, T. Sokabe, T. Asahara, and J. Ando, "Fluid shear stress induces arterial differentiation of endothelial progenitor cells," *J. Appl. Physiol.*, vol. 106, no. 1, pp. 203–11, 2009.

[38] D. B. Cines, E. S. Pollak, C. A. Buck, J. Loscalzo, G. A. Zimmerman, R. P. McEver, J. S. Pober, T. M. Wick, B. A. Konkle, B. S. Schwartz, E. S. Barnathan, K. R. McCrae, B. A. Hug, A.-M. Schmidt, and D. M. Stern, "Endothelial cells in physiology and in the pathophysiology of vascular disorders," *J. Am. Soc. Hematol.*, vol. 91, no. 10, pp. 3527–3561, 1998.

[39] Y. Nakayama, S. Nishi, and H. Ishibashi-Ueda, "Fabrication of drug-eluting covered stents with micropores and differential coating of heparin and FK506," *Cardiovasc. Radiat. Med.*, vol. 4, no. 2, pp. 77–82, 2003.

[40] R. A. Byrne, M. Joner, and A. Kastrati, "Stent thrombosis and restenosis: what have we learned and where are we going?," *Eur. Heart J.*, vol. 36, no. 47, pp. 3320–3331, 2015.

[41] C. Chaabane, F. Otsuka, R. Virmani, and M.-L. Bochaton-Piallat, "Biological responses in stented arteries," *Cardiovasc. Res.*, vol. 99, no. 2, pp. 353–63, Jul. 2013.

[42] E. R. Edelman and C. Rogers, "Pathobiologic responses to stenting," *Am. J. Cardiol.*, vol. 81, no. 7A, p. 4E–6E, Apr. 1998.

[43] K. Van der Heiden, F. J. H. Gijsen, A. Narracott, S. T. Hsiao, I. Halliday, J. Gunn, J. J. Wentzel, and P. C. Evans, "The effects of stenting on shear stress: relevance to endothelial injury and repair," *Cardiovasc. Res.*, vol. 99, no. 2,

pp. 269–75, Jul. 2013.

[44] T. Ramanathan and H. Skinner, "Coronary blood flow," *Contin. Educ. Anaesthesia, Crit. Care Pain*, vol. 5, no. 2, pp. 61–4, Apr. 2005.

[45] L. H. Timmins, M. W. Miller, F. J. Clubb, and J. E. Moore, "Increased artery wall stress post-stenting leads to greater intimal thickening," *Lab. Investig.*, vol. 91, no. 6, pp. 955–67, Jun. 2011.

[46] H. Zahedmanesh, P. A. Cahill, and C. Lally, "Vascular stent design optimisation using numerical modelling techniques," in *Applied Biological Engineering - Principles and Practice*, 2012, pp. 237–58.

[47] R. Virmani, F. D. Kolodgie, A. Farb, and A. Lafont, "Drug eluting stents: are human and animal studies comparable?," *Heart*, vol. 89, no. 2, pp. 133–8, Feb. 2003.

[48] A. Farb, D. K. Weber, F. D. Kolodgie, A. P. Burke, and R. Virmani, "Morphological predictors of restenosis after coronary stenting in humans," *Circulation*, vol. 105, no. 25, pp. 2974–2980, 2002.

[49] S. Apenberg, M. A. Freyberg, and P. Friedl, "Shear stress induces apoptosis in vascular smooth muscle cells via an autocrine Fas/FasL pathway," *Biochem. Biophys. Res. Commun.*, vol. 310, no. 2, pp. 355–359, 2003.

[50] A. K. Mitra and D. K. Agrawal, "In stent restenosis: bane of the stent era," *J. Clin. Pathol.*, vol. 59, no. 3, pp. 232–9, Mar. 2006.

[51] H. C. Lowe, S. N. Oesterle, and L. M. Khachigian, "Coronary in-stent restenosis: current status and future strategies," *J. Am. Coll. Cardiol.*, vol. 39, no. 2, pp. 183–193, 2002.

[52] P. Radke, A. Kaiser, C. Frost, and U. Sigwart, "Outcome after treatment of coronary in-stent restenosis," *Eur. Heart J.*, vol. 24, no. 3, pp. 266–73, Feb. 2003.

[53] E. A. Murphy and F. J. Boyle, "Reducing in-stent restenosis through novel stent flow field augmentation," *Cardiovasc. Eng. Technol.*, vol. 3, no. 4, pp. 353–73, 2012.

[54] H. M. M. van Beusekom, G. Ertaş, O. Sorop, P. W. Serruys, and W. J. van der Giessen, "The Genous endothelial progenitor cell capture stent accelerates stent re-endothelialization but does not affect intimal hyperplasia in porcine coronary arteries," *Catheter. Cardiovasc. Interv.*, vol. 79, no. 2, pp. 231–242, 2012.

[55] W. W. Nichols, M. F. O'Rourke, and C. Vlachopoulos, *McDonald's Blood Flow in Arteries*. Hodder Arnold, 2011.

[56] G. J. Padfield, A. Short, N. L. Mills, K. Samuel, M. Turner, D. E. Newby, G. R. Barclay, and O. Tura-Ceide, "The constituents and mechanisms of generation of 'endothelial cell - colony forming units,'" *Cardiovasc. Res.*, vol. 100, no. 2, pp. 288–296, 2013.

[57] G. Douglas, E. Van Kampen, A. B. Hale, E. McNeill, J. Patel, M. J. Crabtree, Z. Ali, R. A. Hoerr, N. J. Alp, and K. M. Channon, "Endothelial cell repopulation after stenting determines in-stent neointima formation: effects of

bare-metal vs. drug-eluting stents and genetic endothelial cell modification," *Eur. Heart J.*, vol. 34, no. 43, pp. 3378–3388, 2013.

[58] M. Tsuzuki, "Bone marrow-derived cells are not involved in reendothelialized endothelium as endothelial cells after simple endothelial denudation in mice," *Basic Res. Cardiol.*, vol. 104, no. 5, pp. 601–611, 2009.

[59] M. K. Hagensen, M. K. Raarup, M. B. Mortensen, T. Thim, J. R. Nyengaard, E. Falk, and J. F. Bentzon, "Circulating endothelial progenitor cells do not contribute to regeneration of endothelium after murine arterial injury," *Cardiovasc. Res.*, vol. 93, no. 2, pp. 223–231, 2012.

[60] M. Aguilar Pérez, P. Bhogal, E. Henkes, O. Ganslandt, H. Bäzner, and H. Henkes, "In-stent stenosis after p64 flow diverter treatment," *Clin. Neuroradiol.*, 2017.

[61] S. John, M. D. Bain, F. K. Hui, M. S. Hussain, T. J. Masaryk, P. A. Rasmussen, and G. Toth, "Long-term follow-up of in-stent stenosis after Pipeline flow diversion treatment of intracranial aneurysms," *Neurosurgery*, vol. 78, no. 6, pp. 862–867, 2016.

[62] R. Kadirvel, Y.-H. Ding, D. Dai, I. Rezek, D. A. Lewis, and D. F. Kallmes, "Cellular mechanisms of aneurysm occlusion after treatment with a flow diverter," *Radiology*, vol. 270, no. 2, pp. 394–399, 2014.

[63] Z.-F. Li, X.-G. Fang, P.-F. Yang, Q.-H. Huang, W.-Y. Zhao, C. Liang, R. Zhao, and J.-M. Liu, "Endothelial progenitor cells contribute to neointima formation in rabbit elastase-induced aneurysm after flow diverter treatment," *CNS Neurosci. Ther.*, vol. 19, no. 5, pp. 352–357, 2013.

[64] R. Hoffmann and G. S. Mintz, "Coronary in-stent restenosis - predictors, treatment and prevention," *Eur. Heart J.*, vol. 21, no. 21, pp. 1739–49, Nov. 2000.

[65] H. Hamid and J. Coltart, "'Miracle stents' - a future without restenosis," *McGill J. Med.*, vol. 10, no. 2, pp. 105–11, Jul. 2007.

[66] S. Garg and P. W. Serruys, "Coronary stents: current status," *J. Am. Coll. Cardiol.*, vol. 56, no. 10 Suppl, pp. S1-42, Aug. 2010.

[67] W. Khan, S. Farah, A. Nyska, and A. J. Domb, "Carrier free rapamycin loaded drug eluting stent: *in vitro* and *in vivo* evaluation," *J. Control. Release*, vol. 168, no. 1, pp. 70–76, 2013.

[68] R. Waksman, "Biodegradable stents: they do their job and disappear," *J. Invasive Cardiol.*, vol. 18, no. 2, pp. 70–4, Feb. 2006.

[69] A. J. Taylor, P. D. Gorman, A. Farb, T. G. Hoopes, and R. Virmani, "Long-term coronary vascular response to (32)P [beta]-particle-emitting stents in a canine model," *Circulation*, vol. 100, no. 23, pp. 2366–2372, 1999.

[70] G. Sangiorgi, G. Melzi, P. Agostoni, C. Cola, F. Clementi, P. Romitelli, R. Virmani, and A. Colombo, "Engineering aspects of stents design and their translation into clinical practice," *Ann. Ist. Super. Sanita*, vol. 43, no. 1, pp. 89–100, Jan. 2007.

[71] J. A. Ormiston and P. W. S. Serruys, "Bioabsorbable coronary stents," *Circ.*

Cardiovasc. Interv., vol. 2, no. 3, pp. 255–60, Jun. 2009.

[72] A. L. V. Løvdal, S. Calve, S. Yang, W. Van Alstine, C. A. Binkert, and K. Klausen, "Evaluation of a bioabsorbable self-expandable vein stent-base made of poly(L-lactide) *in vitro* and *in vivo*," *Cardiovasc. Intervent. Radiol.*, vol. 40, no. 1, pp. 112–119, 2017.

[73] D. N. Ku, "Blood flow in arteries," *Annu. Rev. Fluid Mech.*, vol. 29, no. 1, pp. 399–434, Jan. 1997.

[74] J. E. Moore, E. Bürki, A. Suciu, S. Zhao, M. Burnier, H. R. Brunner, and J.-J. Meister, "A device for subjecting vascular endothelial cells to both fluid shear stress and circumferential cyclic stretch," *Ann. Biomed. Eng.*, vol. 22, no. 4, pp. 416–22, 1994.

[75] E. D. O'Cearbhaill, M. A. Punchard, M. Murphy, F. P. Barry, P. E. McHugh, and V. Barron, "Response of mesenchymal stem cells to the biomechanical environment of the endothelium on a flexible tubular silicone substrate," *Biomaterials*, vol. 29, no. 11, pp. 1610–9, Apr. 2008.

[76] D. A. McDonald, *Blood flow in arteries*. Edward Arnold, London, 1960.

[77] P. C. Evans and B. R. Kwak, "Biomechanical factors in cardiovascular disease," *Cardiovasc. Res.*, vol. 99, no. 2, pp. 229–31, Jul. 2013.

[78] R. S. Rosenson, A. McCormick, and E. F. Uretz, "Distribution of blood viscosity values and biochemical correlates in healthy adults," *Clin. Chem.*, vol. 42, no. 8, pp. 1189–95, Aug. 1996.

[79] G. D. O. Lowe, A. J. Lee, A. Rumley, J. F. Price, and F. G. R. Fowkes, "Blood viscosity and risk of cardiovascular events: the Edinburgh Artery Study," *Br. J. Haematol.*, vol. 96, no. 1, pp. 168–173, 1997.

[80] P. Evans, "Blood viscosity," *Lancet*, vol. 239, no. 6180, pp. 162–6, 1942.

[81] T. G. Papaioannou and C. Stefanadis, "Vascular wall shear stress: basic principles and methods," *Hell. J. Cardiol.*, vol. 46, no. 1, pp. 9–15, 2005.

[82] J.-J. Chiu and S. Chien, "Effects of disturbed flow on vascular endothelium: pathophysiological basis and clinical perspectives," *Physiol. Rev.*, vol. 91, no. 1, pp. 327–87, 2011.

[83] R. Sinha, S. Le Gac, N. Verdonschot, A. van den Berg, B. Koopman, and J. Rouwkema, "Endothelial cell alignment as a result of anisotropic strain and flow induced shear stress combinations," *Sci. Rep.*, vol. 6, p. 29510, 2016.

[84] J. Peacock, S. Hankins, T. Jones, and R. Lutz, "Flow instabilities induced by coronary artery stents: assessment with an *in vitro* pulse duplicator," *J. Biomech.*, vol. 28, no. 1, pp. 17–26, 1995.

[85] A. M. Malek, S. L. Alper, and S. Izumo, "Hemodynamic shear stress and its role in atherosclerosis.," *JAMA J. Am. Med. Assoc.*, vol. 282, no. 21, pp. 2035–42, Dec. 1999.

[86] V. Peiffer, S. J. Sherwin, and P. D. Weinberg, "Does low and oscillatory wall shear stress correlate spatially with early atherosclerosis? A systematic review," *Cardiovasc. Res.*, vol. 99, no. 2, pp. 242–50, Jul. 2013.

[87] Y. S. Chatzizisis, A. U. Coskun, M. Jonas, E. R. Edelman, C. L. Feldman, and P. H. Stone, "Role of endothelial shear stress in the natural history of coronary atherosclerosis and vascular remodeling: molecular, cellular, and vascular behavior," *J. Am. Coll. Cardiol.*, vol. 49, no. 25, pp. 2379–93, Jun. 2007.

[88] J. García, A. Crespo, J. Goicolea, M. Sanmartín, and C. García, "Study of the evolution of the shear stress on the restenosis after coronary angioplasty," *J. Biomech.*, vol. 39, no. 5, pp. 799–805, Jan. 2006.

[89] P. H. Stone, A. U. Coskun, S. Kinlay, J. J. Popma, M. Sonka, A. Wahle, Y. Yeghiazarians, C. Maynard, R. E. Kuntz, and C. L. Feldman, "Regions of low endothelial shear stress are the sites where coronary plaque progresses and vascular remodelling occurs in humans: an *in vivo* serial study," *Eur. Heart J.*, vol. 28, no. 6, pp. 705–10, Mar. 2007.

[90] R. Mongrain and J. Rodés-Cabau, "Role of shear stress in atherosclerosis and restenosis after coronary stent implantation," *Rev. Española Cardiol.*, vol. 59, no. 1, pp. 1–4, Jan. 2006.

[91] H. Samady, P. Eshtehardi, M. C. McDaniel, J. Suo, S. S. Dhawan, C. Maynard, L. H. Timmins, A. A. Quyyumi, and D. P. Giddens, "Coronary artery wall shear stress is associated with progression and transformation of atherosclerotic plaque and arterial remodeling in patients with coronary artery disease," *Circulation*, vol. 124, no. 7, pp. 779–88, Aug. 2011.

[92] A. O. Frank, P. W. Walsh, and J. E. Moore, "Computational fluid dynamics and stent design," *Artif. Organs*, vol. 26, no. 7, pp. 614–21, Jul. 2002.

[93] S. Chien, S. Li, and J. Y.-J. Shyy, "Effects of mechanical forces on signal transduction and gene expression in endothelial cells," *Hypertension*, vol. 31, no. 1, pp. 162–9, Jan. 1998.

[94] N. Benard, D. Coisne, E. Donal, and R. Perrault, "Experimental study of laminar blood flow through an artery treated by a stent implantation: characterisation of intra-stent wall shear stress," *J. Biomech.*, vol. 36, no. 7, pp. 991–8, Jul. 2003.

[95] M. L. Albuquerque, C. M. Waters, U. Savla, H. W. Schnaper, and A. S. Flozak, "Shear stress enhances human endothelial cell wound closure *in vitro*," *Am. J. Physiol. Hear. Circ. Physiol.*, vol. 279, no. 1, pp. H293-302, Jul. 2000.

[96] J. Ando and K. Yamamoto, "Flow detection and calcium signalling in vascular endothelial cells," *Cardiovasc. Res.*, vol. 99, no. 2, pp. 260–8, Jul. 2013.

[97] S. Reitsma, D. W. Slaaf, H. Vink, M. A. M. J. van Zandvoort, and M. G. A. oude Egbrink, "The endothelial glycocalyx: composition, functions, and visualization," *Pflugers Arch. Eur. J. Physiol.*, vol. 454, no. 3, pp. 345–359, 2007.

[98] Y. C. Lim, S. R. McGlashan, M. T. Cooling, and D. S. Long, "Culture and detection of primary cilia in endothelial cell models," *Cilia*, vol. 4, p. 11, 2015.

[99] H. G. Augustin, "Methods in endothelial cell biology," *Springer Lab Manuals*, 2004.

[100] E. Tzima, M. Irani-Tehrani, W. B. Kiosses, E. Dejana, D. A. Schultz, B. Engelhardt, G. Cao, H. DeLisser, and M. A. Schwartz, "A mechanosensory complex that mediates the endothelial cell response to fluid shear stress," *Nature*, vol. 437, no. 7057, pp. 426–431, 2005.

[101] T. Nagel, N. Resnick, W. J. Atkinson, C. F. Dewey, and M. A. Gimbrone, "Shear stress selectively upregulates intercellular adhesion molecule-1 expression in cultured human vascular endothelial cells," *J. Clin. Invest.*, vol. 94, no. 2, pp. 885–91, 1994.

[102] R. Ananthakrishnan and A. Ehrlicher, "The forces behind cell movement," *Int. J. Biol. Sci.*, vol. 3, no. 5, pp. 303–17, Jan. 2007.

[103] S. T. Hsiao, T. Spencer, L. Boldock, S. D. Prosseda, I. Xanthis, F. J. Tovar-Lopez, H. van Buesekamp, R. Y. Khamis, N. Foin, N. Bowden, A. Hussain, A. Rothman, V. Ridger, I. Halliday, C. Perrault, J. Gunn, and P. C. Evans, "Endothelial repair in stented arteries is accelerated by inhibition of Rho-associated protein kinase," *Cardiovasc. Res.*, vol. 112, no. 3, pp. 689–701, 2016.

[104] B. A. Bryan, E. Dennstedt, D. C. Mitchell, T. E. Walshe, K. Noma, R. Loureiro, M. Saint-Geniez, J.-P. Campaigniac, J. K. Liao, and P. A. D'Amore, "RhoA/ROCK signaling is essential for multiple aspects of VEGF-mediated angiogenesis," *FASEB J.*, vol. 24, no. 9, pp. 3186–3195, 2010.

[105] M. Amano, M. Nakayama, and K. Kaibuchi, "Rho-kinase/ROCK: a key regulator of the cytoskeleton and cell polarity," *Cytoskeleton*, vol. 67, no. 9, pp. 545–554, 2010.

[106] A. Kastrati, J. Mehilli, J. Dirschinger, J. Pache, K. Ulm, H. Schuhlen, M. Seyfarth, C. Schmitt, R. Blasini, F.-J. Neumann, and A. Schomig, "Restenosis after coronary placement of various stent types," *Am. J. Cardiol.*, vol. 87, pp. 34–39, 2001.

[107] M. A. Punchard, E. D. O'Cearbhaill, J. N. Mackle, P. E. McHugh, T. J. Smith, C. Stenson-Cox, and V. Barron, "Evaluation of human endothelial cells post stent deployment in a cardiovascular simulator *in vitro*," *Ann. Biomed. Eng.*, vol. 37, no. 7, pp. 1322–30, Jul. 2009.

[108] N. Duraiswamy, R. T. Schoephoerster, and J. E. Moore, "Comparison of near-wall hemodynamic parameters in stented artery models," *J. Biomech. Eng. - Trans. ASME*, vol. 131, no. 6, 2009.

[109] A. Colombo, G. Stankovic, and J. W. Moses, "Selection of coronary stents," *J. Am. Coll. Cardiol.*, vol. 40, no. 6, pp. 292–301, Sep. 2002.

[110] Y. Kobayashi, J. De Gregorio, N. Kobayashi, T. Akiyama, B. Reimers, L. Finci, C. Di Mario, and A. Colombo, "Stented segment length as an independent predictor of restenosis," *J. Am. Coll. Cardiol.*, vol. 34, no. 3, pp. 651–9, Sep. 1999.

[111] S. Pant, N. W. Bressloff, A. I. J. Forrester, and N. Curzen, "The influence of strut-connectors in stented vessels: a comparison of pulsatile flow through five coronary stents," *Ann. Biomed. Eng.*, vol. 38, no. 5, pp. 1893–907, May 2010.

[112] J. F. LaDisa, L. E. Olson, I. Guler, D. A. Hettrick, S. H. Audi, J. R. Kersten,

D. C. Warltier, and P. S. Pagel, "Stent design properties and deployment ratio influence indexes of wall shear stress: a three-dimensional computational fluid dynamics investigation within a normal artery," *J. Appl. Physiol.*, vol. 97, pp. 424–30, 2004.

[113] H.-M. Hsiao, K.-H. Lee, Y.-C. Liao, and Y.-C. Cheng, "Cardiovascular stent design and wall shear stress distribution in coronary stented arteries," *Micro Nano Lett.*, vol. 7, no. 5, p. 430, 2012.

[114] C. Simon, J. C. Palmaz, and E. A. Sprague, "Influence of topography on endothelialization of stents: clues for new designs," *J. Long. Term. Eff. Med. Implants*, vol. 10, no. 1–2, pp. 143–51, Jan. 2000.

[115] M. Hamuro, J. C. Palmaz, E. A. Sprague, C. Fuss, and J. Luo, "Influence of stent edge angle on endothelialization in an *in vitro* model," *J. Vasc. Interv. Radiol.*, vol. 12, no. 5, pp. 607–11, 2001.

[116] M. J. Suttorp, P. R. Stella, J. Dens, J. M. McKenzie, K. S. Park, and P. Frambach, "Ultra-thin strut cobalt chromium bare metal stent usage in a complex real-world setting (SOLSTICE registry)," *Netherlands Hear. J.*, vol. 23, no. 2, pp. 124–129, 2015.

[117] E. A. Sprague, F. Tio, S. H. Ahmed, J. F. Granada, and S. R. Bailey, "Impact of parallel micro-engineered stent grooves on endothelial cell migration, proliferation, and function: an *in vivo* correlation study of the healing response in the coronary swine model," *Circ. Cardiovasc. Interv.*, vol. 5, no. 4, pp. 499–507, Aug. 2012.

[118] T. Shinke, K. A. Robinson, P. Gilson, M. G. Bruke, N. J. Cheshire, and C. G. Caro, "Novel helical stent design elicits spiral blood flow pattern and inhibits neointima formation in porcine carotid arteries," *Am. J. Cardiol.*, vol. 100, no. 8, p. S186, 2007.

[119] S. G. Carlier, L. C. A. van Damme, C. P. Blommerde, J. J. Wentzel, G. van Langehove, S. Verheye, M. M. Kockx, M. W. M. Knaapen, C. Cheng, F. Gijsen, D. J. Duncker, N. Stergiopulos, C. J. Slager, P. W. Serruys, and R. Krams, "Augmentation of wall shear stress inhibits neointimal hyperplasia after stent implantation: inhibition through reduction of inflammation?," *Circulation*, vol. 107, no. 21, pp. 2741–6, Jun. 2003.

[120] M. Mahmoud, R. Kim, S. Hsiao, R. Xing, K. Van der Heiden, A. Mammoto, J. Chen, I. Gauci, S. Feng, and P. C. Evans, "Disturbed flow promotes atherogenesis through the activation of endothelial-mesenchymal transition," *Heart*, vol. 101, no. Suppl 4, pp. A112-113, 2015.

[121] K. Van der Heiden, A. Hoogendoorn, M. J. Daemen, and F. J. H. Gijsen, "Animal models for plaque rupture: a biomechanical assessment," *Thromb. Haemost.*, vol. 115, no. 3, pp. 501–508, 2016.

[122] L. C. Winkel, A. Hoogendoorn, R. Xing, J. J. Wentzel, and K. Van der Heiden, "Animal models of surgically manipulated flow velocities to study shear stress-induced atherosclerosis," *Atherosclerosis*, vol. 241, no. 1, pp. 100–110, 2015.

[123] J. C. Tsui, "Experimental models of abdominal aortic aneurysms," *Open Cardiovasc. Med. J.*, no. 4, pp. 221–30, 2010.

[124] C. A. Davis, S. Zambrano, P. Anumolu, A. C. B. Allen, L. Sonoqui, and M. R. Moreno, "Device-based *in vitro* techniques for mechanical stimulation of vascular cells: a review," *J. Biomech. Eng.*, vol. 137, no. 4, p. 40801, 2015.

[125] M. J. Levesque and R. M. Nerem, "The elongation and orientation of cultured endothelial cells in response to shear stress," *J. Biomech. Eng.*, vol. 107, no. 4, pp. 341–347, 1985.

[126] H. Tsuboi, J. Ando, R. Korenaga, Y. Takada, and A. Kamiya, "Flow stimulates ICAM-1 expression time and shear stress dependently in cultured human endothelial cells," *Biochem. Biophys. Res. Commun.*, vol. 206, no. 3, pp. 988–96, Jan. 1995.

[127] E. A. Sprague, J. Luo, and J. C. Palmaz, "Human aortic endothelial cell migration onto stent surfaces under static and flow conditions," *J. Vasc. Interv. Radiol.*, vol. 8, no. 1, pp. 83–92, 1997.

[128] A. Benbrahim, G. J. L'Italien, B. B. Milinazzo, D. F. Warnock, S. Dhara, J. P. Gertler, R. W. Orkin, and W. M. Abbott, "A compliant tubular device to study the influences of wall strain and fluid shear stress on cells of the vascular wall," *J. Vasc. Surg.*, vol. 20, no. 2, pp. 184–94, Aug. 1994.

[129] A. Colombo, H. Zahedmanesh, D. M. Toner, P. A. Cahill, and C. Lally, "A method to develop mock arteries suitable for cell seeding and *in-vitro* cell culture experiments," *J. Mech. Behav. Biomed. Mater.*, vol. 3, no. 6, pp. 470–7, Aug. 2010.

[130] R. G. Mannino, D. R. Myers, B. Ahn, Y. Wang, M. Rollins, H. Gole, A. S. Lin, R. E. Guldberg, D. P. Giddens, L. H. Timmins, and W. A. Lam, "Do-it-yourself *in vitro* vasculature that recapitulates *in vivo* geometries for investigating endothelial-blood cell interactions," *Sci. Rep.*, vol. 5, p. 12401, 2015.

[131] K. O. Cardinal, G. T. Bonnema, H. Hofer, J. K. Barton, and S. K. Williams, "Tissue-engineered vascular grafts as *in vitro* blood vessel mimics for the evaluation of endothelialization of intravascular devices," *Tissue Eng.*, vol. 12, no. 12, pp. 3431–8, Dec. 2006.

[132] M. A. Punchard, C. Stenson-Cox, E. D. O'Cearbhaill, E. Lyons, S. Gundy, L. Murphy, A. Pandit, P. E. McHugh, and V. Barron, "Endothelial cell response to biomechanical forces under simulated vascular loading conditions," *J. Biomech.*, vol. 40, no. 14, pp. 3146–54, Jan. 2007.

[133] G. Benndorf, M. Ionescu, M. Valdivia y Alvarado, A. Biondi, J. Hipp, and R. Metcalfe, "Anomalous hemodynamic effects of a self-expanding intracranial stent: comparing *in-vitro* and *ex-vivo* models using ultra-high resolution microCT based CFD," *J. Biomech.*, vol. 43, no. 4, pp. 740–8, Mar. 2010.

[134] E. K. Sackmann, A. L. Fulton, and D. J. Beebe, "The present and future role of microfluidics in biomedical research," *Nature*, vol. 507, no. 7491, pp. 181–9, Mar. 2014.

[135] M. Liu, J. Sun, and Q. Chen, "Influences of heating temperature on mechanical properties of polydimethylsiloxane," *Sensors Actuators A*, vol. 151, pp. 42–5, Apr. 2009.

[136] R. Mukhopadhyay, "When PDMS isn't the best," *Anal. Chem.*, vol. 79, no. 9, pp. 3248–53, 2007.

[137] M. W. Toepke and D. J. Beebe, "PDMS absorption of small molecules and consequences in microfluidic applications," *Lab Chip*, vol. 6, no. 12, pp. 1484–6, Dec. 2006.

[138] J. N. Lee, X. Jiang, D. Ryan, and G. M. Whitesides, "Compatibility of mammalian cells on surfaces of poly(dimethylsiloxane)," *Langmuir*, vol. 20, no. 26, pp. 11684–91, Dec. 2004.

[139] K. Khanafer, A. Duprey, M. Schlicht, and R. Berguer, "Effects of strain rate, mixing ratio, and stress-strain definition on the mechanical behavior of the polydimethylsiloxane (PDMS) material as related to its biological applications," *Biomed. Microdevices*, vol. 11, no. 2, pp. 503–8, Apr. 2009.

[140] A. Mata, A. J. Fleischman, and S. Roy, "Characterization of polydimethylsiloxane (PDMS) properties for biomedical micro/nanosystems," *Biomed. Microdevices*, vol. 7, no. 4, pp. 281–93, Dec. 2005.

[141] J. S. Choi, Y. Piao, and T. S. Seo, "Fabrication of a circular PDMS microchannel for constructing a three-dimensional endothelial cell layer," *Bioprocess Biosyst. Eng.*, vol. 36, no. 12, pp. 1871–8, Dec. 2013.

[142] E. A. Jaffe, R. L. Nachman, C. G. Becker, and C. R. Minick, "Culture of human endothelial cells derived from umbilical veins," *J. Clin. Invest.*, vol. 52, pp. 2745–56, 1973.

[143] N. T. Luu, M. Rahman, P. C. Stone, G. E. Rainger, and G. B. Nash, "Responses of endothelial cells from different vessels to inflammatory cytokines and shear stress: evidence for the pliability of endothelial phenotype," *J. Vasc. Res.*, vol. 47, pp. 451–461, 2010.

[144] A. Sivarapatna, M. Ghaedi, A. V. Le, J. J. Mendez, Y. Qyang, and L. E. Niklason, "Arterial specification of endothelial cells derived from human induced pluripotent stem cells in a biomimetic flow bioreactor," *Biomaterials*, vol. 53, pp. 621–633, 2015.

[145] C. G. Cornelissen, M. Dietrich, K. Gromann, J. Frese, S. Krueger, J. S. Sachweh, and S. Jockenhoevel, "Fibronectin coating of oxygenator membranes enhances endothelial cell attachment.," *Biomed. Eng. Online*, vol. 12, no. 7, 2013.

[146] T. Ziegler, K. Bouzourene, V. J. Harrison, H. R. Brunner, and D. Hayoz, "Influence of oscillatory and unidirectional flow environments on the expression of endothelin and nitric oxide synthase in cultured endothelial cells," *Arterioscler. Thromb. Vasc. Biol.*, vol. 18, no. 5, pp. 686–92, May 1998.

[147] S. J. White, E. M. Hayes, S. Lehoux, J. Y. Jeremy, A. J. G. Horrevoets, and A. C. Newby, "Characterization of the differential response of endothelial cells exposed to normal and elevated laminar shear stress," *J. Cell. Physiol.*, vol. 226, no. 11, pp. 2841–2848, 2011.

[148] A. Benbrahim, G. J. L'Italien, C. J. Kwolek, M. J. Petersen, B. Milinazzo, J. P. Gertler, W. M. Abbott, and R. W. Orkin, "Characteristics of vascular wall

cells subjected to dynamic cyclic strain and fluid shear conditions *in vitro*," *J. Surg. Res.*, vol. 65, no. 2, pp. 119–27, Oct. 1996.

[149] X. Peng, F. A. Recchia, B. J. Byrne, I. S. Wittstein, R. C. Ziegelstein, and D. A. Kass, "*In vitro* system to study realistic pulsatile flow and stretch signaling in cultured vascular cells," *Am. J. Physiol. Cell Physiol.*, vol. 279, no. 3, pp. C797-805, Sep. 2000.

[150] R. Sampath, G. L. Kukielka, C. W. Smith, S. G. Eskin, and L. V McIntire, "Shear stress-mediated changes in the expression of leukocyte adhesion receptors on human umbilical vein endothelial cells *in vitro*," *Ann. Biomed. Eng.*, vol. 23, no. 3, pp. 45–9, 1995.

[151] C. Wang, B. M. Baker, C. S. Chen, and M. A. Schwartz, "Endothelial cell sensing of flow direction," *Arterioscler. Thromb. Vasc. Biol.*, vol. 33, no. 9, pp. 2130–6, 2013.

[152] J. C. Palmaz, S. Bailey, D. Marton, and E. Sprague, "Influence of stent design and material composition on procedure outcome," *J. Vasc. Surg.*, vol. 36, no. 5, pp. 1031–9, 2002.

[153] A. Dardik, L. Chen, J. Frattini, H. Asada, F. Aziz, F. A. Kudo, and B. E. Sumpio, "Differential effects of orbital and laminar shear stress on endothelial cells," *J. Vasc. Surg.*, vol. 41, no. 5, pp. 869–80, 2005.

[154] M. B. Esch, D. J. Post, M. L. Shuler, and T. Stokol, "Characterization of *in vitro* endothelial linings grown within microfluidic channels," *Tissue Eng. Part A*, vol. 17, no. 23–24, pp. 2965–71, 2011.

[155] S. Lakhotia and E. T. Papoutsakis, "Agitation induced cell injury in microcarrier cultures. Protective effect of viscosity is agitation intensity dependent: experiments and modeling," *Biotechnol. Bioeng.*, vol. 39, pp. 95–107, 1992.

[156] T. M. Fischer, "A method to prepare isotonic dextran-salt solutions," *Cytom. Part A J. Int. Soc. Anal. Cytol.*, vol. 77, no. 8, pp. 805–10, Aug. 2010.

[157] C. N. van den Broek, R. A. A. Pullens, O. Frøbert, M. C. M. Rutten, W. F. den Hartog, and F. N. van de Vosse, "Medium with blood-analog mechanical properties for cardiovascular tissue culturing," *Biorheology*, vol. 45, no. 6, pp. 651–661, 2008.

[158] G. Vlastos, D. Lerche, B. Koch, O. Samba, and M. Pohl, "The effect of parallel combined steady and oscillatory shear flows on blood and polymer solutions," *Rheol. Acta*, vol. 36, no. 2, pp. 160–72, Apr. 1997.

[159] Y. Liu, X. Wang, and J. Lu, "Dynamic observation of artery endothelial cell layers in response to bare metal stent and paclitaxel-eluting stent *in vitro*," *J. Interv. Cardiol.*, vol. 27, no. 2, pp. 182–190, 2014.

[160] E. E. Antoine, F. P. Cornat, and A. I. Barakat, "The stentable *in vitro* artery: an instrumented platform for endovascular device development and optimization," *J. R. Soc. Interface*, vol. 13, p. 20160834, 2016.

[161] K. O. H. Cardinal and S. K. Williams, "Assessment of the intimal response to a protein-modified stent in a tissue-engineered blood vessel mimic," *Tissue Eng. Part A*, vol. 15, no. 12, pp. 3869–76, 2009.

[162] S. Morlacchi, B. Keller, P. Arcangeli, M. Balzan, F. Migliavacca, G. Dubini, J. Gunn, N. Arnold, A. Narracott, D. Evans, and P. Lawford, "Hemodynamics and in-stent restenosis: micro-CT images, histology, and computer simulations," *Ann. Biomed. Eng.*, vol. 39, no. 10, pp. 2615–26, Oct. 2011.

[163] J. J. Wentzel, R. Krams, J. C. H. Schuurbiers, J. A. Oomen, J. Kloet, W. J. van der Giessen, P. W. Serruys, and C. J. Slager, "Relationship between neointimal thickness and shear stress after wallstent implantation in human coronary arteries," *Circulation*, vol. 103, no. 13, pp. 1740–5, Apr. 2001.

[164] M. Simão, J. M. Ferreira, J. Mora-Rodriguez, J. Fragata, and H. M. Ramos, "Behaviour of two typical stents towards a new stent evolution," *Med. Biol. Eng. Comput.*, 2016.

[165] C. Chiastra, S. Morlacchi, S. Pereira, G. Dubini, and F. Migliavacca, "Computational fluid dynamics of stented coronary bifurcations studied with a hybrid discretization method," *Eur. J. Mech. B/Fluids*, vol. 35, pp. 76–84, 2012.

[166] D. M. Martin, E. A. Murphy, and F. J. Boyle, "Computational fluid dynamics analysis of balloon-expandable coronary stents: influence of stent and vessel deformation," *Med. Eng. Phys.*, vol. 36, no. 8, pp. 1047–56, 2014.

[167] R. Balossino, F. Gervaso, F. Migliavacca, and G. Dubini, "Effects of different stent designs on local hemodynamics in stented arteries," *J. Biomech.*, vol. 41, no. 5, pp. 1053–61, Jan. 2008.

[168] A. I. Barakat and E. T. Cheng, "Numerical simulation of fluid mechanical disturbance induced by intravascular stents," in *11th International Conference on Mechanics in Medicine and Biology*, 2000.

[169] V. Peiffer, S. J. Sherwin, and P. D. Weinberg, "Computation in the rabbit aorta of a new metric - the transverse wall shear stress - to quantify the multidirectional character of disturbed blood flow," *J. Biomech.*, vol. 46, no. 15, pp. 2651–8, 2013.

[170] R. M. Pedrigi, V. V. Mehta, S. M. Bovens, Z. Mohri, C. B. Poulsen, W. Gsell, J. L. Tremoleda, L. Towhidi, R. de Silva, E. Petretto, and R. Krams, "Influence of shear stress magnitude and direction on atherosclerotic plaque composition," *R. Soc. Open Sci.*, vol. 3, p. 160588, 2016.

[171] F. Migliavacca, F. Gervaso, M. Prosi, P. Zunino, S. Minisini, L. Formaggia, and G. Dubini, "Expansion and drug elution model of a coronary stent," *Comput. Methods Biomech. Biomed. Engin.*, vol. 10, no. 1, pp. 63–73, 2007.

[172] S. Morlacchi and F. Migliavacca, "Modeling stented coronary arteries: where we are, where to go," *Ann. Biomed. Eng.*, vol. 41, no. 7, pp. 1428–44, Jul. 2013.

[173] F. Prati, G. Guagliumi, G. S. Mintz, M. Costa, E. Regar, T. Akasaka, P. Barlis, G. J. Tearney, I. K. Jang, E. Arbustini, H. G. Bezerra, Y. Ozaki, N. Bruining, D. Dudek, M. Radu, A. Erglis, P. Motreff, F. Alfonso, K. Toutouzas, N. Gonzalo, C. Tamburino, T. Adriaenssens, F. Pinto, P. W. J. Serruys, and C. Di Mario, "Expert review document part 2: methodology, terminology and clinical applications of optical coherence tomography for the assessment of interventional procedures," *Eur. Heart J.*, vol. 33, no. 20, pp. 2513–22, 2012.

[174] F. Rikhtegar, F. Pacheco, C. Wyss, K. S. Stok, H. Ge, R. J. Choo, A. Ferrari, D. Poulikakos, R. Müller, and V. Kurtcuoglu, "Compound *ex vivo* and *in silico* method for hemodynamic analysis of stented arteries," *PLoS One*, vol. 8, no. 3, 2013.

[175] R. Akhtar, M. J. Sherratt, J. K. Cruickshank, and B. Derby, "Characterizing the elastic properties of tissues," *Mater. Today*, vol. 14, no. 3, pp. 96–105, 2011.

[176] G. Gamble, J. Zorn, G. Sanders, S. MacMahon, and N. Sharpe, "Estimation of arterial stiffness, compliance, and distensibility from M-mode ultrasound measurements of the common carotid artery," *Stroke*, vol. 25, pp. 11–16, 1994.

[177] S. Windecker, Y. Allemann, M. Billinger, T. Pohl, D. Hutter, T. Orsucci, L. Blaga, B. Meier, and C. Seiler, "Effect of endurance training on coronary artery size and function in healthy men: an invasive followup study," *Am. J. Physiol. Hear. Circ. Physiol.*, vol. 282, no. 6, pp. H2216-23, Jun. 2002.

[178] J. A. Dickerson, H. N. Nagaraja, and S. V Raman, "Gender-related differences in coronary artery dimensions: a volumetric analysis," *Clin. Cardiol.*, vol. 33, no. 2, pp. E44-9, Feb. 2010.

[179] C. Saikrishna, S. Talwar, G. Gulati, and A. S. Kumar, "Normal coronary artery dimensions in Indians," *Indian J. Thorac. Cardiovasc. Surg.*, vol. 22, no. 3, pp. 159–64, 2006.

[180] J. T. Dodge, B. G. Brown, E. L. Bolson, and H. T. Dodge, "Lumen diameter of normal human coronary arteries. Influence of age, sex, anatomic variation, and left ventricular hypertrophy or dilation," *Circulation*, vol. 86, no. 1, pp. 232–46, Jul. 1992.

[181] Z. Kaimkhani, M. Ali, and A. M. A. Faruqui, "Coronary artery diameter in a cohort of adult Pakistani population," *J. Pak. Med. Assoc.*, vol. 54, no. 5, pp. 258–61, May 2004.

[182] I. Ilayperuma, B. G. Nanayakkara, and K. N. Palahepitiya, "Sexual differences in the diameter of coronary arteries in an adult Sri Lankan population," *Int. J. Morphol.*, vol. 29, no. 4, pp. 1444–8, 2011.

[183] W. H. Leung, M. L. Stadius, and E. L. Alderman, "Determinants of normal coronary artery dimensions in humans," *Circulation*, vol. 84, no. 6, pp. 2294–306, Dec. 1991.

[184] S. H. Litovsky, A. Farb, A. P. Burke, I. Y. Rabin, E. E. Herderick, J. F. Cornhill, J. Smialek, and R. Virmani, "Effect of age, race, body surface area, heart weight and atherosclerosis on coronary artery dimensions in young males," *Atherosclerosis*, vol. 123, no. 1–2, pp. 243–50, Jun. 1996.

[185] S. E. Sheifer, M. R. Canos, K. P. Weinfurt, U. K. Arora, F. O. Mendelsohn, B. J. Gersh, and N. J. Weissman, "Sex differences in coronary artery size assessed by intravascular ultrasound," *Am. Heart J.*, vol. 139, pp. 649–52, 2000.

[186] F. Zijlstra, J. van Ommeren, J. H. Reiber, and P. W. Serruys, "Does the quantitative assessment of coronary artery dimensions predict the physiologic

significance of a coronary stenosis?," *Circulation*, vol. 75, no. 6, pp. 1154–61, Jun. 1987.

[187] P. Kaufmann, G. Vassalli, S. Lupi-Wagner, R. Jenni, and O. M. Hess, "Coronary artery dimensions in primary and secondary left ventricular hypertrophy," *J. Am. Coll. Cardiol.*, vol. 28, no. 3, pp. 745–50, 1996.

[188] O. R. Guerra, W. R. Janowitz, A. S. Agatston, L. L. Mantelle, and M. Viamonte, "Coronary artery diameter and coronary risk factors: a study with ultrafast computed tomography," *Am. Heart J.*, vol. 126, no. 3, pp. 600–6, 1993.

[189] H. V Anderson, M. J. Stokes, M. Leon, S. A. Abu-Halawa, Y. Stuart, and R. L. Kirkeeide, "Coronary artery flow velocity is related to lumen area and regional left ventricular mass," *Circulation*, vol. 102, no. 1, pp. 48–54, Jul. 2000.

[190] W. G. Hundley, R. A. Lange, G. D. Clarke, B. M. Meshack, J. Payne, C. Landau, R. McColl, D. E. Sayad, D. L. Willett, J. E. Willard, L. D. Hillis, and R. M. Peshock, "Assessment of coronary arterial flow and flow reserve in humans with magnetic resonance imaging," *Circulation*, vol. 93, no. 8, pp. 1502–8, 1996.

[191] R. Vergallo, M. I. Papafaklis, H. Jia, C. V Bourantas, I. Mcnulty, H. Lee, B. Yu, I. Porto, L. M. Biasucci, F. Crea, C. L. Feldman, L. K. Michalis, P. H. Stone, and I.-K. Jang, "Low endothelial shear stress is associated with high-risk coronary plaque characteristics in humans: a three-dimensional frequency-domain optical coherence tomography study," *Circulation*, vol. 128, no. 22, p. Suppl. S A18072, 2013.

[192] P. H. Stone, A. U. Coskun, S. Kinlay, M. E. Clark, M. Sonka, A. Wahle, O. J. Ilegbusi, Y. Yeghiazarians, J. J. Popma, J. Orav, R. E. Kuntz, and C. L. Feldman, "Effect of endothelial shear stress on the progression of coronary artery disease, vascular remodeling, and in-stent restenosis in humans: *in vivo* 6-month follow-up study," *Circulation*, vol. 108, no. 4, pp. 438–44, Jul. 2003.

[193] X. He and D. N. Ku, "Pulsatile flow in the human left coronary artery bifurcation: average conditions," *J. Biomech. Eng.*, vol. 118, no. 1, pp. 74–82, 1996.

[194] D. N. Ku, D. P. Giddens, C. K. Zarins, and S. Glagov, "Pulsatile flow and atherosclerosis in the human carotid bifurcation: positive correlation between plaque location and low oscillating shear stress," *Arteriosclerosis*, vol. 5, no. 3, pp. 293–302, 2015.

[195] J. T. Marcus, H. G. Smeenk, J. P. Kuijer, R. J. Van der Geest, R. M. Heethaar, and A. C. Van Rossum, "Flow profiles in the left anterior descending and the right coronary artery assessed by MR velocity quantification: effects of through-plane and in-plane motion of the heart," *J. Comput. Assist. Tomogr.*, vol. 23, no. 4, pp. 567–76, 1999.

[196] K. Johnson, P. Sharma, and J. Oshinski, "Coronary artery flow measurement using navigator echo gated phase contrast magnetic resonance velocity mapping at 3.0 T," *J. Biomech.*, vol. 41, no. 3, pp. 595–602, Jan. 2008.

[197] M. M. Schirru and R. S. Dwyer-Joyce, "A model for the reflection of shear

ultrasonic waves at a thin liquid film and its application to viscometry in a journal bearing," *Proc. Inst. Mech. Eng. Part J J. Eng. Tribol.*, vol. 230, no. 6, pp. 667–679, 2015.

[198] J. F. Douglas, J. M. Gasiorek, J. A. Swaffield, and L. B. Jack, *Fluid Mechanics*. Pearson Prentice Hall, 2005.

[199] C. Sadasivan, L. Cesar, J. Seong, A. Rakian, Q. Hao, F. O. Tio, A. K. Wakhloo, and B. B. Lieber, "An original flow diversion device for the treatment of intracranial aneurysms: evaluation in the rabbit elastase-induced model," *Stroke*, vol. 40, no. 3, pp. 952–958, 2009.

[200] F. A. Khorshid, "The effect of the medium viscosity on the cells morphology in reaction of cells to topography- I," in *Proceedings of the 2nd Saudi Science Conference*, 2005, pp. 67–98.

[201] Cole-Parmer, "Reducing pulsation in peristaltic pumping systems," 2017. [Online]. Available: https://www.coleparmer.co.uk/tech-article/reducing-pulsation-peristaltic-pumping.

[202] L. Yin, K. Morishige, T. Takahashi, K. Hashimoto, S. Ogata, S. Tsutsumi, K. Takata, T. Ohta, J. Kawagoe, K. Takahashi, and H. Kurachi, "Fasudil inhibits vascular endothelial growth factor-induced angiogenesis *in vitro* and *in vivo*," *Mol. Cancer Ther.*, vol. 6, no. 5, pp. 1517–1525, 2007.

[203] C. H. Yu, K. Matsumoto, S. Shida, D. J. Kim, and M. Ohta, "A steady flow analysis on a cerebral aneurysm model with several stents for new stent design using PIV," *J. Mech. Sci. Technol.*, vol. 26, no. 5, pp. 1333–40, 2012.

[204] M. C. Brindise, C. Chiastra, F. Burzotta, F. Migliavacca, and P. P. Vlachos, "Hemodynamics of stent implantation procedures in coronary bifurcations: an *in vitro* study," *Ann. Biomed. Eng.*, vol. 45, no. 3, pp. 542–553, 2017.

[205] L. H. Ting, S. Feghhi, S. J. Han, M. L. Rodriguez, and N. J. Sniadecki, "Effect of silanization film thickness in soft lithography of nanoscale features," *J. Nanotechnol. Eng. Med.*, vol. 2, no. 4, pp. 41006-1–5, 2011.

[206] D. Stoeckel, C. Bonsignore, and S. Duda, "A survey of stent designs," *Minim. Invasive Ther. Allied Technol.*, vol. 11, no. 4, pp. 137–47, 2002.

[207] J. Butany, K. Carmichael, S. W. Leong, and M. J. Collins, "Coronary artery stents: identification and evaluation," *J. Clin. Pathol.*, vol. 58, no. 8, pp. 795–804, 2005.

[208] F. Auricchio, M. Ferretti, A. Lefieux, M. Musci, A. Reali, S. Trimarchi, and A. Veneziani, "Parallelizing a finite element solver in computational hemodynamics: a black box approach," *Int. J. High Perform. Comput. Appl.*, no. May, pp. 1–11, 2016.

[209] X. Yu, I. Trase, M. Ren, K. Duval, X. Guo, and Z. Chen, "Design of nanoparticle-based carriers for targeted drug delivery," *J. Nanomater.*, vol. Volume 201, 2016.

[210] K. Kono and T. Terada, "Hemodynamics of 8 different configurations of stenting for bifurcation aneurysms," *Am. J. Neuroradiol.*, vol. 34, no. 10, pp. 1980–6, 2013.

[211] I. Szikora, E. Turanyi, and M. Marosfoi, "Evolution of flow-diverter endothelialization and thrombus organization in giant fusiform aneurysms after flow diversion: a histopathologic study," *Am. J. Neuroradiol.*, vol. 36, no. 9, pp. 1716–20, 2015.

[212] B. Dumé, "Micro-sensors monitor how arteries heal after surgery," *Scientific American*, 2016.

[213] E. Mostaed, M. Sikora-Jasinska, A. Mostaed, S. Loffredo, A. G. Demir, B. Previtali, D. Mantovani, R. Beanland, and M. Vedani, "Novel Zn-based alloys for biodegradable stent applications: design, development and *in vitro* degradation," *J. Mech. Behav. Biomed. Mater.*, vol. 60, pp. 581–602, 2016.

[214] X. Ma, S. Oyamada, F. Gao, T. Wu, M. P. Robich, H. Wu, X. Wang, B. Buchholz, S. McCarthy, Z. Gu, C. F. Bianchi, F. W. Sellke, and R. Laham, "Paclitaxel/sirolimus combination coated drug-eluting stent: *in vitro* and *in vivo* drug release studies," *J. Pharm. Biomed. Anal.*, vol. 54, no. 4, pp. 807–811, 2011.

[215] X. Wang, J. Miao, H. Zhao, C. Mao, X. Chen, and J. Shen, "Fabrication of nonbiofouling metal stent and *in vitro* studies on its hemocompatibility," *J. Biomater. Appl.*, vol. 29, no. 1, pp. 14–25, 2014.

Appendix

Particle Tracks:
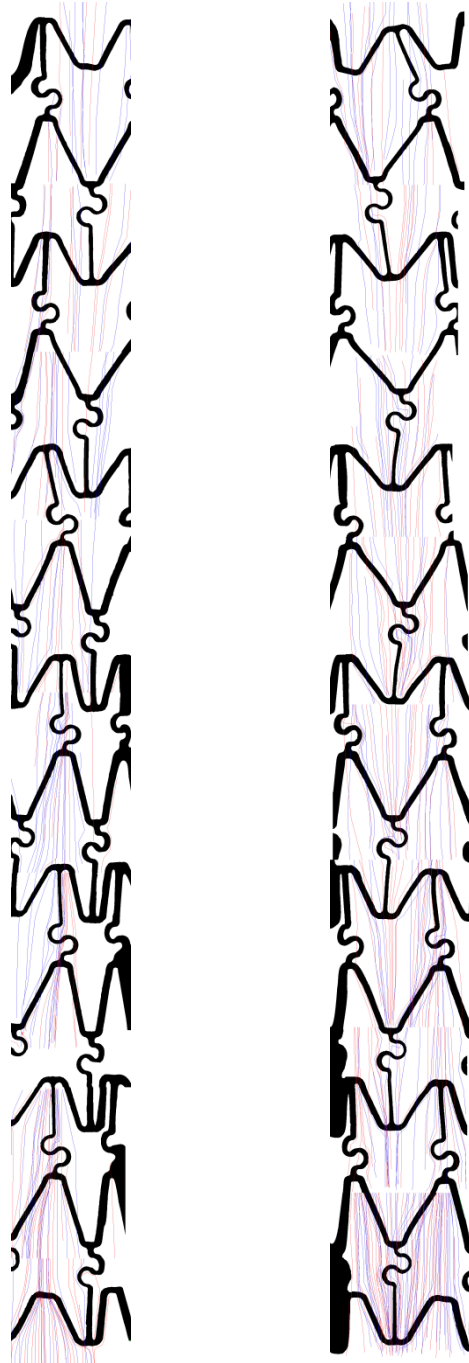
Tracked particle streamlines through BiodivYsio OC coronary stent

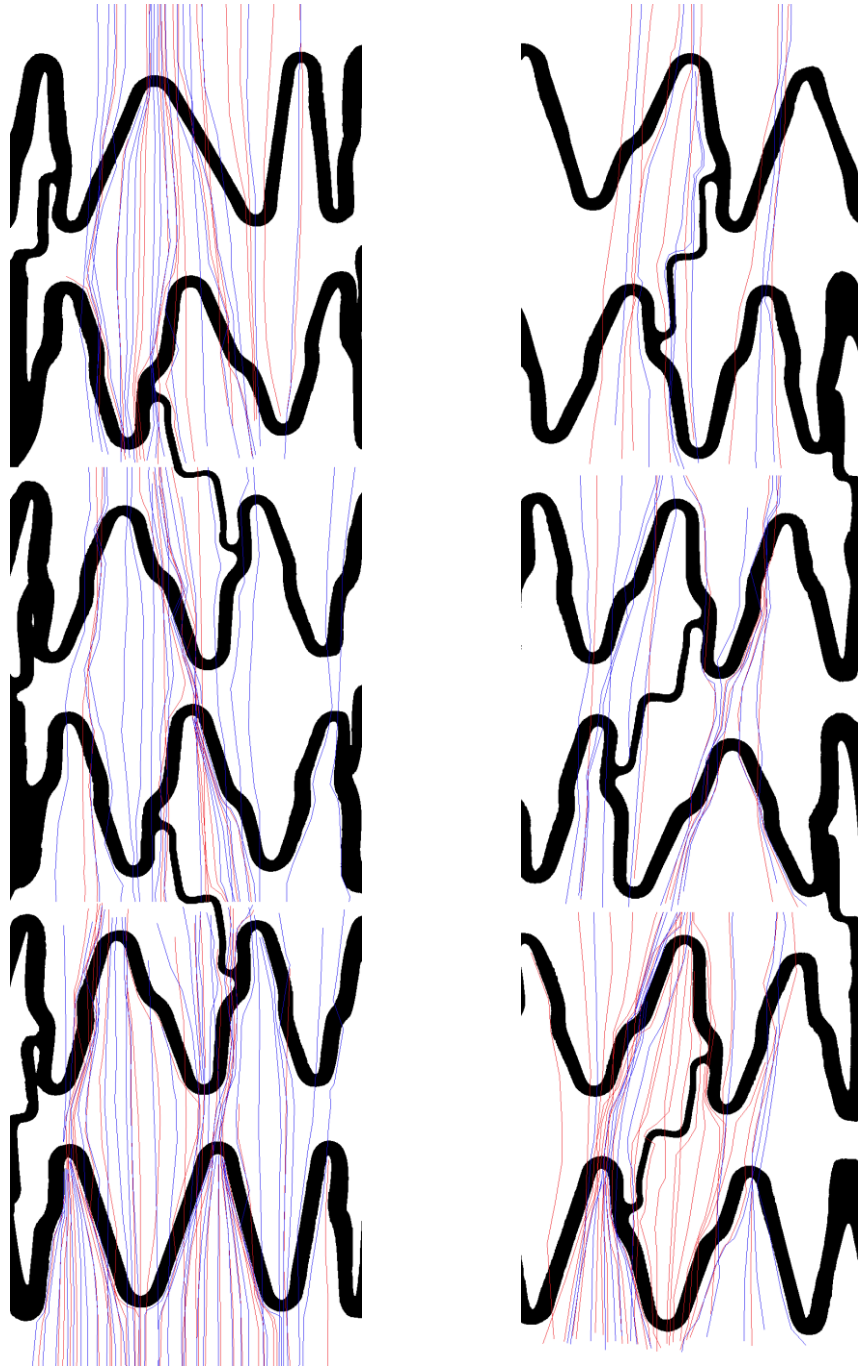Flow from bottom to top, Re = 68 (equivalent to blood flow with 1 Pa wall shear stress).
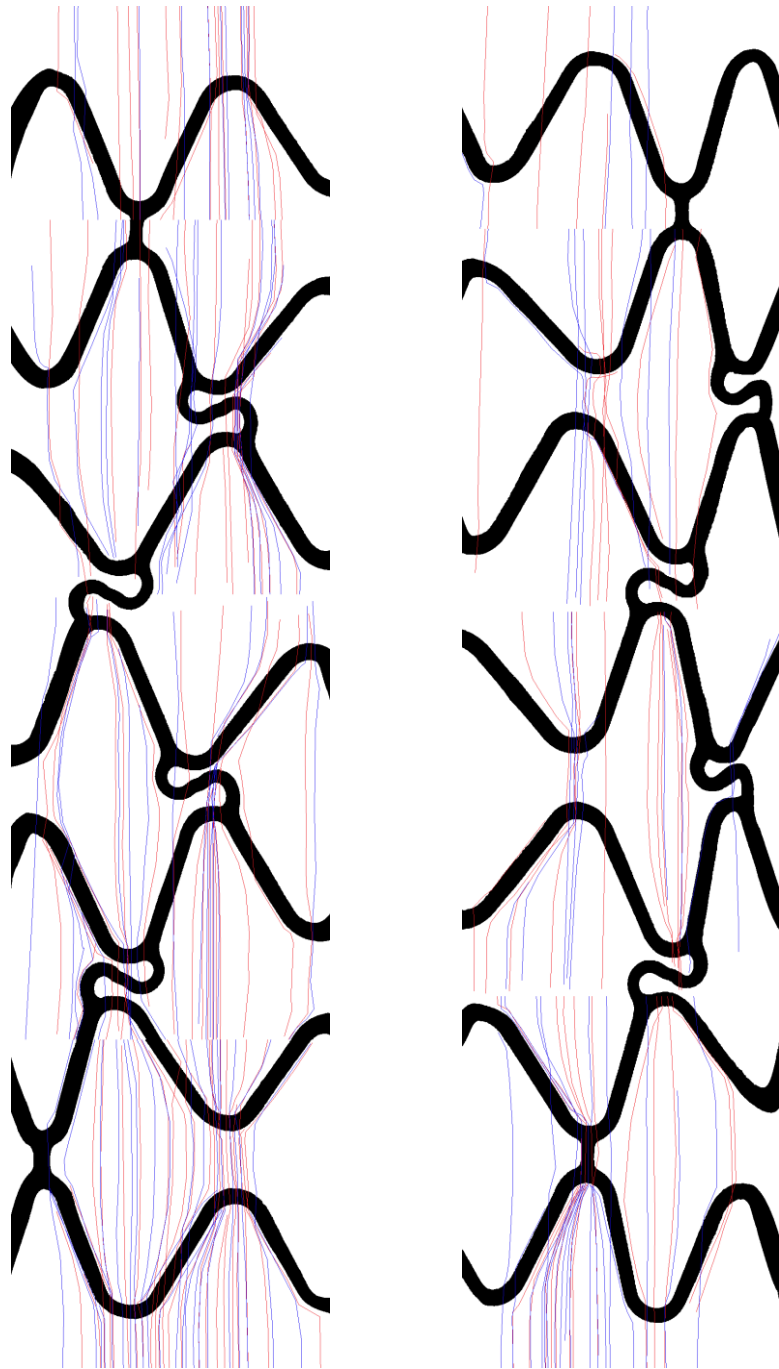
Tracked particle streamlines through Chroma coronary stent

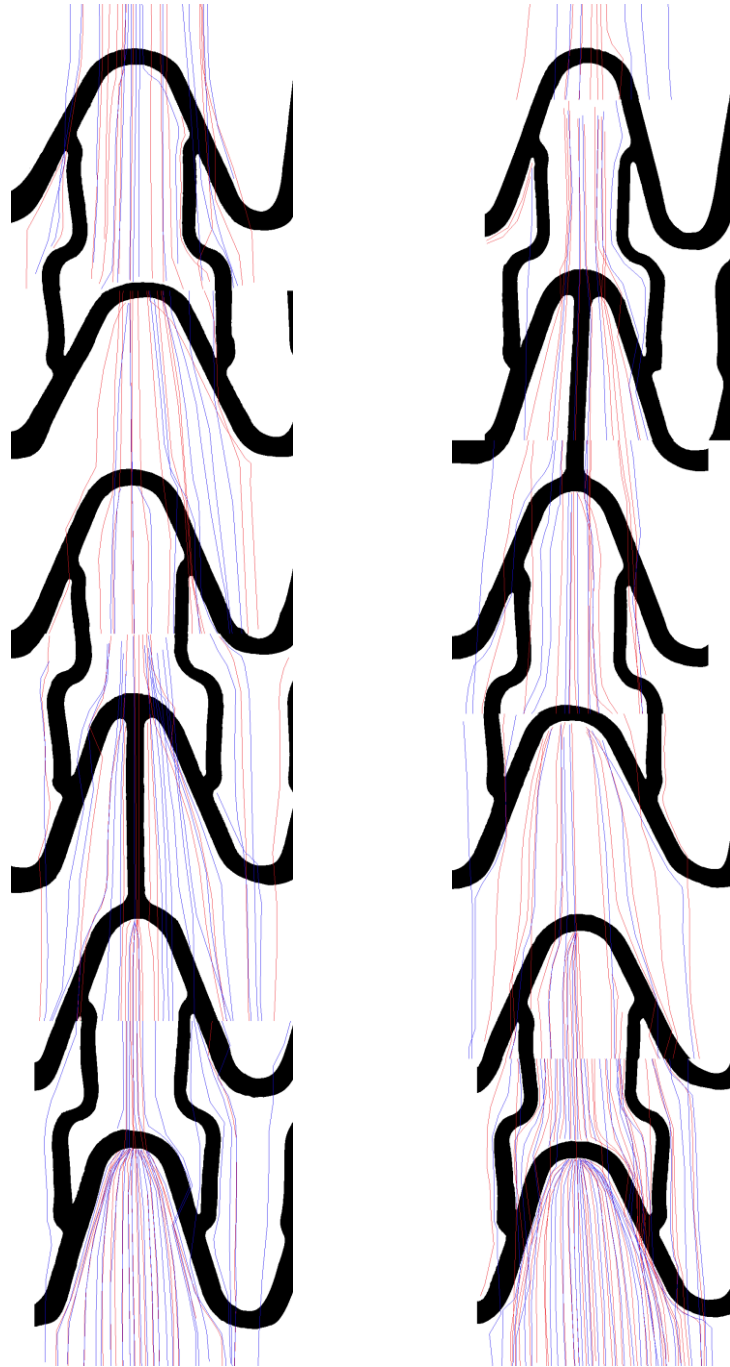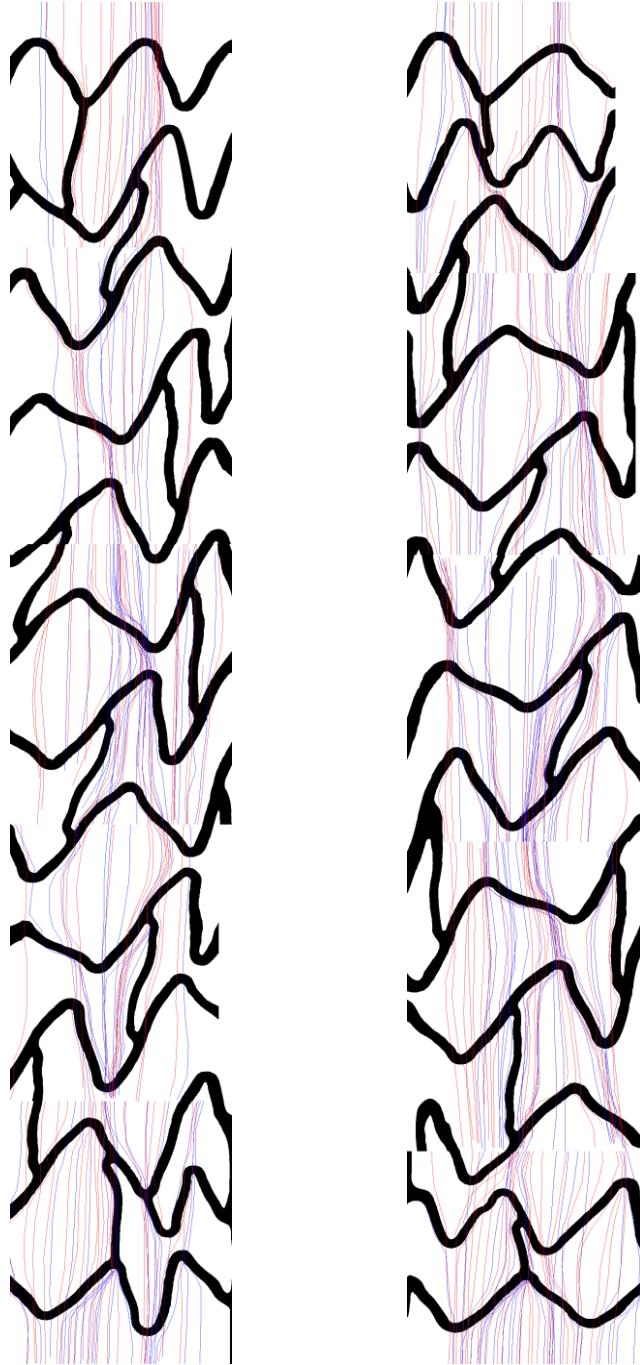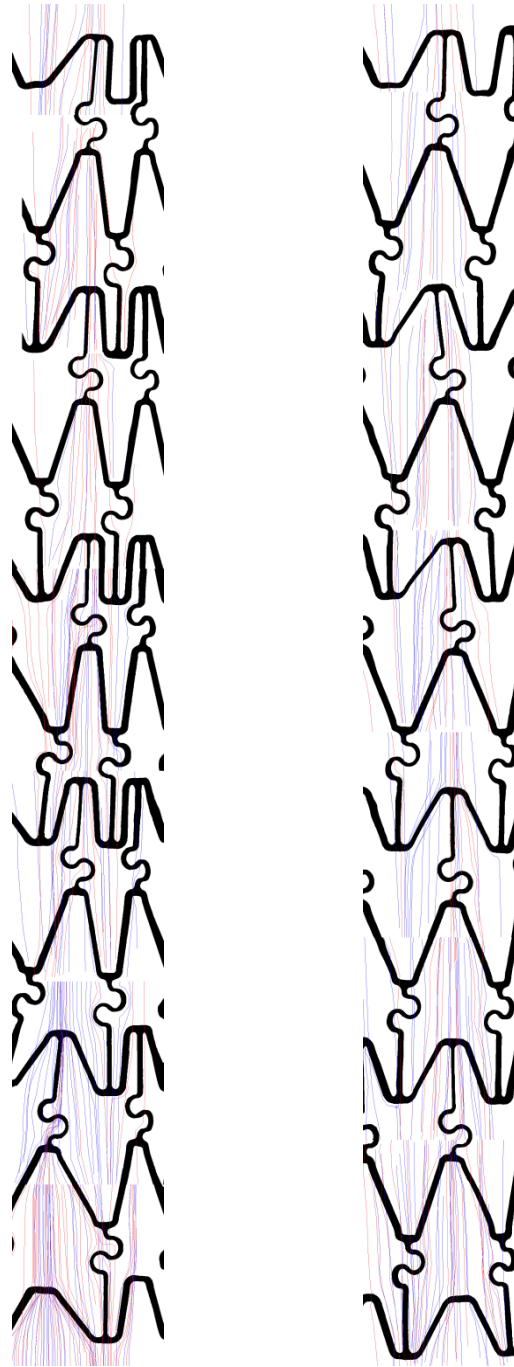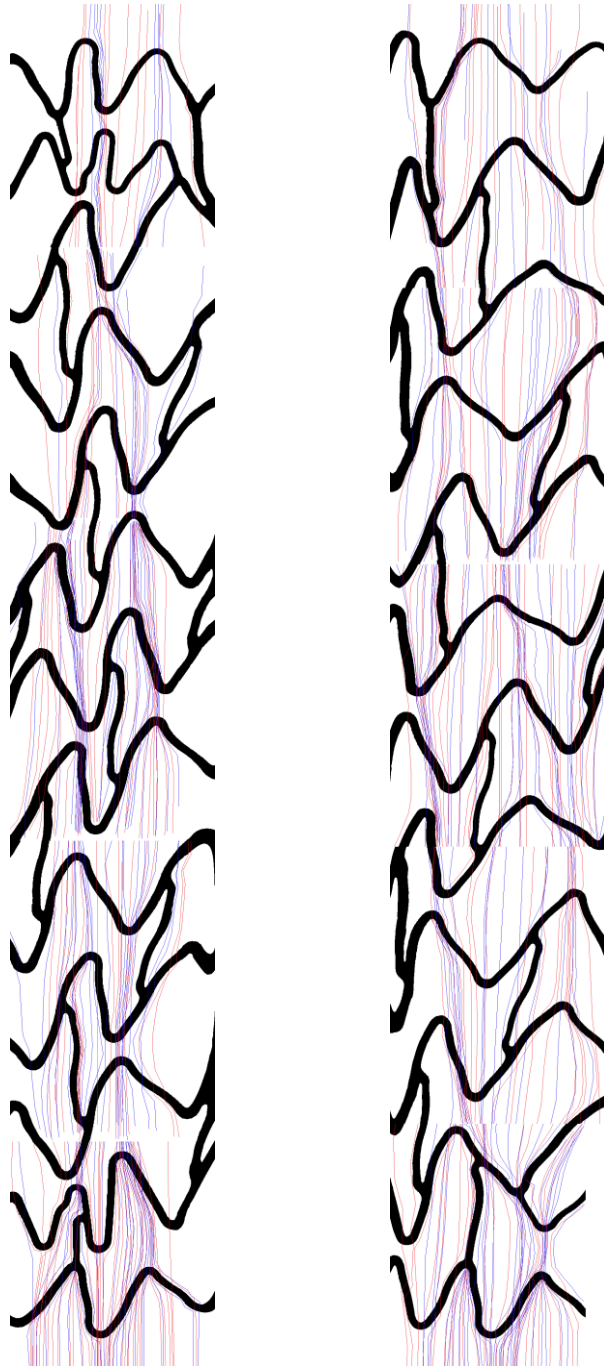Flow from bottom to top, Re = 68 (equivalent to blood flow with 1 Pa wall shear stress).
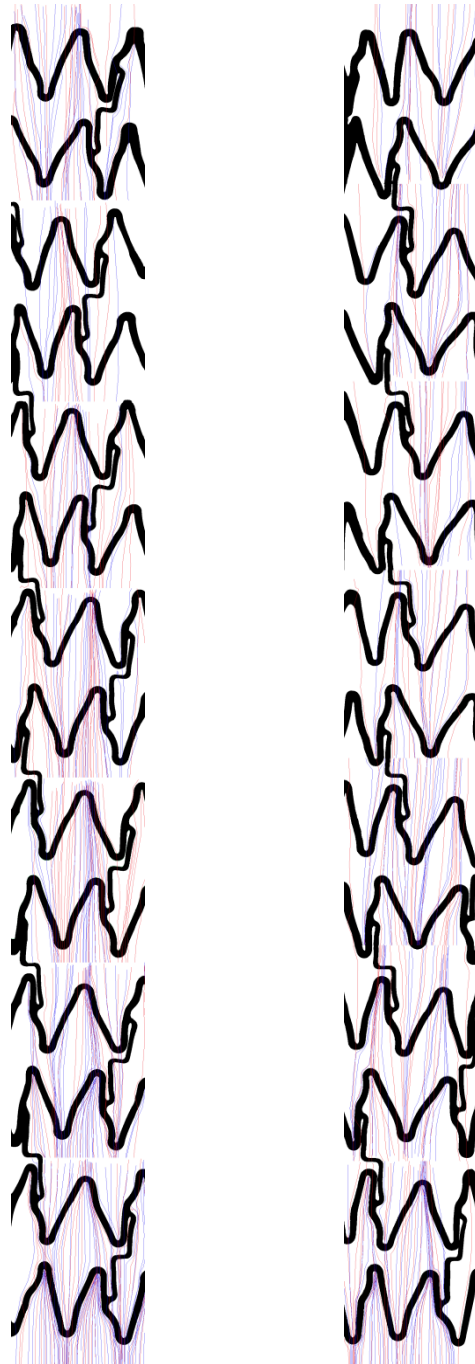
Tracked particle streamlines through Coroflex Blue coronary stent

Flow from bottom to top, Re = 68 (equivalent to blood flow with 1 Pa wall shear stress).

Tracked particle streamlines through Coroflex Blue Neo coronary stent

Flow from bottom to top, Re = 68 (equivalent to blood flow with 1 Pa wall shear stress).

Tracked particle streamlines through Matrix coronary stent

Flow from bottom to top, Re = 68 (equivalent to blood flow with 1 Pa wall shear stress).

Tracked particle streamlines through Orsiro coronary stent

Flow from bottom to top, Re = 68 (equivalent to blood flow with 1 Pa wall shear stress).
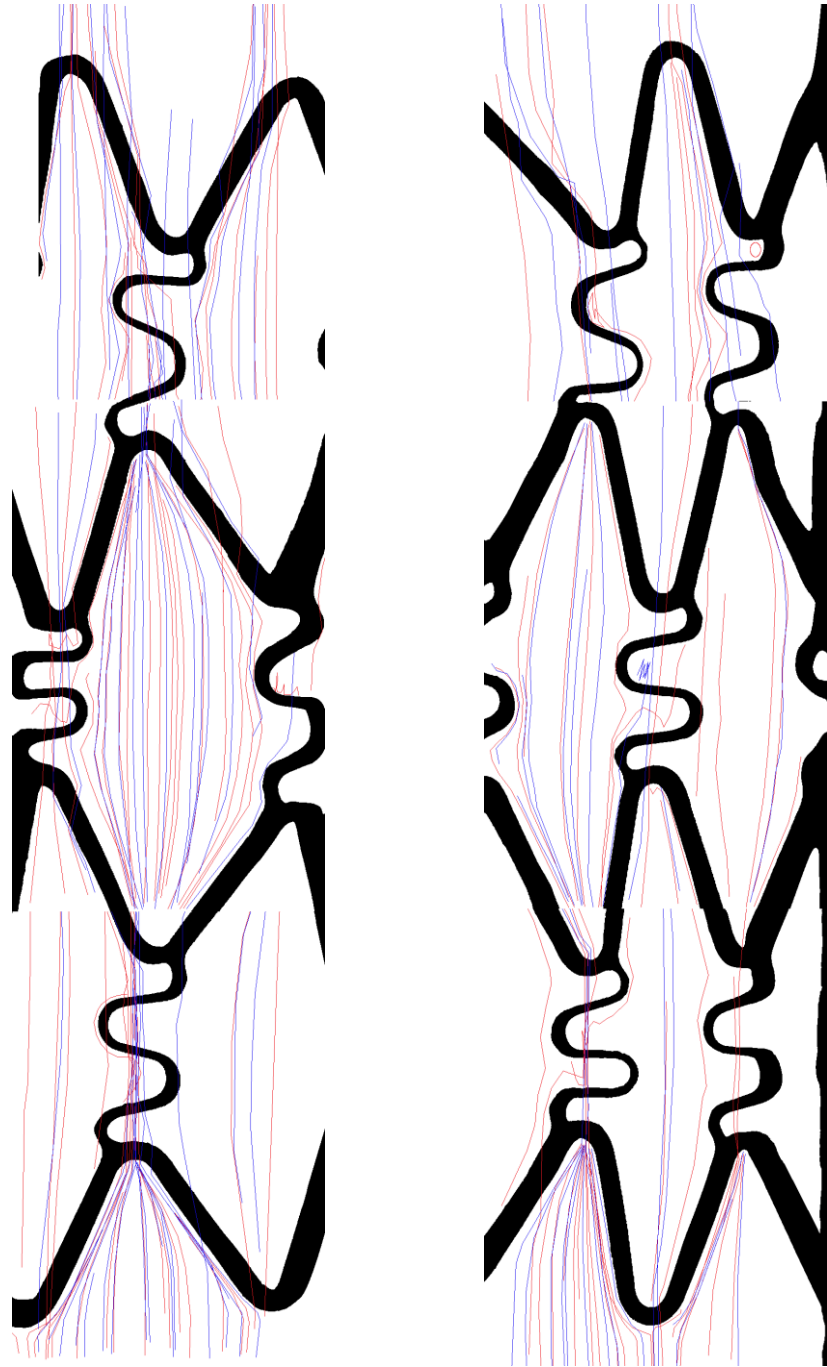
Tracked particle streamlines through Penchant coronary stent

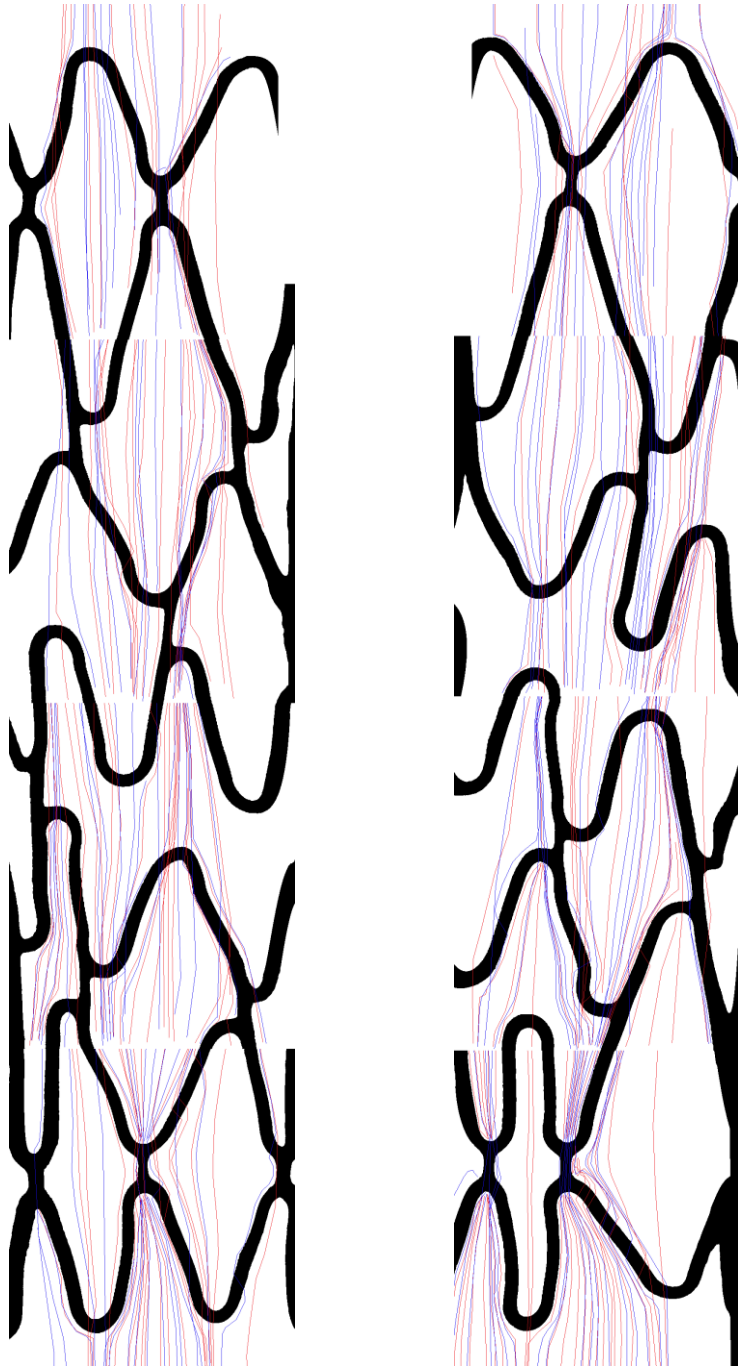Flow from bottom to top, Re = 68 (equivalent to blood flow with 1 Pa wall shear stress).

Tracked particle streamlines through Pro Kinetic Energy coronary stent

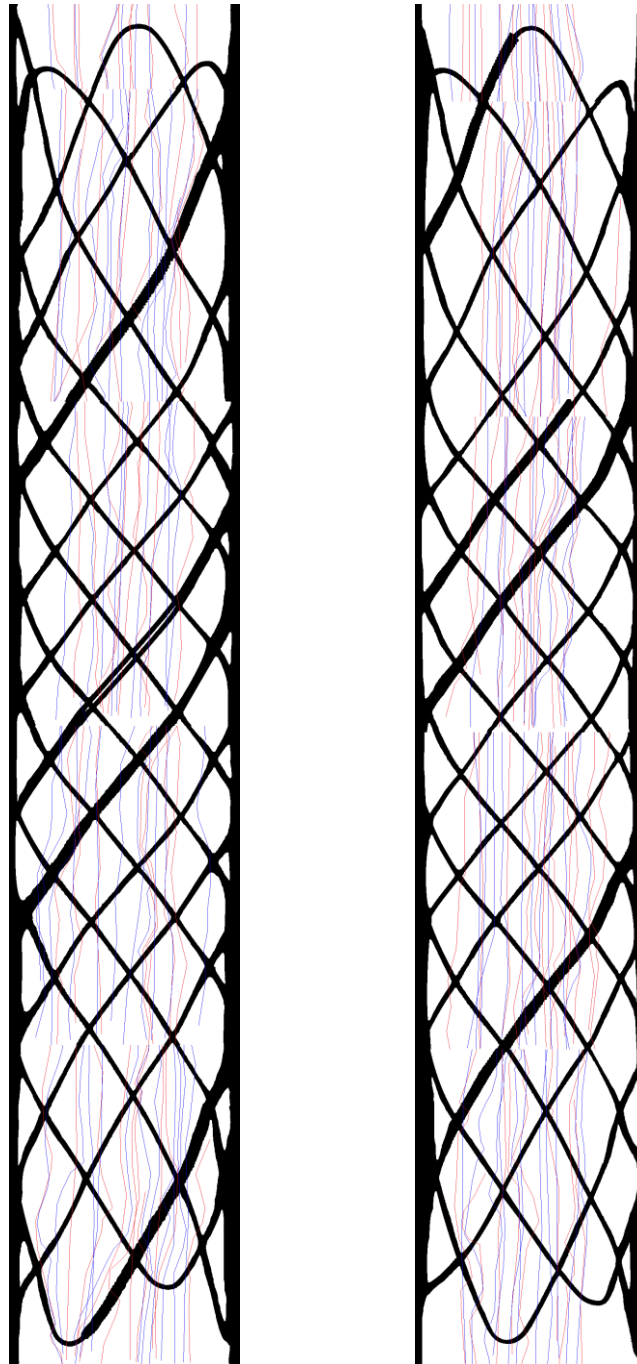Flow from bottom to top, Re = 68 (equivalent to blood flow with 1 Pa wall shear stress).

Tracked particle streamlines through Velocity coronary stent

Flow from bottom to top, Re = 68 (equivalent to blood flow with 1 Pa wall shear stress).
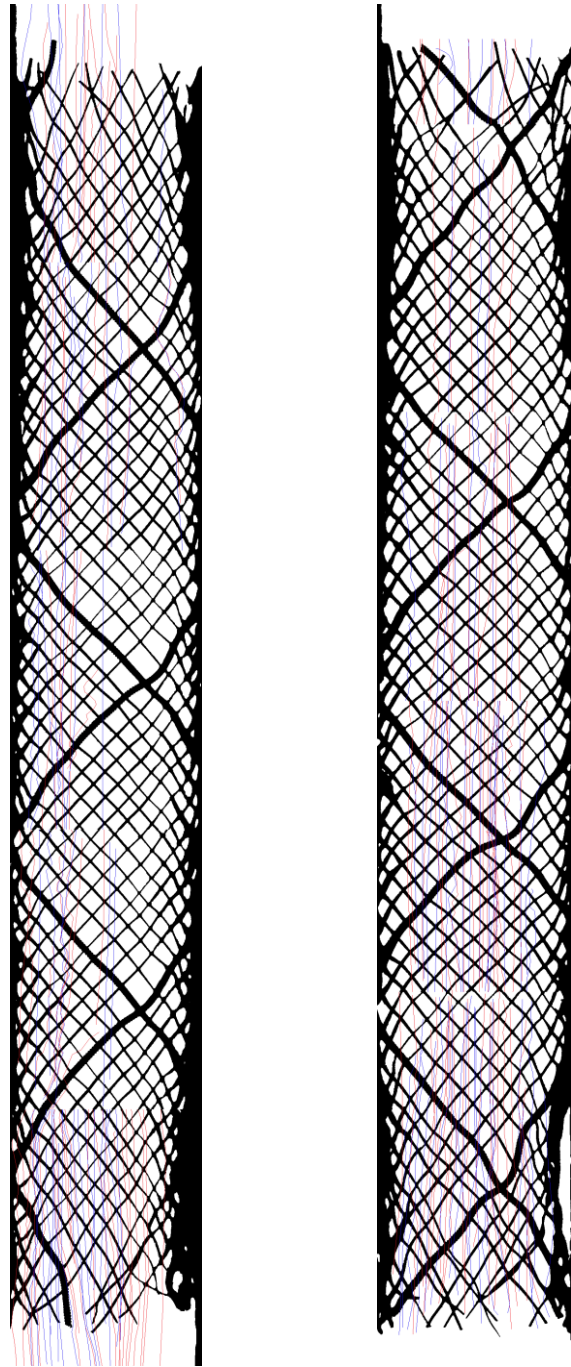
Tracked particle streamlines through XTRM-Track coronary stent

Flow from bottom to top, Re = 68 (equivalent to blood flow with 1 Pa wall shear stress).

Tracked particle streamlines through Leo flow diverter stent

Flow from bottom to top, Re = 43 (equivalent to blood flow with 1 Pa wall shear stress).

Tracked particle streamlines through Silk flow diverter stent

Flow from bottom to top, Re = 43 (equivalent to blood flow with 1 Pa wall shear stress).

Publications:

S. T. Hsiao, T. Spencer, **L. Boldock**, S. D. Prosseda, I. Xanthis, F. J. Tovar-Lopez, H. van Buesekamp, R. Y. Khamis, N. Foin, N. Bowden, A. Hussain, A. Rothman, V. Ridger, I. Halliday, C. Perrault, J. Gunn, and P. C. Evans, "Endothelial repair in stented arteries is accelerated by inhibition of Rho-associated protein kinase," *Cardiovascular Research*, vol. 112, no. 3, pp. 689–701, 2016.

L. Boldock, C. Wittkowske, C. M. Perrault, "Microfluidic traction force microscopy to study mechanotransduction in angiogenesis", *Microcirculation*, vol. 24, no. 5, pp. e12361, 2017.

Oral presentations:

4th Micro and Nano Flows Conference, 2014, London, UK.

Poster presentations:

University of Sheffield Engineering Symposium (USES), 2014, Sheffield, UK.

10th International Symposium on Biomechanics in Vascular Biology and Cardiovascular Disease, 2015, Rotterdam, the Netherlands.

11th International Symposium on Biomechanics in Vascular Biology and Cardiovascular Disease, 2016, Atlanta, USA.

Parliamentary and Scientific Committee STEM for BRITAIN event, 2017, London, UK.

12th International Symposium on Biomechanics in Vascular Biology and Cardiovascular Disease, 2017, Rotterdam, the Netherlands.

7th European Cell Mechanics Meeting, 2017, Lake Windermere, UK.

Awards:

Silver Award, Parliamentary and Scientific Committee STEM for BRITAIN event, 2017.

First place - Department of Mechanical Engineering PhD poster event, 2015.

Four travel grants awarded by the University of Sheffield Learned Society Fund, 2014 - 2017.